



ISSN 1343-2230

CNS-REP-96
March, 2018

Annual Report 2016

Center for Nuclear Study,
Graduate School of Science, the University of Tokyo

Editor
Taku Gunji

Center for Nuclear Study

CNS Reports are available from:
Wako-Branch at RIKEN
Center for Nuclear Study,
Graduate School of Science, the University of Tokyo
2-1 Hirosawa, Wako
351-0198, Japan
Tel: +81-48-464-4191
Fax: +81-48-464-4554

Annual Report 2016

Center for Nuclear Study,
Graduate School of Science, the University of Tokyo

Preface

This is the annual report of the Center for Nuclear Study (CNS), Graduate School of Science, the University of Tokyo, for the fiscal year 2016 (April 2016 through March 2017). In 2016, a new group for fundamental symmetry has been added. During this period, a lot of research activities in various fields of nuclear physics have been carried out and a wide variety of fruitful results have been obtained at CNS. This report summarizes research such activities. I hereby mention some highlights of the report.

The Center for Nuclear Study (CNS) aims to elucidate the nature of nuclear system by producing the characteristic states where the Isospin, Spin and Quark degrees of freedom play central roles. These researches in CNS lead to the understanding of the matter based on common natures of many-body systems in various phases. We also aim at elucidating the explosion phenomena and the evolution of the universe by the direct measurements simulating nuclear reactions in the universe. In order to advance the nuclear science with heavy-ion reactions, we develop AVF upgrade, CRIB and SHARAQ facilities in the large-scale accelerators laboratories RIBF. We started a new project OEDO for a new energy-degrading scheme, where a RF deflector system is introduced to obtain a good quality of low-energy beam. In 2016, a new group for fundamental symmetry has been added. We promote collaboration programs at RIBF as well as RHIC-PHENIX and ALICE-LHC with scientists in the world, and host international meetings and conferences. We also provide educational opportunities to young scientists in the heavy-ion science through the graduate course as a member of the department of physics in the University of Tokyo and through hosting the international summer school.

The NUSPEQ (NUclear SPectroscopy for Extreme Quantum system) group studies exotic structures in high-isospin and/or high-spin states in nuclei. The CNS GRAPE (Gamma-Ray detector Array with Position and Energy sensitivity) is a major apparatus for high-resolution in-beam gamma-ray spectroscopy. Missing mass spectroscopy using the SHARAQ is used for another approach on exotic nuclei. In 2016, the following progress has been made. Experimental data taken in 2013 under the EURICA collaboration has been analyzed for studying octupole deformation in neutron-rich Ba isotopes and preparing publication. Exochemic charge exchange reaction (${}^8\text{He}, {}^8\text{Li}^*(1^+)$) on ${}^4\text{He}$ has been analyzed for studying spin-dipole response of few-body system on the photon line. A new experiment measuring the ${}^4\text{He}({}^8\text{He}, {}^8\text{Be})4n$ reaction was performed for better statistics and better accuracy in order to verify a candidate of the ground state of the tetra neutrons just above the $4n$ threshold, which is under analysis. A DAQ system for the CNS GRAPE was upgraded, where event building system is included for several digitizing modules based on sampling ADCs and FPGAs on boards.

The nuclear astrophysics group in CNS is working for experimental studies with the low-energy RI beam separator CRIB. In FY2016, experiments on the alpha-cluster structure in the ${}^{22}\text{Mg}$ nucleus, ${}^7\text{Be}(n, \alpha)/(n, p)$ astrophysical reactions using the Trojan Horse method, production of ${}^7\text{Be}$ -implanted target, and the proton resonant scattering experiment with ${}^{26}\text{Al}$ isomeric beam were performed at CRIB under international collaborations including Korean, Italian, UK, and Chinese groups. The isomeric ${}^{26}\text{Al}$ beam production at CRIB was for the first time, and a high isomeric purity of over 30% was achieved. A strong indication of an exotic linear-chain cluster structure in ${}^{14}\text{C}$ nucleus was presented based on the ${}^{10}\text{Be}+\alpha$ resonant scattering experiment previously performed at CRIB.

Main goal of the quark physics group is to understand the properties of hot and dense nuclear matter created by colliding heavy nuclei at relativistic energies. The group has been involved in the PHENIX experiment at Relativistic Heavy Ion Collider (RHIC) at Brookhaven National Laboratory, and the ALICE experiment at Large Hadron Collider (LHC) at CERN. As for ALICE, the group has involved in the data analyses, which include the measurement of low-mass lepton pairs in Pb-Pb and p-Pb collisions, heavy flavor baryon measurements in pp and p-Pb collisions, particle correlations with large rapidity gap in p-Pb collisions, and searches for dibaryons in Pb-Pb collisions. The group has involved in the ALICE-TPC upgrade using a Gas Electron Multiplier (GEM). New readout chip

of the TPC upgrade, called as SAMPA, was tested and development of the new data readout system for the TPC upgrade, which aims online data processing by utilizing FPGA and GPU, has begun in 2016.

The Exotic Nuclear Reaction group studies various exotic reactions induced by beams of unstable nuclei. One subject is inverse-kinematics (p, n) reaction. In 2016 a set of neutron counters PANDORA was developed and an in-beam test was performed. Candidate nuclei to study is high spin isomers such as $^{52}\text{Fe}(12^+)$. Development of isomer beam was carried out at HIMAC.

The OEDO/SHARAQ group pursues experimental studies of RI beams by using the high-resolution beamline and the SHARAQ spectrometer. A mass measurement by TOF- $B\rho$ technique for very neutron-rich calcium isotopes around $N=34$ was successfully performed. The parity-transfer charge exchange ($^{16}\text{O}, ^{16}\text{F}$) was studied, since the reaction is expected to probe the 0^- strength in nuclei. The result of the study was recently published. The OEDO project, which is a major upgrade of the high-resolution beamline for RI beams with energies lower than 100 MeV/u, is ongoing. The beam line has been constructed in March 2017. The commissioning of the energy degrading scheme is scheduled in June 2017.

Two types of gaseous active target TPCs called GEM-MSTPC and CATs are developed and used for the missing mass spectroscopy. A new resonance in ^{30}S has been observed via the study of alpha inelastic scattering using GEM-MSTPC. The data analysis of astrophysical reaction (α, p) on ^{18}Ne and ^{22}Mg and the β -decay of ^{16}Ne followed by α emission. The study of Equation of State of nuclear matter using CATs is ongoing. The data analysis of deuteron inelastic scattering on $^{15,16}\text{O}$ and ^{132}Xe measured at HIMAC by using CAT-S is in progress. The measurement of giant monopole resonance in ^{132}Sn by using CAT-S has been done at RIBF in April, 2016. Larger volume active target CAT-M is being developed aiming at 10-times larger yield.

A new measurement of the isobaric analog resonances of RRC31 was analyzed. Due to the low production yield of ^{34}Si beam from ^{48}Ca at 64 MeV/nucleon which was 1 orders magnitudes smaller than the estimation of EPAX-2.15, we could not improve the excitation function though the experimental result was observed to be consistent with the previous measurement. For the development of the exotic targets, the feasibility study of $\text{Ti-}^3\text{H}$ was carried out by making a thin $\text{Ti-}^2\text{H}$ target. The ^2H in the $\text{Ti-}^2\text{H}$ target will desorb when the target is heated upto above 300 degrees in Celsius. As far as the target temperature is kept below 100 degrees, erosion of ^3H from $\text{Ti-}^3\text{H}$ will be 0. Activity measurement after ^{20}Ne beam of 8.2 MeV/nucleon on the $\text{Ti-}^2\text{H}$ target, any strong activity was not measured, meaning that Toyama Univ can decommission the target after the campaign of the experiments. A thin and higher concentration ratio of the target have been also under testing. Single-crystal (sc) diamond detector is considered as a next-generation semiconductor detector. We found that the pulse height defect for fission fragments of ^{252}Cf was almost saturated with the electric field of 2 V/ μm .

One of the major tasks of the accelerator group is the AVF upgrade project that includes development of ion sources, upgrading the AVF cyclotron of RIKEN and the beam line to CRIB. Development of ECR heavy ion source is to provide new HI beams, higher and stable beams of metallic ions, and to improve the control system. The Hyper ECR and the Super ECR sources provide all the beams for the AVF cyclotron and support not only CRIB experiments but also a large number of RIBF experiments. Injection beam monitoring and control are being developed and studied in order to measure four-dimensional emittance. Detailed studies of the optics from the ion sources in consideration of the space charge effect are expected to improve transmission and qualities of beams for the RIBF facility.

In 2016, The beam intensities of some light ions accelerated by AVF cyclotron have been doubled by improving the extraction system of the Hyper ECR.

To investigate the matter-antimatter asymmetry (CP violation) in the universe, and to understand the CP violating components in the fundamental interactions, the experimental project to search for the electric dipole moment (EDM) of the ^{210}Fr is going on. The thermal ionizer to produce the ^{210}Fr

with fusion reaction, an optical lattice to accumulate the cooled atoms, and an atomic interferometer to measure the frequency of the spin precession of ^{210}Fr are ready now. The yield of the Fr ions with 10^6 Fr⁺/s has been achieved, and the improvement of the trapping efficiency to get the high intensity cooled Fr atoms will be done by upgrading the laser optics.

The nuclear theory group participate a project, “ Priority Issue 9 to be tackled by using the Post-K Computer ” and promotes computational nuclear physics utilizing supercomputers. In 2016, we revealed the quantum phase transition of nuclear shape in neutron-rich Zr isotopes by the Monte Carlo shell model. In parallel, we have been promoting the CNS-RIKEN collaboration project on large-scale nuclear structure calculations and performed shell-model calculations under various collaborations with many experimentalists for investing the exotic structure of neutron-rich nuclei, such as $^{38,40}\text{P}$, ^{48}Ca , ^{55}Ca , ^{128}Cd , and ^{132}Sn .

The 15th CNS International Summer School (CNSSS16) has been organized in August 2016 with many invited lecturers including four foreign distinguished physicists.

Finally, I thank Mr. Oki and other administrative staff members for their heartfelt contributions throughout the year.

Susumu Shimoura
Director of CNS

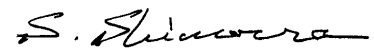


Table of Contents

1a. Experimental Nuclear Physics: Low and Intermediate Energies

Simulation of the $^{79}\text{Se}(d, p)^{80}\text{Se}^*$ reaction measurement at OEDO	1
<i>N. Imai, M. Dozono, S. Michimasa, S. Ota, T. Sumikama, O. Beliuskina, S. Hayakawa, C. Iwamoto, K. Kawata, N. Kitamura, S. Masuoka, P. Schrock, H. Shimizu, S. Shimoura, K. Wimmer, K. Yako, H. Yamaguchi, L. Yang, N. Chiga, D. Nagae, S. Naimi, S. Omika, H. Otsu, H. Sakurai, D. Suzuki, K. Yamada, S. Takeuchi, S. Kawase, N. Aoi, E. Ideguchi, H.J. Ong</i>	
Search for double Gamow-Teller giant resonance in ^{48}Ti via the $(^{12}\text{C}, ^{12}\text{Be}\gamma)$ reaction	3
<i>M. Takaki, T. Uesaka, N. Aoi, M. Dozono, T. Furuno, C. Iwamoto, T. Kawabata, M. Kobayashi, Y. Matsuda, M. Matsushita, S. Michimasa, S. Ota, M. Sasano, L. Stuhl, A. Tamii, M. Tsumura, R. Yokoyama, J. Zenihiro and S. Shimoura</i>	
Development of a radioactive tritium target for two-neutron transfer reactions	5
<i>T. Koiwai, T. Kumon, Y. Shimizu, K. Wimmer, N. Imai, M. Niikura, Y. Hatano, and P. Shi</i>	
Perspectives for Missing Mass Studies at OEDO	7
<i>P. Schrock, N. Imai, H. J. Ong, D. Suzuki, K. Wimmer, and H. Yamaguchi</i>	
Experimental investigation of a linear-chain structure in ^{14}C	9
<i>H. Yamaguchi, D. Kahl, S. Hayakawa, Y. Sakaguchi, K. Abe, T. Nakao, T. Suhara, N. Iwasa, A. Kim, D.H. Kim, S.M. Cha, M.S. Kwag, J.H. Lee, E.J. Lee, K.Y. Chae, Y. Wakabayashi, N. Imai, N. Kitamura, P. Lee, J.Y. Moon, K.B. Lee, C. Akers, H.S. Jung, N.N. Duy, L.H. Khiem, C.S. Lee</i>	
Measurements of the $^7\text{Be}+n$ Big-Bang Nucleosynthesis reactions at CRIB by the Trojan Horse method	11
<i>S. Hayakawa, K. Abe, O. Beliuskina, S. M. Cha, K. Y. Chae, S. Cherubini, P. Figuera, Z. Ge, M. Gulino, J. Hu, A. Inoue, N. Iwasa, D. Kahl, A. Kim, D. H. Kim, G. Kiss, S. Kubono, M. La Cognata, M. La Commara, L. Lamia, M. Lattuada, E. J. Lee, J. Y. Moon, S. Palmerini, C. Parascandolo, S. Y. Park, D. Pierroutsakou, R. G. Pizzone, G. G. Rapisarda, S. Romano, H. Shimizu, C. Spitaleri, X. D. Tang, O. Trippella, A. Tumino, P. Vi, H. Yamaguchi, L. Yang, and N. T. Zhang</i>	
Mixed isomeric and ground state ^{26}Al proton scattering	13
<i>D. Kahl, H. Shimizu, H. Yamaguchi, K. Abe, O. Beliuskina, S. M. Cha, K. Y. Chae, A. A. Chen, Z. Ge, S. Hayakawa, N. Imai, N. Iwasa, A. Kim, D. H. Kim, M. J. Kim, S. Kubono, M. S. Kwag, J. Liang, J. Y. Moon, S. Nishimura, S. Oka, S. Y. Park, A. Psaltis, T. Teranishi, Y. Ueno, and L. Yang</i>	
Optical model potentials for $^6\text{He} + ^{64}\text{Zn}$ from $^{63}\text{Cu}(^7\text{Li}, ^6\text{He})^{64}\text{Zn}$ reaction analysis	15
<i>L. Yang, C. J. Lin, H. M. Jia, N. R. Ma, L. J. Sun, D. X. Wang, F. Yang, and X. X. Xu</i>	
Direct mass measurement of neutron-rich calcium isotopes beyond $N = 34$	17
<i>M. Kobayashi, S. Michimasa, Y. Kiyokawa, H. Baba, G. P. A. Berg, M. Dozono, N. Fukuda, T. Furuno, E. Ideguchi, N. Inabe, T. Kawabata, S. Kawase, K. Kisamori, K. Kobayashi, T. Kubo, Y. Kubota, C. S. Lee, M. Matsushita, H. Miya, A. Mizukami, H. Nagakura, D. Nishimura, H. Oikawa, S. Ota, H. Sakai, S. Shimoura, A. Stolz, H. Suzuki, M. Takaki, H. Takeda, S. Takeuchi, H. Tokieda, T. Uesaka, K. Yako, Y. Yamaguchi, Y. Yanagisawa, R. Yokoyama, and K. Yoshida</i>	
Measurement of Isoscalar Giant Monopole Resonance in ^{132}Sn using CAT-S	19
<i>S. Ota, H. Tokieda, C. Iwamoto, M. Dozono, U. Garg, S. Hayakawa, K. Kawata, N. Kitamura, M. Kobayashi, S. Masuoka, S. Michimasa, A. Obertelli, D. Suzuki, R. Yokoyama, J. Zenihiro, H. Baba, O. Beliuskina, S. Chebotaryov, P. Egelhof, T. Harada, M.N. Harakeh, K. Howard, N. Imai, M. Itoh, Y. Kiyokawa, C.S. Lee, Y. Maeda, Y. Matsuda, E. Milman, V. Panin, H. Sakaguchi, P. Schrock, S. Shimoura, L. Stuhl, M. Takaki, K. Taniue, S. Terashima, T. Uesaka, Y.N. Watanabe, K. Wimmer, K. Yako, Y. Yamaguchi, Z. Yang, and K. Yoneda</i>	
Production of a ^7Be implanted target for the study of the primordial ^7Li problem in the Big-Bang Nucleosynthesis ..	21

A. Inoue, A. Tamii, H. Yamaguchi, K. Abe, S. Adachi, N. Aoi, M. Asai, M. Fukuda, G. Gey, T. Hashimoto, S. Hayakawa, E. Ideguchi, J. Isaak, N. Kobayashi, Y. Maeda, H. Makii, K. Matsuta, M. Mihara, M. Miura, T. Shima, H. Shimizu, R. Tang, D. T. Tran, L. Yang

Searching for the experimental evidence of α -cluster structure in ^{22}Mg	23
<i>K.Y. Chae, S.M. Cha, K. Abe, S.H. Bae, D.N. Binh, S.H. Choi, N.N. Duy, K.I. Hahn, S. Hayakawa, B. Hong, N. Iwasa, D. Kahl, L.H. Khiem, A. Kim, D.H. Kim, E.J. Kim, G.W. Kim, M.J. Kim, K. Kwag, M.S. Kwag, E.J. Lee, S.I. Lim, B. Moon, J.Y. Moon, S.Y. Park, V.H. Phong, H. Shimizu, H. Yamaguchi, L. Yang, and Z. Ge</i>	
Measurement of $^4\text{He}(^8\text{He}, ^8\text{Be})$ reaction for verifying tetra-neutron resonance	25
<i>S. Masuoka, S. Shimoura, M. Takaki, D. S. Ahn, H. Baba, M. Dozono, N. Fukuda, T. Harada, E. Ideguchi, N. Imai, N. Inabe, C. Iwamoto, K. Kawata, N. Kitamura, M. Kobayashi, Y. Kondo, T. Kubo, Y. Maeda, F. M. Marqu, M. Matsushita, S. Michimasa, R. Nakajima, T. Nakamura, N. Orr, S. Ota, H. Sakai, H. Sato, P. Schrock, L. Stuhl, T. Sumikama, H. Suzuki, H. Takeda, K. Taniue, H. Tokieda, T. Uesaka, K. Wimmer, K. Yako, Y. Yamaguchi, Y. Yanagisawa, R. Yokoyama, K. Yoshida and J. Zenihiro</i>	
Development of producing high-spin isomer beam by ^{58}Ni fragmentation reactions	27
<i>K. Kawata, K. Yako, S. Ota, M. Dozono, J. Zenihiro, C. Iwamoto, N. Kitamura, M. Kobayashi, H. Sakai, M. Sasano, M. Takaki, S. Masuoka, S. Michimasa, R. Yokoyama, L. Stuhl, E. Takada</i>	

1b. Experimental Nuclear Physics: PHENIX Experiment at BNL-RHIC and ALICE Experiment at CERN-LHC

Low mass dielectron measurements with ALICE at the LHC	29
<i>T. Gunji for the ALICE Collaboration</i>	
Charm baryon measurements with ALICE at the LHC	31
<i>Y. S. Watanabe for the ALICE Collaboration</i>	
J/ψ production in p-Pb collisions at $\sqrt{s_{\text{NN}}} = 5.02$ TeV	33
<i>S. Hayashi, H. Hamagaki, and T. Gunji</i>	
Measurement of two particle correlations in p-Pb collisions at LHC-ALICE	35
<i>Y. Sekiguchi, H. Hamagaki, and T. Gunji</i>	
π^0 and η measurement of direct photons via external conversions in pp collisions at $\sqrt{s} = 5.02$ TeV	37
<i>H. Murakami for the ALICE collaboration</i>	

2. Accelerator and Instrumentation

Construction of OEDO beamline	39
<i>S. Michimasa, S. Shimoura, M. Matsushita, N. Imai, K. Yako, H. Yamaguchi, S. Ota, S. Nakajima, M. Dozono, E. Ideguchi, H. Sakurai, K. Yoshida, Y. Yanagisawa, K. Kusaka, M. Ohtake, T. Sumikama, and K. Yamada</i>	
Development of the high intensity surface ionizer to search for the permanent EDM with Fr atoms	41
<i>Y. Sakemi, K.S. Tanaka, K. Harada, H. Kawamura, T. Inoue</i>	
Feasibility study of a noble gas scintillation counter as a heavy ion detector	43
<i>Y. Matsuda, J. Okamoto, J. Zenihiro, S. Ota, O. Beliuskina, M. Dozono, S. Hayakawa, N. Imai, C. Iwamoto, S. Michimasa, Y. Mizoi, R. Nakajima, E. Takada, K. Yako, and R. Yokoyama</i>	
Construction of multi wire drift chambers for focal-plane tracking detectors in BigRIPS	45
<i>K. Yako, S.Y. Matsumoto, T. Nishi, M. Takaki, H. Fujioka, K. Itahashi, T. Kawabata, A. Sakaue, Y.K. Tanaka, T. Uesaka, Y.N. Watanabe, and J. Zenihiro</i>	
Characterization of a tritium target for (t, p) experiments at TRIUMF	47

N. Kitamura, K. Wimmer, P. C. Bender, G. Hackman, J. Henderson, N. Imai

GEM-TPC Development Collaboration - Development of a new active target CAT-M -	49
<i>S. Ota, C. Iwamoto, R. Kojima, H. Tokieda, M. Dozono, T. Gunji, S. Hayakawa, N. Imai, S. Michimasa, Y. Mizoi, D. Suzuki, H. Yamaguchi</i>	
Performance evaluation of a Dual Gain Multi-layer Thick GEM for CAT-M	51
<i>C. Iwamoto, S. Ota, H. Tokieda, R. Kojima, C.S. Lee, T. Gunji, H. Yamaguchi, S. Michimasa, Y. Mizoi, D. Suzuki, M. Dozono, O. Beliuskina, R. Nakajima, Y. Matuda, R. Yokoyama, S. Hayakawa, N. Imai, J. Zenihiro, J. Okamoto, K. Yako, and E. Takada</i>	
Event Search in CAT	53
<i>H. Tokieda, S. Ota, C. Iwamoto, and R. Kojima</i>	
Energy/timing measurements with single crystal diamond detector at HIMAC	55
<i>O. Beliuskina, N. Imai, S. Michimasa, R. Yokoyama, M. Dozono, S. Hayakawa, C. Iwamoto, Y. Matsuda, Y. Mizoi, R. Nakajima, J. Okamoto, S. Ota, E. Takada, K. Yako, and J. Zenihiro</i>	
Beam transport analysis of RIKEN AVF Cyclotron injection line by four-dimensional emittance in view of the space charge effect	57
<i>Y. Kotaka, Y. Ohshiro, H. Yamaguchi, N. Imai, Y. Sakemi, T. Nagatomo, J. Ohnishi, A. Goto, M. Kase, K. Hatanaka, H. Muto and S. Shimoura</i>	
Beam extraction from concave plasma boundary in Hyper ECR ion source	59
<i>Y. Ohshiro, Y. Kotaka, H. Muto, H. Yamaguchi, N. Imai, Y. Sakemi and S. Shimoura</i>	
Development of an active stopper for isomer tagging	61
<i>M. Dozono, K. Yako, S. Ota, H. Tokieda, C. Iwamoto, L. Stuhl, K. Kawata, S. Michimasa, M. Takaki, R. Yokoyama, N. Kitamura, S. Masuoka, T. Uesaka, J. Zenihiro, and E. Takada</i>	
PANDORA, a large volume low-energy neutron detector with real-time neutron-gamma discrimination	63
<i>L. Stuhl, K. Yako, M. Sasano, J. Yasuda, H. Baba, S. Ota, and T. Uesaka</i>	

3. Theoretical Nuclear Physics

Shell-model study on double Gamow-Teller transition of ^{48}Ca	65
<i>N. Shimizu, J. Menéndez, and K. Yako</i>	
Monte Carlo shell model calculations for structure of ^{66}Ni	67
<i>Y. Tsunoda, T. Otsuka, N. Shimizu, M. Honma, and Y. Utsuno</i>	
Quantum phase transition in the shape of Zr isotopes	69
<i>T. Togashi, Y. Tsunoda, T. Otsuka, and N. Shimizu</i>	
Structure of Be and C nuclei in Monte Carlo shell model	71
<i>T. Yoshida, N. Shimizu, T. Abe, and T. Otsuka</i>	
Search for super and normal deformed states in nuclei around $A = 40$ using large-scale shell-model calculations	73
<i>T. Ichikawa, N. Shimizu, Y. Utsuno, and T. Otsuka</i>	
Recent progress in the calculation of exotic nuclei based on nuclear force	75
<i>N. Tsunoda, T. Otsuka, and N. Shimizu</i>	

4. Other Activities

The 15th CNS International Summer School CNSSS16	77
<i>N. Imai, T. Gunji, E. Hiyama, H. Liang, S. Michimasa, Y. Mizoi, S. Ota, T. Otsuka, H. Sakai, H. Sakurai, N. Shimizu, S. Shimoura, H. Ueno, T. Uesaka, Y. Utsuno, K. Yako, H. Yamaguchi, and T. Yoshida</i>	
Laboratory Exercise for Undergraduate Students	79
<i>S. Ota, M. Niikura, N. Kitamura, T. Saito, K. Yako, H. Sakurai and S. Shimoura</i>	

Appendices

Symposium, Workshop, Seminar, PAC and External Review	81
CNS Reports	82
Publication List	83
Talks and Presentations	92
Personnel	97

Experimental Nuclear Physics: Low and Intermediate Energies

Simulation of the $^{79}\text{Se}(d, p)^{80}\text{Se}^*$ reaction measurement at OEDO

N. Imai, M. Dozono, S. Michimasa, S. Ota, T. Sumikama^a, O. Beliuskina, S. Hayakawa, C. Iwamoto, K. Kawata, N. Kitamura, S. Masuoka, P. Schrock, H. Shimizu, S. Shimoura, K. Wimmer^b, K. Yako, H. Yamaguchi, L. Yang, N. Chiga^a, D. Nagae^a, S. Naimi^a, S. Omika^a, H. Otsu^a, H. Sakurai^a, D. Suzuki^a, K. Yamada^a, S. Takeuchi^c, S. Kawase^d, N. Aoi^e, E. Ideguchi^e, H.J. Ong^e

Center for Nuclear Study, Graduate School of Science, University of Tokyo

^a*RIKEN Nishina Center*

^b*Department of Physics, Univ. of Tokyo*

^c*Tokyo Institute of Technology*

^d*Department of Advanced Energy Science and Engineering, Kyushu Univ.*

^e*RCNP, Osaka Univ.*

After the uranium is burned in the nuclear power plant, some amount of nuclear wastes remain. Among them, the elements whose half-lives are longer than 200 thousands years are called as long lived fission products (LLFP). They are ^{79}Se , ^{93}Zr , ^{99}Tc , ^{107}Pd , ^{126}Sn , ^{129}I , and ^{135}Cs . The precise cross sections of (n, γ) reaction of these nuclei are required for designing the nuclear power plant and for decommissioning them. The ImpACT program aims at searching for effective ways of decommissioning four LLFPs, ^{79}Se , ^{93}Zr , ^{107}Pd , ^{126}Sn . The target of these nuclei are needed to measure (n, γ) reactions. However, because these nuclei are radioactive, it is in general hard to make targets of these enriched isotopes. Though the (n, γ) cross sections on ^{93}Zr [1], ^{107}Pd [2] and ^{126}Sn [3] were recently measured, in the case of ^{79}Se , because the selenium is chemically toxic, the reaction of ^{79}Se has never been measured. As a result, the uncertainty of the (n, γ) cross section is much larger than those of other LLFPs.

The cross section of $^{79}\text{Se}(n, \gamma)$ was studied with the indirect ways. The reaction can be considered to be divided to two processes, the formation of the compound nucleus and the γ decay from the unbound states. The first one can be evaluated by using the global optical potential. The probability of the γ decay depends on the nuclear structure of the nucleus. The reverse reaction $^{80}\text{Se}(\gamma, \gamma')$ was measured [4] to study the dipole strength distribution of ^{80}Se . However to get (n, γ) reaction cross sections, some theoretical assumption are needed.

The surrogate method is another indirect method to determine the nuclear reaction involving the radioactive nucleus [5]. The method was originally proposed to study the neutron induced fission reaction. The method depends on the Weisskopf-Ewing limit of the Hauser-Feshbach theory which assumes that the decay probability from the unbound states of the compound nucleus is independent from the spin parity. With this assumption, the γ decay probability from the unbound states can be evaluated from the other nuclear reaction even if the final spin-parity distributions after the reactions are different from each other. However, recent study of the surrogate reaction for the (n, γ) reaction reports that the Weisskopf-Ewing assumption does not work at low energy neutron capture [6]. To compensate the mismatch of the angular momenta in the final states between the transfer

reaction and the capture reaction, the surrogate ratio method is employed [7]. In this method, two surrogate reactions are measured. While one is the aimed reaction, the other is the reaction whose (n, γ) reactions have been already measured. The ratio of the aimed (n, γ) to the transfer reaction is assumed to be same as that of the others. In this study, we will also measure the $^{77}\text{Se}(d, p)^{78}\text{Se}$ reaction as well as $^{79}\text{Se}(d, p)^{80}\text{Se}$. Since the $^{77}\text{Se}(n, \gamma)^{78}\text{Se}$ reactions were already measured [8], we can deduce the $^{79}\text{Se}(n, \gamma)^{80}\text{Se}$ reaction cross section by using the surrogate ratio method.

The new point of the proposed experiment is that we will not measure the γ rays from the unbound states and, this determine the γ decay probability. The surrogate reactions including the surrogate ratio method have been performed in the normal kinematics so far. Because the reaction residue cannot be detected, the γ decay probability is deduced from the measurement of γ rays. Tracing the cascade transition from the high excited state is difficult. On the other hand, since we will measure the transfer reaction in inverse kinematics, the residue of the reaction can be identified, which means that we are free from the complex γ cascade transition. Comparing the yields of ^{80}Se and ^{79}Se measured in coincidence with recoiled proton can give the γ decay probability from the unbound state in ^{80}Se .

The ^{79}Se beam around 20 MeV/nucleon will be produced by the OEDO beamline. The beam will be directed on a deuterated polyethylene CD_2 target of 2 mg/cm². The recoiled particles will be detected by six telescope, each of which consists of SSD and CsI(Tl) detectors. The telescope will cover the scattering angles from 100 to 150 degrees. The SSD is divided to 16 channels in angle. Each strip covers about 3 degrees. Figure 1 shows the energy of the recoiled protons from the (d, p) reaction as a function of scattering angle in the laboratory frame. The one neutron separation energy of ^{80}Se is 9.913 MeV. The energy resolution of the proton is mostly due to the uncertainty of the reaction point in the target. With the current thickness of 2 mg/cm², the resolution of the final state will be 750 keV in the center of mass frame by measuring the recoiled proton. The momentum of the outgoing particles ^{80}Se will be analyzed by the first dipole (D1) magnet of the SHARAQ spectrometer. At the exit of the D1 magnet, two PPACs and the ionization chamber will be installed. PPACs will give

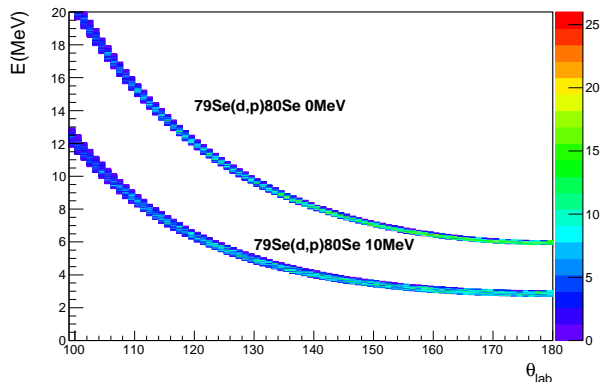


Figure 1. The simulated proton energy distribution of $^{79}\text{Se}(d,p)^{80}\text{Se}$. Two final states, the ground state and an excited state at 10 MeV, are assumed.

the time-of-flight (TOF) of ions. The ionization chamber will tell us the energy loss (dE) and the range in the gas. The TOF- dE -range and $B\rho$ information enables us to identify the ions. The experiment will be performed in fall of 2017. The preparation of the experiment is on-going.

References

- [1] R.L. Macklin, *Astrophys. Spa. Sci* 115 71 (1985).
- [2] K. Terada et al., *Progress in Nuclear Energy* 82, 118-121 (2015).
- [3] S. Zhang et al., *Radiochim. Acta* 94, 385 (2006).
- [4] A. Makinaga et al., *Phys. Rev. C.* 94 044304 (2016).
- [5] J. E. Escher et al., *Rev. of Mod. Phys.* 84, 353 (2012).
- [6] G. Boutox et al., *Phys. Lett. B* **712**, 319 (2012). (2012).
- [7] S.Q. Yan et al., *Phys. Rev. C.* **94** 015804 (2016).
- [8] S. Kawada, M. Igashira, T. Katabuchi, and M. Mizumoto, *J. Nucl. Sci. Tech.* 47, 643 (2010).

Search for double Gamow-Teller giant resonance in ^{48}Ti via the (^{12}C , $^{12}\text{Be}\gamma$) reaction

M. Takaki, T. Uesaka^a, N. Aoi^b, M. Dozono, T. Furuno^c, C. Iwamoto^b, T. Kawabata^c,
M. Kobayashi, Y. Matsuda^d, M. Matsushita, S. Michimasa, S. Ota, M. Sasano^a, L. Stuhl, A. Tamii^b,
M. Tsumura^c, R. Yokoyama, J. Zenihiro^a and S. Shimoura

Center for Nuclear Study, Graduate School of Science, University of Tokyo

^aRIKEN (The Institute of Physical and Chemical Research)

^bResearch Center for Nuclear Physics, Osaka University

^cDepartment of Physics, Kyoto University

^dCyclotron and Radio Isotope Center, Tohoku University

Giant resonances in nuclei are attributed to the highly collective vibrations. Such collective vibrations are often called phonons acting as bosons. Up to now, several types of multiphonon excitations, double isobaric analogue states, double dipole resonances and double quadrupole resonances, were observed, though their dependences on spin degree-of-freedom have not been confirmed unexpectedly [1]. A double Gamow-Teller (GT) giant resonance (DGTGR) is composed of two single GT giant resonances, and is the second order spin-isospin excitation. The DGTGR is a unique research object to study if the DGT transitions are just superposition of single GT excitations, or the spin-dependent correlations cause further changes to structures and responses of DGT states. The information on DGTGRs will provide a comprehensive understanding of the collective behavior in terms of phonon degrees of freedom.

Relevance of the transition process to $\beta\beta$ -decays (DBD) makes the DGT studies more attractive. Both the DGT transition and the DBD are described by the same spin-isospin operators. The $\beta\beta$ -decay occupies a small portion of the total DGT transition strength (sum rule [2]) of 0.01-0.1%, whereas the DGTGR covers a large portion of the strength. Thus, the observation of such large DGT strength serves as an alternative calibrator of the nuclear structure calculation for $\beta\beta$ -decay processes.

The DGTGR was firstly predicted by Auerbach *et al.*, in 1989 [3]. However, none of the experiments have successfully observed the DGTGR. One possible reason is that there is no clear probe for the DGT study. For the DGT transition, the double spin-isospin flip should occur, and thus, heavy-ion double charge exchange reactions (HIDCXs) are promising. In addition, a (p, n)-type HIDCX probe is much more effective to investigate the DGTGRs in heavy nuclei appearing the large collectivity, while a (n, p)-type probe can excite the DGT states only weakly [4]. We, thus, invented a new probe, (^{12}C , $^{12}\text{Be}\gamma$) reaction, on the basis of the results of our first HIDCX experiment [5]. The probe has significant advantages for the DGT study,

1. the transition from the ground state of ^{12}C to the second 0^+ state of ^{12}Be has strong DGT strength,
2. and the $^{12}\text{Be}(0_2^+)$ state is the isomeric state with the lifetime of 331 ns [6], and thus, the state can be dis-

tinguished by detecting the decay gamma rays and evaluating their characteristics.

The first point can not be satisfied by other stable ion induced reactions. The second point makes experiments easier because the isomeric state survives until reaching a final focal plane of a spectrometer. Then, the decay γ -rays can be detected far from a target position where the background level is considerably lower than around the target position.

This study aims at the observation of the DGTGR in ^{48}Ti through the $^{48}\text{Ca}(^{12}\text{C}, ^{12}\text{Be}\gamma)$ reaction experiment. We have conducted the experiment by employing the high-resolution magnetic spectrometer Grand Raiden at Research Center for Nuclear Physics, Osaka University. Detailed descriptions of the experimental setup can be found in ref. [7].

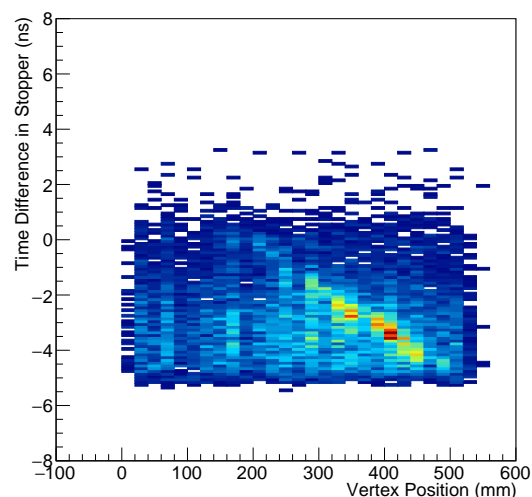


Figure 1. Correlation plot of the horizontal implantation position of ^{12}Be versus the vertex point of two-511-keV γ -rays.

The key of the experiment is the identification of the final state of the ^{12}Be nucleus by detecting the decay γ -rays. Several issues were observed and revisited as summarized in Ref. [7, 8]. Afterwards, the signal-to-noise ratio of the identification of $^{12}\text{Be}(0_2^+)$ was improved very much. Figure 1 shows the correlation of the horizontal position of the implantation measured by the time difference from two PMTs attached to the stopper scintillator versus the ver-

tex point of the two-511-keV γ -rays, where the coincidence events can be seen. With the selection of the events, the S/N ratio improves by factor of two.

Figure 2 shows the decay timing spectrum. It is seen that the decay time distribution has the exponential shape, which is from the coincidence events. The accidental coincidence events have a flat distribution as is shown as a gray line in Fig. 2. The black line is the result of the fitting with a function of $A + B \exp(-t/\tau)$. The τ parameter corresponds to the lifetime and the measured lifetime is 355 ± 45 ns, which is consistent with the known lifetime of 331 ns. The main background source is that the accidental coincidence of ^{12}Be and the β^+ -decay of the ^{11}C produced in the stopper plastic scintillator with knock-out reactions on ^{12}C .

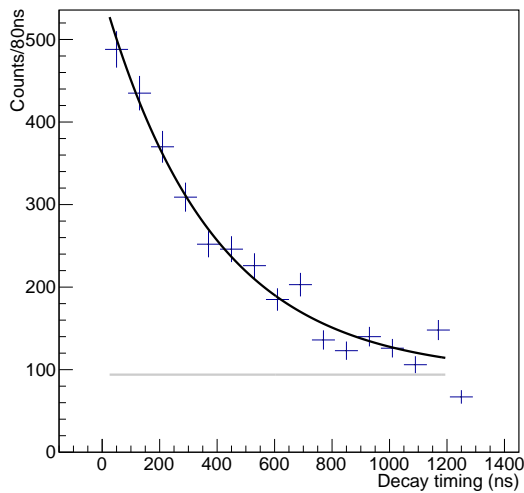


Figure 2. Decay timing spectrum of the $^{12}\text{Be}(0_2^+)$ state. The black curve shows the fitting result with the function of $A + B \exp(-t/\tau)$. The accidental coincidence background is shown with the gray line.

The further analysis to obtain the double differential cross section of the $^{48}\text{Ca}(^{12}\text{C}, ^{12}\text{Be}\gamma)$ reaction and the property of the DGT excitation is on-going.

References

- [1] Ph. Chomaz and N. Frascaria, *Physics Reports* **252**, 275 (1995).
- [2] H. Sagawa and T. Uesaka, *Phys. Rev. C* **94**, 064325 (2016).
- [3] N. Auerbach, L. Zamick and D.C. Zheng, *Annals of Physics* **192**, 77 (1989).
- [4] J. Blomgren *et al.*, *Phys. Lett. B* **362**, 34 (1995).
- [5] M. Takaki *et al.*, *JPS Conf. Proc.* **6**, 020038 (2015).
- [6] S. Shimoura *et al.*, *Phys. Lett. B* **560**, 31 (2003); *ibid* **654**, 87 (2007).
- [7] M. Takaki *et al.*, *CNS Rep.* **95**, 15 (2017).
- [8] M. Takaki *et al.*, *CNS Rep.* **94**, 9 (2016).

Development of a radioactive tritium target for two-neutron transfer reactions

T. Koiwai^a, T. Kumon^a, Y. Shimizu^a, K. Wimmer^a, N. Imai^b, M. Niikura^a, Y. Hatano^c, and P. Shi^c

^a Department of Physics, University of Tokyo

^b Center for Nuclear Study, Graduate School of Science, University of Tokyo

^c Hydrogen Isotope Science Center, Toyama University

The large neutron excess combined with the rather simple structure of the tritium nucleus as a bound system of one proton and two neutrons makes it an ideal probe or target nucleus for two-neutron pair transfer reactions as well as charge exchange reactions. Two-neutron transfer reactions are a well-known tool to study pairing properties in atomic nuclei. While they have been applied a lot in the past using tritium beams on stable targets, renewed interest in these kind of reaction comes from the fact that it is now possible to combine high intensity radioactive ion beams with a tritium target in inverse kinematics. The simultaneous transfer of two neutrons probes pairing properties of the nucleus and features that cannot be investigated with other methods. Two-neutron transfer reactions with radioactive beams have first been applied at REX-ISOLDE (CERN). In pioneering experiments [1,2] excited 0^+ states have been identified and characterized. Tritium can also serve as a probe for charge-exchange reactions. ($t, {}^3\text{He}$) reactions allow to study the Gamow-Teller strength distributions and to gain information on fundamental physics of the weak interaction as well as important input for understanding the double beta decay and astrophysics. Charge exchange reactions towards the other direction, converting the proton into another neutron, will result in a system of three neutrons. Precise missing mass spectroscopy of reactions like $t(X, 3n)Y$ will be used to investigate three neutron resonances. Such reactions give access to three nucleon forces in a new $T = 3/2$ channel. Experimental constraints on the isospin dependence of three nucleon forces are required for many applications in nuclear structure they also influence the structure of neutron stars through the equation of state of nuclear matter.

In order to study reactions with a radioactive tritium target at the RIBF, a target system is being designed. The tritium target can be used with fast beams from projectile fragmentation or in-flight fission at BigRIPS as well as with energy degraded beams at the future OEDO facility [3]. The challenge in building a radioactive tritium target for RIBF is twofold. First the size of the target has to be sufficiently large. At the RIBF typical beam spot sizes are several cm FWHM in stark contrast to the values of around 1 mm that are achieved through post acceleration at ISOL facilities. In order to perform two-neutron transfer reactions at RIBF a tritium target with an area of $2.5 \times 2.5 \text{ cm}^2$ is required. Secondly, the effective thickness of the tritium target material has to be sufficient to achieve reasonable luminosities for experiments with radioactive beams at RIBF. The target thickness has to result in a total activity below the limit of 10 TBq, but also has to be suitable for a wide variety of experiments with different physics goals as well as beam energies. The approach used for RIBF is loading a titanium

foil with hydrogen. Theoretically a hydrogen to titanium ratio H:Ti = 2:1 can be reached. However the large amount of hydrogen affects the mechanical stability critically [4]. This is a challenge for the construction of a large area tritium target. In order to establish a production and handling method for a tritium target, prototypes containing non-radioactive deuterium instead of tritium are used.

A first prototype target with D:Ti ratio of 0.24:1 has been produced at Toyama University by loading a 20 μm thick Ti foil with deuterons. The target has been characterized in an in-beam test at the AVF. The goals of the test experiment were:

1. determine the hydrogen content of the target independently
2. examine the stability of the target under high beam currents
3. evaluate the production of long-lived radioactive contaminants in the target by fusion reactions with the Ti carrier material

The experiment was performed at the E7b beam line. The TiD target was irradiated with a ${}^{20}\text{Ne}$ beam at an energy of 8.2 MeV/u. The setup is shown in Fig. 1. In laboratory for-

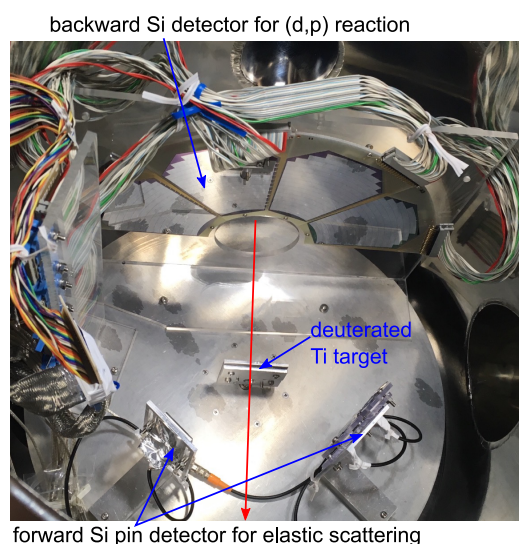


Figure 1. Experimental setup at the E7b beam line. The setup consists of the deuterated target foil in the center, three PIN diode detectors to monitor the elastic scattering, and an array of silicon strip detectors upstream of the target.

ward direction, three PIN diodes detected elastic scattered deuterons. They were shielded with an Al cover to stop elastic scattered beam. Upstream of the target an

silicon strip detectors was placed to simultaneously observe protons from (d, p) transfer reactions.

Downstream of the target, outside of the main scattering chamber, a stack of Ti foils was placed. These foils were used to investigate the activation of the target carrier material through the beam. Due to the relatively low beam energy, fusion and multi nucleon transfer reactions can result in the production of long-lived radio-nucleids. The activated foils were later measured with four GRAPE detector modules. The resulting γ -ray energy spectrum is shown in Fig. 2. The spectrum is dominated by room background.

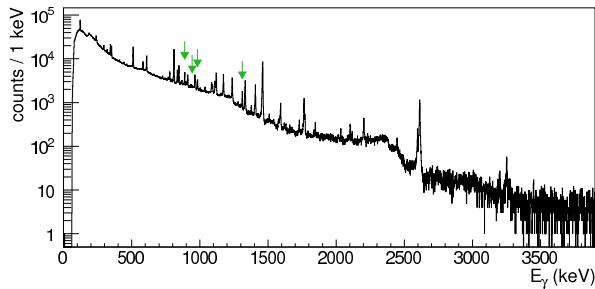


Figure 2. γ -ray energy spectrum of the activated Ti foils measured with GRAPE.

Four candidate transitions in ^{46}Sc and ^{48}V were found. This shows that activation of the target is not an issue for the eventual decommissioning of a tritium loaded target.

If the target is heated up to temperatures of several hundred degrees C a release of the stored hydrogen is expected. Therefore the residual gas in the chamber was monitored using a quadrupole mass spectrometer. The beam intensity was varied from 5 pA to 200 pA. Up to 20 pA (corresponding to $1.3 \cdot 10^{11}$ pps) the partial pressure of $A/q = 2$ was stable at background level. At higher currents release of deuterium from the target was observed. This intensity is far higher than any radioactive beam that will be used with the final tritium loaded target, and therefore no release of tritium is expected.

After this initial test, the production of target foils with a higher hydrogen content was investigated. For the production Ti foils with thickness of 2 and 5 μm were placed in an evacuated glass tube. The sample is sandwiched between two layers of Al_2O_3 , a porous material which ensures that the flatness of the sample. The sample was heated to 550° C, then deuterium gas was introduced. As the deuterium gas is absorbed into the Ti carrier material, the pressure in the chamber decreases. This is shown in Fig. 3 (a) for a 5 μm thick Ti foil. Several samples have been loaded, but the results depend on the sample. It is suspected that oxidation of the Al_2O_3 sandwich also affects the loading speed. For some samples the initial temperature was raised to 800° C. Higher temperatures should increase the hydrogen diffusion into the material. On the other hand the saturation concentration of deuterium in titanium decreases with increased temperature. Therefore, when saturation is reached, and the pressure does not decrease anymore, the temperature is lowered. This is shown in Fig. 3 (b) for a 2 μm thick Ti foil. Overall the different samples showed great variation in their behavior. Therefore an in-beam test

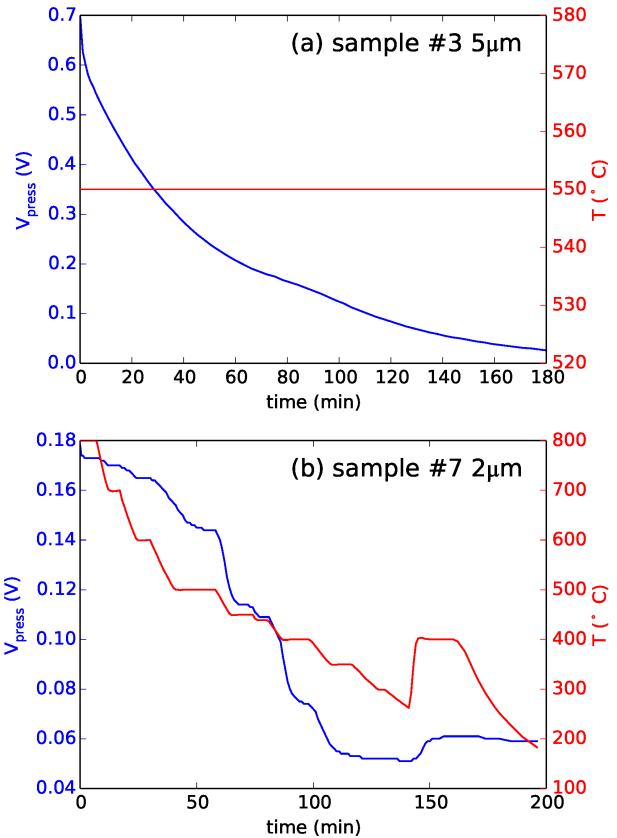


Figure 3. Pressure and temperature during the deuterium loading is planned to quantify the deuterium content with an improved setup.

References

- [1] K. Wimmer et al., Phys. Rev. Lett. 105 (2010) 252501.
- [2] K. Nowak, K. Wimmer et al., Phys. Rev. C 93 (2016) 044335.
- [3] S. Shimoura, Letter of Intent for OEDO project, the 14th NPPAC for nuclear physics experiment at RIBF, June 2014.
- [4] I. Lewkowicz, Solid State Phenomena, 49-50 (1996) 239.

Perspectives for Missing Mass Studies at OEDO

P. Schrock, N. Imai, H. J. Ong^a, D. Suzuki^b, K. Wimmer^c, and H. Yamaguchi

Center for Nuclear Study, Graduate School of Science, University of Tokyo

^a*Research Center for Nuclear Physics, Osaka University*

^b*RIKEN Nishina Center*

^c*Department of Physics, University of Tokyo*

1. Introduction

Transfer reactions are powerful tools in nuclear physics to study the structure of atomic nuclei. In such studies one or several nucleons are added to or removed from the nucleus of interest. By adding a single neutron to a certain nucleus, a single-particle orbital is populated and respective measurements reveal important information about the nuclear shell structure and astrophysical processes. For instance, the stability of exotic nuclear matter is investigated by probing the appearance of closed shells, the so-called magic numbers [1]. The derived single-particle structure and the neutron-capture cross sections are important quantities for astrophysical calculations of the r -process (rapid neutron capture) in nucleosynthesis [2] which describes the formation and abundance of heavy elements in the universe. The transfer of two neutrons is the optimal method for measurements of neutron-neutron pairing correlations in neutron-rich matter [3] which provide essential input for the description of surface properties of neutron stars [4].

Transfer reactions on unstable nuclei are studied in inverse kinematics, i.e. a radioactive isotope beam (RIB) is impinging on a target containing deuterons or tritons. Typically, the optimal beam energy for such reactions is in the order of 10 MeV/u. From the 4-momenta of the incoming beam and the recoiling protons the excitation energy is reconstructed (missing mass method). Additional γ -ray detection can improve the determination of the excitation energy due to the better energy resolution (see Sec. 3). After the selection of the excited state, the measured angular-differential cross section of the recoiled protons is compared to theoretical calculations and the respective shell structure information is derived. Typical differential cross sections as a function of the lab angle ϑ_{lab} are shown in Fig. 1 for two different momentum transfers Δl . The reaction $^{56}\text{Cr}(d, p)$ in inverse kinematics at 10 MeV/u beam energy is taken as an example. The clearly different patterns allow an assignment of the momentum quantum number of the selected state.

The RIB Factory (RIBF) at RIKEN provides at the moment the world's highest intensities for high-energy RIB beams. The "Optimized Energy Degrading Optics for RIB" (OEDO) beamline of CNS is aimed to degrade the beam energy, which is typically about 200 MeV/u, down to about 10 MeV/u. Hence, OEDO will allow for transfer reaction studies on a variety of neutron-rich nuclei which could not be studied so far.

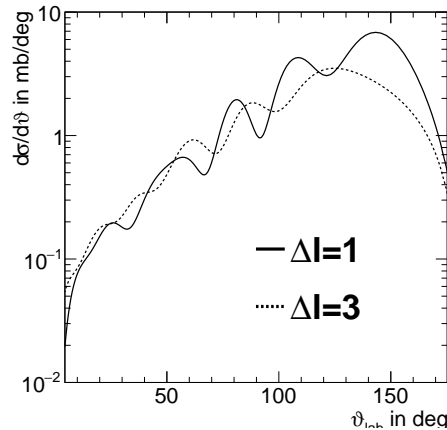


Figure 1. Typical angular-differential cross section for protons emitted in (d, p) transfer reactions in inverse kinematics.

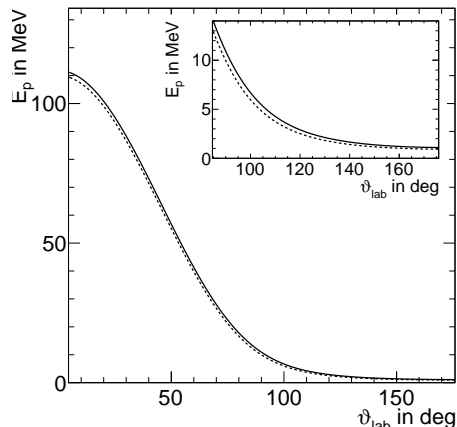


Figure 2. Typical proton kinetic energy from a (d, p) transfer reaction to the ground state (solid) and a state at 1 MeV (dashed).

2. Silicon Setup for Transfer Reactions

To utilize OEDO for transfer reactions, a silicon detector setup for position and energy measurements of the recoiling protons has been designed in a joint project of CNS, RCNP Osaka and RIKEN Nishina Center. Since the protons from transfer reactions in inverse kinematics are mainly emitted in backward direction in the laboratory system (see Fig. 1), the focus is on measurements at lab angles $\vartheta_{\text{lab}} > 90$ deg. A characteristic example for the proton kinetic energy as a function of the lab angle is shown in Fig. 2. The solid line represents the population of the ground state and the dashed line an excited state at 1 MeV. The inset shows the same functions only for the backward angles showing that the maximum proton energy is about 10 MeV.

The silicon array consists of 10×10 cm² Double Sided

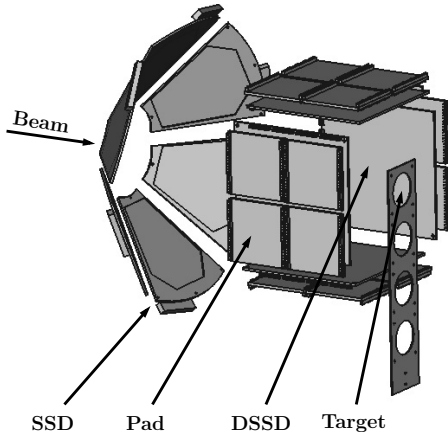


Figure 3. Technical drawing of the silicon setup.

Silicon Strip Detectors (DSSD) with 128×128 strips [5], $5 \times 5 \text{ cm}^2$ Silicon pads and annular-shaped Single Sided Silicon Strip Detectors (SSD) with 16 strips [6]. All detectors have thicknesses of approximately $300 \mu\text{m}$. The maximum energy loss of the recoiled protons in the silicon detectors is 6 MeV.

A technical drawing of the detector configuration is shown in Fig. 3. The beam is coming from the left side. Four DSSDs are arranged in an open-cube shape parallel to the beam with the center of the active area being 6 cm upstream of the target. The protons emitted close to 90 deg will punch through the detector ($E_p \approx 10 \text{ MeV}$, $\Delta E_{max} \approx 6 \text{ MeV}$). Therefore, an additional layer of pads will be installed in a 2×2 configuration behind each DSSD to stop the protons and to measure the total energy. Six SSDs will be placed 26 cm upstream of the target at a ϑ angle of 50 deg. The whole setup is compact enough to fit into the γ -ray detector array GRAPE [7]. Downstream of the target the diameter of the vacuum tube will be reduced in order to place the forward GRAPE units closer to the target and, thus, increase the detection efficiency.

3. Simulations

Simulations of several physics cases have been performed to study the performance of the setup. The beam profile of the OEDO beam (spread in position, angle and energy), the (expected) position and angle resolutions of the beamline detectors, the energy losses in the target (assuming $1 \text{ mg/cm}^2 \text{ CD}_2$) and the energy resolutions of the silicon detectors are taken into account. The whole setup covers ϑ_{lab} angles from 100 to 170 deg. Due to the larger cross sections for protons from (d, p) and (t, p) in backward direction, as shown in Fig. 1, the acceptance of the setup for these protons is about 55-60%, depending on the physics case. An excitation energy (missing mass) resolution of 250 keV FWHM can be achieved.

For certain physics cases this resolution might be insufficient to resolve excited states. In such cases, the additional γ -ray detection with GRAPE will allow to separate excited states of the heavy ejectile. Simulations with the full 18 units of GRAPE, in which the attenuation of γ -rays by the silicon detectors and the vacuum chamber are taken into account, show a full-energy peak efficiency of 1% and

an energy resolution of 1% for 1 MeV γ -rays. These values are in reasonable agreement with experimentally achieved values [8].

4. Status and Outlook

The mechanical design and construction of the support structure of the silicon setup is ongoing and expected to be completed in summer 2017.

A proposal for a first (d, p) experiment using this setup at RIPS (RIKEN) has been approved at the 17th NP-PAC meeting of RIKEN Nishina Center. An international collaboration for this upcoming pilot experiment has been established and a continuing campaign at OEDO is foreseen.

This setup is also suitable for two-neutron transfer reactions using the tritium loaded titanium target which is currently under development at CNS [9]. A further upgrade to cover measurements of higher-energetic light particles in forward direction (cf. Fig. 2) would allow for complementary experiments using the neutron removal or proton transfer reactions.

References

- [1] K. L. Jones et al., Nature **465** (2010) 09048.
- [2] R. L. Kozub et al., Phys. Rev. Lett. **109** (2012) 172501.
- [3] K. Wimmer et al., Phys. Rev. Lett. **105** (2010) 252501.
- [4] M. Hjorth-Jensen, Prog. Theor. Phys. Supplement **146** (2002) 289.
- [5] <http://www.micronsemiconductor.co.uk/pdf/cat.pdf> page 50-52
- [6] <http://www.micronsemiconductor.co.uk/pdf/cat.pdf> page 36
- [7] S. Shimoura, NIM A **525** (2004) 188.
- [8] M. Niikura et al., EPJ A **42** (2009) 471.
- [9] T. Koiwai et al., elsewhere in this report

Experimental investigation of a linear-chain structure in ^{14}C

H. Yamaguchi, D. Kahl^a, S. Hayakawa, Y. Sakaguchi, K. Abe, T. Nakao^b, T. Suhara^c, N. Iwasa^d,
A. Kim^{e,f}, D.H. Kim^f, S.M. Cha^e, M.S. Kwag^e, J.H. Lee^e, E.J. Lee^e, K.Y. Chae^e,
Y. Wakabayashi^g, N. Imai, N. Kitamura, P. Lee^h, J.Y. Moonⁱ, K.B. Leeⁱ, C. Akersⁱ, H.S. Jung^j,
N.N. Duy^{k,l}, L.H. Khiem^k, C.S. Lee^h

Center for Nuclear Study, Graduate School of Science, the University of Tokyo

^a*School of Physics and Astronomy, the University of Edinburgh,*

^b*Advanced Science Research Center, Japan Atomic Energy Agency*

^c*Matsue College of Technology*

^d*Department of Physics, Tohoku University*

^e*Department of Physics, Sungkyunkwan University*

^f*Department of Science Education, Ewha Womans University*

^g*RIKEN Nishina Center*

^h*Department of Physics, Chung-Ang University*

ⁱ*Institute for Basic Science*

^j*Wako Nuclear Science Center (WNSC), KEK*

^k*Institute of Physics, Vietnam Academy of Science and Technology*

^l*Dong Nai University*

Atomic nuclei are frequently observed to manifest effects of a clustered substructure within, and the particular importance of α particle clustering was pointed out even in the earliest works of nuclear physics. In 1956, Morinaga [1] came up with the novel idea of a particular cluster state: the linear-chain cluster state (LCCS). Now the LCCS is commonly considered as extreme and exotic, due to its presumed propensity to exhibit bending configurations. A theoretical prediction of LCCS in ^{14}C was made by Suhara and En'yo [2, 3] with an antisymmetrized molecular dynamics (AMD) calculation, yielding a prolate band (spin and parity $J^\pi = 0^+, 2^+, 4^+$) that has a configuration of an LCCS at a few MeV or more above the $^{10}\text{Be}+\alpha$ threshold. They showed that the LCCS is stabilized by its orthogonality to lower-lying states. At lower excitation energy in ^{14}C , there are triaxially deformed cluster states, which are constructed by bases with bending configurations. To fulfill the orthogonality condition between different states, higher-excited LCCSes are prohibited from bending. This is in stark contrast with ^{12}C , where no triaxial bands exist, and therefore such an LCCS-stabilizing mechanism does not work.

In the present work [4] we applied the $^{10}\text{Be}+\alpha$ resonant scattering method [5,6] in inverse kinematics to identify the predicted LCCS band in ^{14}C . Two similar measurements have been independently planned, carried out and published recently. The first work by Freer *et al.* [7] had a similar setup to ours, but with a more limited angular sensitivity. Another work by Fritsch *et al.* [8] used an active target setup, but detection was only possible for side scattering angles.

The present measurement was performed at the low-energy radioactive isotope beam separator CRIB. [9–11]. The ^{10}Be beam had a typical intensity of 2×10^4 particles per second, and the beam purity was better than 95%. The ^{10}Be beam at 25.8 MeV impinged on the gas target, which

was a chamber filled with helium gas at 700 Torr (930 mbar) and covered with a 20- μm -thick Mylar film as the beam entrance window. The measured ^{10}Be beam energy at the entrance of the helium gas target, after the Mylar film, was 24.9 ± 0.3 MeV. α particles recoiling to the forward angles were detected by ΔE - E detector telescopes.

Finally we obtained the excitation function of the $^{10}\text{Be}+\alpha$ resonant elastic scattering for 13.8–19.1 MeV, as shown in Fig. 1a, where events with $\theta_{\text{lab}} = 0$ – 8° ($\theta_{\text{cm}} = 164$ – 180°) were selected. We performed an R-matrix calculation to deduce the resonance parameters. The best fit parameters obtained from the analysis are summarized in Table 1. The angular dependence of the differential cross section, partly shown in Fig. 1b and 1c, were accounted for the assignment of J^π . Although the analysis was performed without any assumption from the theoretical calculation, we identified three resonances perfectly corresponded to the predicted LCCS band; J^π are identical, and their energies and spacings are consistent with the theoretical prediction. We claim this as the strongest indication of the LCCS ever found. It is also shown that both sets of level energies can be plotted almost on a line, $E_J = E_0 + \hbar^2/2\mathfrak{I}(J(J+1))$, where \mathfrak{I} is the moment of inertia of the nucleus. The linearity allows us to interpret the levels as a rotational band, and the low $\hbar^2/2\mathfrak{I} = 0.19$ MeV implies the nucleus could be strongly deformed, consistent with the interpretation of an LCCS. The experimental Γ_α of these resonances are also compared with the theoretical predictions in terms of the dimensionless partial width θ_α^2 in Table 1, although the precision of both is quite limited. The calculation qualitatively reproduces the feature that the experimental θ_α^2 is anti-correlated with J .

In summary, we searched for resonances in ^{14}C in the energy range $E_{\text{ex}}=14$ – 19 MeV with the resonant elastic scattering method and found several α -cluster-like states, ob-

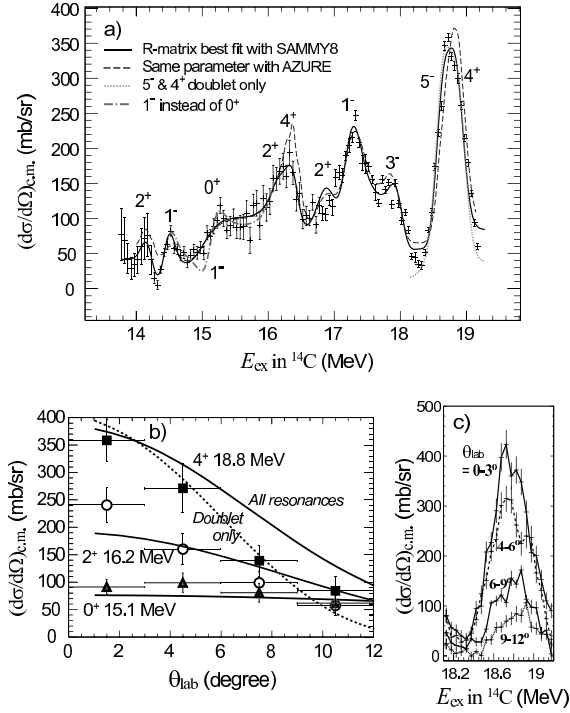


Figure 1. Experimental center-of-mass cross section of the $^{10}\text{Be}+\alpha$ resonant scattering $(d\sigma/d\Omega)_{\text{c.m.}}$. a) Excitation function for $\theta_{\text{lab}} = 0-8^\circ$, fitted with R-matrix calculations; the best R-matrix fit with SAMMY8 (solid curve, $\chi^2/n_{\text{dof}} = 62/82$), the same fit but with the 0^+ resonance replaced with 1^- (dash-dotted curve), and another fit only with a doublet of 4^+ and 5^- around 18.7 MeV (dotted curve). The dashed curve is with the above best fit parameters but calculated with AZURE. b) Angular distribution of $(d\sigma/d\Omega)_{\text{c.m.}}$ at the resonant energies of the 0^+ , 2^+ and 4^+ levels. The present experimental data points are compared with the R-matrix calculations, drawn as the curves. c) Peak profiles around 18.7 MeV for several angular ranges.

taining new spectroscopic information as displayed in Table 1. In spite of many previous measurements with various methods, the knowledge of observed resonances was quite limited, or completely absent. We put a particular emphasis on the discovery of broad and low-spin resonances around 15 MeV, which was not possible in previous measurements. This was made possible by the α -resonant elastic scattering with the thick-target method in inverse kinematics.

As investigated in the theoretical calculation of the ^{14}C system, the orthogonality between different quantum mechanical states is considered to play a key role in stabilizing the LCCS. Further studies may reveal whether this mechanism is universal in nuclear systems or particular to ^{14}C .

References

- [1] H. Morinaga, Phys. Rev. **101** (1956) 254.
- [2] T. Suhara and Y. Kanada-En'yo, Phys. Rev. C **82** (2010) 044301.
- [3] T. Suhara and Y. Kanada-En'yo, Phys. Rev. C **84** (2011) 024328.
- [4] H. Yamaguchi et al., Phys. Lett. B **766** (2017) 11.

Table 1. The resonance parameters in ^{14}C determined by the present work, compared with the AMD calculation [2]. Parameters in bold letters are for LCCS predicted in the calculation, and corresponding experimental resonances.

Present Work			
E_{ex} (MeV)	J^π	Γ_α (keV)	θ_α^2
14.21	(2^+)	17(5)	3.5%
14.50	1^-	45(14)	4.5%
15.07	0^+	760(250)	34(12)%
16.22	2^+	190(55)	9.1(27)%
16.37	(4^+)	15(4)	3.0%
16.93	(2^+)	270(85)	10.3%
17.25	(1^-)	190(45)	5.5%
18.02	(3^-)	31(19)	1.3%
18.63	5^-	72(48)	9.4%
18.87	4^+	45(18)	2.4(9)%

Suhara & En'yo [2]		
E_{ex} (MeV)	J^π	θ_α^2
15.1	0^+	16%
16.0	2^+	15%
19.2	4^+	9%

- [5] K. P. Artemov et al., Sov. J. Nucl. Phys. **52** (1990) 408.
- [6] H. Yamaguchi et al., Phys. Rev. C **87** (2013) 034303.
- [7] M. Freer et al., Phys. Rev. C **90** (2014) 054324.
- [8] A. Fritsch et al., Phys. Rev. C **93** (2016) 014321.
- [9] S. Kubono *et al.*, Eur. Phys. J. A **13** (2002) 217.
- [10] Y. Yanagisawa *et al.*, Nucl. Instrum. Methods Phys. Res., Sect. A **539** (2005) 74.
- [11] H. Yamaguchi *et al.*, Nucl. Instrum. Meth. Phys. Res., Sect. A **589**, (2008) 150–156.

Measurements of the ${}^7\text{Be}+n$ Big-Bang Nucleosynthesis reactions at CRIB by the Trojan Horse method

S. Hayakawa^a, K. Abe^a, O. Beliuskina^a, S. M. Cha^b, K. Y. Chae^b, S. Cherubini^{c,d}, P. Figuera^{c,d}, Z. Ge^e, M. Gulino^{c,f}, J. Hu^g, A. Inoue^h, N. Iwasaⁱ, D. Kahl^j, A. Kim^k, D. H. Kim^k, G. Kiss^e, S. Kubono^{a,e,g}, M. La Cognata^c, M. La Commara^{l,m}, L. Lamia^{c,d}, M. Lattuada^{c,d}, E. J. Lee^b, J. Y. Moonⁿ, S. Palmerini^{o,p}, C. Parascandolo^m, S. Y. Park^k, D. Pierrousakou^m, R. G. Pizzone^{c,d}, G. G. Rapisarda^c, S. Romano^{c,d}, H. Shimizu^a, C. Spitaleri^{c,d}, X. D. Tang^g, O. Trippella^{o,p}, A. Tumino^{c,f}, P. Vi^e, H. Yamaguchi^a, L. Yang^a, and N. T. Zhang^g

^aCenter for Nuclear Study, Graduate School of Science, University of Tokyo

^bDepartment of Physics, Sungkyunkwan University

^cIstituto Nazionale di Fisica Nucleare - Laboratori Nazionali del Sud

^dDepartment of Physics and Astronomy, Univ. of Catania

^eRIKEN Nishina Center

^fFaculty of Engineering and Architecture, Kore Univ. of Enna

^gInstitute of Modern Physics, Chinese Academy of Sciences

^hResearch Center for Nuclear Physics, Osaka University

ⁱDepartment of Physics, Tohoku University

^jSchool of Physics and Astronomy, University of Edinburgh

^kDepartment of Physics, Ewha Womans University

^lDepart. of Phys. 'E. Pancini', Univ. of Naples Federico II

^mIstituto Nazionale di Fisica Nucleare - Section of Naples

ⁿHigh Energy Accelerator Research Organization (KEK)

^oIstituto Nazionale di Fisica Nucleare - Section of Perugia

^pDepartment of Physics and Geology, University of Perugia

It has been known that the primordial ${}^7\text{Li}$ abundance predicted by the standard Big-Bang Nucleosynthesis (BBN) model [1] is about 3 times larger than the observation, so called the cosmological ${}^7\text{Li}$ problem. The ${}^7\text{Be}(n,p){}^7\text{Li}$ reaction is considered as the main process to destruct ${}^7\text{Be}$ during the BBN, which is also crucial in determining the ${}^7\text{Li}$ abundance. The resonance structure of the ${}^7\text{Be}(n,p){}^7\text{Li}$ reaction was well investigated by the R -matrix analysis [2] on several experimental data. However, the contribution of the transition to the first excited state of ${}^7\text{Li}$ at the BBN energies (~ 25 keV–1 MeV) has never been discussed. The other interesting reaction channel of the neutron induced reaction, ${}^7\text{Be}(n,\alpha){}^4\text{He}$, has not been investigated until recently [3–5] in terms of the relevance to the BBN scenario. Note that both of the new measurements [4, 5] were done only for partial waves in limited energy ranges, which thus lack the information on the total ${}^7\text{Be}(n,\alpha){}^4\text{He}$ cross section in the BBN energy region.

We performed indirect measurements of the ${}^7\text{Be}(n,p){}^7\text{Li}$ and ${}^7\text{Be}(n,\alpha){}^4\text{He}$ reactions simultaneously by the Trojan Horse Method (THM) [6] at Center for Nuclear Study Radioactive Isotope Beam (CRIB) separator [7]. The THM is an indirect technique which allows us to approach a 2-body reaction at astrophysical energies via a 3-body reaction by selecting the quasi-free (QF) kinematics. Moreover, the THM is useful as a “virtual neutron source” for neutron-induced reactions by using a deuteron target [8]. As done earlier in the first application of THM to

RI+ n reaction [9] performed at INFN-LNL in collaboration with us, we used a ${}^7\text{Be}$ beam and a deuteron target which induce the ${}^7\text{Be}(d,{}^7\text{Li}p){}^1\text{H}$ and ${}^7\text{Be}(d,\alpha\alpha){}^1\text{H}$ reactions in inverse kinematics to study the ${}^7\text{Be}(n,p){}^7\text{Li}$ and ${}^7\text{Be}(n,\alpha){}^4\text{He}$ reactions, respectively. We produced a ${}^7\text{Be}$ beam at 22.1 ± 0.14 MeV with an intensity of 1×10^6 pps on target. The experimental setup consisted of two PPACs (Parallel-Plate Avalanche Counters) for beam tracking, a CD_2 target, and six ΔE - E position-sensitive silicon-detector (PSD) telescopes at $\pm 12^\circ$, $\pm 34^\circ$ and $\pm 56^\circ$, as shown in Fig 1. The thickness of the CD_2 target was $64 \mu\text{g}/\text{cm}^2$. A use of such a thin target was enable to reduce the energy spread to about 120 keV. This is expected to help with separation of the first excited state of ${}^7\text{Li}$ (478 keV) in the reconstructed Q -value spectrum.

The PSDs were charge-division type and we calibrated their positions using the ${}^7\text{Li}$ primary beam scattering on a gold target with masks with $\phi 1$ -mm holes in 5-mm pitch mounted right in front of the PSDs. Those PSDs shows non-

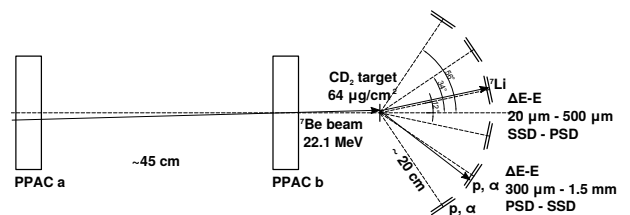


Figure 1. Schematic view of the experimental setup.

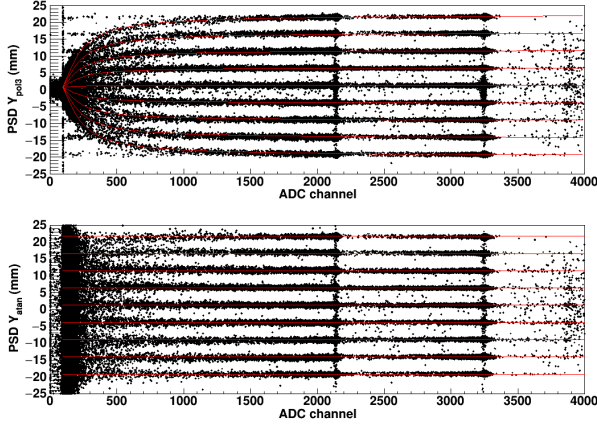


Figure 2. Position calibration of one of the charge-division PSDs.

linearity which was corrected with a 3-degree polynomial as a function of both X and Y positions with fitting parameters a_i ;

$$X_{\text{pol3}} = a_0 + a_1X + a_2Y + a_3X^2 + a_4Y^2 + a_5XY + a_6X^3 + a_7Y^3 + a_8X^2Y + a_9XY^2. \quad (1)$$

Then the positions X_{pol3} and Y_{pol3} show energy dependence as shown in the top panel of Fig. 2. This effect was corrected by fitting a phenomenological function to the original position X_{pol3} and Y_{pol3} which is drawn as red curves in Fig. 2;

$$X_{\text{pol3}} = \frac{2}{\pi b_2}(X_{\text{atan}} - b_3) \times \arctan[b_1(E_{\text{raw}} - b_0)] + b_3, \quad (2)$$

where X_{atan} is the actual mask position, E_{raw} is the ADC channel of the energy of the PSD, and b_i are the fitting parameters. By solving Eq. 2 for X_{atan} (or Y_{atan}), the corrected position became like the bottom panel of Fig. 2.

We observed p - ${}^7\text{Li}$ and α - α coincidental events, and confirmed that they were kinematically consistent with the expected 3-body exit channels. Figs. 3 and 4 show the energy correlations of the ${}^7\text{Li}$ - p and the α - α channels. Figure 5 shows the 3-body Q -value spectra of those channels. The peak energies are consistent with the known Q values of -0.580 MeV and 16.766 MeV within the resolution of about 250 keV and 500 keV (rms), respectively. This resolution is expected to be improved down to 150 – 200 keV with more precise energy and angular calibrations and further corrections. Accordingly, one can resolve the ground and the first excited state of ${}^7\text{Li}$. By selecting corresponding kinematic region, we estimate about 3000 QF events for the ${}^7\text{Be}(n,p){}^7\text{Li}$ channel in total. Further analysis is in progress.

This work is supported by JSPS KAKENHI (Grant No. 15K17631).

References

- [1] A. Coc *et al.*, J. Cosm. and Astropart. Phys. **40**, 050 (2014).

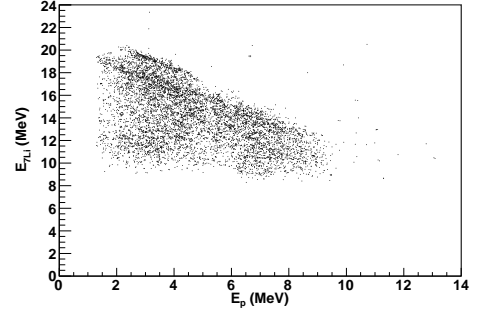


Figure 3. Energy correlation of ${}^7\text{Li}$ and proton.

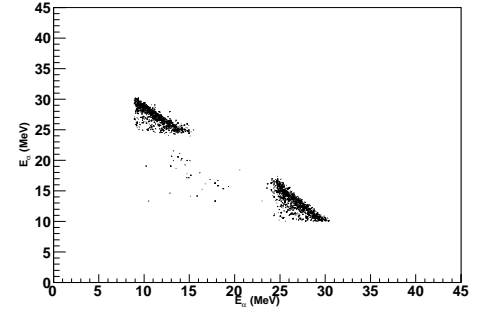


Figure 4. Energy correlation of two α particles.

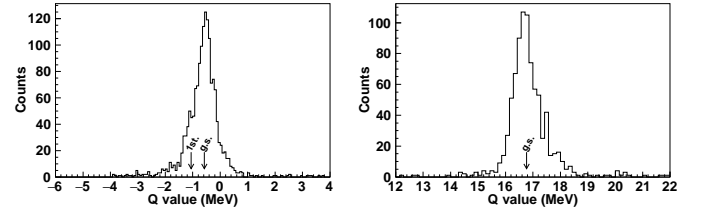


Figure 5. Q -value spectra of the ${}^7\text{Be}(d,{}^7\text{Li})p$ (left) and the ${}^7\text{Be}(d,\alpha)\alpha$ (right) reactions.

- [2] A. Adahchour and P. Descouvemont, J. Phys. G **29**, 395 (2003).
 [3] S. Q. Hou *et al.*, Phys. Rev. C **91**, 055802 (2015).
 [4] M. Barbagallo *et al.*, Phys. Rev. Lett. **117**, 152701 (2016).
 [5] T. Kawabata *et al.*, Phys. Rev. Lett. **118**, 052701 (2017).
 [6] C. Spitaleri *et al.*, Phys. Atom. Nucl. **74**, 1725 (2011).
 [7] Y. Yanagisawa *et al.*, Nucl. Instrum. and Meth. A **539**, 74 (2005).
 [8] M. Gulino *et al.*, Phys. Rev. C **87**, 012801 (2013).
 [9] L. Lamia *et al.*: Proc. 14th International Symposium on Nuclei in the Cosmos, JPS Conf. Proc., in publication.

Mixed isomeric and ground state ^{26}Al proton scattering

D. Kahl, H. Shimizu^a, H. Yamaguchi^a, K. Abe^a, O. Beliuskina^a, S. M. Cha^b, K. Y. Chae^b, A. A. Chen^c, Z. Ge^d, S. Hayakawa^a, N. Imai^a, N. Iwasa^e, A. Kim^f, D. H. Kim^f, M. J. Kim^b, S. Kubono^d, M. S. Kwag^b, J. Liang^c, J. Y. Moon^{g,h}, S. Nishimura^d, S. Okaⁱ, S. Y. Park^f, A. Psaltis^c, T. Teranishiⁱ, Y. Uenoⁱ, and L. Yang^a

School of Physics and Astronomy, the University of Edinburgh, Edinburgh, UK

^aCenter for Nuclear Study, Graduate School of Science, the University of Tokyo, Wako, Japan

^bDepartment of Physics, Sungkyunkwan University, Suwon, Korea

^cDepartment of Physics and Astronomy, McMaster University, Hamilton, Ontario, Canada

^dRIKEN Nishina Center, RIKEN, Wako, Japan

^eDepartment of Physics, Tohoku University, Sendai, Japan

^fDepartment of Physics, Ewha Womans University, Seoul, Republic of Korea

^gInstitute for Basic Science, Daejeon, Republic of Korea

^hWako Nuclear Science Center, KEK, Wako, Japan

ⁱDepartment of Physics, Kyushu University, Fukuoka, Japan

In the 1980s, the 1.809 MeV γ -ray line associated with the decay of ^{26}Al was the first specific radioactivity to be detected in our Galaxy. As the 7×10^5 yr half-life of its ground state, ^{26g}Al , is short on galactic timescales, its observation in the interstellar medium of the Milky Way is considered to be one of the most definitive pieces of evidence demonstrating that stellar nucleosynthesis is ongoing up to the present epoch. Such astrophysical observables attract significant attention from astronomers and physicists, because they allow us to link the nuclear physics inputs to stellar models which in turn are used to predict abundances with the theory of galactic chemical evolution.

The nucleosynthesis of ^{26}Al is complicated by a low-lying isomeric state, ^{26m}Al , at 228 keV, with a half-life of only 6.3 s, which decays predominately to the ground state of ^{26}Mg without emitting the characteristic 1.809 MeV γ -ray. The species $^{26g,m}\text{Al}$ are often treated as thermally linked, but separate species in nuclear reaction networks [1]. The amount of thermal transitions increase significantly with temperature, and thus production and destruction of ^{26m}Al has an influence on the ejected mass of ^{26g}Al , particularly in energetic environments like supernovae. In particular, the $^{26m}\text{Al}(p, \gamma)$ reaction rate is highly uncertain owing to a lack of experimental information [2].

To address the explosive destruction of ^{26m}Al , we performed a measurement of ^{26}Al proton resonant elastic scattering at the Center for Nuclear Study low-energy radioactive ion beam separator (CRIB) [3]. Isomeric beams can be a challenge to produce because of the small mass difference between the ground and isomeric states. The only previous measurement of proton scattering with an isomeric beam was performed with ^{18m}F which has $T_{1/2} = 163$ ns [4], where the authors tagged the events of interest in coincidence with their characteristic γ -rays. Such a method is unsuitable for longer lived isomers such as ^{26m}Al , and a new experimental method is necessary.

We conducted a radioactive beam production test for two days in July 2016 [5] and subsequently carried out the main

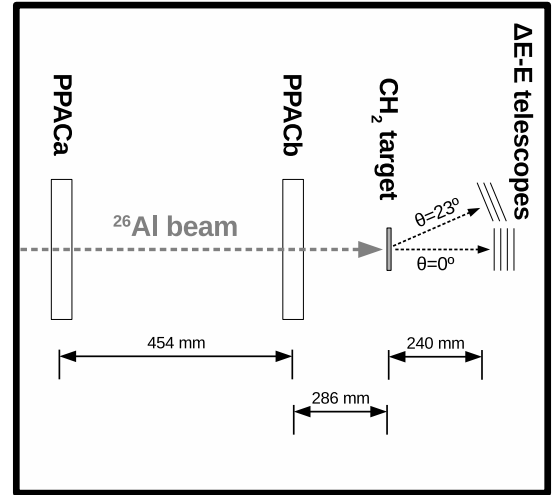


Figure 1. Experimental setup in the CRIB F3 scattering chamber. NaI array placed over the target not depicted. See the text.

proton scattering measurement over eleven days in March 2017. We produced the species of interest via the (p, n) charge-exchange reaction in inverse kinematics [6], bombarding the CRIB cryogenic gas cell [7] filled with H_2 gas with a primary beam of ^{26}Mg . The ^{26}Mg beam was extracted from the ion source containing $^{\text{nat}}\text{Mg}$ and accelerated for the first time at the RIKEN Nishina Center, relying only on the 11% natural abundance of ^{26}Mg —which turned out to be quite successful—with typically 25 to 50 pA delivered to CRIB. We produced modestly differing $^{26g,m}\text{Al}$ ratios by changing the primary beam and production target conditions. The nominal primary beam energy during the main experiment was 6.65 MeV/u, although in some runs we degraded the energy further with an additional 2.5 μm Havar foil upstream of the CRIB production target. The employed H_2 gas pressures at the production target ranged from 130 to 290 Torr (0.5 to 1.0 mg/cm^2). The ^{26}Al beam arrived at the experimental scattering chamber with an aver-

age intensity of 1.5×10^5 pps, a purity of 93%, and with on-target incident energies of 68, 83, and 90 MeV depending on the CRIB conditions. We injected 7×10^{10} ^{26}Al ions for more than five days of data accumulation for proton scattering measurements in March 2017.

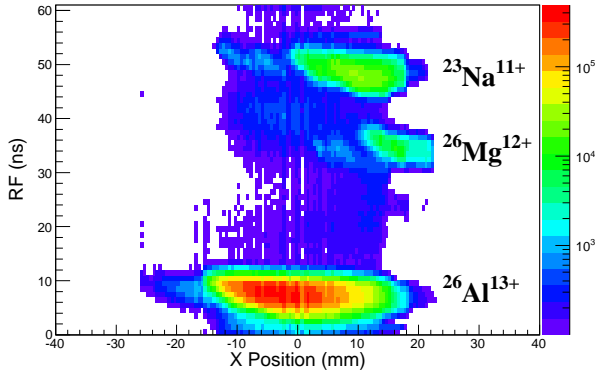


Figure 2. RF versus PPACa X position for the unscattered beam, showing locii of different species.

A portion of the setup at the experimental focal plane is depicted in Fig. 1, showing how we measured proton scattering with a thick target in inverse kinematics. We tracked the position and timing of the cocktail beam event-by-event using two parallel plate avalanche counters (PPACs) as shown in Fig. 2. The beam impinged on and completely stopped in a 7.5 mg/cm^2 CH_2 foil, which served as the proton target. We also took intermittent measurements with a 10.6 mg/cm^2 C foil to evaluate the background with a $\text{CH}_2:\text{C}$ measurement ratio of 4:1. Scattered protons were detected at forward laboratory angles with two $\Delta E-E$ telescopes comprised of several layers of silicon strip detectors (SSDs). The first SSD layer was around $70 \mu\text{m}$ thick, with 16×16 orthogonal strips on each side, thus providing the energy loss ΔE and position of each proton. The subsequent SSD layers were 1.5 mm thick and we summed their signals to obtain each proton's residual energy E . A preliminary proton spectrum showing significant structure is shown in Fig. 3. Finally, we placed an array of ten NaI detectors over the target; each detector crystal was $50 \times 50 \times 100 \text{ mm}^3$.

We performed regular measurements of the isomeric purity, defined as $^{26\text{m}}\text{Al}/^{26}\text{Al}$, with a pulsed beam mode of 12 s on and 12 s off. We alternately triggered with the NaI array (to measure 511 keV annihilation γ -rays) and SSDs (to measure β^+ 's) where we assumed these particles were associated with the decay of $^{26\text{m}}\text{Al}$. Analysis is ongoing including comparison with a GEANT4 simulation, but the preliminary absolute isomeric purity was around 20–40%, with a maximum relative isomeric purity difference of around 25% between the beams we produced. It cannot be doubted that our beam contained a substantial fraction of $^{26\text{m}}\text{Al}$, as seen by the β^+ spectra obtained by the forward angle SSD telescope in Fig. 4. As the proton scattering of $^{26\text{g}}\text{Al}$ has been previously measured and observed to show no structure [8], knowing the isomeric purity is sufficient to make a statistical background subtraction of pure Rutherford scattering attributed to $^{26\text{g}}\text{Al}$.

We are presently analyzing these data and will soon publicize further. We kindly thank the ECR ion source and AVF cyclotron operators.

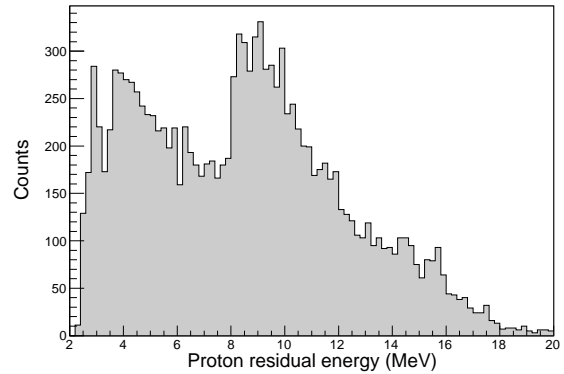


Figure 3. Laboratory proton spectrum obtained over twelve hours in July 2016 with a CH_2 target as measured at 0° .

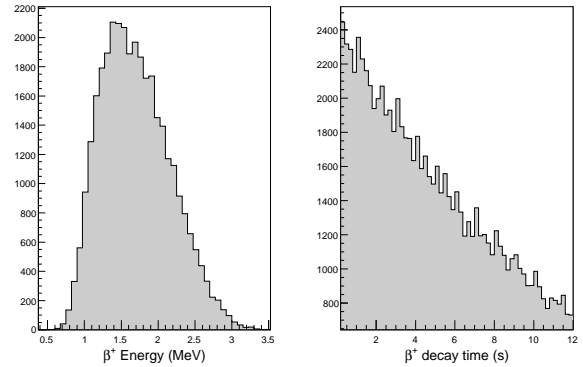


Figure 4. β^+ decay measurements: (a) Energy spectrum and (b) Decay timing. Both are consistent with $^{26\text{m}}\text{Al}$.

References

- [1] R.C. Runkle, A. E. Champagne, and J. Engel, *Astrophys. J* **556** (2001) 970.
- [2] C. Iliadis, *et al.*, *Astrophys. J Supp* **193** (2011) 16.
- [3] Y. Yanagisawa, *et al.*, *Nucl. Instrum. Methods in Phys. Res., Sect. A* **539** (2005) 74.
- [4] J.A. Brown, *et al.*, *Phys. Rev. C* **51** (1995) 1312.
- [5] D. Kahl, *et al.* *Il Nuovo Cimento C* **39** (2017) 362.
- [6] R.T. Skelton, R.W Kavanagh, and Sargood D.G., *Phys. Rev. C*, **35** (1987) 45.
- [7] H. Yamaguchi, *et al.*: *Nucl. Instr. Meth. A* **589** (2008) 150.
- [8] S.T Pittman, *et al.*, *Phys. Rev. C*, **85** (2012) 065804.

Optical model potentials for ${}^6\text{He} + {}^{64}\text{Zn}$ from ${}^{63}\text{Cu}({}^7\text{Li}, {}^6\text{He}){}^{64}\text{Zn}$ reaction analysis

L. Yang^{a,b}, C. J. Lin^b, H. M. Jia^b, N. R. Ma^b, L. J. Sun^b, D. X. Wang^b, F. Yang^b, and X. X. Xu^b

^aCenter for Nuclear Study, Graduate School of Science, the University of Tokyo

^bDepartment of Nuclear Physics, China Institute of Atomic Energy

In the study of the reaction mechanism, the nuclear interaction, which is universally described by the optical model potential (OMP), is one of the most basic ingredients. Knowledge on the phenomenological OMP, which includes all dynamics effects, can help us to make a comprehensive understanding on the complicated reaction mechanisms induced by exotic nuclei.

However, due to the limitations of intensity and quality of available radioactive ion beams (RIBs), it is difficult to extract the reliable OMPs of exotic nuclear systems directly from an elastic scattering measurement. In view of this fact, we try to use the transfer reaction as an alternative method to study the interaction of the exotic nuclei system in the exit channel [1, 2]. In the present work, this method was applied to extract the OMP of the halo nuclear system ${}^6\text{He} + {}^{64}\text{Zn}$ through the measurement of transfer reaction ${}^{63}\text{Cu}({}^7\text{Li}, {}^6\text{He}){}^{64}\text{Zn}$.

The experiment was performed at the China Institute of Atomic Energy, with a ${}^7\text{Li}$ beam accelerated by the HI-13 tandem accelerator. The angular distributions of the elastic scattering of ${}^7\text{Li} + {}^{63}\text{Cu}$, as well as the ones of one-proton transfer reactions ${}^{63}\text{Cu}({}^7\text{Li}, {}^6\text{He}){}^{64}\text{Zn}$ were measured at energies from above to below the Coulomb barrier, as $E_{\text{lab}}({}^7\text{Li}) = 12.67, 15.21, 16.33, 23.30, 27.30$ and 30.96 MeV, respectively. The details of the experiment can be found in Ref. [3]. At the highest incident energy of 30.96 MeV, in addition to the angular distribution of proton transferred from ${}^7\text{Li}$ to the ground state of ${}^{64}\text{Zn}$, the experimental result with ${}^{64}\text{Zn}$ populated the first excited state ($E^* = 0.99$ MeV) was also observed. While for $E_{\text{lab}}({}^7\text{Li}) = 15.21$ MeV, only the angular distribution with the first excited state of ${}^{64}\text{Zn}$ as the final state was recorded. All of the data sets are shown in Fig. 1.

To extract the OMP parameters of the halo system ${}^6\text{He} + {}^{64}\text{Zn}$ in the exit channel, the transfer reaction angular distributions were then fitted within the distorted-wave Born approximation (DWBA) and coupled reaction channels (CRC) frameworks, and the fitting results are shown in Fig. 1 with dashed and solid curves, respectively. The derived real and imaginary potential strengths are present in Fig. 2, with the radius and diffuseness parameters fixed at 5.82 (7.21) and 0.70 (1.19) fm for the real (imaginary) potential. Compared with the radius and diffuseness parameters of the real part, the corresponding values of the imaginary part are larger, indicating that the absorption of flux from the elastic channel of ${}^6\text{He} + {}^{64}\text{Zn}$ will occur at a larger distance, implying a large reaction cross section. This feature is consistent with the experimental result pointed out in Ref. [4], where a large yield of α particles was observed

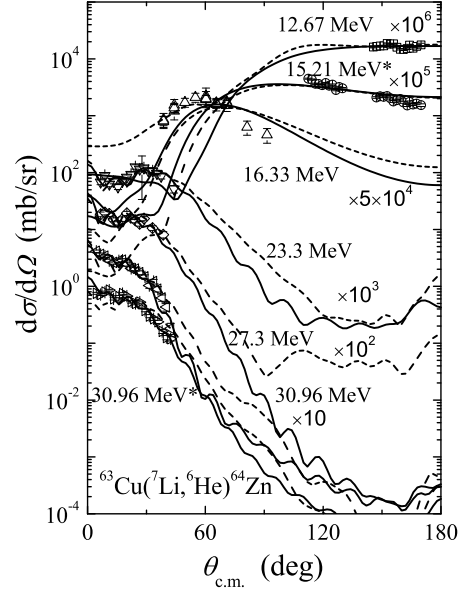


Figure 1. Angular distributions of transfer reactions ${}^{63}\text{Cu}({}^7\text{Li}, {}^6\text{He}){}^{64}\text{Zn}^*$. The energies labeled with a “*” correspond to the one-proton transfers to the first excited state of ${}^{64}\text{Zn}$ ($E^* = 0.99$ MeV). The solid and dashed curves are the fitting results with CRC and DWBA methods, respectively.

due to the transfer and breakup reactions.

As shown in Fig. 2, it can be seen that there exists significant difference between the DWBA and CRC fitting results. In the CRC calculations, the main coupling effects arising from the entrance channel can be considered explicitly, thus a relative pure effective OMP of the system in the exit channel can be extracted; while for the DWBA calculations, such influences originated from the couplings between ${}^7\text{Li}$ and ${}^6\text{He}$ cannot be removed. However, in the previous work [2], where the OMPs of ${}^6\text{He} + {}^{209}\text{Bi}$ were studied with the transfer reactions ${}^{208}\text{Pb}({}^7\text{Li}, {}^6\text{He}){}^{209}\text{Bi}^*$, the fitting results of DWBA and CRC are almost the same. This result indicates that the coupling effects of ${}^7\text{Li}$ interacted with heavy target ${}^{208}\text{Pb}$ are much weaker than that with medium-mass target ${}^{63}\text{Cu}$, for which the Coulomb repulsion is weaker, and more significant influence from nuclear structure effect may present.

The energy range measured in the present work is near and above the Coulomb barrier due to the limitations of the ${}^7\text{Li}$ beam. Therefore there is no chance to explore the intensive variation of the optical potential at sub-barrier energies. Within the above barrier region, the variation of the potential with the reaction energy is rather smooth, thus constants can be adopted to simply describe the OMPs, as $V = 70.34$ MeV, $W = 28.74$ MeV for the DWBA results, and $V = 11.69$

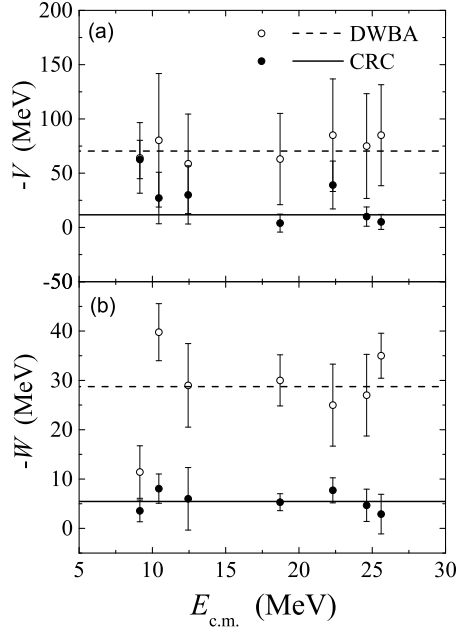


Figure 2. Depths of (a) real and (b) imaginary potentials vary with the reaction energy of the ${}^6\text{He} + {}^{64}\text{Zn}$ system. The errors were derived by χ^2 analysis with a confidence level of 68.3%. The full and empty circles represent the results obtained with the CRC and DWBA methods, respectively. Solid and dashed lines are the corresponding linear fitting results with errors as weights.

MeV, $W = 5.45$ MeV for the CRC calculations, as shown with dashed and solid curves in Fig. 2, respectively.

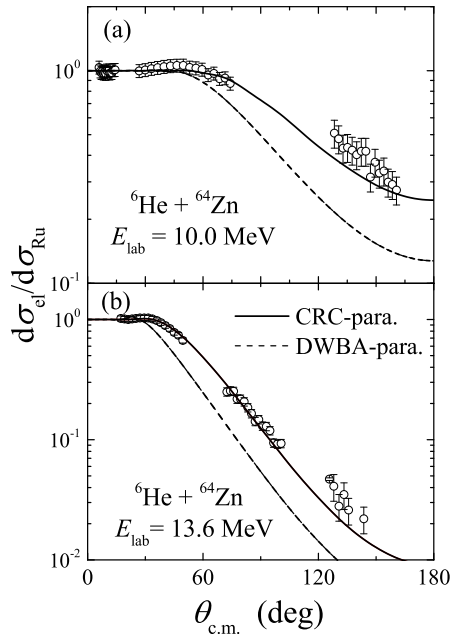


Figure 3. Elastic scattering of the ${}^6\text{He} + {}^{64}\text{Zn}$ system at (a) $E_{\text{lab}}({}^6\text{He}) = 10.0$ and (b) 13.6 MeV. Open circles are the experimental data taken from Ref. [4]. The solid and dashed curves denote the calculation results with the systematic OMPs obtained by the CRC and DWBA methods, respectively.

In order to investigate the reliability of the OMPs ex-

tracted by the transfer method, we calculated the angular distributions of elastic scattering of ${}^6\text{He} + {}^{64}\text{Zn}$ at $E_{\text{lab}}({}^6\text{He}) = 10.0$ and 13.6 MeV with the OMPs extracted, and compared with the experimental data taken from Ref. [4], as shown in Fig. 3.

It can be seen that the CRC-parameters can reproduce the experimental data properly, while the calculation results with the DWBA-parameters underestimate the experimental data greatly. As discussed above, the CRC calculation can obtain an accurate effective OMPs of the exit channel by considering the strong coupling effects from the entrance channel explicitly. Thus only the OMPs derived from the CRC fittings can describe the elastic scattering data satisfactorily, especially when there exist strong coupling effects.

References

- [1] C. J. Lin, F. Yang, P. Zhou *et al.*, AIP Conf. Proc. **853**, (2006) 81.
- [2] L. Yang, C. J. Lin, H. M. Jia *et al.*, Phys. Rev. C **89**, (2014) 044615.
- [3] L. Yang, C. J. Lin, H. M. Jia *et al.*, Phys. Rev. C **95**, (2017) 034616.
- [4] A. Di Pietro, P. Figuera, F. Amorini *et al.*, Phys. Rev. C **69**, (2004) 044613.

Direct mass measurement of neutron-rich calcium isotopes beyond $N = 34$

M. Kobayashi, S. Michimasa, Y. Kiyokawa, H. Baba^a, G. P. A. Berg^b, M. Dozono, N. Fukuda^a, T. Furuno^c, E. Ideguchi^d, N. Inabe^a, T. Kawabata^c, S. Kawase, K. Kisamori, K. Kobayashi^e, T. Kubo^a, Y. Kubota, C. S. Lee, M. Matsushita, H. Miya, A. Mizukami^f, H. Nagakura^e, D. Nishimura^f, H. Oikawa^f, S. Ota, H. Sakai^a, S. Shimoura, A. Stolzg, H. Suzuki^a, M. Takaki, H. Takeda^a, S. Takeuchi, H. Tokieda, T. Uesaka^a, K. Yako, Y. Yamaguchi^e, Y. Yanagisawa^a, R. Yokoyama, and K. Yoshida^a

Center for Nuclear Study, Graduate School of Science, University of Tokyo

^aRIKEN Nishina Center

^bDepartment of Physics and Joint Institute for Nuclear Astrophysics, University of Notre Dame

^cDepartment of Physics, Kyoto University

^dResearch Center for Nuclear Physics, Osaka University

^eDepartment of Physics, Rikkyo University

^fDepartment of Physics, Tokyo University of Science

^gNSCL, Michigan State University, USA

1. Introduction

The mass of atomic nuclei is a fundamental quantity as it reflects the sum of all interactions within the nucleus, which is the quantum many-body system comprised of two kinds of fermions, protons and neutrons. Changes in the shell structure in nuclei far from stability can be directly probed by mass measurements.

The shell evolution of the neutron $2p_{1/2}$ and $1f_{5/2}$ orbitals in neutron-rich calcium region has attracted much attention over recent years. The presence of a large subshell gap at $N = 34$ between the orbitals in the Ca isotopes was theoretically predicted [1], and the measurement of $E(2_1^+)$ in ^{54}Ca suggested the possible onset of a sizable subshell closure at $N = 34$ [2]. One of the most critical information on existence of the subshell gap at $N = 34$ is the atomic masses of the calcium isotopes beyond $N = 34$. We challenged the first mass measurements of neutron-rich calcium isotopes beyond $N = 34$ to probe shell evolution of the neutron $2p_{1/2}$ and $1f_{5/2}$ orbitals.

2. Experiment

The experiment was performed at the Radioactive Isotope Beam Factory (RIBF) at RIKEN, which is operated by RIKEN Nishina Center and Center for Nuclear Study, University of Tokyo. The masses were measured directly by the TOF- $B\rho$ technique using the equation of motion:

$$\frac{m}{q} = \frac{B\rho}{\gamma L/t} = \frac{B\rho}{c} \sqrt{\left(\frac{ct}{L}\right)^2 - 1}, \quad (1)$$

where m/q is the mass-to-charge ratio of the ion, $B\rho$ is the magnetic rigidity, L is the flight length, t is the time-of-flight, and γ is the Lorentz factor.

Neutron-rich isotopes were produced by fragmentation of a ^{70}Zn primary beam at 345 MeV/u in a ^9Be target. The fragments were separated by the BigRIPS separator [3], and transported in the High-Resolution Beam Line to the SHARAQ spectrometer [4]. The beam line and SHARAQ were operated in the dispersion matching mode allowing

a momentum resolution of 1/14700. A schematic view of the beamline with the detectors used in the experiment is shown in Fig. 1. The TOF was measured with newly developed diamond detectors [5] installed at BigRIPS-F3 and the final focal plane of SHARAQ (S2). The flight path length between F3 and S2 is ~ 105 m along the central ray. We installed two low pressure multi-wire drift chambers (LP-MWDCs) [6] at both F3 and S2 to correct the flight pass lengths using the tracking information on an event-by-event basis. The $B\rho$ value was measured by a parallel-plate avalanche counter (PPAC) [7] located at the target position of SHARAQ (S0). At the focal plane S2, we mounted two silicon strip detectors for identification of the proton numbers of the fragments. To identify the isomers, which leads to a systematic shift towards higher masses, we placed a plastic stopper downstream of S2 and a γ -ray detector array consisting of 2 HPGe clovers [8].

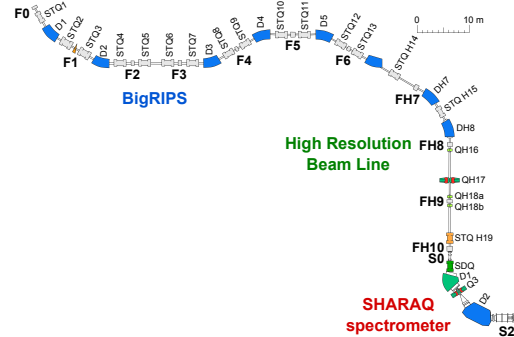


Figure 1. Schematic view of the BigRIPS separator, the High-Resolution Beam Line, and the SHARAQ spectrometer.

3. Analysis

To determine the atomic masses, the m/q and atomic number of each nucleus were measurement with event-by-event basis. In Eq. 1, $B\rho$ and L mainly relates to the horizontal position of S0 (x_0), which is the largest dispersive focus in the beamline, however all of the beam parameters are also connected to trajectories at F3 and S2. Therefore, we considered a polynomial expansion of Eq. 1 with beam parameters such as hit positions and angles at F3 (x_3, a_3, y_3, b_3) and S2 (x_2, a_2, y_2, b_2) as well as x_0 . Consequently, to calculate the m/q value, we used the 4th-order polynomial function

$$\frac{m}{q} = \sum_{j_0+\dots+j_9=0}^4 C_j \cdot t^{j_0} x_3^{j_1} a_3^{j_2} y_3^{j_3} b_3^{j_4} x_0^{j_5} x_2^{j_6} a_2^{j_7} y_2^{j_8} b_2^{j_9}. \quad (2)$$

Here, $C_j \equiv C_{(j_0, \dots, j_9)}$ are the fitting parameters to be determined from the data on the reference nuclei, of which the mass-to-charge ratios are precisely determined, with the least-squares method. The reference nuclei were $^{52-54}\text{Ca}$, $^{49,51-53}\text{K}$, $^{46-48}\text{Ar}$, $^{43-46}\text{Cl}$, $^{41,42}\text{S}$, $^{38-42}\text{P}$, and $^{36-40}\text{Si}$ [9–12]. These nuclei have mass precision in the literature of < 320 keV and do not have known long-lived ($T_{1/2} > 100$ ns) isomeric states.

Figure 2 shows the differences between the deduced m/q values and the literature ones for the reference nuclei. From the standard deviation of the data points, the systematic uncertainty in the mass determination was estimated to be 6.1 keV/ q , and we added another systematic error of 3.3 keV/ q , originated from Z dependence of detector resolutions, for calcium isotopes.

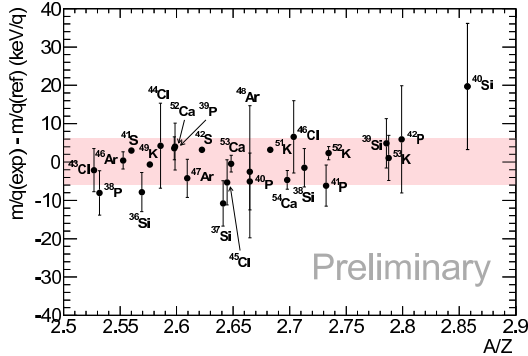


Figure 2. Differences between the deduced m/q values and the literature ones as a function of A/Z . The red band indicates the region within the systematic uncertainty. Error bars represent the uncertainties in the literature values.

4. Results

We obtained the evolution of the two-neutron separation energies (S_{2n}) in neutron-rich calcium isotopes from the atomic masses in the present experiment, as shown in Fig. 3. In the figure, the squares are the experimental S_{2n} values determined for the first time. The circles are the literature values obtained from Ref. [13]. The solid curves indicate the theoretical predictions by using KB3G [14], MBPT [15], IM-SRG [16], and modified SDPF-MU [17] interactions, respectively. The reduction steepness of S_{2n} between $N = 34$

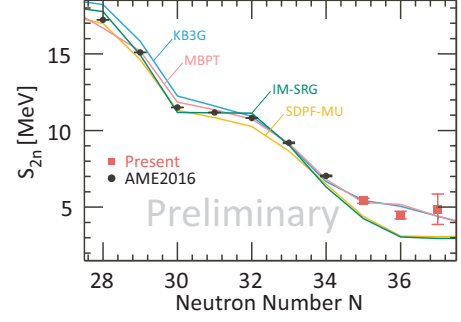


Figure 3. The two-neutron separation energies in neutron-rich Ca isotopes. The squares are determined values for the first time, and the circles are cited from AME2016 database [13]. The solid curves are shown the theoretical predictions [14–17].

and 35 significantly indicate the energy gap between neutron $2p_{1/2}$ and $1f_{5/2}$ orbitals as those at $N = 28-29$ and $32-33$ respectively show the magicities at $N = 28$ and 32 . Therefore, the experimental result argues for a sizable subshell gap at $N = 34$, comparable to that at $N = 32$. However it is found not to be as large as recent predictions by SDPF-MU and IM-SRG interactions.

In summary, we successfully performed the direct mass measurements of neutron-rich isotopes in the vicinity of ^{54}Ca using the TOF- $B\rho$ technique, and we are preparing a physics article to report the shell evolution in neutron-rich Ca isotopes beyond $N = 34$.

References

- [1] T. Otsuka *et al.*, Phys. Rev. Lett. **87**, 082502 (2001).
- [2] D. Steppenbeck *et al.*, Nature **502**, 207 (2013).
- [3] T. Kubo, Nucl. Instrum. Methods Phys. Res., Sect. B **204**, 97 (2003).
- [4] T. Uesaka *et al.*, Prog. Theor. Exp. Phys. **2012**, 03C007 (2012).
- [5] S. Michimasa *et al.*, Nucl. Instrum. Methods Phys. Res., Sect. B **317**, 710 (2013).
- [6] H. Miya *et al.*, Nucl. Instrum. Methods Phys. Res., Sect. B **317**, 701 (2013).
- [7] H. Kumagai *et al.*, Nucl. Instrum. Methods Phys. Res., Sect. A **470**, 562 (2001).
- [8] Y. Kiyokawa, Master thesis (2016).
- [9] M. Wang *et al.*, Chinese Phys. C **36**, 1603 (2012).
- [10] F. Wienholtz *et al.*, Nature **498**, 346 (2013).
- [11] M. Rosenbusch *et al.*, Phys. Rev. Lett. **114**, 202501 (2015).
- [12] Z. Meisel *et al.*, Phys. Rev. Lett. **114**, 022501 (2015).
- [13] Meng Wang *et al.*, Chinese Phys. C **41**, 030003 (2017).
- [14] A. Poves *et al.*, Nucl. Phys. A **694**, 157 (2001).
- [15] J. D. Holt *et al.*, J. Phys. G: Nucl. Part. Phys. **39**, 085111 (2012).
- [16] S. R. Stroberg *et al.*, Phys. Rev. Lett. **118**, 032502 (2017).
- [17] Y. Utsuno *et al.*, Phys. Rev. C **86**, 051301 (2012).

Measurement of Isoscalar Giant Monopole Resonance in ^{132}Sn using CAT-S

S. Ota, H. Tokieda, C. Iwamoto, M. Dozono, U. Garg^a, S. Hayakawa, K. Kawata, N. Kitamura, M. Kobayashi, S. Masuoka, S. Michimasa, A. Obertelli^b, D. Suzuki^c, R. Yokoyama, J. Zenihiro^c, H. Baba^c, O. Beliuskina, S. Chebotaryov^c, P. Egelhof^d, T. Harada^e, M.N. Harakeh^f, K. Howard^a, N. Imai, M. Itoh^g, Y. Kiyokawa, C.S. Lee, Y. Maeda^h, Y. Matsuda^g, E. Milman^c, V. Panin^c, H. Sakaguchiⁱ, P. Schrock, S. Shimoura, L. Stuhl^c, M. Takaki, K. Taniue^h, S. Terashima^j, T. Uesaka^c, Y.N. Watanabe^k, K. Wimmer, K. Yako, Y. Yamaguchi, Z. Yang^c, and K. Yoneda^c

Center for Nuclear Study, Graduate School of Science, the University of Tokyo

^a*Department of Physics, University of Notre Dame*

^b*Le Centre CEA de Saclay*

^c*RIKEN Nishina Center*

^d*GSI Helmholtzzentrum für Schwerionenforschung GmbH*

^e*Department of Physics, Toho University*

^f*KVI, Center for Advanced Radiation Technology*

^g*Cyclotron and Radio Isotope Center, Tohoku University*

^h*Department of Applied Physics, University of Miyazaki*

ⁱ*Research Center for Nuclear Physics, Osaka University*

^j*Beihang University*

^k*Department of Physics, the University of Tokyo*

The equation of state (EoS) of nuclear matter does not only govern the femto-scale quantum many-body system, namely nuclei, but also plays an important role in the structure of neutron stars and in supernova phenomena. In particular, the EoS of isospin asymmetric nuclear matter attracts much more interest from the view point of the existence of heavy neutron stars. The asymmetric term of incompressibility, K_τ , can be a benchmark for various EoSs because it can be directly deduced from the energies of the isoscalar giant monopole resonance (ISGMR) measured along an isotopic chain, such as tin isotopes [1]. The present value of K_τ is -550 ± 100 MeV and its error is relatively larger than those of other parameters of the EoS. In order to improve the K_τ value, the measurement on the isotopic chain should be extended to the unstable nuclei. A doubly magic nucleus in tin isotope, ^{132}Sn , has been chosen as a flagship of the measurements in unstable tin isotopes because of its large isospin asymmetry and double magic nature.

The excitation energy and scattering angle in the center-of-mass frame are extracted by means of missing-mass spectroscopy, where the low-energy recoil deuteron has to be measured. In order to measure such low-energy recoils, a gaseous active target system, CNS Active Target (CAT), has been employed. The CAT consists of a time-projection chamber (TPC) and an array of silicon detectors on both sides of TPC. A stack of thick gas electron multipliers (THGEM) are used for electron multiplication in the TPC. The THGEM has three-fold segmented electrodes. The center electrode is for measuring the beam particles and the side electrodes are for measuring the recoil particles. The multiplication factors at beam and recoil region can be controlled independently, which enables us to oper-

ate the CAT with high-intensity beam such as 10^6 particles per second [2].

The experiment was performed at RIBF at RIKEN. The secondary ^{132}Sn beam was produced as a fission fragment of ^{238}U beam impinging on the primary target of beryllium. The maximum intensity of the primary beam was 37 pA. The typical intensity of the secondary beam at F3 and F7 was 8.5×10^5 and 3.2×10^5 particles per second, respectively. In order to identify the particles in such a high-intensity beam on an event-by-event basis, the new method of TOF- $B\rho$ - $B\rho$ [3] was introduced. The TOF was measured by diamond detectors of 200 μm thick located at F3 and F7. The $B\rho$ was determined using the positions and angles measured by low-pressure multi-wire drift chambers at F3, F5, and F7. The main components of the secondary beam were ^{132}Sn , ^{133}Sb , and ^{134}Te with the purity of 21%, 46%, and 25% at F7, respectively. The data from the beam-line detectors at each focus are taken by using MOCO [4]. The CAT was placed at F8 with a collimator in front of it. The CAT was operated with deuterium gas at 0.4 atm and the stack of three THGEMs. The signals from the CAT were digitized using V1740 module (CAEN) and digitized samples were transferred through the optical link to the computer. Physics trigger for the data acquisition was made by using the trigger out from the V1740 and HINP-16 (Heavy Ion Nuclear Physics, 16 channel), which is the readout system used for the silicon detectors. ESPRI (Elastic scattering of protons with RI beams) system was placed at F12 [5] to measure the deuteron elastic scattering off ^{132}Sn for large scattering angles in order to determine the optical potential parameters.

The excitation-energy resolution for the ground state, determined from the analysis of recoil particles stopped in TPC, is 1 MeV in one deviation. The energy of ISGMR

will be deduced from the multipole-decomposition analysis of double-differential cross sections. The analysis is in progress.

References

- [1] T. Li *et al.*, Phys. Rev. Lett. **99**, 162503 (2007).
- [2] S. Ota *et al.*, J. Radioanal. Nucl. Chem. **305**, 907-911 (2015).
- [3] S. Ota *et al.*, RIKEN Accel. Prog. Rep. **49** 15 (2017)
- [4] H. Baba *et al.*, to be appered in RIKEN Accelerator Progress Report (2017)
- [5] J. Zenihiro *et al.*, to be appered in RIKEN Accelerator Progress Report (2017)

Production of a ^7Be implanted target for the study of the primordial ^7Li problem in the Big-Bang Nucleosynthesis

A. Inoue, A. Tamii, H. Yamaguchi^a, K. Abe^a, S. Adachi, N. Aoi, M. Asai^b, M. Fukuda^c, G. Gey, T. Hashimoto^d, S. Hayakawa^a, E. Ideguchi, J. Isaak, N. Kobayashi, Y. Maeda^e, H. Makii^b, K. Matsuta^c, M. Mihara^c, M. Miura, T. Shima, H. Shimizu^a, R. Tang, D. T. Tran, L. Yang^a

Research Center for Nuclear Physics, Osaka University

^a*Center for Nuclear Study, Graduate School of Science, University of Tokyo*

^b*Japan Atomic Energy Agency*

^c*Department of Physics, Osaka University*

^d*Rare Isotope Science Project, Institute for Basic Science*

^e*Department of Applied Physics, Faculty of Engineering, University of Miyazaki*

Our research purpose is the measurement of the $^7\text{Be}(d, p)^8\text{Be}$ reaction to solve the ^7Li problem in the Big-Bang Nucleosynthesis (BBN).

The ^7Li problem is an overestimation of the primordial ^7Li abundance in the standard BBN model. The recent theoretical BBN model predicts a primordial ^7Li abundance that is 3 times larger than the recent precise observation [1]. The difference is quite large while the abundance of the other light nuclei are reproduced well by theory. This is one of the biggest problems in the BBN models and this is nothing short of ignorance about the process of the primordial formation of our universe.

Light nuclei were produced up to ^7Be by nuclear reactions in several hundred seconds following the Big Bang (Fig. 1). ^7Li nuclei were considered to be predominantly produced by the β decay of ^7Be in the standard BBN model. The β decay half life of ^7Be , 5 million seconds, is much longer than the light nucleus production after the Big Bang. Thus, one possible scenario to solve the ^7Li problem is that ^7Be was destructed in the time scale of the nuclear reactions.

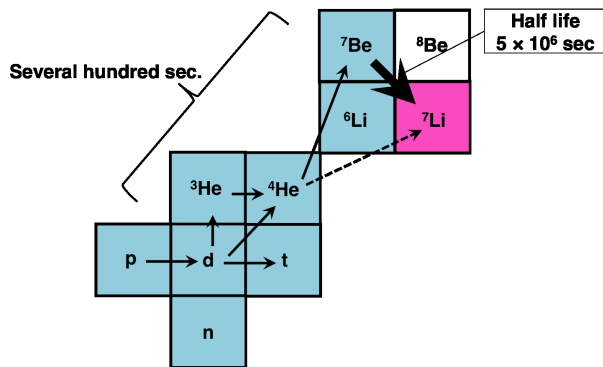


Figure 1. Light nuclei were produced in several hundred seconds following the Big Bang. ^7Li was produced by the beta decay of ^7Be . The β decay half life of ^7Be is 5 million seconds, which is much longer than the time of the nuclear reactions.

The $^7\text{Be}(d, p)^8\text{Be}$ and the $^7\text{Be}(n, \alpha)^4\text{He}$ reactions are two promising processes of destructing ^7Be . We focus on the $^7\text{Be}(d, p)^8\text{Be}$ reaction since the contribution from $^7\text{Be}(d, p)^8\text{Be}$ is suggested to be larger than $^7\text{Be}(n, \alpha)^4\text{He}$ [2, 3].

We plan to measure the cross section of the $^7\text{Be}(d, p)^8\text{Be}$ reaction in the BBN energy region of 100 - 400 keV. The available data are insufficient in the accuracy or in the energy range [4, 5]. We are developing an unstable ^7Be target for the measurement of the $^7\text{Be}(d, p)^8\text{Be}$ reaction with high incident-energy resolution in normal kinematics. The development of unstable nucleus target is a big technical challenge. We apply the *Implantation method*; ^7Be particles are implanted by irradiating a gold host target with a ^7Be beam.

We performed an experiment to produce a ^7Be implanted target at CRIB, Center for Nuclear Study (CNS), University of Tokyo in June, 2016. The experimental setup is shown in Fig. 2 [6, 7]. The primary beam was $^7\text{Li}^{2+}$ at 5.6 MeV/nucleon. The secondary beam was produced by the $^1\text{H}(^7\text{Li}, ^7\text{Be})$ reaction. The secondary beam energy was 4.0 MeV/nucleon. The ^7Be beam was directed on to a 10 μm thick gold foil as a host material after an energy degrader made of gold with a thickness of 15 μm and 2 mm ϕ collimator.

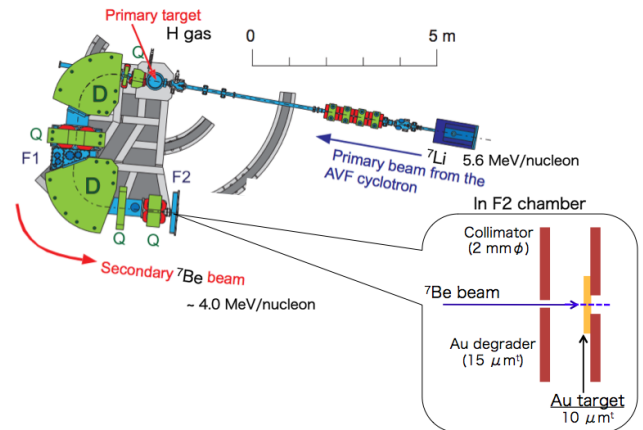


Figure 2. Experimental setup at CRIB. The primary beam was $^7\text{Li}^{2+}$ at 5.6 MeV/nucleon. The secondary beam was produced by the $^1\text{H}(^7\text{Li}, ^7\text{Be})$ reaction. The ^7Be particles were implanted in the gold target at F2.

We evaluated the amount of the implanted ^7Be by detecting 477 keV γ rays with a LaBr_3 detector after the implantation. The γ ray is emitted in the electron capture decay pro-

cess of ${}^7\text{Be}$ with a branching ratio of 10.5 %. We achieved 1.3×10^{11} ${}^7\text{Be}$ particles after 19 hours of irradiation. Fig. 3 shows the measured γ ray spectrum. This γ -ray yield corresponds to the beam density of 5.7×10^5 pps/mm 2 , which is still smaller than our goal of 9.0×10^6 pps/mm 2 . We suspect that the beam spot size and the beam profile at F2 were not fully optimized for the high-intensity ${}^7\text{Be}$ beam downstream of the collimator and not maintained well during the long irradiation time.

As the next step, we plan to have a development beam time to achieve a high-intensity ${}^7\text{Be}$ beam by optimizing the beam line and CRIB parameters at CRIB in spring, 2017.

We are grateful to the support of Dr. A. Yoshida for our project.

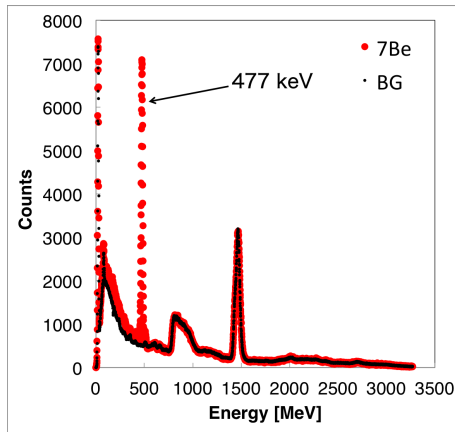


Figure 3. The γ -ray energy spectrum of the implanted ${}^7\text{Be}$ (red dotted line) and the background spectrum (black solid line). The 477 keV peak from the decay of ${}^7\text{Be}$ can be seen obviously.

References

- [1] R. H. Cyburt *et al.*, *J. Cosmol. Astropart. Phys.* **11**, 012 (2008).
- [2] S. Q. Hou *et al.*, *Phys. Rev. C* **91**, 055802 (2015).
- [3] T. Kawabata *et al.*, *Phys. Rev. Lett.* **118**, 052701 (2017).
- [4] R. W. Kavanagh *et al.*, *Nucl. Phys.* **18**, 493 (1960).
- [5] C. Angulo *et al.*, *Astrophys. J.* **630**, L 105 (2005).
- [6] H. Yamaguchi *et al.*, *Nucl. Instr. Meth. A* **589**, 150 (2008).
- [7] G. Amadio *et al.*, *Nucl. Instr. Meth. A* **590**, 191 (2008).

Searching for the experimental evidence of α -cluster structure in ^{22}Mg

K.Y. Chae,^a S.M. Cha^a, K. Abe^b, S.H. Bae^c, D.N. Binh^d, S.H. Choi^c, N.N. Duy^{a,e}, K.I. Hahn^f, S. Hayakawa^b, B. Hong^g, N. Iwasa^{h,i}, D. Kahl^j, L.H. Khiem^{k,l}, A. Kim^m, D.H. Kim^m, E.J. Kimⁿ, G.W. Kim^m, M.J. Kim^a, K. Kwag^o, M.S. Kwag^a, E.J. Lee^a, S.I. Lim^m, B. Moon^g, J.Y. Moon^p, S.Y. Park^m, V.H. Phongⁱ, H. Shimizu^b, H. Yamaguchi^b, L. Yang^b, and Z. Geⁱ

^aDepartment of Physics, Sungkyunkwan University

^bCenter for Nuclear Study, Graduate School of Science, University of Tokyo

^cDepartment of Physics and Astronomy, Seoul National University

^d30 MeV Cyclotron Center, Tran Hung Dao Hospital

^eDepartment of Physics, Dong Nai University

^fDepartment of Science Education, Ewha Womans University

^gDepartment of Physics, Korea University

^hDepartment of Physics, Tohoku University

ⁱRIKEN Nishina Center

^jSchool of Physics and Astronomy, University of Edinburgh

^kInstitute of Physics, Vietnam Academy of Science and Technology

^lGraduate University of Science and Technology, Vietnam Academy for Science and Technology

^mDepartment of Physics, Ewha Womans University

ⁿDivision of Science Education, Chonbuk National University

^oDepartment of Physics, School of Natural Science, Ulsan National Institute of Science and Technology (UNIST)

^pInstitute for Basic Science

The α -cluster structure is one of the most interesting subjects in modern nuclear physics. The clustering structure in self-conjugate $4N$ nuclei with $N = Z$ such as ^8Be , ^{12}C , ^{16}O , and ^{20}Ne , has been studied for a long time [1–3]. The energy levels with large α reduced widths form a rotational band in these nuclei, which results from a molecular structure of cluster levels. Although our understandings on the α -cluster structure for the $N > Z$ neutron-rich nuclei such as ^{10}Be , ^{12}Be , ^{14}C , and ^{22}Ne [4–9] are enhanced to some extent with the help of new theoretical models and rare isotope beams, the experimental information for the $N < Z$ proton-rich nuclei is still rare.

The theoretical investigation on the α -cluster structure in proton-rich ^{22}Mg radionuclide was performed by M. Dufour and P. Descouvemont [10, 11]. Generator Coordinate Method (GCM) calculations were used in their studies and doubling states with $J^\pi = 1^-$ and 3^- around $E_x = 12 - 13$ MeV were predicted, as one can find in its mirror nuclide ^{22}Ne . These doublets, however, were not found in the experiment performed by Goldberg *et al.*, owing to the insufficient amount of data for independent analysis at the time [9].

In more recent work by M. Kimura, the hybrid GCM calculation predicted new singlet states with negative parities at the energy range of $E_x = 14 - 20$ MeV, which arise from the $\alpha + ^{18}\text{O}$ molecular band in the ^{22}Ne nucleus [8]. By considering the similarities in the level structures between two mirror nuclei, it can be expected that the ^{22}Mg nucleus also has those of singlet states with negative parities.

In order to study the α -cluster structure information in ^{22}Mg ($^{18}\text{Ne} + \alpha$ system), the $^{18}\text{Ne}(\alpha, \alpha)^{18}\text{Ne}$ scattering was measured in inverse kinematics at the Center for Nu-

clear Study Radioactive Ion Beam Separator (CRIB) at the RIBF, operated by RIKEN Nishina Center. Because the energy levels derived from the α -cluster structure have relatively large α reduced widths, experimental evidences of the cluster structure in ^{22}Mg can be provided through present work. By adopting the thick target method [12], a wide energy range of ^{22}Mg levels ($E_x = 8.6 - 18$ MeV) could be investigated.

The ^{18}Ne radioactive ion beam was produced via the $^3\text{He}(^{16}\text{O}, n)^{18}\text{Ne}$ reaction by in-flight method. The primary $^{16}\text{O}^{6+}$ beam from the AVF cyclotron ($E_{\text{beam}} = 8.026$ MeV/u) bombarded with the ^3He gas target. By using the the liquid nitrogen cooling system [13], low temperature of ~ 90 K and areal thickness of 1.54 mg/cm² was achieved for the ^3He production gas target.

Figure 1 shows a schematic diagram of the experimental setup. The secondary ^{18}Ne beam particles at the energies of 2.54 MeV/u were delivered to the ^4He gas target chamber located at the last focal plane of CRIB. The reaction target chamber was filled with ^4He gas at 470 Torr. In order to monitor the beam intensity and the position, two Parallel Plate Avalanche Counters (PPACs) were used at the upstream of target chamber. The typical beam intensity was $\sim 3.5 \times 10^5$ pps and the beam purity was $\sim 60\%$. A 21.5 μm -thick aluminized mylar foil was used to isolate the ^4He gas target from the vacuum side of the beam line.

Scattered α particles were detected by two $\Delta E - E$ silicon detector telescopes and identified by a standard energy loss technique. Each telescope consisted of two or three layers of silicon strip detectors, which can fully stop the most energetic scattered α particles. In order to study the instrumental background, independent measurement with 87 Torr

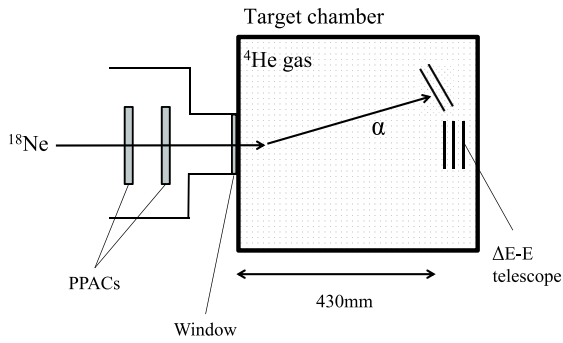


Figure 1. The experimental setup. The ^{18}Ne beam impinged on the 470 Torr of ^4He gas target. Recoiling α particles were detected by two silicon detector telescopes. Two PPACs located upstream of target chamber were used for beam monitoring.

of Ar gas target was also performed.

A preliminary α particle energy spectrum is shown in Fig. 2. The black solid line indicates the scattered α particles from the ^4He gas target and the red cross represents the α particles from the background. According to the α particle energies and the reaction kinematics, the energy levels of ^{22}Mg up to $E_x \sim 18$ MeV were populated in this experiment. The strongest α peak near 13 MeV was originated from the fusion evaporation reactions at the beam production target chamber and selected by the same rigidity values of two dipoles, which were optimized to select the ^{18}Ne beam particles. Even after passing through the Wien filter, still comparable amount of these α particles were transported to the telescope.

In order to obtain precise α energy spectra, careful energy calibrations and reconstructions for each silicon strip are needed. In order to rule out the probability of observing small background from inelastic scattering, peak shift method will be used. This method was proven to be valid for experimental data obtained at CRIB [14]. After subtracting the normalized background, the excitation function of $^{18}\text{Ne} + \alpha$ will be extracted. By comparing the theoretical R -matrix calculations [15] with our measured excitation function, the energy level properties of ^{22}Mg such as spins, parities, and α reduced widths will be deduced. It will also provide the ^{22}Mg level properties in $E_x > 14$ MeV region for the first time. Finally, the α -cluster structure of ^{22}Mg will be investigated using experimental information obtained from the present work.

References

- [1] K. Ikeda *et al.*, Prog. Theor. Phys.**68** (1986) 1.
- [2] H. Horiuchi *et al.*, Suppl. Prog. Theor. Phys.**192** (2012) 1.
- [3] M. Freer, Rep. Prog. Phys.**70** (2007) 2149.
- [4] M. Freer *et al.*, Phys. Rev. C **63** (2001) 034301.
- [5] H. Yamaguchi *et al.*, Phys. Lett. B **766** (2017) 11.
- [6] M. Freer *et al.*, Phys. Rev. Lett. **82** (1999) 1383.
- [7] S. Torilov *et al.*, J. Lett.**94** (2011) 6.

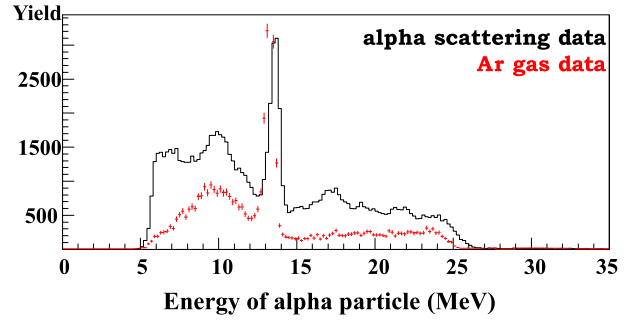


Figure 2. An α energy spectrum. The black solid line and red cross symbols indicate the α particle energies from the ^4He - and Ar-gas runs, respectively. Data from two measurements were normalized by the beam intensity.

- [8] M. Kimura, Phys. Rev. C **75** (2007) 034312.
- [9] V. Z. Goldberg *et al.*, Phys. Rev. C **69** (2004) 024602.
- [10] M. Dufour and P. Descouvemont, Nucl. Phys. A **726** (2003) 53.
- [11] M. Dufour and P. Descouvemont, Nucl. Phys. A **738** (2004) 447.
- [12] K. P. Artemov *et al.*, Sov. J. Nucl. Phys. **52** (1990) 408.
- [13] H. Yamaguchi *et al.*, Nucl. Inst. Meth. Phys. Res. A **589** (2008) 150.
- [14] J. J. He *et al.*, Phys. Rev. C, **76** (2007) 055802.
- [15] A. M. Lane and R. G. Thomas, Rev. Mod. Phys. **30**, (1958) 257.

Measurement of ${}^4\text{He}({}^8\text{He}, {}^8\text{Be})$ reaction for verifying tetra-neutron resonance

S. Masuoka, S. Shimoura, M. Takaki, D. S. Ahn^a, H. Baba^a, M. Dozono, N. Fukuda^a, T. Harada^b, E. Ideguchi^c, N. Imai, N. Inabe^a, C. Iwamoto, K. Kawata, N. Kitamura, M. Kobayashi, Y. Kondo^d, T. Kubo^a, Y. Maeda^e, F. M. Marqués^f, M. Matsushita, S. Michimasa, R. Nakajima, T. Nakamura^d, N. Orr^f, S. Ota, H. Sakai^a, H. Sato^a, P. Schrock, L. Stuhl^b, T. Sumikama^a, H. Suzuki^a, H. Takeda^a, K. Taniue^e, H. Tokieda, T. Uesaka^a, K. Wimmer^g, K. Yako, Y. Yamaguchi, Y. Yanagisawa^a, R. Yokoyama, K. Yoshida^a, and J. Zenihiro^a

Center for Nuclear Study, Graduate School of Science, the University of Tokyo

^aRIKEN Nishina Center

^bDepartment of Physics, Toho University

^cResearch Center for Nuclear Physics, Osaka University

^dDepartment of Physics, Tokyo Institute of Technology

^eFaculty of Engineering, Univ. of Miyazaki

^fLaboratoire de Physique Corpusculaire, IN2P3-CNRS, ENSICAEN et Université de Caen

^gDepartment of Physics, the University of Tokyo

Nuclei which are composed of only neutrons have been discussed for over a half century, but their existence has not been confirmed. In 2002, a candidate bound state of the tetra-neutron, which consists of four neutrons, was reported. [1] An *ab-initio* calculation suggested that there might be a tetra-neutron ($4n$) resonance, but a bound $4n$ was not reproduced. [2] An experimental search for the $4n$ resonance state conducted using the exothermic double charge exchange (DCX) ${}^4\text{He}({}^8\text{He}, {}^8\text{Be})4n$ reaction was performed at the SHARAQ spectrometer in RIBF [3]. As a result, four candidate events were found with a 4.9σ significance level, and the energy of the $4n$ resonance was determined as $E_{4n} = 0.83 \pm 0.65(\text{stat.}) \pm 1.25(\text{syst.})$ MeV. It has not precision enough to determine that the tetra-neutron is the bound state, or resonance state. To confirm the existence of $4n$ resonance, we performed a new measurement with higher statistics and with smaller energy uncertainty.

the secondary ${}^8\text{He}$ beam was about 186 MeV/nucleon. The beam intensity was increased from that in the previous experiment. The rate of the secondary beam at F3 was increased from about 2.0 MHz to 3.5 MHz. Six low-pressure multi-wire drift chambers (LP-MWDCs) [4] were installed for tracking the beam. ‘‘F6’’ was set as a dispersive focal plane, so that the momentum of the beam could be measured by the focus position. At ‘‘S0,’’ a liquid He target system (CRYPTA) [5] was installed. At the final focal plane, ‘‘S2,’’ 2 α particles from the decay of outgoing ${}^8\text{Be}$ were detected using 2 cathode readout drift chambers (CRDCs) with taking the waveform from anode signal by flash ADC.

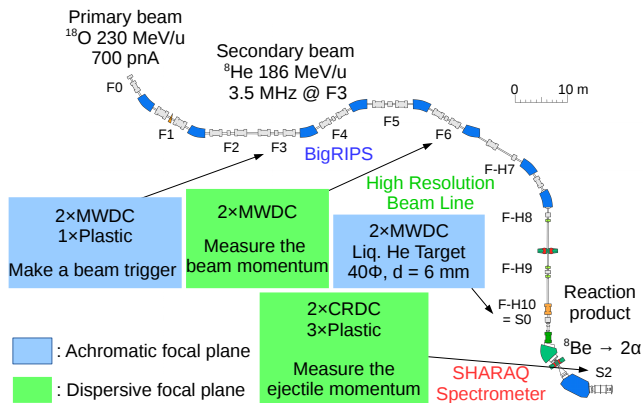


Figure 1. Detector setup of BigRIPS/SHARAQ beam line.

Figure 1 shows a schematic view of the setup for this experiment. A primary ${}^{18}\text{O}$ beam was accelerated to about 230 MeV/nucleon by AVF+RRC+SRC. The intensity of the primary beam was about 700 particle nA. The energy of

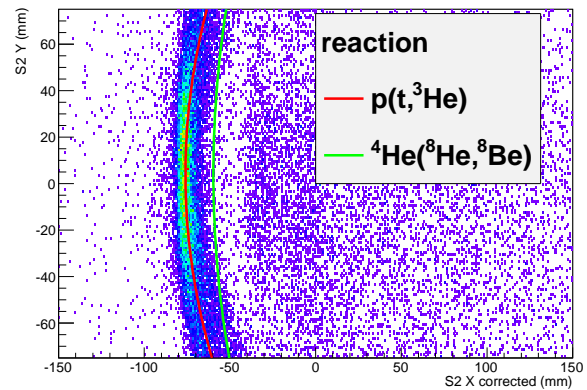


Figure 2. A preliminary hit pattern of the ${}^1\text{H}({}^t, {}^3\text{He})$ reaction at S2 for the energy calibration with a reaction kinematics curve. The X and Y axes correspond to the missing momentum and the vertical scattering angle, respectively.

In the present experiment, the method of missing-momentum calibration was changed to reduce the systematic error of the $4n$ energy. The triton beam which use for the ${}^1\text{H}({}^t, {}^3\text{He})$ reaction with the same magnetic rigidity as the ${}^8\text{He}$ beam (8.3 Tm) was employed as a reference of the energy. The energy can be calibrated without changing the

magnetic settings. Figure 2 shows an S2 image of outgoing ^3He particles from the $^1\text{H}(^3\text{H},^3\text{He})$ reaction. The red line indicates the fitted kinematics curve of the reaction. The threshold energy of the $4n$ state can be determined from the curve.

Further analysis is now in progress.

References

- [1] F.M. Marqués et. al., Phys. Rev. C **65**, 044006 (2002).
- [2] S.C. Pieper, Phys. Rev. Lett. **90**, 252501 (2003).
- [3] K. Kisamori et al., Phys. Rev. Lett. **116**, 052501 (2016).
- [4] H. Miya, et. al., Nucl. Instr. Meth. B **317** 701-704 (2013).
- [5] H. Ryuto, et. al., Nucl. Instr. Meth. A **555** 1-5 (2005).

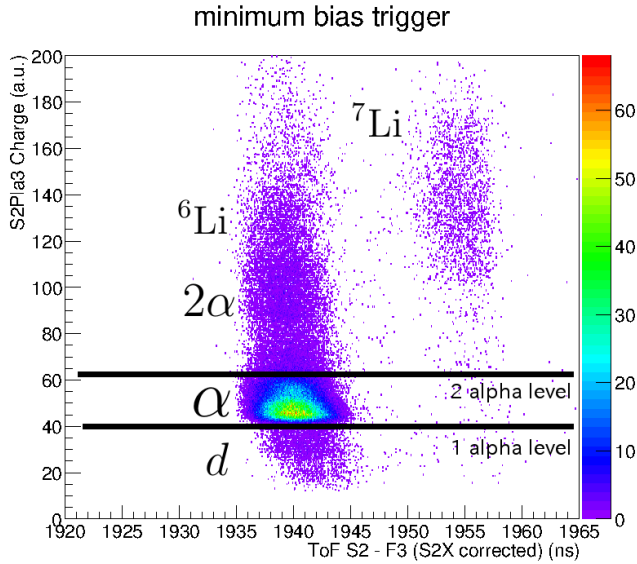


Figure 3. PID plot at S2 final focal plane by ΔE -TOF method. Vertical axis is the TOF between F3 to S2, and horizontal axis correspond to the energy loss on S2 plastic using “minimum bias” trigger.

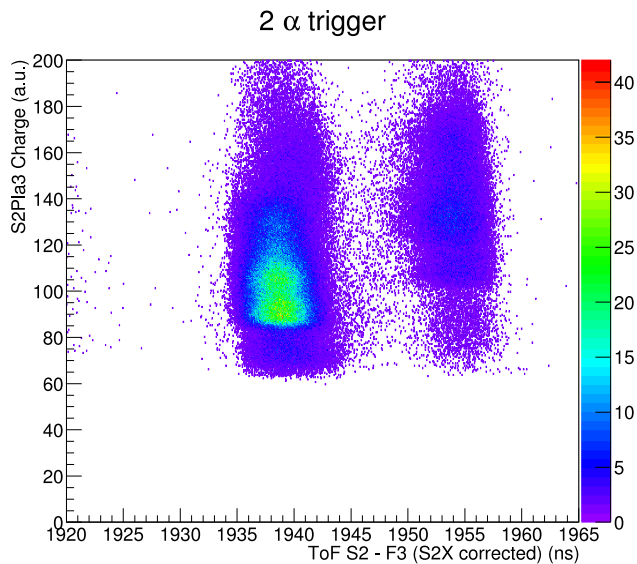


Figure 4. PID plot the same as Fig. 3 using “2 alpha” trigger

Figure 3 shows the particle identification of ejectile products by the double charge exchange reaction. 4 different event trigger, “beam”, “minimum bias”, “1 alpha” and “2 alpha”, were generated on this experiment for taking the true event with high efficiency. At the trigger circuit, for S2 plastic, 3 different threshold level were tuned. Figure 3 and Fig. 4 PID plots are different from the trigger. According to the Fig. 4, higher levels of charge was gated by the trigger.

Development of producing high-spin isomer beam by ^{58}Ni fragmentation reactions

K. Kawata, K. Yako, S. Ota, M. Dozono, J. Zenihiro^A, C. Iwamoto, N. Kitamura, M. Kobayashi, H. Sakai^A, M. Sasano^A, M. Takaki, S. Masuoka, S. Michimasa, R. Yokoyama, L. Stuhl, E. Takada^B,

Center for Nuclear Study, Graduate School of Science, the University of Tokyo
^ARIKEN Nishina Center
^BNIRS

Secondary reactions with excited nuclei is exciting in nuclear physics. These reactions are strongly related to the nucleosynthesis inside the stars since high temperature circumstance in the star may populate the high excited state. Accordingly, the reaction with the excited state may play an important role. Limit of spin in nuclei is also an interesting topic. The higher spin may be produced if the reaction starting with high spin. In order to measure such reactions, we need excited nuclei as a target or a beam. The typical lifetime of the excited state is order of femto or picosecond, however, some excited states have longer lifetimes more than nanosecond differences between the state and the lower excited state. We call these long-lifetime excited states as isomeric states, or isomers in short. If we can produce enough amount of isomer as a beam for instance, we can perform the secondary reaction measurement with hot nuclei.

One of the interesting isomer is ^{52m}Fe . In this study, aiming at the secondary reaction with ^{52}Fe isomer, we develop the production method of isomer beam by using projectile fragmentation reactions. It decays into excited state in ^{52}Mn via beta decay and de-excited via γ ray emission. The configuration of the isomer is considered as 2 proton holes and 2 neutron holes. It has 2 proton holes and 2 neutron holes, so that those holes form isomer. Previously we work on isomer in secondary beam nuclei by fragmentation of ^{58}Ni . ^{52}Fe has 12^+ spin state at 7 MeV and its half-life is 46 seconds. At MSU, the isomer ratio of ^{52}Fe was measured to be about 0.3 % by nearly same reaction production of ^{58}Ni fragmentation [2]. In order to perform isomer beam experiment effectively, the improvement of isomer ratio, namely the purification of isomer is necessary. We want to make the isomer ratio of ^{52}Fe 10 % by considering the statics for identifying the ground state and the isomer.

How to purify isomer in projectile fragmentation is important. When we measure secondary reaction, we need isomer beam in intermediate energy especially for Gamow Teller transition. That's because we need to use fragmentation reaction for producing isomer beam. Here, we define parallel momentum transfer. In a solid target, the momentum transfer is defined as the momentum of ^{52}Fe in ^{58}Ni minus the momentum of ^{52}Fe in fragment. We expect that the large angular momentum transfer condition become dominant by giving large parallel momentum transfer to the fragment nuclei which is same as previous research [3] [4]. This is the analogy of the knockout reaction. We can calculate

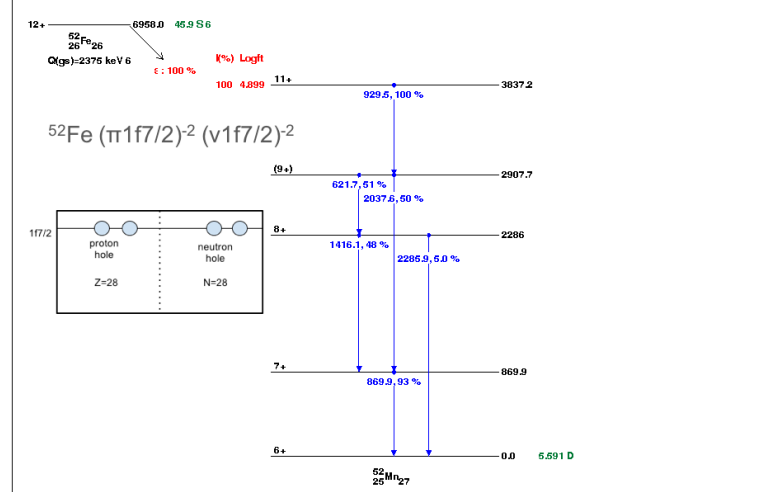


Figure 1. This is level scheme of ^{52}Fe isomer. We identify $^{52}\text{Fe}(12^+)$ by β -delayed γ [1].

the angular momentum L which is necessary for the nucleus to become the isomer state by assuming the spherical nuclei.

For example L of $^{52}\text{Fe}(12^+)$ state is about 440 MeV/c. In

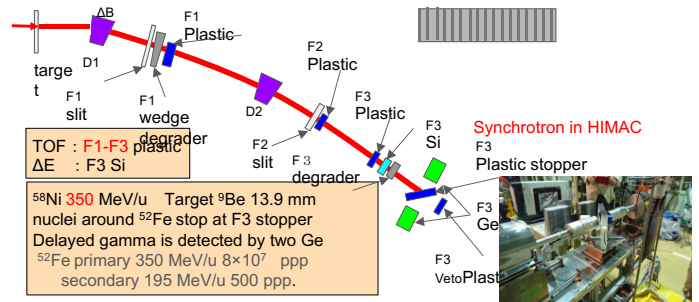


Figure 2. Beam line settings -particle Identify at HIMAC. The secondary beam stop at F3 plastic stopper. HIMAC has cyclotron, the beam come at every 3.3 second. As we count prompt γ ray, we stop beam coming at every 99 second.

this experiment, we controlled parallel momentum transfer by changing $B\rho$. And we define isomer ratio as next formula $R = \text{number of isomer} / \text{sum of isomer and ground nuclei}$. We carried out the experiment at HIMAC in Chiba. We used the primary beam of ^{58}Ni 350 MeV/u and the production target of 13.9 mm thick of ^9Be . In our purpose, we

measured the isomer ratio of nuclei around ^{52}Fe as a function of the momentum transfer. We identified secondary particle by TOF (time of flight) - ΔE method. The start timing of TOF was obtained by F1 plastic detector, while the stop signal was detected by the F3 plastic. The ΔE is measured by the Si detector placed at F3. Nuclei around ^{52}Fe stopped in the plastic stopper and the delayed gamma ray was detected by 2 Ge detectors. We used 2 Ge detectors of relative efficiency 60% and measured timing and energy of delayed from implanted isomer in plastic stopper. Detection efficiency was about 1% at 1 MeV. We show Particle

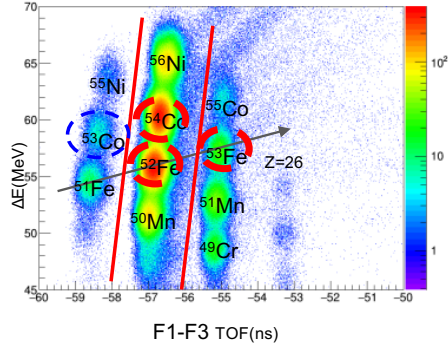


Figure 3. TOF(time of flight) - ΔE plot. Horizontal axis is TOF, vertical axis is ΔE MeV. TOF start from F1 to F3 and ΔE detected by Si. $dE \propto Z^2/\beta^2$. Red circle shows analyzed isomer blue circle shows nuclei having isomeric state.

identify plot, TOF- ΔE plot. Horizontal axis is TOF, vertical axis is ΔE MeV. When we counted the number of secondary particle projection to ΔE and count it.

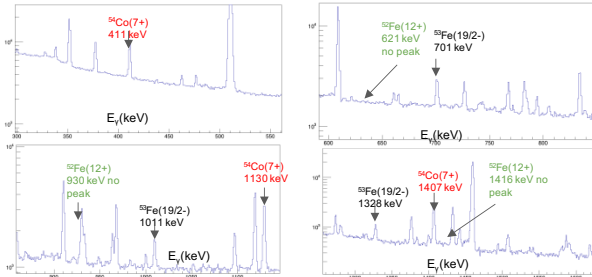


Figure 4. The γ ray energy plot spectra in keV measured with two germanium detectors.

Figures 4 presents the energy spectra of gamma rays. The energy resolution was 2 keV for 1.4 MeV γ ray. Though the γ rays associated with ^{54m}Co and ^{53m}Fe were observed, the γ rays from ^{52m}Fe were not measured.

Figures 5 shows the isomer ratios of ^{53}Fe and ^{54}Co as a function of the momentum transfer. For $^{54}\text{Co}(7^+)$, the lowest isomer ratio of 30 % in our measurement was observed when the momentum transfer was 230 MeV/c. For $^{53}\text{Fe}(19/2^-)$, the lowest isomer ratio of 10 % was obtained at 710 MeV/c while the highest ratio of 16 % was at 1130 MeV/c. Here, we assumed the primary beam energy 350 MeV/u. As the momentum transfer increases, isomer ratio rises. $^{52}\text{Fe}(12^+)$ wasn't observed in this condition for the low isomer ratio by determining the S/N. The isomer ratios depending on the momentum suggest that we can purify the

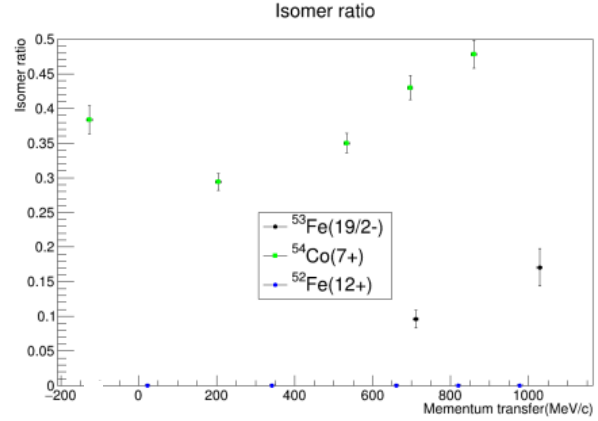


Figure 5. Isomer ratio-momentum transfer plot. Horizontal axis is momentum transfer (MeV/c), vertical axis is isomer ratio via ^{58}Ni fragmentation reaction.

isomers by selecting the large momentum transfers.

As the next plan, we will measure the isomer ratio at the finite scattering angles to bring the transverse angular momentum into the outgoing particles. In addition, the primary beam will change from ^{58}Ni to ^{59}Co . The spin and parity of ^{59}Co is $7/2^-$ which is considered as a proton hole and thus is similar to the configuration of the isomeric state.

References

- [1] D. F. Geesaman *et al.*, Phys.Rev.C.**19**1938(1979).
- [2] K. Minamisono *et al.*, Phys.Rev.Lett. **171** 252501(1986)
- [3] W.-D. Schmidt-Ott *et al.*, Z. Phys. A **359**, 215-219(1994).
- [4] X. L. TU *et al.*, Phys.Rev.C.**95**014610(2017).

**Experimental Nuclear Physics: PHENIX
Experiment at BNL-RHIC and ALICE
Experiment at CERN-LHC**

Low mass dielectron measurements with ALICE at the LHC

T. Gunji for the ALICE Collaboration

Center for Nuclear Study, Graduate School of Science, The University of Tokyo

1. Introduction

Photons and dileptons are useful probes to study the thermodynamical properties of the medium created in heavy-ion collisions since the production rates depend on temperature, degree of freedom, equation of state, and transport parameters [1]. Different invariant mass regions of the dielectron pairs are particularly sensitive to different aspects of heavy-ion collisions. The low mass region ($m_{\pi^0} \leq m_{ee} \leq m_{\eta}$) is a window for the measurements of the virtual photons, while the mass region around $m_{ee} \leq m_{\rho}$ has a link to the vacuum or in-medium modification of the spectral functions of short-lived mesons (ρ , ω , ϕ) [2]. Dielectrons with $1 \leq m_{ee} \leq 3 \text{ GeV}/c^2$ are dominated by the correlated pairs from heavy-flavor decays, where the initial productions are modified due to energy loss in the medium. In this paper, the status of the low-mass dielectron measurements in all collision systems at the LHC-ALICE is summarized

2. Data set and analysis

Data analysis of low mass dielectrons is very challenging due to their small signal-to-background ratio ($\sim 10^{-3}$). By using data taken by ALICE [3] during RUN 1 (300M pp MB collisions at $\sqrt{s} = 7 \text{ TeV}$, 100M MB p–Pb collisions at $\sqrt{s_{NN}} = 5.02 \text{ TeV}$, and 17M+12M 0–10% + 20–50% central Pb–Pb collisions at $\sqrt{s_{NN}} = 2.76 \text{ TeV}$), the analysis strategies of low mass dielectrons including electron identification, rejection of conversions, background subtraction, etc. have been developed. Electrons with $p_T \geq 0.2 \text{ GeV}/c$ are identified by using dE/dx in the Time Projection Chamber (TPC) and the outer four layers of the Inner Tracking System (ITS). Additionally the Time-of-Flight detector (TOF) is used for $p_T \geq 0.4 \text{ GeV}/c$ to reject kaons and protons. The hadron contamination in pp, and Pb–Pb, is at most 1% and 10%, respectively, for all p_T range. Electrons from photon conversions, which are one of the main backgrounds, are rejected based on tight track quality cuts, V0 tagging [4], and orientation pair angle in the magnetic field. After making electron and positron pairs (unlike-sign pairs), the combinatorial background is subtracted by using the like-sign pairs, corrected for acceptance difference between unlike and like-sign pairs, which is estimated by using mixed event pairs. The subtracted data are corrected for efficiency, which is determined via Monte Carlo (MC) simulations including a realistic description of the detector responses.

3. Dielectrons in pp and p–Pb collisions

Figure 1 and Figure 2 show the corrected dielectron invariant mass spectra in pp and p–Pb collisions, respectively. The data are compared to the expected dielectron decays from known hadronic sources (hadronic cocktail). Those hadronic contributions are based on measured differential

cross-sections of π^0 , η , ϕ , and J/ψ in pp collisions [5–7], and based on those of charged pions for p–Pb collisions [8]. The contributions from remaining light-hadrons are based on m_T scaling. The correlated pairs from heavy-flavor decays are estimated by using MNR parametrizations of PYTHIA 6 scaled to the charm/bottom cross section measured by ALICE [9]. In both pp and p–Pb collisions, the corrected dielectron yields are in agreement with the cocktail within the statistical and systematic uncertainties.

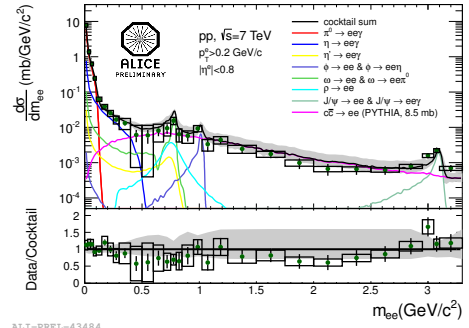


Figure 1. Dielectron invariant mass spectrum in pp collisions at $\sqrt{s} = 7 \text{ TeV}$ compared to the hadronic cocktail

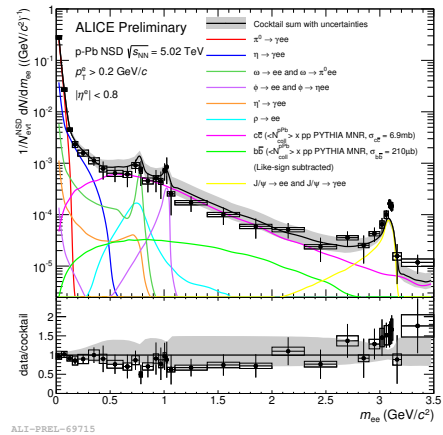


Figure 2. Dielectron invariant mass spectrum in p–Pb collisions at $\sqrt{s_{NN}} = 5.02 \text{ TeV}$

4. Dielectrons in Pb–Pb collisions

The first measurement of the dielectron invariant mass spectrum in Pb–Pb collisions at $\sqrt{s_{NN}} = 2.76 \text{ TeV}$ has been performed. Figure 3 shows the dielectron invariant mass spectrum below $0.7 \text{ GeV}/c^2$ in 0–10% central collisions and comparison with known hadronic cocktails, where the measured π^0 differential cross-section is used [10], m_T scaling

is applied for the other light-flavor contributions, and contributions from heavy-flavors are based on PYTHIA 6 scaled by the number of binary collisions.

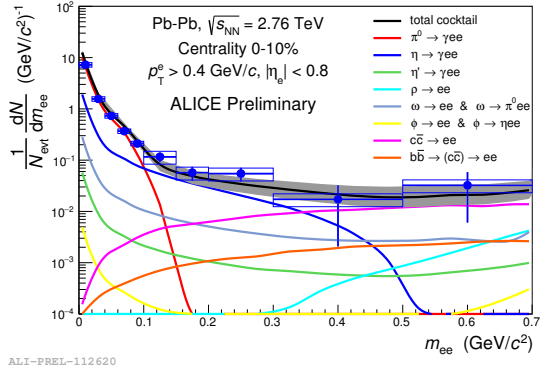


Figure 3. Dielectron invariant mass below $0.7 \text{ GeV}/c^2$ in Pb–Pb collisions and comparison with known hadronic sources

Figure 4 shows the comparison between data (point), hadronic cocktail (black line), and model calculations with medium effects such as thermal radiation from the medium and in-medium modification of the ρ meson (red line) [11]. From Fig. 3 and Fig. 4, we do not have any good sensitivity to disentangle the medium effects.

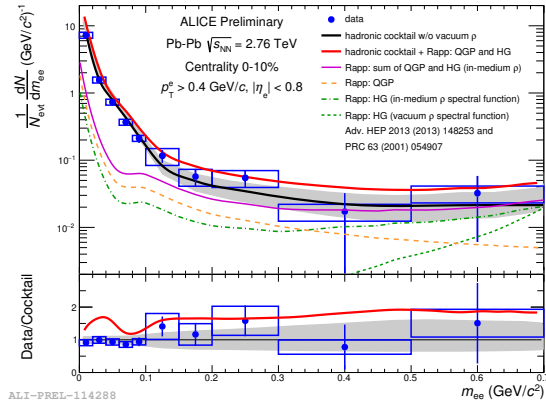


Figure 4. Theoretical comparison with inclusion of thermal radiation and in-medium modification of the ρ meson

5. Future prospects

ALICE is going to upgrade some key detectors, readout and data acquisition systems for RUN 3 to inspect 50kHz Pb–Pb collisions [12]. Our CNS contributes the upgrade of the TPC in order to run the TPC continuously and gain the event rate by a factor of 100. With those upgrades, the first measurements of thermal direct radiation around $1\text{--}3 \text{ GeV}/c^2$ will be possible for the study of the temperature dependence of medium properties.

6. Summary

ALICE has measured dielectron production in pp, p–Pb, and Pb–Pb collisions at different energies. In pp and p–Pb collisions, the corrected invariant mass spectra are consistent with known hadronic sources. First dielectron mea-

surements in Pb–Pb collisions show that the corrected yield is not significantly larger than the known hadronic sources and not yet sensitive to the modification of the ρ meson due to large uncertainty and large charm contributions. More dielectron measurements will come from RUN 2, and the ALICE upgrades will allow precision measurements in RUN 3 and RUN 4.

References

- [1] E. V. Shuryak, Phys. Lett. B78 (1978) 150.
- [2] R. Rapp and J. Wambach, Advances in Nuclear Physics, 25, pp. 1–205 (2000).
- [3] K. Aamodt et al. (The ALICE Collaboration) JINST, 3, S08002 (2008).
- [4] B. Abelev et al. (The ALICE Collaboration), Int. J. Mod. Phys. A 29 (2014) 1430044.
- [5] K. Koch (The ALICE Collaboration), Nucl. Phys. A, 855, pp. 281–284 (2011).
- [6] B. Abelev et al. (The ALICE Collaboration), Eur. Phys. J. C, 72, p. 2183 (2012).
- [7] K. Aamodt et al. (The ALICE Collaboration), Phys. Lett. B, 704, pp. 442–455 (2011).
- [8] B. Abelev et al. (The ALICE Collaboration), Phys. Rev. Lett., 110, 082302 (2013).
- [9] B. Abelev et al. (The ALICE collaboration), JHEP01, 128 (2012).
- [10] B. Abelev et al. (The ALICE Collaboration), Eur. Phys. J. C, 74, 10, p. 3108 (2014).
- [11] R. Rapp, private communication
- [12] B. Abelev et al. (The ALICE Collaboration), J. Phys. G, 41, 087002 (2014).

Charm baryon measurements with ALICE at the LHC

Y. S. Watanabe

Center for Nuclear Study, Graduate School of Science, University of Tokyo

1. Introduction

Charm quarks are an ideal probe to study the properties of quark-gluon plasma (QGP) created in heavy-ion collisions. The production of charm quarks is limited to the initial stage of the collisions because the mass of charm quark is much larger than the temperature of the QGP, and thus, the information concerning the whole system evolution is imprinted on their final observables. While the production of charm mesons (D^0 , D^+ , D^{*+} , D_s^+) in heavy-ion collisions is extensively studied by ALICE and CMS at the LHC, there is no measurement of charm baryons up to now. The measurement of charm baryons are interesting because they provide unique information about the properties of the QGP, such as the correlation between light quarks, “diquark”. The existence of diquark correlations in QGP could enhance the production of Λ_c^+ by a factor of 4–8 compared to the case without such correlations [1].

This report presents the measurements of Λ_c^+ and Ξ_c^0 via their semileptonic decays ($\Lambda_c^+ \rightarrow e^+\Lambda\nu$ and $\Xi_c^0 \rightarrow e^+\Xi^-\nu$) in pp collisions at $\sqrt{s} = 7$ TeV. (Charge conjugates are also implied throughout this report.) The measurement in pp collisions provides an essential baseline for the understanding of heavy-ion collision data, and at the same time, are interesting in its own right. Some theories predict that charm baryon production could be enhanced even in pp collisions compared to e^+e^- collisions due to interactions between produced quarks and gluons, such as color reconnection [2].

2. Experimental apparatus

Electrons, Λ -baryons and Ξ^- -baryons originating from the charm baryons are reconstructed and identified by the ALICE central barrel detectors. Details of ALICE detectors can be found in [3]. The central barrel detectors include the Inner Tracking System (ITS), Time Projection Chamber (TPC) and Time-of-Flight detector (TOF). Electrons are identified by the dE/dx information of TPC and by the time-of-flight information of the TOF. The electron identification cuts are tuned such that the hadron contamination is kept to be about 2%. Λ (Ξ^-) baryons with a long lifetime of about 5 cm are identified by their characteristic V-shaped (cascade-like) decay topology.

3. Data analysis

In this section, the analysis of Λ_c^+ baryons is described. Similar analysis procedure is taken for the analysis of Ξ_c^0 . Λ_c^+ baryons are studied using the semileptonic decay by detecting $e^+\Lambda$ pairs. Due to the missing momentum of neutrino, the invariant mass distribution of $e^+\Lambda$ pairs does not show a peak at the Λ_c^+ mass (~ 2.286 GeV/ c^2 [4]). The contribution from background $e^+\Lambda$ pairs are estimated using $e^-\Lambda$ pairs by exploiting the fact that the Λ_c^+ semileptonic decay is charge asymmetric: Λ_c^+ decays into $e^+\Lambda\nu$ (right-

sign, RS) but not into $e^-\Lambda\nu$ (wrong-sign, WS), while most of the background sources are charge symmetric. This way of background estimation using WS pairs are previously introduced by ARGUS and CLEO collaborations in e^+e^- collisions [5, 6].

WS pair yields are subtracted from RS pair yields and the subtracted yields are further corrected for the Λ_b^0 contribution in WS pairs, $\Xi_c^{0,+}$ contributions in RS pairs, missing momentum of neutrino, the geometrical acceptance and the selection efficiency. Λ_b baryons contribute to WS pairs via the decay mode, $\Lambda_b^0 \rightarrow e^-\Lambda_c^+X \rightarrow e^-\Lambda X$. This contribution is evaluated using the Λ_b^0 measurement by CMS [7] and found to grow with p_T reaching 10% of the Λ_c^+ signal in the highest p_T interval. Ξ_c^0 contribute to RS pairs via the decay mode, $\Xi_c^- \rightarrow e^+\Xi^-X \rightarrow e^+\Lambda X$. This contribution is evaluated using the measured cross section from this analysis and found to be about 50% of the Λ_c^+ signal over the measured p_T range. The transverse momentum distribution of $e^+\Lambda$ pairs is corrected for the missing momentum of the neutrino using unfolding techniques. The unfolding is performed with the RooUnfold implementation of the Bayesian unfolding technique, which is an iterative method based on Bayes’ theorem [8]. The product of the geometrical acceptance and the selection efficiency is estimated using the full detector simulation with realistic detector configurations. The geometrical acceptance and the selection efficiency increase from 0.5% to 10% as going towards higher p_T .

4. Results

The p_T differential cross section of the Λ_c^+ baryon is shown in Figure 1 for the p_T interval $1 < p_T < 8$ GeV/ c . The vertical line and boxes around the data points show the statistical and the systematic uncertainties. The result of this analysis is compared with the analyses using the hadronic decays of Λ_c^+ baryons, such as $\Lambda_c^+ \rightarrow pK^-\pi^+$ and $\Lambda_c^+ \rightarrow pK_s^0$. The results obtained with different decay modes are compatible within statistical and systematic uncertainties. Figure 2 shows the Ξ_c^0 cross section multiplied by branching ratio into the semileptonic decay mode obtained with a similar analysis procedure as Λ_c^+ . The absolute branching ratio of the Ξ_c^0 semileptonic decay is currently not known [4]. This is the first measurement of Ξ_c^0 production in pp collisions at the LHC.

Figure 3 shows the comparison of the Λ_c^+/D^0 ratio to various model calculations [2, 9]. The results from different decay modes are averaged to obtain a more precise cross section. Currently all the available models are found to underestimate the measured ratio. This indicates the lack of our understanding of charm quark hadronization even in pp collisions.

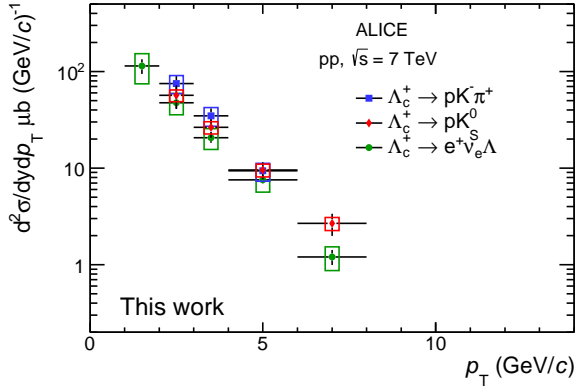


Figure 1. The p_T differential cross section of the Λ_c^+ baryon for the transverse momentum range $1 < p_T < 8$ GeV/c in pp collisions at $\sqrt{s} = 7$ TeV. Different markers indicate the results obtained with different decay modes.

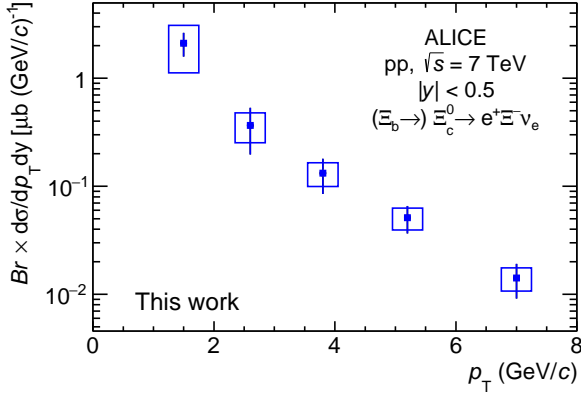


Figure 2. The p_T differential cross section of the Ξ_c^0 baryon multiplied by the branching ratio into $e^+ \Xi^- \nu$ for the transverse momentum range $1 < p_T < 8$ GeV/c in pp collisions at $\sqrt{s} = 7$ TeV.

5. Summary and outlook

We reported on the measurements of Λ_c^+ and Ξ_c^0 baryons via their semileptonic decays in pp collisions at $\sqrt{s} = 7$ TeV. The Λ_c^+ cross section from this analysis is compatible with the ones obtained with hadronic decay analyses. Theoretical models are found to underestimate the production of charm baryons. Thus, this measurement could provide an important constraint on the models of charm quark hadronization in pp collisions. Once the analysis in pp collisions is finalized, the analysis of Pb–Pb data is going to be performed to elucidate the “diquark” structure in the QGP.

References

- [1] S. H. Lee, K. Ohnishi, and S. Yasui, I. Yoo and C. M. Ko, Phys. Rev. Lett. **100** (2008) 222301.
- [2] J. R. Christiansen and V. Khachatryan *et al.*, JHEP **08** (2015) 003.
- [3] K. Aamodt *et al.*, JINST **3** (2008) S08002.
- [4] Particle Data Group, Chin. Phys. **C40** (2016) 100001.
- [5] ARGUS Collaboration, Phys. Lett. **B303** (1993) 368.
- [6] CLEO Collaboration, Phys. Rev. Lett. **74** (1995) 3113.

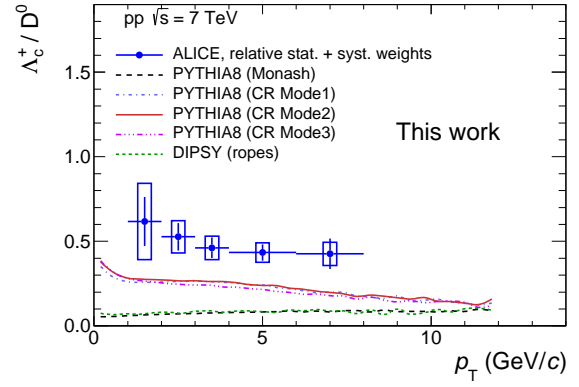


Figure 3. The Λ_c^+ / D^0 ratio measured in pp collisions, compared with different theoretical model calculations.

- [7] CMS Collaboration, Phys. Lett. **B714** (2012) 136.
- [8] G. D’Agostini, Nucl. Instrum. Meth. **A362** (1995) 487.
- [9] C. Bierlich and J. R. Christiansen, Phys. Rev. **D92** (2015) 094010.

J/ψ production in p-Pb collisions at $\sqrt{s_{NN}} = 5.02$ TeV

S. Hayashi, H. Hamagaki^a, and T. Gunji

Center for Nuclear Study, Graduate School of Science, University of Tokyo

^aNagasaki Institute of Applied Sciences

Quantum Chromodynamics predicts quark deconfinement and the transition to strongly interacting matter, quark-gluon plasma (QGP), at extremely high temperature and density. Relativistic heavy ion collisions are an unique tool to study the properties of QGP. Since the yield of J/ψ is expected to decrease in QGP due to Debye screening of color charges, J/ψ suppression is one of the strong signatures of QGP formation [1].

PHENIX experiment at the Relativistic Heavy Ion Collider (RHIC) in the Brookhaven National Laboratory observed strong suppression of J/ψ production in Au–Au collisions at $\sqrt{s_{NN}} = 200$ GeV [2]. The J/ψ yields measured by the ALICE experiment at the Large Hadron Collider (LHC) in the European Organization for Nuclear Research were also suppressed in Pb–Pb collisions at $\sqrt{s_{NN}} = 2.76$ TeV [3].

Furthermore, Non-negligible suppression of the J/ψ yield was also observed in d–Au collisions at $\sqrt{s_{NN}} = 200$ GeV at RHIC [4]. Suppression in d–Au collisions is thought as normal nuclear matter effects such as gluon shadowing and nuclear absorption. The understanding of normal nuclear matter effects is essential in the discussion of the QGP effects in relativistic heavy ion collisions. In this report, we present the measurement of inclusive J/ψ production in minimum bias p–Pb collisions at $\sqrt{s_{NN}} = 5.02$ TeV at mid-rapidity ($-1.37 < y < 0.43$) with the ALICE central barrel detectors. The main aim of this analysis is the investigation of normal nuclear matter effects in relativistic heavy ion collisions at LHC energy.

J/ψ is detected via dielectron decay channels by calculating their invariant mass. In the ALICE central barrel, electrons are reconstructed using the Inner Tracking System (ITS) and the Time Projection Chamber (TPC) in $|\eta| < 0.9$. Figure 1 shows the p_T -integrated invariant mass spectra of unlike-sign, expected background, and background subtracted pairs. Since the main source of the background is combinatorial pairs, event mixing technique is used to estimate the shapes of the background.

After background subtraction, the raw yields are corrected by the reconstruction efficiency calculated using Monte-Carlo simulation generated by Geant3. The measured production cross section of inclusive J/ψ in p–Pb collisions at $\sqrt{s_{NN}} = 5.02$ TeV at mid-rapidity ($-1.37 < y < 0.43$) is determined by

$$\frac{d\sigma_{J/\psi}}{dy} = 930 \pm 83 \text{ (stat)} \pm 74 \text{ (syst)} \mu\text{b}. \quad (1)$$

In order to investigate nuclear matter effects in p–Pb collisions, the nuclear modification factor (R_{pPb}) is introduced.

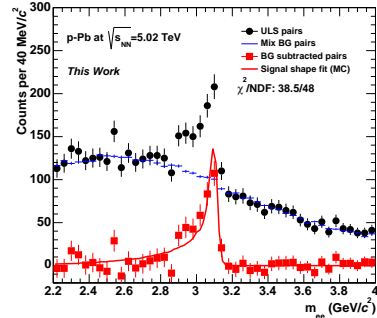


Figure 1. Invariant mass distribution of unlike-sign, mixing background, and background subtracted pairs in p–Pb collisions. The solid red line shows the result of the fitting to the subtracted signal.

R_{pPb} is defined as

$$R_{pPb} = \frac{Y_{pPb}}{\langle N_{coll} \rangle Y_{pp}}, \quad (2)$$

where Y_{pPb} and Y_{pp} are the invariant yield of J/ψ in pp and p–Pb collisions, respectively. $\langle N_{coll} \rangle$ is the average number of binary nucleon–nucleon collisions in p–Pb collisions. R_{pPb} expresses a deviation of yields from expected yields under the assumption that p–Pb collisions are approximated as a superposition of nucleon–nucleon collisions. Since there is no measurement of J/ψ production in pp collisions at $\sqrt{s} = 5.02$ TeV, the pp reference spectrum at $\sqrt{s} = 5$ TeV is estimated by the interpolation from the measured pp spectra at various collision energies [5]. R_{pPb} of inclusive J/ψ production at mid-rapidity ($-1.37 < y < 0.43$) is extracted as

$$R_{pPb} = 0.74 \pm 0.07 \text{ (stat)} \pm 0.13 \text{ (syst)}. \quad (3)$$

Compared with R_{pPb} at forward rapidity via dimuon decay, the magnitude of R_{pPb} at mid-rapidity is compatible within the uncertainties. The upper panel of Fig. 2 shows the comparison of the rapidity dependence of R_{pPb} with the gluon shadowing model calculations [6, 7]. At mid-rapidity, both EPS09 NLO and LO calculations are consistent with the experimental results within the uncertainties. The rapidity dependence of R_{pPb} is also described by the EPS09 LO calculation. The lower panel of Fig. 2 shows the comparison of the rapidity dependence of R_{pPb} with the coherent energy loss model calculation [8]. The coherent energy loss model with typical transport coefficient \hat{q} shows a reasonable description of the rapidity dependence of the measured R_{pPb} . Figure 3 shows the comparison of the transverse momentum dependence between the measured R_{pPb} and the model calculations [6, 8, 9]. The coherent energy loss model shows a reasonable description of both rapidity

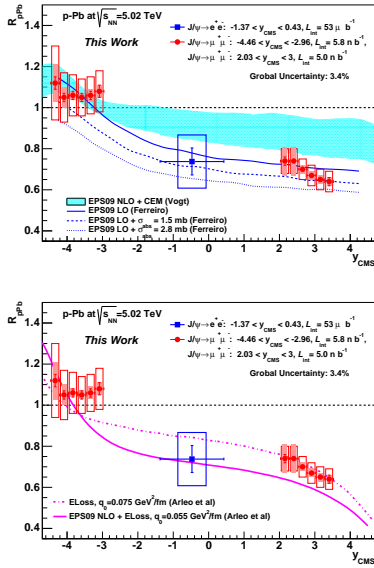


Figure 2. Comparison of the rapidity y dependence of the data to the gluon shadowing models (Up) and the coherent energy loss model (Bottom) in p–Pb collisions at $\sqrt{s_{NN}} = 5.02$ TeV [6–8].

and transverse momentum dependence of measured R_{pPb} . However, the uncertainties of both data and model calculations are still large. The main sources of the uncertainties in the current measurement are the statistical uncertainty and the systematic uncertainty from the extraction of pp reference spectrum. The further reduction of the uncertainties is needed to obtain the conclusive explanation of normal nuclear matter effects in heavy ion collisions at LHC.

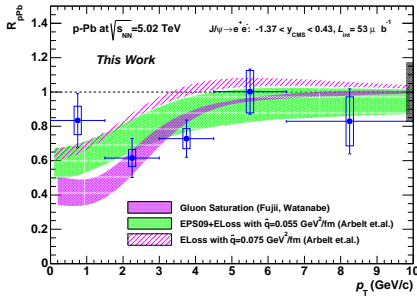


Figure 3. Comparison of the p_T dependence between the measured R_{pPb} and the model calculations in p–Pb collisions at $\sqrt{s_{NN}} = 5.02$ TeV. The violet, green, and magenta bands show the calculation based on gluon saturation with CGC framework, coherent energy loss with EPS09 nPDF parametrization, and coherent energy loss with the proton PDF parametrization [6, 8, 9].

Under the assumption that the effect of gluon shadowing is dominant compared to other normal nuclear matter effects, normal nuclear matter effects in R_{AA} are approximated by the convolution of R_{pPb} [10]. Figure 4 shows the surviving fraction (S_{AA}) defined as

$$S_{AA} = \frac{R_{AA}}{R_{pA}(-y) \times R_{pA}(y)}. \quad (4)$$

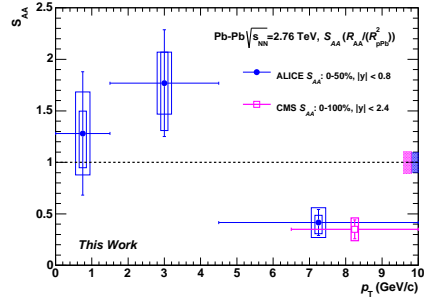


Figure 4. Surviving fraction (S_{AA}) of J/ψ production in Pb–Pb collision.

A suppression of J/ψ production is seen at high p_T above 4.5 GeV/c. This suppression is qualitatively consistent with the color screening pictures. On the other hand, the enhancement of the J/ψ yield is observed at lower p_T . This is expected due to the regeneration of J/ψ from uncorrelated $c\bar{c}$ pairs in Pb–Pb collisions [11]. The understanding of this enhancement at low p_T is quite important to study the dynamics of heavy quarks in QGP and the hadronization process. Thermalization of heavy quarks in QGP is correlated to the viscosity of QGP via fluctuation–dissipation theorem.

In LHC-Run2 (from 2015), more abundant data for both pp and p-Pb collisions is available. The extraction of J/ψ R_{pPb} with significant reduction of the uncertainties is promising and it is possible to perform more precise analysis for J/ψ production mechanism.

References

- [1] T. Matsui and H. Satz, Phys. Lett. B **178** (1986) 416.
- [2] A. Adare *et al*, Phys. Rev. Lett. **98** (2007) 232301.
- [3] A. Andronic, arXiv:1409.5778 (2015).
- [4] A. Adare *et al*, Phys. Rev. Lett. **107** 142301 (2011).
- [5] F. Bossu *et al*, arXiv:1103.2394 (2011).
- [6] R. Vogt, Phys. Rev. C **81** (2010) 044903.
- [7] E. Ferreiro *et al*, Phys. Rev., C **88** (2013) 047901.
- [8] F. Arleo *et al*, JHEP03 122, JHEP05 155 (2013).
- [9] H. Fujii and K. Watanabe, J. Nucl. Phys. A. **2013** 06 011, arXiv:1304.2221 (2013).
- [10] E. Ferreiro *et al*, Phys. Lett. B **680** 50-55, T. Gunji, Phys. Rev. C **76** (2007) 051901.
- [11] K. Zhou *et al*, Phys. Rev. C **89** (2014) 054911

Measurement of two particle correlations in p -Pb collisions at LHC-ALICE

Y. Sekiguchi, H. Hamagaki, and T. Gunji for the ALICE Collaboration

Center for Nuclear Study, Graduate School of Science, The University of Tokyo

1. introduction

Measurement of the correlations in the particle production as a function of the azimuthal angle and rapidity is very useful for investigating particle production in high-energy nucleus-nucleus collisions. The long-range correlations in the rapidity space in near-side angular pairs of dihadrons were firstly observed in Au-Au collisions at $\sqrt{s_{NN}}=200$ GeV at RHIC [1, 2]. The long-range correlations are derived from the collective expansion of the initial geometry fluctuations. Unexpectedly, a similar structure has also been observed in high-multiplicity pp collisions at 7 TeV by the LHC-CMS experiment [3]. The high-density gluon fields in small x (Bjorken x) of nucleus and the collision of two high-density gluon sheets can explain the long-range correlations [4]. The measurements of the particle productions with large rapidity gaps and the centrality dependence are important for quantifying the collective expansion. This analysis aims to explore the partonic collectivity by measuring long-range two-particle correlations using forward detectors in p -Pb collisions at $\sqrt{s_{NN}}=5.02$ TeV.

2. Analysis

The minimum bias data of p -Pb collisions at $\sqrt{s_{NN}}=5.02$ TeV in 2016 are used (~ 600 M events). The main subsystems in ALICE used in this analysis are time projection chamber (TPC) and Forward Multiplicity Detector(FMD). The TPC is the main tracking detector and is used for particle identification by measuring the specific energy loss. They have a common pseudorapidity acceptance $|\eta| < 0.9$. The FMD is composed of three arrays at $-3.4 < \eta < -1.7$, $1.7 < \eta < 3.68$, and $3.68 < \eta < 5$, respectively(Table.1). They are usually used to measure multiplicity and event

Array	Ring	ϕ segments	η coverage
FMD1	-	20	3.68 -5.03
FMD2	FMD2i	20	2.28 -3.68
	FMD2o	40	1.70 - 2.29
FMD3	FMD3i	20	-2.29 - -1.70
	FMD3o	40	-3.40 - -2.01

Table 1. FMD pseudo rapidity coverage and azimuthal segments.

plane. To define centrality, VZEROA detector which is located in the Pb-going direction ($|\eta| > 8$) is used. The position of the reconstructed vertex along the beam direction is required to be within 10 cm from the detector center. The correlations between trigger particles and associated particles are measured as a function of the azimuthal angle difference $\Delta\phi$ and pseudo-rapidity difference $\Delta\eta$. The trigger particles are unidentified charged hadrons, while FMD channels are used as associated particles. FMD cannot measure transverse momentum p_T and the multiplicity in each

channel is used as the number of tracks in the average ϕ and η of each channel. The correlation function as a function of $\Delta\eta$ and $\Delta\phi$ between two charged particles is defined as:

$$\frac{1}{N_{\text{trig}}} \frac{d^2 N_{\text{asso}}}{d\Delta\eta d\Delta\phi} = \frac{S(\Delta\eta, \Delta\phi)}{B(\Delta\eta, \Delta\phi)} \quad (1)$$

where N_{trig} is the total number of triggered particles in the event class and p_T interval, the signal distribution $S(\Delta\eta, \Delta\phi) = \frac{1}{N_{\text{trig}}} \frac{d^2 N_{\text{same}} \times w_i}{d\Delta\eta d\Delta\phi}$ is the associated yield per trigger particle from the same event, and the background distribution $B(\Delta\eta, \Delta\phi) = \alpha \frac{d^2 N_{\text{mixed}} \times w_i}{d\Delta\eta d\Delta\phi}$ accounts for pair acceptance and pair efficiency. It is constructed by taking the correlations between trigger particles in one event and associated particles from other events in the same event class. w_i is the multiplicity in each FMD channel. The α factor is chosen so that it is unity at the maximum bin. This correlation function is studied for different pseudo-rapidity intervals and different event classes.

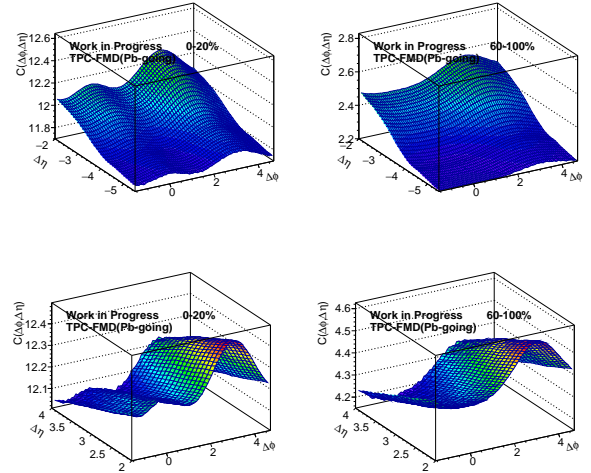


Figure 1. Associated yield per trigger particle for TPC-FMD1,2 (top) and TPC-FMD3(bottom) for the 0-20%(left) and 60-100%(right) event classes.

Figure 2 shows the projection of subtracted correlation functions of TPC-FMD1,2. The near-side yield decreases with increasing $\Delta\eta$ in 0-20%, while no near-side yield in 60-100%. The template method is used to remove the auto-correlations from jets. The correlation function is assumed to sum of peripheral distribution scaled up by a multiplicative factor and the ridge distribution as Eq(2).

$$Y(\Delta\phi) = AY^{\text{peri}} + G(1 + 2c_2 \cos(2\Delta\phi) + 2c_3 \cos(3\Delta\phi)) \quad (2)$$

A and G are free parameters. The data is described by a fit with Eq. (2) well(Fig. 3). The second-order term is

the dominant harmonic coefficient. Figure 4 shows the extracted c_2 and c_3 coefficients as a function of η of FMD. c_2 of TPC-FMD1,2 seems larger than that of TPC-FMD3, but it need to be correct the detector effect.

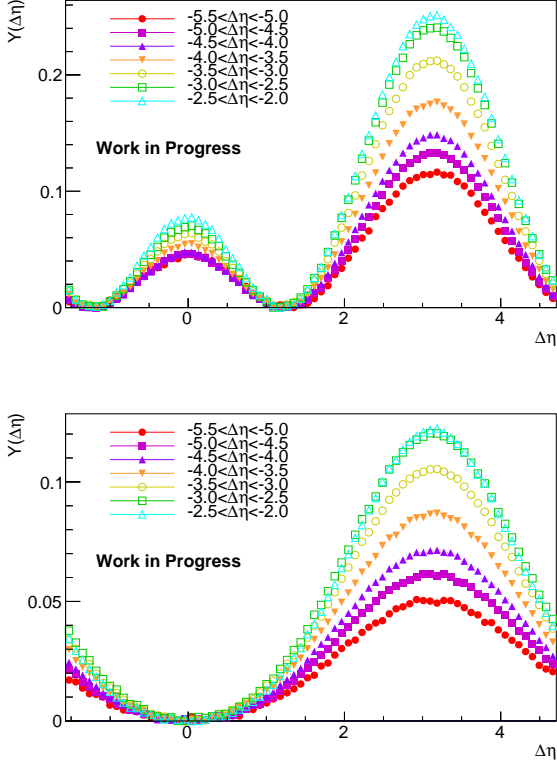


Figure 2. Projection of the correlation function of the associated FMD1,2 per trigger in 0-20%(top) and in 60-100%(bottom).

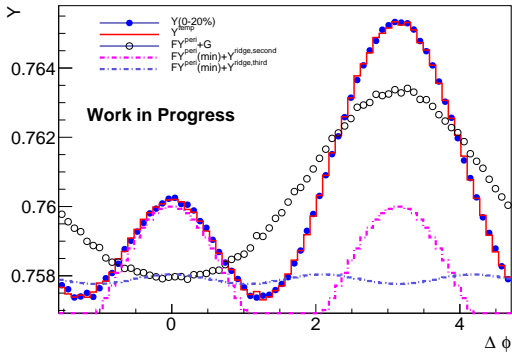


Figure 3. Template fit for TPC-FMD1,2 at $4.6 < \eta < 4.9$.

3. Summary and Outlook

Two-particle correlations between unidentified charged hadrons and channels of FMD in p -Pb collisions at $\sqrt{s_{NN}}=5.02$ TeV are measured. c_2 and c_3 are extracted using template fit method. The estimation of detector effect is on going to extract v_2 as a function of η .

References

[1] STAR Collaboration, Phys. Rev. C80 (2009) 064912

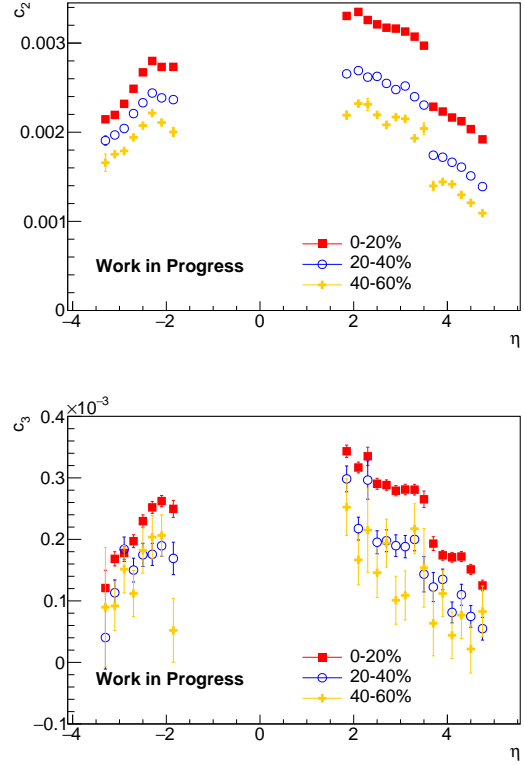


Figure 4. c_2 of TPC-FMD1,2(top) and TPC-FMD3(bottom).

- [2] PHOBOS Collaboration, Phys. Rev. Lett. 104 (2010) 062301
- [3] CMS Collaboration, JHEP 09 (2010) 091
- [4] K. Dusling and R. Venugopalan, Phys. Rev. D 87 (2013) 054014
- [5] ALICE Collaboration, Phys. Lett. B, 726 (2013) 164-177

π^0 and η measurement of direct photons via external conversions in pp collisions at $\sqrt{s} = 5.02$ TeV

H. Murakami and T. Gunji^a for the ALICE collaboration

Department of Physics, University of Tokyo

^a *Center for Nuclear Study, Graduate School of Science, University of Tokyo*

1. Introduction

The observations of collective behavior of hadrons in high multiplicity pp and p-Pb collisions at the LHC is one of the most surprising discoveries in recent years [1]. Such a collective behavior indicates the formation of thermalized systems such as a new state of matter, quark-gluon plasma (QGP) even in small collision systems [2]. If the QGP is created in high-multiplicity events in small collision systems, many features in heavy ion collisions are also seen in such systems and the thermal photons are expected to be emitted from the QGP.

A direct photon is an ideal probe to study the properties of QGP, as it is an electromagnetic probe and has no final state interaction. To obtain the direct photons, decay photons from π^0 and η decays have to be subtracted from inclusive photons.

In this study, we looked for the direct photon in pp at $\sqrt{s} = 5.02$ TeV and p-Pb collisions at $\sqrt{s_{NN}} = 5.02$ TeV to prove that the QGP is created in small systems. The former measurement is compared to the other in which the direct photon was observed. This report presents the current status of π^0 and η measurements in pp collisions.

2. Direct photon analysis overview

In hadronic collisions, photons are emitted at every stage of the space-time evolution. The emitted photons are categorized into two groups: direct photons and decay photons. The former photons are the thermal radiation and photons produced in elementary hard QCD process such as $q\bar{q} \rightarrow qg$ and $qg \rightarrow q\gamma$. The latter photons are decay photons from $\pi^0 \rightarrow \gamma\gamma$ and $\eta \rightarrow \gamma\gamma$. We first deduce the inclusive photon spectrum and then statistically subtract the spectra of decay photons. The invariant yield of direct photons $\gamma_{\text{dir}}(p_T)$ can be expressed in terms of the inclusive photons $\gamma_{\text{inc}}(p_T)$ and that of decay photons $\gamma_{\text{dec}}(p_T)$:

$$\gamma_{\text{dir}}(p_T) = \gamma_{\text{inc}}(p_T) - \gamma_{\text{dec}}(p_T) \quad (1)$$

$$= (1 - R_\gamma^{-1}(p_T)) \cdot \gamma_{\text{inc}}(p_T), \quad (2)$$

where $R_\gamma(p_T) = \gamma_{\text{dec}}(p_T)/\gamma_{\text{inc}}(p_T)$ is the fraction of photons from π^0 and η decays. By using $R_\gamma(p_T)$, the common systematic uncertainties in decay photon and inclusive photon measurements are canceled. In order to obtain decay photon spectra, π^0 and η which are the major sources of decay photons are deduced by various techniques, which includes photon conversion method and calorimeter method. Other sources are estimated by using m_T scaling from measured π^0 and η p_T spectra.

3. Data analysis

In the ALICE experiment, photons are detected in two ways: the measurement of their energy deposit in calorimeters or the measurement of e^+e^- pairs from photon conversions. The photon conversion method has an advantage of to measure photons down to low p_T , where thermal photons dominate.

The main tracking system [3] of the ALICE detector consists of the Inner Tracking System (ITS), the Time Projection Chamber (TPC) and the Time of Flight (TOF). Photons convert into e^+e^- in the material of the ITS and TPC. The event multiplicity is estimated with V0 detectors, which are made of two arrays of scintillation counters placed on forward and backward of the ALICE interaction point.

In 2015, ALICE successfully collected over 128 M events which correspond to 2.5 nb^{-1} in pp collisions at $\sqrt{s} = 5.02$ TeV with minimum bias (MB) trigger and this data sample is used in this analysis. The e^+e^- pairs from photon conversions are reconstructed with the V^0 reconstruction method which find particles from off vertex decay. To select photon samples, electron identification cuts based on the dE/dx in the TPC (Fig.1) is applied to V^0 particles. To improve photon purity, several selection criteria, like constraints on the opening angle, on the reconstructed invariant mass, cut of the Armenteros-Podolanski plot [4] are applied. Furthermore, 2 dimensional cut based on the distance closest approach (dca) of z-direction and χ^2/ndf which represents "photon-likeliness" is applied to reject photons from out-of-bunch pile up. Photons are paired after these cuts applied. Figures 2 and 3 show the invariant mass distribution of photon pairs around π^0 mass and η mass respectively. Black points show the same event pairs, and blue open points show combinatorial background which calculated with photons from different events. After the combinatorial BG subtraction, extracted signal (red points) are well described with the result of the Monte Carlo simulation which assumed the true mesons.

4. Summary and outlook

In this report, current status of neutral meson measurement in pp collisions are presented. Currently corrected yield calculation and systematic uncertainty estimation are ongoing. Then, we will evaluate the invariant cross section of π^0 and η and start to analyze p-Pb collisions.

References

- [1] The CMS collaboration, J. High Energy Phys. 09 (2010) 091.
- [2] C.Shen et al, Phys. Rev. Lett. 116, 072301
- [3] The ALICE Collaboration, JINST 3, S08002 (2008).

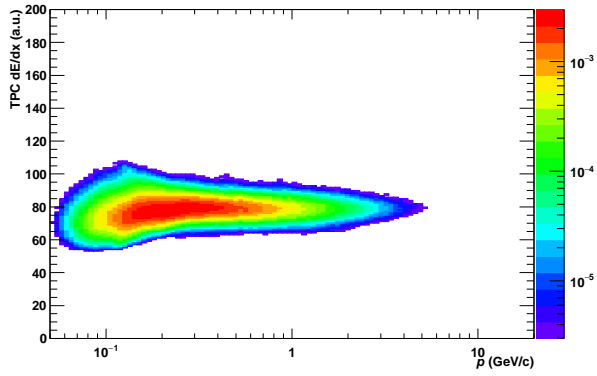


Figure 1. Specific energy loss (dE/dx) of conversion electrons after the $n\sigma_{e^-} dE/dx$ cuts.

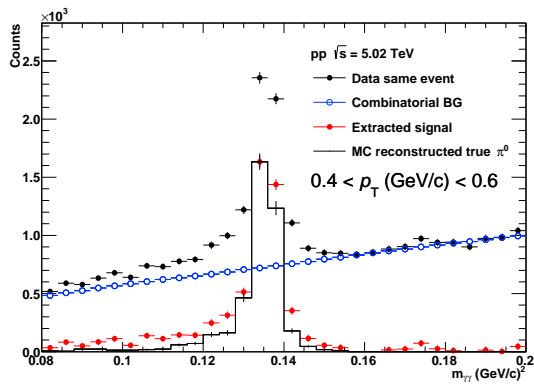


Figure 2. Invariant mass distribution of reconstructed photon pairs of data (black points) and MC (blue line).

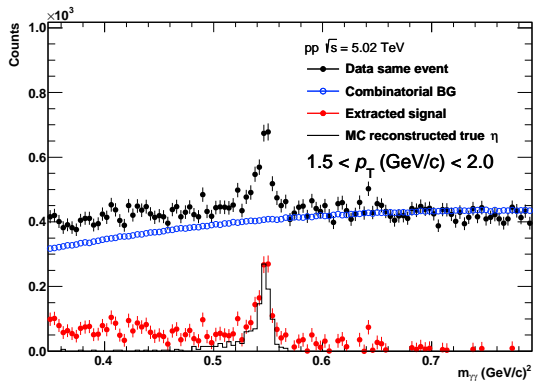


Figure 3. Invariant mass distribution of reconstructed photon pairs of data (black points) and MC (blue line).

Accelerator and Instrumentation

Construction of OEDO beamline

S. Michimasa, S. Shimoura, M. Matsushita, N. Imai, K. Yako, H. Yamaguchi, S. Ota, S. Nakajima, M. Dozono, E. Ideguchi^a, H. Sakurai^b, K. Yoshida^b, Y. Yanagisawa^b, K. Kusaka^b, M. Ohtake^b, T. Sumikama^b, and K. Yamada^b

Center for Nuclear Study, Graduate School of Science, University of Tokyo

^aRCNP, Osaka University

^bRIKEN Nishina Center

The OEDO system is a new beamline proposed for providing high-quality slow-down RI beams [1]. The OEDO is an abbreviation of **O**ptimized **E**nergy **D**egrading **O**ptics for RI beam. The idea of OEDO is to manipulate the timing degree-of-freedom in the phase space of RI beam. To obtain a high-quality beam with a small spot size and a small energy spread, the OEDO system transforms the spreads of positions and angles to the timing spread of the beam, which corresponds to the rotation of the phase space ellipse on the position- (angle)-timing plane to obtain a small position (angle) spread. Radiofrequency (RF) electric ion-optical elements can rotate a phase space ellipse of spatial and timing components, as beams from a cyclotron have an RF bunch structure.

The main components of the OEDO system are: An RF deflector (RFD) [2] synchronized with the cyclotron's RF and 2 sets of triplet quadrupole (TQ) magnets to achieve point-to-parallel/parallel-to-point ion optics. The OEDO system is installed downstream of a momentum-dispersive focus with a reasonable dispersion. The first TQ associates the beam energy with beam angle at the RF deflector, and the second TQ makes a small achromatic focus. This dispersion condition is fulfilled in the first half of the High-Resolution (HR) beamline [3]. Therefore, the OEDO system was implemented in the HR beamline by installing new electric/magnetic elements and rearranging the existing magnets.

The OEDO project was launched in FY2014. A superconducting triplet quadrupole (STQ) magnet was delivered in December, 2016, and the RFD was delivered in March, 2017. The STQ is the same as ones installed at the BigRIPS beamline. The specification of RFD was listed in Table 1. The magnet rearrangement from the HR beamline to the

Table 1. Specification of RF deflector for the OEDO system

Frequency	18.25 ± 0.25 MHz
Maximum input power	40 kW (CW)
Maximum voltage	360 kV
Gap between electrodes	200 mm
Length of electrodes	1200 mm
Width of electrodes	400 mm
Vacuum	5×10^{-6} Pa

OEDO beamline was also finished in March 2017. Figure 1 shows the arrangement of magnets in the OEDO beamline downstream of the FE7 focal plane, which corresponds to

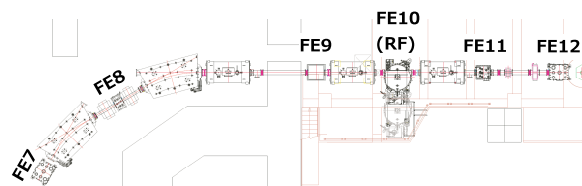


Figure 1. Magnet configuration of the OEDO beamline

the FH7 focal plane of the HR beamline. The OEDO system was installed between the FE9 and FE11 foci. The FE12 focus is the target position of the SHARAQ spectrometer.

Figure 2 shows the present status of the OEDO system.



Figure 2. A photograph of the OEDO system installed between FE9 and FE11.

The 24-hour operation test of RFD was completed in March 2017, and then the designed performance was confirmed. Figure 3 is a snapshot of an RFD control panel and an oscilloscope when the RFD operates. The RF amplitude

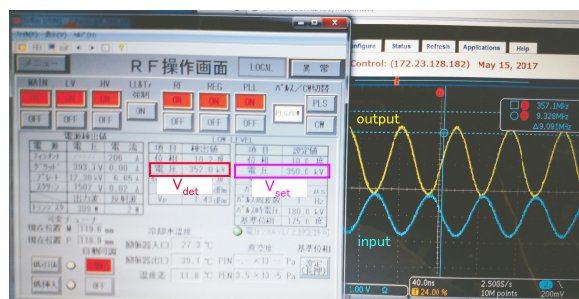


Figure 3. A snap shot of an RFD control panel and an oscilloscope when the RFD operates at 350 kV.

for RFD was set at 350 kV (V_{set}). The waves on the oscilloscope show an input RF signal for the RFD (blue) and a pickup signal of voltage oscillation of RFD electrodes (yellow). The frequency of the input RF was set at 18.25 MHz. The detected pickup signal corresponded to 352 kV (V_{det}).

The commissioning run of the OEDO system is planned in June, 2017. The slow-down RI beams will be demonstrated by using the system.

This work was funded by ImPACT Program of Council for Science, Technology and Innovation (Cabinet Office, Government of Japan).

References

- [1] S. Shimoura *et al.*, CNS Annual Report 2013, CNS-REP-93, 56 (2015) 56.
- [2] K. Yamada *et al.*, Nucl. Phys. A **746**, 156c (2004).
- [3] S. Michimasa *et al.*, Nucl. Instrum. Meth. in Phys. Res. **B317**, 305 (2013).

Development of the high intensity surface ionizer to search for the permanent EDM with Fr atoms

Y.Sakemi, K.S.Tanaka^a, K.Harada^a, H.Kawamura^b, T.Inoue^b

Center for Nuclear Study, Graduate School of Science, The University of Tokyo

^a *Cyclotron and Radioisotope Center, Tohoku University*

^b *Frontier Research Institute for Interdisciplinary Sciences, Tohoku University*

In the Standard Model (SM) of elementary particle physics, fundamental discrete symmetries, Charge (C), Parity (P) and Time-reversal (T) play significant role and advanced our knowledge of how different forces/interactions between particles operate in Nature. Of these, the time-reversal (T) symmetry and the combined charge-parity (CP) symmetry are the least understood so far, which hold valuable clues to unravel Nature's secrets. Every sub-atomic particle is postulated to possess inherently a distinct property known as the permanent electric dipole moment (EDM) due to their spin. EDM of a particle which together with the P- and T-violating interactions with the other elementary particles or nucleus manifest in giving rise to the EDM for an atom [1]. Atoms and molecules being many-particle systems are the ideal candidates to probe a rich variety of both T-violation and CP-violation interactions. The paramagnetic atoms, which have a single valence electron in their outer electronic shell, are sensitive to the subtle signal of CP-violation arising from the leptonic sector, i.e., the EDM of the electron.

The magnitude of the coupling constant one is seeking here, is so small that, the current experimental sensitivity ($< 10^{-29}$ ecm) needs to be improved by almost ten orders of magnitude to test the prediction of the Standard Model (10^{-38} ecm) which appears impossible in the foreseeable future. However, there are many extended models of the SM which predicted the EDM for the electron to be of the same order as the reach of the current and/or the proposed EDM experiments. Thus, the EDMs provide alternative tests for the predictions of various models of particle physics including the most attractive super symmetry models (SUSY). The EDM can be described by the simple SUSY as follows with the eq. (1), and the new CP phase (θ_μ) and the mass (M) of the unknown particles such as SUSY particles can be discussed with the EDM measurement, which means that we can prove the heavy mass region more than TeV that can not be accessed by the high energy collider experiment in near future, and the mass hierarchy of SUSY particles can be studied with the EDM.

$$d_e \sim \frac{\alpha}{4\pi} \frac{m_\tau}{M_i^2} \frac{\mu m_{\tilde{b}}}{M_i^2} \sin\theta_\mu \tan\beta \quad (1)$$

Francium being the heaviest alkali atom is more sensitive to the electron EDM and thus provides a rich laboratory for understanding CP-violation arising from the leptonic sector.

The electronic structure of Fr is like Rb and Cs, its large nuclear charge significantly enhances the atomic EDM to approximately 895 times that of a free electron [2]. Hence, Fr is one of the most promising candidates for the electron EDM experiment. To achieve the EDM measurement accuracy of 10^{-29} ecm, which will be the highest accuracy of the electron EDM in the world, below given experimental parameters are required; the enhancement factor of e-EDM ~ 895 , the applied electric field ~ 10 kV/cm, the interaction time ~ 10 s, measurement time of 3 months, and the number of trapped Fr atoms $\sim 10^6$ or more. Of all the parameters mentioned above, the number of trapped Fr atoms is the most important as the others would be realized with the current development works. In this context, the development and test of a high-intensity surface ionizer to produce sufficient flux of Fr is in progress for the proposed experiment in E7 experimental room at the RIBF in RIKEN.

The EDM will be measured by the technique of an atomic interferometer with Fr, which has the largest enhancement factor of the electron EDM in the atomic systems. In this experimental plan, we will use quantum optics techniques such as laser cooling and trapping and optical lattice to achieve longer interaction time and better use of radioactive atoms as discussed below. The Fr will be produced by nuclear fusion evaporation reaction, and the obtained low energy Fr ions will be transported to the measurement area. These Fr ions will be neutralized by depositing on a suitable neutralizer element, rapidly decelerated and trapped by the laser cooling technique in a magneto-optical trap (MOT). Then the trapped Fr in MOT will be transferred to an optical lattice trap apparatus which also contain the electric field plates [3]. The spin precession of Fr atoms will be measured with the Ramsey resonance method. As the Fr ion source, we selected the surface ionizer using a molten target to achieve a stable yield of Fr ions $\sim 10^6$ Fr⁺/s with high extraction efficiency of Fr ions to realize the measurement sensitivity of EDM $\sim 10^{-29}$ ecm.

Francium is produced with the nuclear fusion reaction by the primary beam ^{18}O supplied from AVF cyclotron and ^{197}Au as target. The beam energy will be adjusted just above the coulomb barrier ~ 100 MeV, which has the maximum cross section for the $^{18}\text{O}+^{197}\text{Au}$ reaction to produce ^{210}Fr isotope. The produced Fr diffuse inside the gold target, and some fraction will reach to the surface of the target. When

the Fr is desorbed from the heated surface of the target, then the electron of the Fr is stripped according to the equation,

$$\frac{n^+}{n^0} = \frac{1}{2} \exp\left(\frac{E_{WF} - E_{IP}}{kT}\right) \quad (2)$$

The extraction efficiency of the Fr ions from the target depends on the target temperature. In the development up to now, we have observed drastic increase of the extraction efficiency to about 30% at and above the melting point of the Au target (1064 °C) due to the change of the diffusion constant in the liquid phase, as shown in the right plot of Fig.1. So we decided to realize the surface ionizer with the molten target. The target size will be optimized from the primary beam size, and the simulation of the ion optics and the profile measurement, which shows the FWHM 5 mm with typical high intensity beam, shows the diameter of the target with 10 mm is enough. The target will be heated by the primary beam power and an additional heater installed at the bottom of the target. The electrode with the parabola shape to confine the extracted Fr ion beam will be surrounded around the target, and the detailed design is being performed by the OPERA/TOSCA simulation code to get the large acceptance and high transmission efficiency along the beam line.

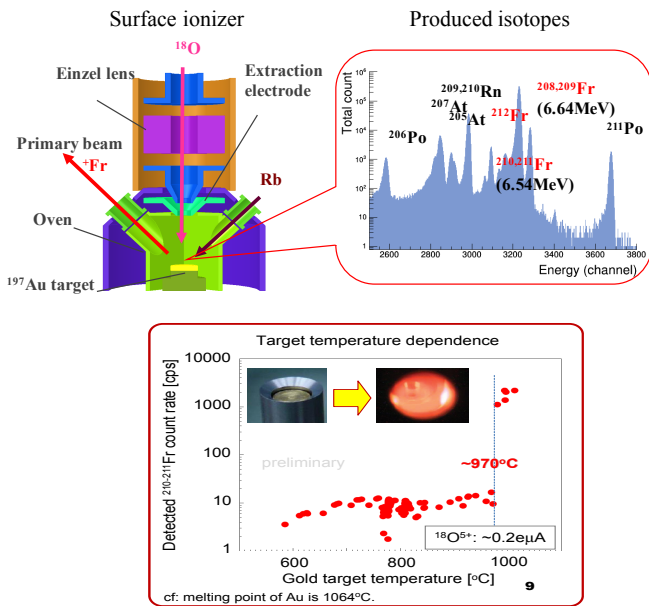


Fig.1. The prototype surface ionizer, obtained α decaying spectrum, and Fr yield.

We can choose several combinations of the primary beam and the target material. But the chemically stable and not active material is preferred for the target, since we apply the surface ionization to get the Fr ion beam, and the work function of the target surface should be stable, without the chemical property change such as the oxidation etc. So the candidates are $^{18}\text{O}+^{197}\text{Au}$ to ^{210}Fr and Fluorine (^{19}F)+

Platinum (^{198}Pt) to ^{212}Fr . The ^{212}Fr isotope is a very good candidate for the EDM experiment, since it has half-life longer than ^{210}Fr , so we can manipulate and work with it much sufficient time. Unfortunately, the primary beam of F has possibility to damage the components of the accelerator due to the causticity, then we decided to use the ^{18}O beam as the first step.

The primary beam will be injected to the target from top without exciting the dipole magnet of DMC7 in the E7 room through C11 beam line from DMC1 to DMC7. The newly developed surface ionizer will be installed at the lower space of the DMC7 with the beam diagnosis system for beam tuning. The produced Fr ions will be extracted at 45 degrees direction by the bending magnet which will be moved from SPring-8 and re-used at E7 experimental room. Then the extracted Fr will be accelerated to about few kV, and transported to the beam profile monitor which is also newly developed based on the micro channel plate (MCP). The Proposed experimental setup at RIKEN is shown in Fig.2.

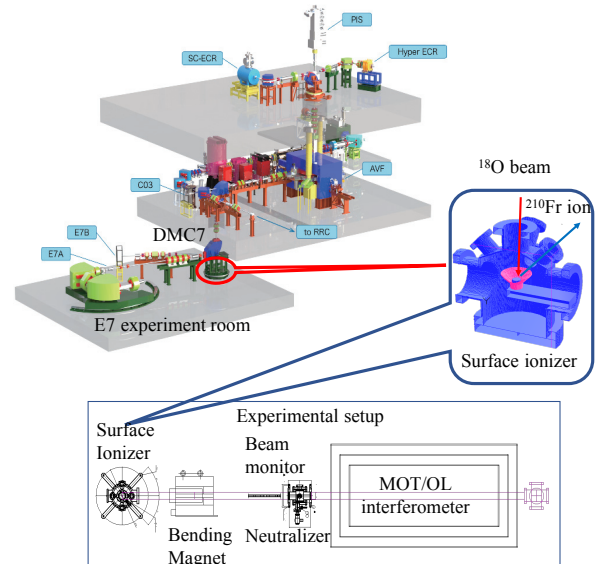


Fig.2. The experimental setup of the surface ionizer and beam monitor in E7.

References:

- [1] Maxim Pospelov, Adam Ritz, *Annals Phys.* 318 (2005) 119-169.
- [2] B.K. Sahoo, T. Aoki, B.P. Das, Y. Sakemi, *Phys.Rev. A93* (2016) 032520.
- [3] U.Dammalapati, K.Harada, Y.Sakemi, *Phys.Rev.A93*(2016)043407.

Feasibility study of a noble gas scintillation counter as a heavy ion detector

Y. Matsuda, J. Okamoto, J. Zenihiro^a, S. Ota^b, O. Beliuskina^b, M. Dozono^b, S. Hayakawa^b, N. Imai^b, C. Iwamoto^b, S. Michimasa^b, Y. Mizoi^{b,c}, R. Nakajima^b, E. Takada^d, K. Yako^b, and R. Yokoyama^b

Cyclotron and radioisotope center, Tohoku University

^a*RIKEN Nishina Center*

^b*Center for Nuclear Study, Graduate School of Science, University of Tokyo*

^c*Osaka Electro-Communication University*

^d*National Institute of Radiological Sciences*

With the recent increase of the beam intensity of the heavy-ion accelerators, it becomes increasingly important to develop detectors for high-intensity beams. The requirements for such detectors are (1) superior radiation hardness, (2) low material, (3) tolerance to high-intensity beams, and (4) good energy and time resolution. Unfortunately, it is difficult for organic scintillators and semiconductor detectors to satisfy the former requirements due to the solid state. Therefore, a gas scintillation counter is considered as one of the candidates. (1) By flowing the gas continuously, we can neglect the radiation hardness. Running cost of the gas flow may be the demerit. However, this will be compensated in the long-time operation due to the fact that the solid state detectors must be replaced for many times and no replacement is needed for a gas counter. This demerit further decreases when we introduce a gas purification and circulatory system. (2) By making a thin gas chamber, we can reduce the material. Decreasing pressure might be improper in some cases since the time of flight in the chamber becomes long and has larger fluctuations. (3) As a gas scintillator, we will test noble gases first. Table 1 shows the basic properties. Because the decay time of the scintillation is fast (nsec), tolerance for the beam intensity is as good as a plastic scintillation counter. (4) Since an averaged energy to produce a scintillation photon is less than half of a plastic scintillator, good energy and time resolution will be expected. However, the wavelength of the scintillation photon from the noble gases is the vacuum ultraviolet region, for which many materials have low transmittance and reflectance. The number of photons whose wave lengths are longer than 200 nm is only ~ 1 per keV. Impurities such as O_2 and N_2 also reduce the scintillation photons by the quenching process and the absorption process. On the other hand, the decay time and wavelength from Xe-doped Ar or Kr are faster and longer than those from pure Ar or Kr by the energy transfer process [1–3]. Therefore, Xe-doped Ar or Kr might be a candidate instead of pure noble gases. In this report, we have checked the scintillation light from Xe gas as well as a mixture with Ar in order to discuss the possibility to use a gas scintillation as a high-intensity heavy ion detector.

Figure 1 shows the schematic view of the test chamber. The body is made of Aluminum, whose purity is more than 99%. A 40-mm-diameter hole is the entrance window of the beam. The surface roughness is several tens μm . The open-

Table 1. Basic properties of liquified noble gases for relativistic electrons [1]

	Wavelength (nm)	Scintillation (photons/keV)	Decay time [nsec]
Ar	128	40	6.3, 1500
Kr	147	25	2, 91
Xe	174	42	2.2, 27, 45

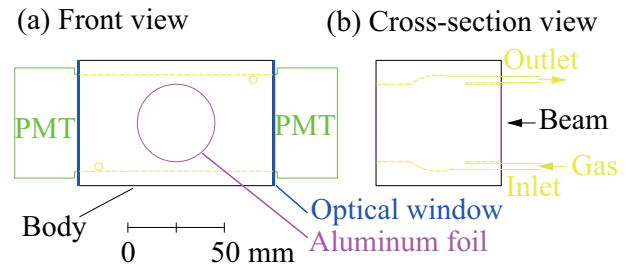


Figure 1. Schematic view of the test chamber: (a) front and (b) side views are shown.

ing areas are sealed with 0.1-mm-thick aluminum foils. By using metallic tubes attached to the body, we continuously flowed Xe gas as well as a mixture with Ar into the body. The chamber was operated under atmospheric pressure.

The scintillation photons are detected with photomultipliers (HAMAMATSU, R6041-506), which are attached on both sides of the chamber. Resistances of the voltage divider circuit are 2 M Ω for the first three stages and the last two stages. The others are 1 M Ω . The supply voltage are negative. As optical windows, quartz glasses (Shin-Etsu Quartz Products, SUPRASIL-P700) are placed between the body and the photomultipliers. By using the glass which cuts off the light whose wavelength is shorter than 150 nm, we can monitor the scintillation photons from Xe, mainly.

The experiment (15H307) was performed at HIMAC in NIRS. The test chamber was irradiated by a 200 MeV/ u ^{132}Xe beam. The beam intensity was 4k particles per pulse (pulse width : 1 sec; repetition rate: 1/3.3 Hz).

Figure 2 shows pictures of signals from two PMTs. The supplied voltages were 830 V and 790 V for the PMTs, respectively. The clear pulse was observed from Xe gas as well as the mixture of Xe and Ar.

Figure 3 shows intrinsic time resolution(rms) as a function of the bias voltage. The resolutions for the left and right

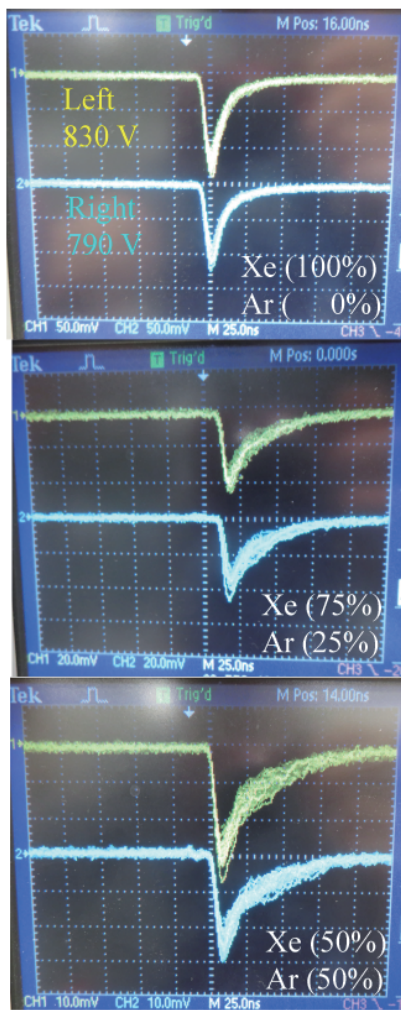


Figure 2. Pictures of signals from the PMTs. Upper: Xe(100%). Middle: Xe(75%) and Ar(25%). Lower: Xe(50%) and Ar(50%).

PMTs are calculated from the time difference between the two PMTs and time of flight extracted by two PMTs and a plastic scintillation counter which was placed behind the test chamber. For Xe gas, about 0.1 nsec was achieved. It is demonstrated that the gas scintillation counter could be used as a timing counter.

In terms of the number of photons, the accumulated photons was about several counts per keV for Xe gas. The photons from the vacuum ultraviolet region seems to be lost due to the impurity. Thus it is considered that the pulse shape in Fig. 2 and the resolution in Fig. 3 gradually change with an increase of the ratio of Xe gas without the energy transfer process.

In summary, we have studied the feasibility of the gas scintillation counter as a heavy-ion detector. In order to observe the scintillation light, we constructed the test chamber. For Xe gas, the intrinsic time resolution was about 0.1 nsec and the accumulated number of photons was several counts per keV. Further studies including the purification, the gas mixture, the evaluation of the quantum efficiency, and opti-

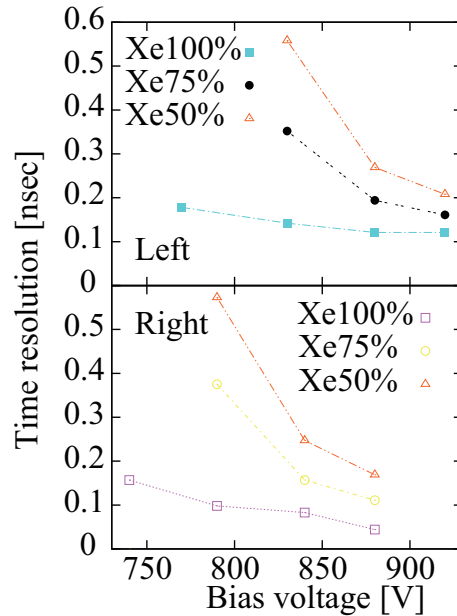


Figure 3. Intrinsic time resolution as a function of the bias voltage. The resolution for the left(right) PMT is shown in the upper(bottom) part. Cubic: Xe(100%). Circle: Xe(75%) and Ar(25%). Triangle: Xe(50%) and Ar(50%).

mization of the design will be conducted in the future.

References

- [1] T. Doke and K. Masuda, Nucl. Instr. and Meth. A **420** (1999) 62.
- [2] O. Cheshnovsky, B. Raz and J. Jortner, J. Chem. Phys. **57** (1972) 4628.
- [3] T. Nanba, N. Nagasawa and M. Ueta, J. Phys. Soc. Jpn **37** (1974) 1031.

Construction of multi wire drift chambers for focal-plane tracking detectors in BigRIPS

K. Yako, S.Y. Matsumoto^a, T. Nishi^b, M. Takaki, H. Fujioka^a, K. Itahashi^b, T. Kawabata^a,
A. Sakaue^a, Y.K. Tanaka^c, T. Uesaka^b, Y.N. Watanabe^d, and J. Zenihiro^a

Center for Nuclear Study, Graduate School of Science, University of Tokyo

^a*Department of Physics, Kyoto University*

^b*RIKEN (The Institute of Physical and Chemical Research)*

^c*GSI Helmholtzzentrum für Schwerionenforschung GmbH*

^d*Department of Physics, University of Tokyo*

We constructed two sets of multi-wire drift chambers (MWDCs) for study of double Gamow-Teller giant resonance (DGTGR) [1] and systematic high-precision spectroscopy of pionic atoms (piAF) [2]. The ($^{12}\text{C}, ^{12}\text{Be}(0^+)$) and ($d, ^3\text{He}$) reactions are used in the above missing-mass studies of DGTGR and piAF, respectively. The same detector configuration will be used: the primary beams hit the targets at F0, the emitted particles are momentum-analyzed in F0-F5 of BigRIPS and are detected at F5 dispersive focal plane. At F5 we decided to install a set of MWDCs, which is generally regarded as a better choice than PPACs for detecting lighter particles.

In these reactions the reaction channels of interest are relatively minor, i.e. DGTGR measurement is performed with MHz triton background and piAF with MHz protons. In order to avoid loss of efficiency due to high rate background as well as inefficiencies due to the cell structure, the wire and plane configuration should be highly redundant. Also we note that in the preceding experiment of piAF in 2014, a wire configuration with a half-cell shift was used and that the spectra showed non-negligible inhomogeneity due mainly to uncertainty in the drift time to drift length conversion in the proximity of the wire. It was demonstrated by a Monte-Carlo study that the inhomogeneity of this kind persists as long as the resolution of the drift time is substantial (~ 5 ns) [3]. Another requirement is that the MWDCs should be located in the vacuum chamber for reasonable angular resolution of missing-mass spectroscopy (1 mr).

The two sets of MWDCs are identical. The dimensions are $445^W \times 353^H \times 134^D$ mm³ and the sensitive area is $240^W \times 144^H$ mm². The chamber windows are $25 \mu\text{m}^t$ aramid foils. A photo is shown in Fig. 1. Each MWDC consists of 9 wire planes with a gap of 10 mm, and each wire plane share the cathode plane of $2 \mu\text{m}^t$ aluminized mylar foil (double-sided). Each wire plane consists of 24 anode wires and 25 field wires alternately stretched out. The half-cell size is 5 mm. The wires in the first plane are set vertically, and thus are sensitive to the horizontal direction (X). The wire positions for the second plane (X') are shifted by a one-third cell (-3.33 mm) with respect to the X plane, and the third plane (X'') shifted by the same length in the opposite direction ($+3.33$ mm) as shown schematically in Fig. 2. This configuration allows one to solve the left-right ambiguities and at the same time one can avoid using the drift time information from wires where the hit is very close to the

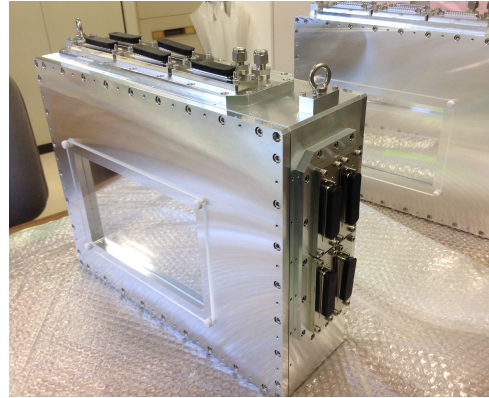


Figure 1. Photo of MWDCs.

sense / field shaping wires. The wires in the fourth, fifth, and sixth planes are inclined by $+30^\circ$ with respect to the vertical axis, and are sensitive to ' U ' direction. Similarly, the seventh, eighth, and ninth planes, inclined by -30° , are sensitive to ' V ' direction. Therefore the wire configuration of the MWDC as a whole is $XX'X''UU'U''VV'V''$. The specifications are summarized in Table 1.

Based on the previous experiment, a high-rate capability (0.1 – 1 MHz in total, equivalent to 4 – 40 kHz per cell) and a position resolution (300 μm (FWHM)) of the detector are expected. The angular resolution of the particle track determined by the set of MWDCs located at a distance of 50 cm is expected to be 0.15 mr and 0.35 mr in horizontal and vertical direction, respectively. The effect of multiple scatterings including the contribution from the chamber windows is estimated to be 0.3 mr.

At the same time, upgrade of the readout system for the new MWDCs is in progress, which is necessary to accomplish high-speed data handling of the multi channel [4]. The beam test will be performed in 2017.

References

- [1] T. Uesaka et al., NP1512-RIBF141 (2015).
- [2] K. Itahashi et al., NP1512-RIBF135 (2015).
- [3] Y.K. Tanaka, doctoral dissertation, Univ. Tokyo (2015).
- [4] S.Y. Matsumoto et al., in Acc. Prog. Rep. 50 (2017).

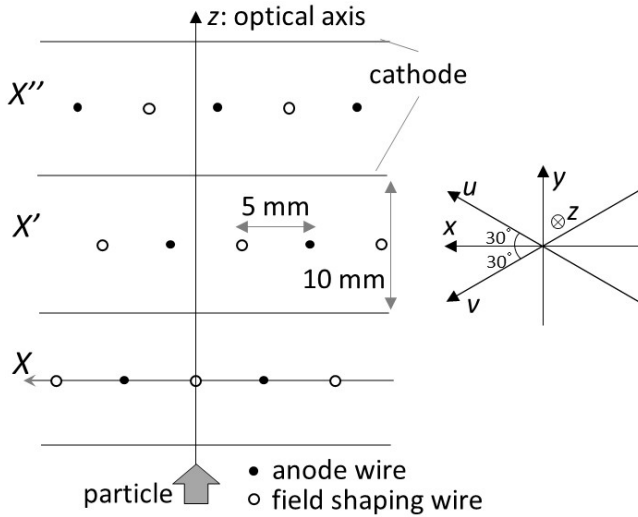


Figure 2. (left) Wire configuration of MWDC for $XX'X''$ planes.
(right) definition of u and v axes.

Table 1. Specifications of the MWDC

Dimensions	$445^W \times 353^H \times 134^D \text{ mm}^3$
Active area	$240^W \times 144^H \text{ mm}^2$
Wire configuration	$[X(0^\circ), U(30^\circ), V(-30^\circ)]$ $XX'X''UU'U''VV'V''$
Cell number	24
Cell width	10 mm
Cell gap	10 mm
Anode sense wires	$20 \mu\text{m}^\phi$ W (gold plated)
Field shaping wires	$70 \mu\text{m}^\phi$ Cu-W
Cathode film	$2 \mu\text{m}^t$ Al-mylar (double-sided)
Window film	$25 \mu\text{m}^t$ Al-aramid

Characterization of a tritium target for (t, p) experiments at TRIUMF

N. Kitamura, K. Wimmer^a, P. C. Bender^b, G. Hackman^c, J. Henderson^c, N. Imai

Center for Nuclear Study, Graduate School of Science, University of Tokyo

^a*Department of Physics, University of Tokyo*

^b*National Superconducting Cyclotron Laboratory, Michigan State University*

^c*TRIUMF*

(t, p) two-nucleon transfer reactions allow for studies of pairing correlations and shape coexistence phenomena in atomic nuclei. While (t, p) transfer reactions have been performed extensively in the past using triton beams, at radioactive beam facilities only few (t, p) experiments have been carried out [1–3]. The reaction has to be performed in inverse kinematics requiring a radioactive target. In the approach realized at ISOLDE, ANL, and TRIUMF, the target is based on a titanium foil loaded with tritium.

Several experiments employing a radioactive tritium target have been approved at TRIUMF [4, 5]. For the analysis and for the planning of future experiments, it would be beneficial to measure the target thickness. Because of the extremely low Q -value of beta-decaying tritium (19 keV), direct detection of the activity is not possible. Therefore, we performed a measurement of elastic scattering at the ISAC-II facility, TRIUMF. This measurement was conducted as a part of the S1481 experiment [4]. A beam of ^{84}Kr was accelerated to 6 MeV/nucleon with an average intensity of 1.5×10^6 particles per second and irradiated the tritium target (titanium thickness 0.5 mg/cm^2) for about 4 hours. For the detection of the recoils, SHARC, the Silicon Highly-segmented Array for Reactions and Coulex [6], was employed. SHARC consists of ΔE - E telescopes to identify and measure light particles. The downstream part of the array covers forward angles ranging from 30 to 80 degrees in the laboratory frame. The number of beam particles was counted by a scintillator placed at the beam dump.

Light particles are identified by the ΔE - E method (see Figure 1). Besides recoiled tritons, other hydrogen isotopes and alpha particles have been observed. Cuts on the ΔE - E plane allowed for the clear extraction of elastically scattered particles as shown in Figure 2. The elastically scattered protons arise most likely from surface contamination of the target. To deduce the number of tritons and protons in the target, the measured differential cross section was scaled to optical model calculations (using parameters from [7]), to yield the luminosity shown in Figure 3. Together with the measured beam current, the number of target nuclei was deduced. The resulting tritium thickness amounts to $4(1) \times 10^{18} \text{ cm}^{-2}$, considering the uncertainty in the optical model parameters. This value is in agreement with the design value of $6 \times 10^{18} \text{ cm}^{-2}$ (corresponding to $10 \text{ GBq } \mu\text{m}^{-1} \text{ cm}^{-2}$). The proton contamination is less than 10% of the tritium content.

To summarize, we characterized a tritium target at TRIUMF by an elastic scattering measurement. Preliminary results show that the tritium thickness is a bit less, albeit consistent with the design value. The target is ready for physics

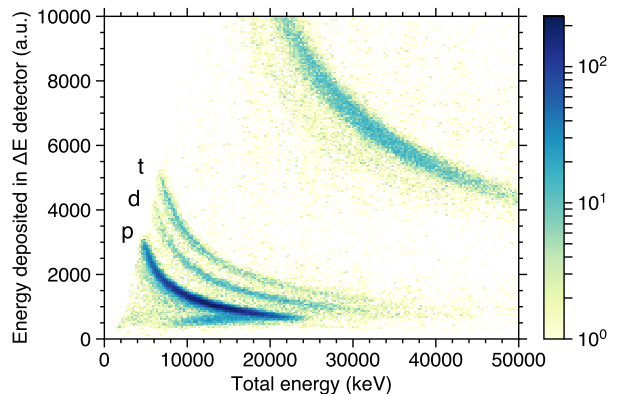


Figure 1. Particle identification of the recoils. Protons, deuterons, and tritons are well separated by the ΔE - E method. The energy loss has been corrected for the impact angle on the silicon detector.

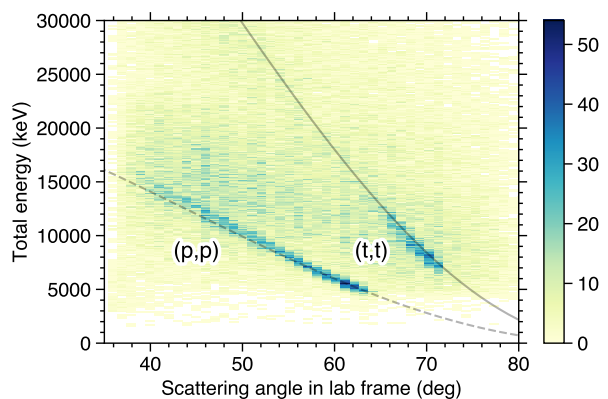


Figure 2. Kinematics curves of (t, t) and (p, p) elastic scattering. Particle identification cuts for tritons and protons are applied beforehand. The continuous background comes from fusion evaporation reactions.

experiments.

References

- [1] M. S. Golokov *et al.*, Phys. Lett. B **672**, 22 (2009).
- [2] K. Wimmer *et al.*, Phys. Rev. Lett. **105**, 252501 (2010).
- [3] K. Nowak *et al.*, Phys. Rev. C **93**, 044335 (2016).
- [4] P. C. Bender *et al.*, “Shape evolution towards $N = 60$: characterization of 0^+ states by two-neutron transfer reactions”, TRIUMF approved proposal S1481 (2015).
- [5] A. O. Macchiavelli *et al.*, “Pairing vibrations beyond $N = 82$ ”, TRIUMF approved proposal S1633 (2016).

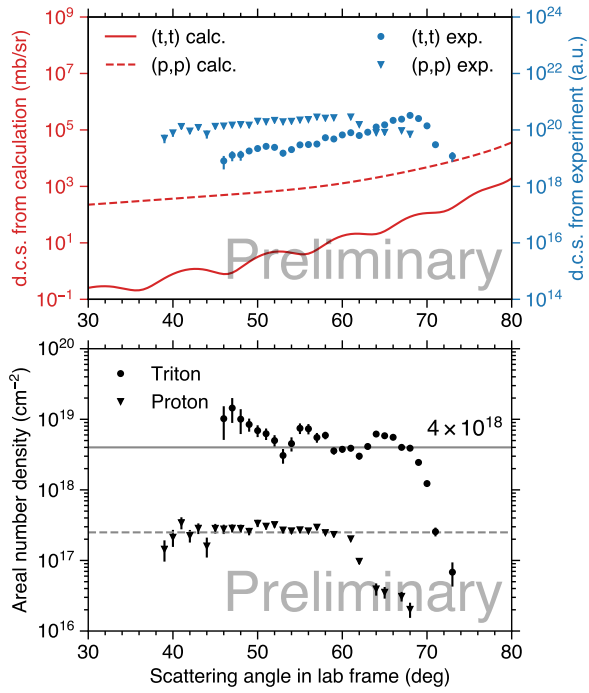


Figure 3. Differential cross sections extracted from the experiment (in arbitrary units) in comparison with optical model calculations (top panel). The luminosities are calculated by scaling the experimental cross sections to optical model calculations. Together with the integrated beam current, the number densities of target nuclei are then deduced (bottom panel).

- [6] C. Aa. Diget *et al.*, *J. Instrum.* **6**, P02005 (2011).
 [7] C. M. Perey and F. G. Perey, *At. Data Nucl. Data Tables* **17**, 1 (1976).

GEM-TPC Development Collaboration

- Development of a new active target CAT-M -

S. Ota^a, C. Iwamoto^a, R. Kojima^a, H. Tokieda^a, M. Dozono^a, T. Gunji^a, S. Hayakawa^a, N. Imai^a,
S. Michimasa^a, Y. Mizoi^{a,b}, D. Suzuki^c, H. Yamaguchi^a

^aCenter for Nuclear Study, Graduate School of Science, University of Tokyo

^bOsaka Electro-communication University

^cRIKEN Nishina Center

We are developing GEM-based time projection chambers (GEM-TPCs) under an inter-group collaboration in CNS, aiming at the measurement of nuclear reactions of short-lived nuclei at RIBF and the measurement of heavy ion collision at ALICE. In general, process of electron multiplication in GEM (and other so-called micro-pattern gas detectors) is quick relative to the multiplication process around wire. Thanks to the quick response, high-rate particle measurement can be realized. If the beam particles are impinged into an active area of GEM-TPC, nuclear reactions can occur in the active area. The TPC used in such an operation is called active target, which enables us to measure low-energy recoils and reaction vertex precisely. Within our collaboration, two active targets based on the GEM-TPC, called GEM-MSTPC and CAT-S are developed and used for the missing mass spectroscopy of short-lived nuclei at RIBF. By using CAT-S, the first forward-angle measurement of deuteron inelastic scattering off ¹³²Sn has been done in 2016, aiming at revealing isospin dependence of nuclear matter equation of state [1].

In this report, we describe development of a new active target called CAT-M in order to expand our playing field of inelastic scattering to measure giant resonances in A~100 unstable nuclei.

Basic conceptual design of CAT-M is similar to that of CAT-S [2]. The CAT-M consists of TPC and Silicon detectors. A preliminary design sketch is shown in Fig. 1. Six 9×9-cm² silicon detectors will be placed at each side of TPC to measure high-energy recoil particles. The TPC consists of field cage to define active volume, GEM to multiply primary electrons created along the trajectories of beam and recoil particles, and readout circuits. Each readout pad in a readout board is of equilateral triangle with 7-mm side in order to discriminate the signal of the recoil particle from that of delta ray. The total number of readout channels will be about 4000. The size of active volume is 310×280×200-mm³. The effective target length becomes five times larger and the typical measurable range becomes three times larger than those of CAT-S. The statistics per unit time per unit beam intensity will be ten times larger than CAT-S according to the estimation taking minimum length of trajectory. Figure 2 shows estimated acceptances and yields for CAT-S and CAT-M, respectively, in left and right panels. Horizontal and vertical axes in each panel are excitation energy and scattering angle in center-of-mass frame, respectively. The statistics is estimated for each active volume assuming

100-kcps ¹³²Sn beam is impinged into 0.4-atm deuterium gas. Assumed angular and excitation energy distributions are, respectively, a lowest-order (*l* = 0) spherical Bessel and Lorentzian distribution with center of 14.5 MeV and width of 4 MeV, where the momentum transfer depending on the excitation energy is taken into account. The energy integrated cross section at zero degrees is assumed to be 100 mb/sr. The overall statistics will be twenty-times larger, which improves statistical accuracy in multipole decomposition analysis as well as that of giant resonance energy.

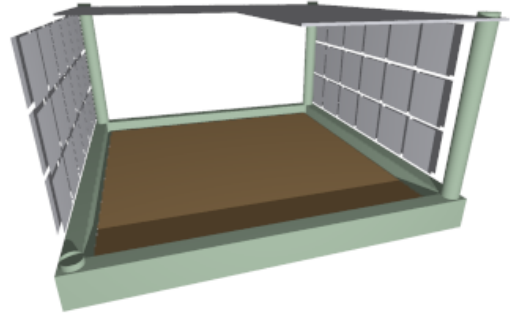


Figure 1. Preliminary design sketch of CAT-M, which consists of TPC and silicon detectors. The size of active volume is 310×280×200-mm³.

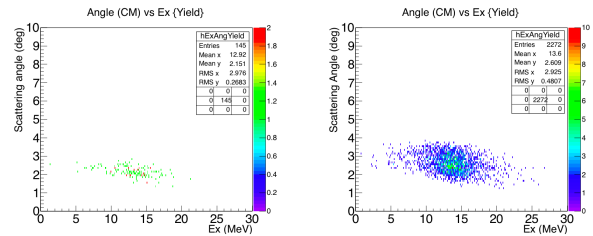


Figure 2. Estimation of yields using the TPCs in CAT-S (left panel) and CAT-M (right panel) for a measurement of deuteron inelastic scattering, assuming 10-days measurement with 100-kcps beam intensity. Horizontal and vertical axes in each panel are, respectively, excitation energy and scattering angle in center-of-mass frame. See text for the detail.

In order to realize the large active area of TPC, we introduce M-THGEM developed by M. Cortesi *et al.* [3] in order to keep spatial uniformity of electron multiplication

factor(gain). The thickness of 0.4 mm, which is the thickness of THGEM in CAT-S, is not thick enough to maintain itself flat, thus the gain varies depending on the gap among the THGEMs and readout board. The M-THGEM consists of alternative layers of electrode and insulators. Our M-THGEM has three layers of insulators resulting in a total thickness of 1.2 mm, which make the deflection small enough. We produced a prototype of dual-gain M-THGEM (DG-M-THGEM) with three regions, similar to DG-THGEM [2], where the gains can be controlled independently. Test experiment using ^{132}Xe heavy ion beam was performed at HIMAC (proposal number 15H307). The detail of the DG-M-THGEM and the test experiment is described in the paper by C. Iwamoto *et al.* in this report.

The design and construction of the whole system of CAT-M is in progress, aiming at the commissioning by the end of fiscal year of 2017 .

References

- [1] S. Ota *et al.*, submitted in the CNS Annual Report 2016 CNS-REP-96 (2017).
- [2] S. Ota *et al.*, J. of Radioanal. Nucl. Chem. 305, 907 (2015).
- [3] M. Cortesi *et al.*, Rev. of Sc. Instrum. 88, 013303 (2017).
- [4] S. Iwamoto *et al.*, submitted in the CNS Annual Report 2016 CNS-REP-96 (2017).

Performance evaluation of a Dual Gain Multi-layer Thick GEM for CAT-M

C. Iwamoto, S. Ota, H. Tokieda, R. Kojima, C.S. Lee, T. Gunji, H. Yamaguchi, S. Michimasa, Y. Mizoi^a, D. Suzuki^b, M. Dozono, O. Beliuskina, R. Nakajima, Y. Matuda^c, R. Yokoyama, S. Hayakawa, N. Imai, J. Zenihiro^b, J. Okamoto^c, K. Yako, and E. Takada^d

Center for Nuclear Study, Graduate School of Science, University of Tokyo

^aOsaka Electro-Communication University

^bRIKEN Nishina Center

^cCyclotron Radioisotope Center, Tohoku University

^dNational Institutes for Quantum and Radiological Science and Technology

A low-pressure gaseous active target called CAT-S based on a time projection chamber (TPC) was developed for the study of unstable nuclei using missing mass spectroscopy. For the injection of the high intensity beams, dual gain thick gas electron multiplier (DGTHGEM) is used as a multiplication part of the TPC [1]. The CAT-S have been operated successfully in a physics experiment of a deuteron inelastic scattering with the high intensity ^{132}Sn beam of several 10^5 Hz [2]. In order to get larger yield, we are developing a larger active target called CAT-M [3]. The active area of the CAT-M will be $280 \times 310 \text{ mm}^2$ while the one of the CAT-S is about $100 \times 100 \text{ mm}^2$.

In the CAT-S, the multiplication part consist of three sheets of THGEMs with the thickness of 0.4 mm. If area of the THGEMs become larger with the same thickness, the THGEMs are bended by their own weight and the electric field in the THGEMs will be distorted. A multi-layer THGEM (M-THGEM) developed by M. Cortesi et al. [4], is a good candidate for the multiplication part of the CAT-M because the distortion of the M-THGEM is expected to be small thanks to the thickness of the M-THGEM. The bending deflection of FR-4 with the thickness of 1.2 mm is calculated to be 10 times thinner than that with the thickness of 0.4 mm by the one-dimensional calculation in the condition of fixing at both end of FR4. In order to inject high intensity beams using the M-THGEM, a gain in a region along the beam of the M-THGEM should be as low as 100 while a gain in side regions should be about 2000 to observe light recoil particles. A prototype of the dual gain M-THGEM (DG M-THGEM) have been produced to evaluate its effective gas gain, the energy resolution, the position and the time dependence of the gain. In this report, the structure of the prototype DG M-THGEM and the preliminary result of the evaluation are reported.

Figure 1 shows a schematic view of the DG M-THGEM. A plate is made by stacking four copper electrodes and three FR-4 insulators alternately and the holes are drilled in the electrode region of the plate. The hole diameter and the pitch are 0.3 mm and 0.7 mm, respectively. The thickness of the electrodes and insulators of the top, middle and bottom are $18 \mu\text{m}$, $400 \mu\text{m}$, $380 \mu\text{m}$ and $400 \mu\text{m}$, respectively. A total thickness of the DG M-THGEM is about 1.2 mm. The electrodes V2, V3 and V4 are divided into three region in order to control the gain at each region independently. The electrode V1 is not divided in order to avoid the ac-

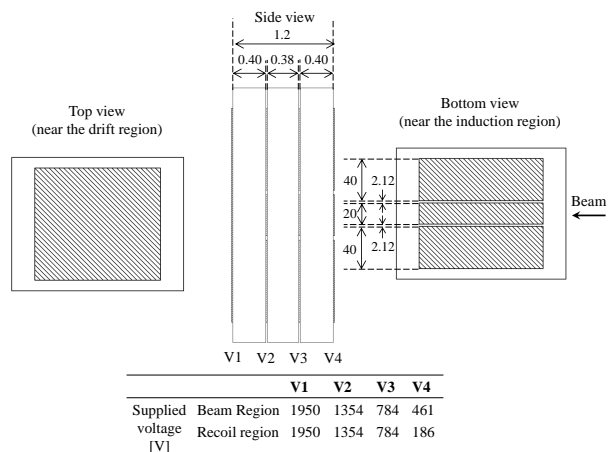


Figure 1. Schematic view of the DG M-THGEM. The hatched regions are the electrodes. The unit of values is mm.

cumulation of electrons on insulator and the distortion of the electric field around the surface of the DG M-THGEM in the drift region. The width of the central region, called beam region, is 20 mm to cover the envelope of the beam. The width of the side region, called recoil region, is 40 mm on both sides. The length of a gap between the electrodes of the beam and the recoil region is 2.12 mm in order to allow to supply voltage about 300V in the H_2 gas of 40 kPa.

Gain curves for the recoil region of the DG M-THGEM was measured using a standard alpha source. The setup was similar with the previous measurement [5]. Collimated alpha particles from ^{241}Am source was introduced to a drift region filled by H_2 gas at the pressure of 40kPa. Electrons made by ionization of the H_2 gas in the drift region were amplified by the DG M-THGEM and were measured by a readout pad. The collected electrons on the readout pad were integrated with a charge-sensitive preamplifier (RPA-211 product of REPIC). The output signal from the preamplifier was pulse-shaped by a shaping amplifier (ORTEC 572A) and the pulse height of the shaped signal was taken by a multi-channel analyzer (Kromek 102 product of Kromek Group plc). The same voltage set was applied to the beam and recoil regions in this measurement. The effective gas gain G_{eff} is defined as ratio of the amplified charges to the initial charge,

$$G_{eff} = \frac{Q}{e \cdot \Delta E / W} \quad (1)$$

where Q is the collected charges on the readout pad, ΔE is the energy deposit of the incident particles in the active region, $W = 37\text{eV}$ is the mean energy for ion-electron pair creation of the H_2 gas and e is the elementary charge. Figure 2 shows the gain curves of the DG M-THGEM measured by the first experiment. A required effective gas gain to measure recoil particles is between 2000 and 3000 at this gas pressure. The required gain was obtained with about 590V supplied between electrodes of the DG M-THGEM. The voltage value was about 100V lower than the case of non-multilayer THGEMs [6].

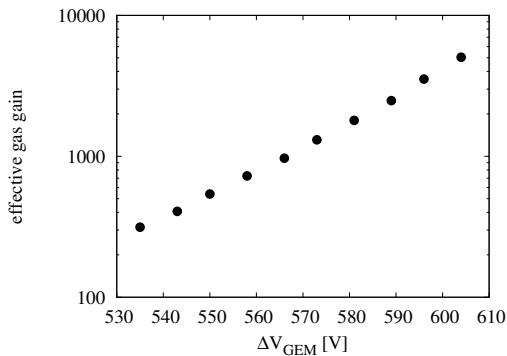


Figure 2. Gain curves of the DG M-THGEM as a function of the potential difference between the electrodes in H_2 gas at the pressure of 40kPa.

The effective gas gains of the beam region controlled with low gain was measured at Heavy Ion Medical Accelerator in Chiba (HIMAC) in the National Institute of Radiological Science. The DG-MTHGEM was mounted in the CAT-S chamber. The primary beam of ^{132}Xe with an energy of 185MeV/u was introduced to the entrance of the CAT-S chamber. Two collimators were installed upstream of the CAT-S to cut the multiple scattering. An alpha source of ^{241}Am was also installed at the position of 225 mm upstream from the edge of active region of the CAT-S and 4mm to the right side from the beam axis as viewed from the upstream. The kinetic energy of the alpha particles became 3.64 MeV at the entrance of the active region of the CAT-S. Figure 3 shows the gain curves of the beam region controlled with low gain when the recoil region was controlled with high gain. In order to evaluate the effective gas gain, specific straight lines are assumed as the path of the beam and alpha particles, respectively. When the particles passed through only the specific straight line and hit 26 readout pads on the line, the events were analyzed and the total charge was calculated as the Q of the equation (1). By following this procedure, the gain between 25 and 600 was achieved in the beam region when the gain of the recoil region was 2000. Two types of setting to supply voltage to the electrodes of the DG M-THGEM were measured. Open circles in Figure 3 are the data where the ratio among the potential differences between V1 and V2, V2 and V3, and V3 and V4 was kept constant. Solid circles are the data

where the only potential difference between the electrode V3 and V4 was changed. The lower gain was achieved by supplying the voltages at the constant ratio. Gains and energy resolutions of each readout pad will be evaluated in further analysis.

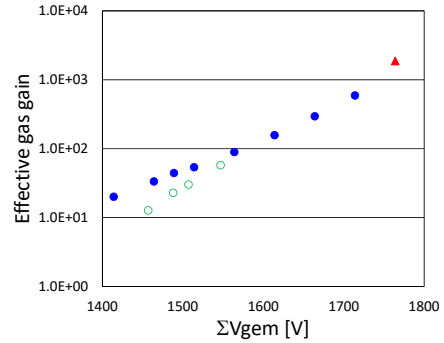


Figure 3. Gain curves of the beam region controlled with low gain as a function of the sum of the all potential differences between the electrodes in H_2 gas at the pressure of 40kPa. Open circles are the data where the ratio among the potential differences between the electrodes was constant. Solid circles are the data where the only potential difference between the electrode V3 and V4 was changed. Solid triangle data is of the recoil region.

References

- [1] S. Ota *et al.*, Journal of Radioanalytical and Nuclear Chemistry, **305**, 907-911(2015).
- [2] S. Ota *et al.*, submitted in the CNS Annual Report **2016** CNS-REP-96 (2017).
- [3] S. Ota *et al.*, submitted in the CNS Annual Report **2016** CNS-REP-96 (2017).
- [4] M. Cortesi *et al.*, Review of Scientific Instruments **88**, 013303 (2017).
- [5] C. S. Lee *et al.*, JINST **9** (2014) C05014.
- [6] C. S. Lee, Master Thesis, the University of Tokyo **2013**.

Event Search in CAT

H. Tokieda, S. Ota, C. Iwamoto, and R. Kojima

Center for Nuclear Study, Graduate School of Science, University of Tokyo

We are developing a GEM-based gaseous active target called CNS active target (CAT). One major goal of the development is to study isoscalar giant monopole resonance via the deuteron inelastic scattering (d, d') and β^+ -type Gamow-Teller strength $B(\text{GT}^+)$ via the ($d, {}^2\text{He}$) reaction. CAT consists of a time projection chamber (TPC) with equilateral triangular readout pads and a silicon detector array surrounding the field cage of TPC [1]. The event search of CAT was reported in [2]. This article describes improvement in the data analysis of ${}^{16}\text{O}$ deuteron inelastic scattering experiment at HIMAC.

In order to identify the scattering events, we first focus the hits in the side region (recoil region) of the readout pad. In the previous algorithm of hit clustering, the criterion parameter for the clustering search in XZ plane (pad plane) was the difference in pad ID. However, because the pad ID becomes useless when the size and position of the pad change, the distance between the pads ΔR_{XZ} is used as the parameter. Thus, the condition of clustering is that ΔR_{XZ} and the difference of the drift distance ΔY_{drift} are within a certain cylinder (Fig. 1). Typical ΔR_{XZ} and ΔY_{drift} values are 15 mm and 20 mm (corresponds to $\sim 2 \mu\text{s}$), respectively. If there are multiple clusters, the cluster with the largest number of hits is chosen. This is because the number of hits is large in the case of long tracks while it is not large in the noise hit cluster. In the data of ${}^{16}\text{O}$ deuteron inelastic scattering experiment, when the ${}^{16}\text{O}$ beam at 100 MeV/u and an intensity of about 300 kcps injected into the CAT with deuterium gas of 0.4 atm, the ratio of multiple cluster events was about 5% of the events with single cluster.

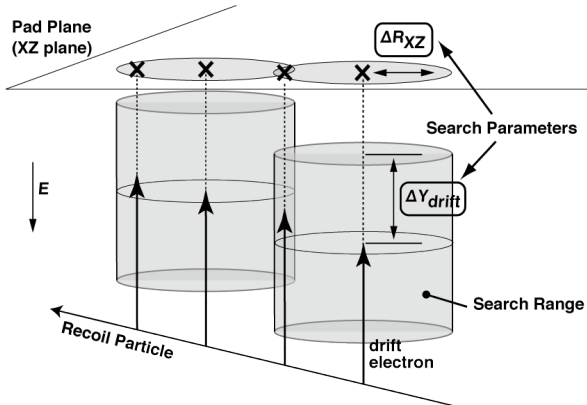


Figure 1. Illustration of hit clustering. The condition of clustering is that ΔR_{XZ} and the difference of the drift distance ΔY_{drift} are within a certain spheroid made.

When a part of the beam particles (beam-like particles) pass through the recoil region, they may also create a hit

cluster like a recoil particle. To remove the beam-like particle events, we perform the analysis using the principal axis of inertia. The analysis using the principal axis of inertia is often used in an image analysis. In our analysis, a cluster is regarded as one rigid body, where the principal axis of inertia is obtained with deposited charges as a weight, and the cluster is distinguished from the beam-like particle by the z (beam axis)-component of the principal axis of inertia (see Fig. 2). Figure. 3 and 4 show the spectrum of z -component of the principal axis of inertia and the examples of the hit pattern, respectively. The left and right panel of Fig. 4 show the hit pattern of events of the z -component of the principal axis of inertia less than 0.1 and that greater than 0.95, respectively. The principal component is normalized to 1. The number of events of the z -component of the principal axis of inertia greater than 0.95 is about nine times as large as that less than 0.95. The former events are similar with the hit pattern seen in the right panel of Fig. 4 and seem to be mostly beam-like particles events, and are removed so far. Further analysis will be performed by checking the correlation between the z -component of the principal axis of inertia and the scattering angle.

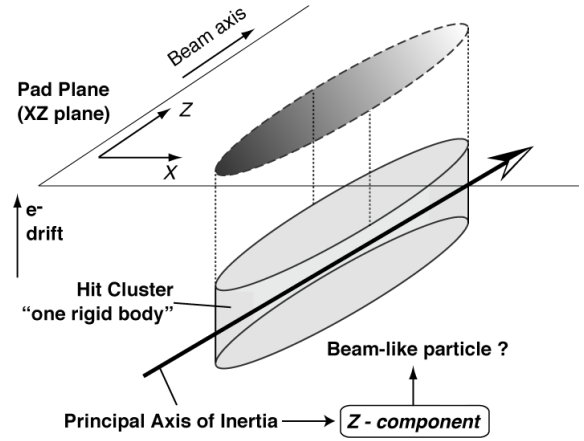


Figure 2. Illustration of principal axis of inertia of hit cluster. In our analysis, the cluster is regarded as one rigid body, the principal axis of inertia is obtained with deposited charges as a weight, and the cluster is distinguished from the beam-like particle by the z (beam axis)-component of the principal axis of inertia.

As for the recoil particles, protons via deuteron breakup reactions are included in addition to deuterons. Currently, analysis for identification of recoil particles are ongoing.

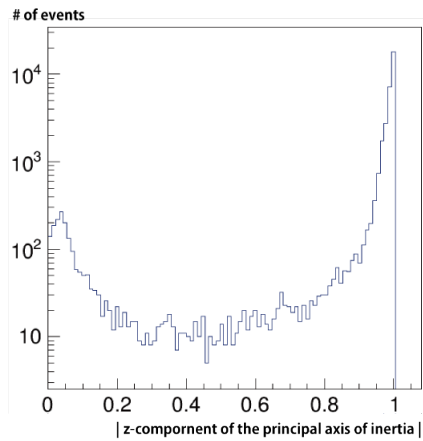


Figure 3. Spectrum of z -component of the principal axis of inertia.

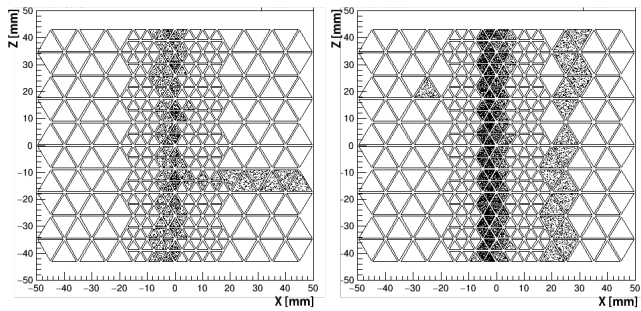


Figure 4. Examples of the hit pattern of events of the z -component of the principal axis of inertia less than 0.1 and that greater than 0.95 are shown in left and right panel, respectively.

References

- [1] S. Ota *et al.*, *Journal of Radioanalytical and Nuclear Chemistry*, **305** (2015) 907-911
- [2] H. Tokieda *et al.*, *CNS Annual Report 2014 CNS-REP* **94** (2016) 53

Energy/timing measurements with single crystal diamond detector at HIMAC

O. Beliuskina^a, N. Imai^a, S. Michimasa^a, R. Yokoyama^a, M. Dozono^a, S. Hayakawa^a, C. Iwamoto^a, Y. Matsuda^b, Y. Mizoi^{a,c}, R. Nakajima^a, J. Okamoto^a, S. Ota^a, E. Takada^d, K. Yako^a, and J. Zenihiro^e

^aCenter for Nuclear Study, Graduate School of Science, University of Tokyo

^bCyclotron Radioisotope Center, Tohoku University

^cOsaka Electro-Communication University

^dNational Institute of Radiological Sciences

^eRIKEN Nishina Center

An attractive advantage of the single crystal CVD diamond detectors (sc) is in the possibility to measure time and energy signals simultaneously with an excellent resolution. Nevertheless for a successful usage of sc the special state-of-art preamplifiers are required. The main goal of the diamond test in this experiment was to find a preamplifier suitable for both, energy and timing, at the same time. For this we measured the energy and timing resolution of the sc for the high intensity beam detection application with a broadband and charge sensitive preamplifiers.

The experiment (15H307) was performed at The Heavy Ion Medical Accelerator in Chiba (HIMAC) at National Institute of Radiological Sciences (NIRS), Japan. Accelerated ¹⁶O and ¹³²Xe primary beams with energies of 220 and 200 MeV/u respectively passed through the CAT (an active target) [1] and different detectors including a polycrystalline CVD diamond detector (pc) before they hit a sc installed at 0 degrees in the respect to the beam direction. Sketch of the experimental setup is presented in the Figure 1. The sc (pad type) with 1 readout manufactured by CIVIDEC [2] has an active area of 4 x 4 mm² and thickness of 140 μm. In our experiment we tested a sc with the charge sensitive (CIVIDEC CSA) and the broadband (CIVIDEC 40 dB and Caen wideband A1423B with 39 and 18 dB gains) preamplifiers (PA) and without any preamplifier. Signals generated by the sc were split into two to provide both the energy and time information.

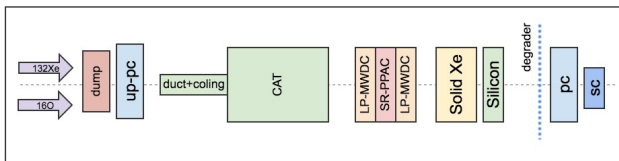


Figure 1. Sketch of the experimental setup

As a start detector for the time-of-flight (ToF) measurements the pc with an active area of 28 x 28 mm² and the thickness of 200 μm was used [3]. This detector has readouts on the both sides. Side A has 1 pad (4 readouts) and side B has 4 strips (8 readouts). In our experiment we used only 1 strip of this detector with 3 readouts: left, right and pad. Such configuration is helpful to minimize the dependence on hit position of heavy ions and can be used directly for position corrections. All three outputs were connected to broadband PAs (Cividec 40 dB). The distance between pc and sc was about 25 mm. Values of the electrical field ap-

plied to the pc and sc were 1 and 2 V/μm respectively. Additionally we had one run with ¹³²Xe without the preamplifier for the sc when we applied the electrical field of 1V/μm.

To have two energies for all cases and be able to perform the energy calibration we used Al degraders: one of 31 mm thickness for the ¹⁶O case and another one of 1 mm thickness for the ¹³²Xe case. The energy losses in the sc estimated by Lise++ were about 12 and 27 MeV for the oxygen case and 786 and 945 MeV for the xenon case.

Table 1. Experimental results

E (MeV)	σ_e (MeV)	$\Delta E/E$ (%)	σ_τ (ps)	σ_{cor} (ps)
Caen 39 dB				
12	0.584	11.4	124	39
27	0.471	4.1	62	21
CIVIDEC CSA				
12	0.634	12.4	101	35
27	0.655	5.7	152	23
CIVIDEC 40 dB				
12	0.447 ¹	8.6 ¹	148	48
27	N/A ²	N/A ²	58	37
Caen 18 dB				
786	18.2	5.4	38	12
945	7.6	1.9	36	14
No PA				
786	19.1	5.7	31	12
786	25.7 ³	7.6 ³	37	14

¹ rough evaluation, ² out of the PA range, ³ at 1V/μm

To obtain a better energy resolution we used the pulse area instead of the pulse height. For this we used a CTC (the charge-to-time converter with a leading edge discriminator manufactured by Fuji Diamond [4]) and a TDC (the time-to-digital-converter).

To get the best timing resolution we used a high speed discriminators, TACs (the time-to-amplitude converter) and an ADC (the analog-to-digital converter). The timing resolution of the measurement system was estimated to be ~12 ps (in the standard deviation sigma, σ). The “beginning” of the TAC-signals was formed by the “pad”-output of the

pc TAC_0 . The “end” of the TAC signals were formed by the left and right signals from the pc and signal from the sc, TAC_{pc}^L , TAC_{pc}^R and TAC_{sc} respectively:

$$TAC_{ToF} = TAC_0 - TAC_{sc}, \quad (1)$$

$$TAC_L = TAC_0 - TAC_{pc}^L, \quad (2)$$

$$TAC_R = TAC_0 - TAC_{pc}^R. \quad (3)$$

Thus we had the time-of-flight between the pc and the sc and the left and right “signal traveling time” from a pc and were able to make corrections of the position dependence in the pc for the ToF:

$$ToF_{cor} = TAC_{ToF} - \frac{TAC_L + TAC_R}{2} \quad (4)$$

Experimental results are presented in Table 1. Here, E is the energy deposited in the sc, in MeV. σ_e is the standard deviation obtained by the gaussian fitting of the energy spectra, in MeV. $\Delta E/E$ is the ratio of the FWHM to the deposited energy, in %. σ_τ is the standard deviation obtained by gaussian fitting of the time-of-flight spectra. Finally, σ_{cor} is the standard deviation obtained by gaussian fitting of the time-of-flight spectra after the position dependence correction. Footnotes ¹ and ² indicate the resulting σ_e for the energy spectra obtained with Cividec 40 dB preamplifier presented only as a rough estimation of the energy resolution because in the case of higher energy deposition the maximum of the signal pulse was out of the range of the preamplifier. Nevertheless for the timing measurements it is not a problem. Footnote ³ means the result for the energy resolution of the diamond detector without the preamplifier at working electric field of $1V/\mu m$ is the rough estimation because we had only a single measurement with this setting.

The best energy resolution of about 2% was obtained with a sc in a combination with the broadband Caen preamplifier (18 dB gain) for the highest energy deposit of ~ 945 MeV. Based on this value and taking into account the beam straggling along setup parts we estimated the detector thickness tolerance as about 1%. The beam energy straggling along all setup parts estimated by Lise++ together with the thickness uncertainty can explain only a part of the energy uncertainty. The sc energy resolution including readout electronics is up to 5% depends on the case.

The best timing resolution of 12 ps was obtained for the combination of the sc with a broadband Caen preamplifier (18 dB gain) and the pc taking into account the position dependence correction in it. Same result was obtained for the combination of the sc without any preamplifier and the the pc taking into account the position dependence correction in it.

With the position dependence correction we were able to improve the time-of-flight resolution significantly. For the large energy deposit we achieved $\sigma_\tau = 12$ ps which is the limit for our electronics in this experiment as it mentioned above.

The timing resolution depends on many different factors, like an energy deposit, an amplitude-to-threshold ratio, etc. Our data reveal that if the energy deposit closer to the PA upper limit or beyond this value, the timing resolution is better. Taking into account experimental data from [3] one can conclude if the energy deposit is close to 150 MeV or more the timing resolution is about 10-12 ps. Our data are not full enough to make the final conclusion on the dependency trend for the energy resolution versus the deposited energy.

Our measurements with a large energy deposit of about 1 GeV showed an encouraging results for the diamond detector without the preamplifier. The energy and timing resolutions are almost the same as with broadband PAs.

References

- [1] S. Ota, H. Tokieda, C. S. Lee, Y. N. Watanabe, J. Radioanal. Nucl. Chem. **305** (2015) 907.
- [2] CIVIDEC Instrumentation, <https://cividec.at>.
- [3] S. Michimasa *et al.*, Nucl. Instr. Meth. **B42** (2013) 710.
- [4] Fuji Diamond International Co., LTD, <https://fujidiamond.jp>.

Beam transport analysis of RIKEN AVF Cyclotron injection line by four-dimensional emittance in view of the space charge effect

Y. Kotaka, Y. Ohshiro, H. Yamaguchi, N. Imai, Y. Sakemi, T. Nagatomo^a
J. Ohnishi^a, A. Goto^a, M. Kase^a, K. Hatanaka^b, H. Muto^c and S. Shimoura

Center for Nuclear Study, Graduate School of Sciences, University of Tokyo

^aRiken Nishina Center

^bResearch Center for Nuclear Physics, Osaka University

^cCenter of General Education, Tokyo University of Science, Suwa

1. Introduction

For the purpose of increasing the beam intensity of AVF cyclotron, we focused on the improvement of the injection beam intensity because the beam transmission efficiency of the injection beam line is lower as the beam intensity is higher. Therefore we decided to optimize the injection beam transport system. As a means of the optimization, we planned to calculate the injection beam orbit by using a measured 4-dimensional emittance as an initial value and to design a beam injection orbit which fits the acceptance of AVF Cyclotron.

2. Calculation method and magnetic fields

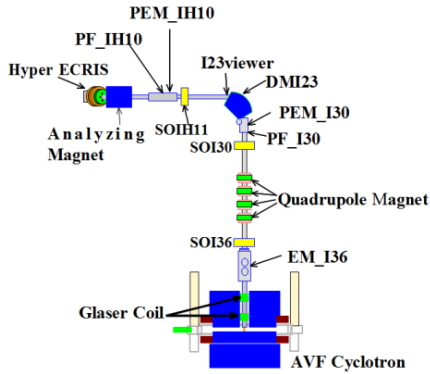


Figure 1. the beam injection line of AVF cyclotron

Figure 1 shows the beam injection line of AVF cyclotron. We measured the 4-dimensional emittance by the pepper-pot emittance monitor [1] (PEM_IH10 [2]) and solved the motion equation of the injection beam orbit by Runge-Kutta method using the 4-dimensional emittance as the initial value.

There are three solenoid-coils, a dipole-magnet, four quadrupole-magnets and two Glaser-coils set behind PEM_IH10. We had adopted 2 types of the calculation models for electromagnets [3]. We adopted the calculated magnetic field for the calculation in the solenoid-coils

and quadrupole-magnets because the effective lengths of these magnets are shorter for hard-edge model of magnets field.

For the same reason, we adopted the calculated magnetic field for the dipole-magnet (DMI_23) currently. This means we use the calculated magnet field for all magnets.

3. Introducing the space charge effect

The calculation method in section 2 was tested by ${}^4\text{He}^{2+}$ 25.4 keV ion beam of $5\epsilon\mu\text{A}$. The calculated beam orbit was mostly consistent with the measured results at the beam viewer (I23viewer), profile monitor (PF_I30) and the 2-dimensional emittance monitor (EM_I36). To see the performance of the method for the high intensity beam, we tested ${}^4\text{He}^{2+}$ 15.4 keV ion beam of $240\epsilon\mu\text{A}$. The calculated beam orbit was not consistent. The reason was most likely that the space charge effect was neglected [3]. Therefore, we decide to introduce the space charge effect into the calculation.

There are some calculation models for the space charge effect. The model we adopted first was a uniform circle model that the beam cross-section was circle and the transverse and longitudinal beam densities were uniform. After that, we adopted a uniform ellipse model instead of a uniform circle model because the beam cross-section would rather be an ellipse than a circle.

When the cross-section is a uniform ellipse, the motion equation of the space charge effect is below [4].

$$\frac{d^2x}{ds^2} = \frac{4\lambda r_p}{\beta^2\gamma^3 a(a+b)}x, \quad \frac{d^2y}{ds^2} = \frac{4\lambda r_p}{\beta^2\gamma^3 b(a+b)}y \quad \left(r_p = \frac{q^2}{4\pi\epsilon_0 mc^2} \right) \quad (1)$$

In Eq. (1) s is beam axis, (x, y) is transverse phase-space coordinate, λ is the number of particles per unit length, β and γ are Lorentz factors, a and b are ellipse radii of the beam and r_p is the classical radius of the particle.

The left image of Fig. 2 is a sample of a beam distribution in an x - y plane measured by PEM_IH10. Although its shape is not an ellipse, we decided to approximate it to an ellipse. The right image of Fig. 2 is a statistically calculated ellipse from the left image of Fig. 2 and we presumed it to be a beam cross-section.

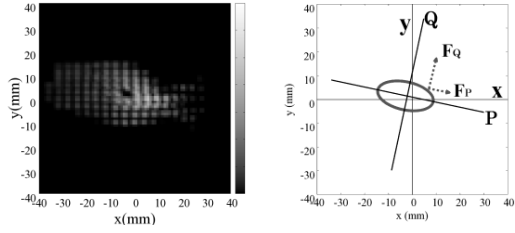


Figure 2. The left image is a measured beam distribution on an x - y plane. The right image is the ellipse calculated from the left image statistically. P-Q system is rotated from x - y system not to incline the ellipse. F_P and F_Q are the right-hand side of motion equation in Eq. (1).

By the way, the ellipse is inclined. In order to use Eq. (1), the ellipse must not incline. Therefore, we prepare P-Q system, in which the ellipse is not inclined, by rotating the x - y system. F_P and F_Q indicate the right-hand side of motion equation (corresponding to force) of the P and Q direction, respectively. So, one can obtain the motion equation in x - y system by rotating F_P and F_Q back into x - y system.

4. Analysis for beam injection line

We tested two types of injection beam orbits. This means the magnetic field intensities of some focusing elements are changed but the 4-dimensional emittance as an initial value measured by PEM_IH10 is same for both types. The ion beam is ${}^4\text{He}^{2+}$ 15.4 keV ion beam of 240 μA which is the same one related in section 3. We solved the motion equation by using the calculated magnetic field for all magnets and the uniform inclined ellipse model of the space charge effect.

In order to evaluate the calculation of two types of injection beam orbits, we compared them with the 2-dimensional emittances, which are u - u' emittance (u - u') and w - w' emittance (w - w'), measured by EM_I36. The u - w system of EM_I36 is rotated by 45 degree against the x - y system. The comparison about u - u' and w - w' of the first type of injection beam orbit are shown in Fig. 3 and Fig. 4, respectively. In the same way, the comparison about u - u' and w - w' of the second type are shown in Fig. 5 and Fig. 6, respectively.

As a result, in case of first type, the shapes of the calculated 2-dimensional emittances are close to the 2-dimensional emittances measured by EM_I36. On the contrary, in case of second type, the directions of structures are similar but the shapes of u - u' are particularly different. The calculation including the space charge effect is thought to be more effective than the calculation excluding the space charge effect, but the difference between the calculation and the measurement still remains. We do not understand this reason now but we know that the uniform ellipse model of the space charge effect is not enough to approximate the beam cross-section. It is necessary to consider another model of the space charge.

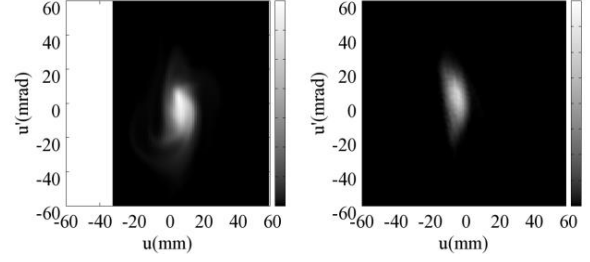


Figure 3. The left is the image of u - u' measured by EM_I36 and the right is the image of u - u' calculated by the measured 4-dimensional emittance of the first type.

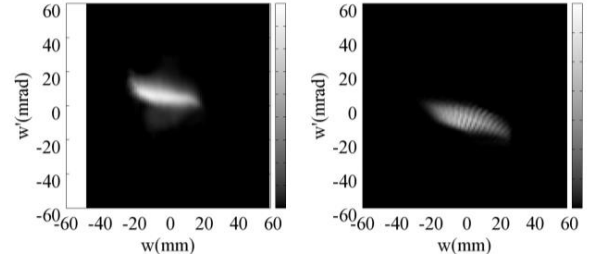


Figure 4. The left is the image of w - w' measured by EM_I36 and the right is the image of w - w' calculated by the measured 4-dimensional emittance of the first type.

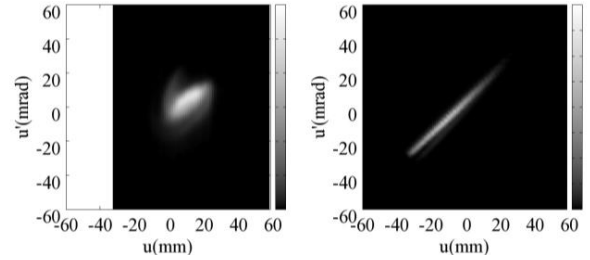


Figure 5. The left is the image of u - u' measured by EM_I36. The right is the image u - u' calculated by the measured 4-dimensional emittance of the second type.

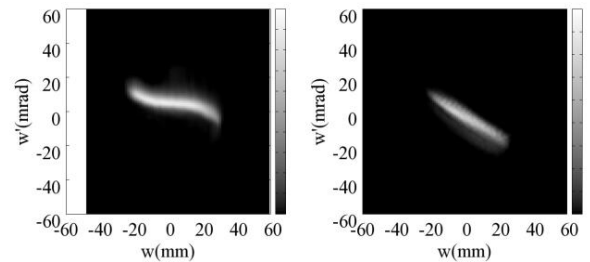


Figure 6. The left is the image of w - w' measured by EM_I36. The right is the image of w - w' calculated by the measured 4-dimensional emittance of the second type.

References

- [1] T.Hoffmann et al., Proc. 9th BIW 2000, Cambridge, USA, PP.432-439.
- [2] Y.Kotaka et al., CNS Ann. Rep. 2014 (2016) 61.
- [3] Y.Kotaka et al., CNS Ann. Rep. 2015 (2017) 57.
- [4] S. Y. Lee: *Accelerator Physics 1st ed.* (Singapore, World Scientific, 1999)

Beam extraction from concave plasma boundary in Hyper ECR ion source

Y. Ohshiro, Y. Kotaka, H. Muto^a, H. Yamaguchi, N. Imai, Y. Sakemi and S. Shimoura

Center for Nuclear Study, Graduate School of Sciences, University of Tokyo

^aCenter of General Education, Tokyo University of Science, Suwa

1. Introduction

The Hyper ECR ion source injected a variety of gaseous and metallic ion beams into the RIKEN AVF Cyclotron [1,2,3]. This year, the beams such as H^+ , $^2H^+$, $^4He^{2+}$ were extracted from the cyclotron with an intensity of 22, 24, 30 μA , respectively. Also other light ion beams with high intensities were supplied for RI production.

When a $^4He^{2+}$ beam was extracted from the cyclotron with an intensity of 30 μA , a high intensity beam of 430 μA was injected from the ion source. Therefore, the beam transmission efficiency was 7%. So, we examined the quality of the beam extracted from the ion source to increase the transmission efficiency.

So far, we fixed the plasma boundary of the ion source with a mesh and found that the beam emittance of the concave boundary in the beam direction was improved [4]. This year, we developed a strongly focused beam extraction system of the ion source. The new system always forms a concave plasma boundary without the mesh. This system is currently used for light ion beam.

2. Beam extraction system

A schematic diagram of the tested extraction system is shown in Fig. 1. The aperture of a plasma electrode and an extraction one are 14 mm and 6 mm, respectively, and the gap is 20 mm. The beam leaving the plasma electrode is converged to the extraction electrode by the action of the concave spherical equipotential surface and the magnetic field of the mirror coil.

Beam trajectories are also shown in Fig 1. A $^4He^{2+}$ beam with an intensity of 300 μA was extracted with a voltage of 7.69 kV. Beam emittance was measured at 113.5 mm from the plasma electrode and the trajectory was traced towards that electrode at the X and X' values of the emittance [5]. Since the beam is focused in the passing region of the extraction electrode, the plasma boundary is concave and the beam at E1 is uniformly distributed in space.

3. Optimization of electrode shape

The shape of the plasma and extraction electrode was optimized to extract the beam of high intensity and low emittance from the ion source.

1) For the purpose of matching to the beam transport downstream, the electrode and the system geometry was designed so that the focal point of the beam from the plasma electrode comes to the object point of the

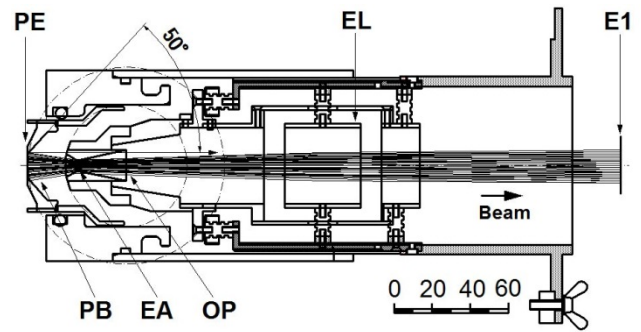


Fig. 1: Schematic diagram of the extraction system of the Hyper ECR ion source that contains the beam ray trace. An angle from the beam direction to the plasma electrode is 50 degree. PE: Plasma electrode PB: Plasma boundary EA: Extraction electrode aperture OP: Object point of the analyzing magnet EL: Einzel lens E1: Beam slit

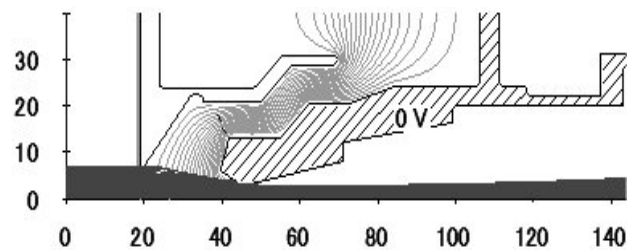


Fig. 2: Schematic diagram of simulated beam trajectory using IGUN code. The beam is the $^4He^{2+}$ ion extracted at 7.69 kV. The focal point of the beam is about 50 mm from the plasma electrode.

analyzing magnet. As shown in Fig. 1, the object point was located 52 mm from the tip of the plasma electrode. Therefore, the tip of the plasma and the extraction electrode form a spherical surface concentric with the object point of the magnet.

2) Figure 2 shows the simulated beam trajectory using the IGUN code. The beam is the $^4He^{2+}$ ion extracted at 7.69 kV. The aperture of the extraction electrode was placed 5 mm from the tip of the extraction electrode. As a result, the focal point of the beam approached the object point of the magnet, and the beam emittance was improved.

3) The emittance diagram and the cross section of the $^4He^{2+}$ ion beam extracted at 7.69 kV are shown in Fig. 3. When the angles from the beam direction to the

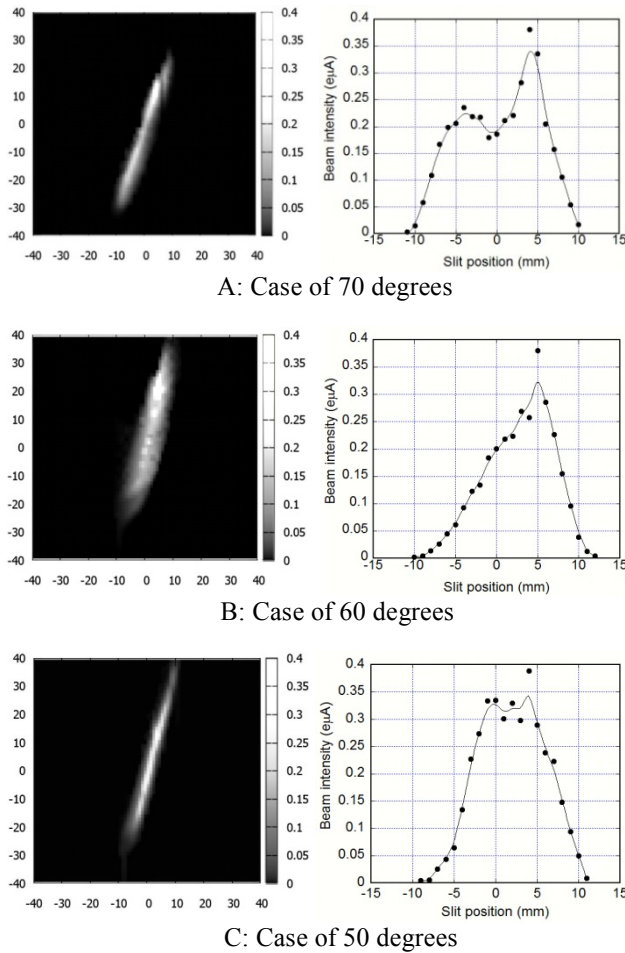


Fig. 3: Examples of the emittance diagram and the cross section of the ${}^4\text{He}^{2+}$ beam. The beam intensity and the extraction voltage are 300 μA and 7.69 kV. The 95% beam emittance of A, B, C are 111, 92, 84 $\pi\text{mm}^*\text{mrad}$, respectively.

plasma electrode were 70, 60 and 50 degrees, the measured beam emittances were 111, 92 and 84 $\pi\text{mm}^*\text{mrad}$, respectively. The angle of the electrode when the beam was most focused with the smallest emittance was 50 degrees. Therefore, we routinely use a plasma electrode with an angle of 50 degrees.

4. Status of light ion beam supply

The new beam extraction system of the ion source was used to supply the high intensity light ion beam for RI beam production. The behavior of the beam transported from the ion source to the cyclotron has the following tendency.

1) The diagram of the beam emittance measured after each beam time was similar, and the ions uniformly distributed in the phase space. The intensity distribution in the cross section of the beam trajectory was almost flat. Thus, the relatively uniform beam was extracted from the ion source.

2) Typically, the beam transmission efficiency from the upstream to the central region of the cyclotron has

increased from the conventional 25% to more than 35%. For example, when a ${}^4\text{He}^{2+}$ beam extracted at 7.69 kV was injected into the cyclotron with a 160 μA , the beam intensity of 57 μA arrived in the central region. The efficiency was improved especially in experiments with high intensity beam injection.

3) Large fluctuations of the beam intensity rarely occurred while the high intensity beam was supplied for RI production. The beam diverged by 6 mm or more by the change of the plasma boundary of the ion source is blocked by the aperture of the extraction electrode. Therefore, the intensity of the beam delivered from the ion source onto the target has become quite stable.

We were able to control the beam extracted from the ion source. Matching with beam transport elements downstream is underway to improve the overall beam transmission efficiency.

5. Summary

We introduced a strongly focused extraction system to Hyper ECR ion source and supplied high intensity light ion beams. The beam size extracted from the ion source was controlled. We plan to improve the transmission efficiency to the cyclotron by matching the system with the beam transport elements downstream.

References

- [1] Y. Ohshiro, S. Yamaka, S. Watanabe, K. Kobayashi, Y. Kotaka *et al.*, Rev. Sci. Instrum. **85** (2014) 02A912.
- [2] Y. Ohshiro, S. Yamaka *et al.*, RIKEN Accel. Prog. Rep. **39** (2005) 231.
- [3] Y. Ohshiro, S. Watanabe *et al.*, CNS Annual Report 2004 (2003) 71.
- [4] Y. Ohshiro, Y. Kotaka *et al.*, CNS Annual Report 2015 (2014) 59.
- [5] Y. Ohshiro, Y. Kotaka *et al.*, CNS Annual Report 2016 (2015) 59.

Development of an active stopper for isomer tagging

M. Dozono, K. Yako, S. Ota, H. Tokieda, C. Iwamoto, L. Stuhl, K. Kawata, S. Michimasa, M. Takaki, R. Yokoyama, N. Kitamura, S. Masuoka, T. Uesaka^a, J. Zenihiro^a, and E. Takada^b

Center for Nuclear Study, Graduate School of Science, University of Tokyo

^a*RIKEN Nishina Center*

^b*National Institute of Radiological Sciences*

Nuclear isomers continue to make key contributions to the progress of nuclear structure physics [1, 2]. The understanding of their occurrence and degree of stability provides new insights into nuclear structure. Various aspects of nuclear structure such as shape coexistence and K -mixing have been investigated from isomer studies.

Isomers can be also used as probe particles. Because isomeric states can be easily identified by detecting delayed γ -rays (or particles) from the states, reactions including isomers can be powerful probes with good signal-to-noise ratio. Interesting examples are (^{12}C , $^{12}\text{Be}(0_2^+)$) [3] and (^{16}O , $^{16}\text{N}(0^-)$) reactions [4]. The new probes allow us to investigate little-studied excitation modes in nuclei such as double Gamow-Teller resonances and 0^- excitation modes.

Following these situations, we are developing a new γ -ray detector system as an active stopper for isomer tagging. The active stopper consists of an ion stopper and a delayed γ -ray detector, where both are integrated in one detector volume (These two parts are separated in a conventional system). This detector system has following advantages: First, a solid angle of 4π sr can be covered, and second, there is no materials that attenuate γ -rays (In a conventional case, there is always an attenuation in the stopper). Thus, the active stopper can be an extremely efficient tool for isomer tagging.

With this idea, we plan experiments with the (^{16}O , $^{16}\text{N}(0^-)$) reaction at a beam energy of ~ 250 MeV/u. Here the $^{16}\text{N}(0^-)$ state is an isomer with an excitation energy of $E_x = 120$ keV and a lifetime of $T_{1/2} = 5.25$ μs . In these experiments, the outgoing $^{16}\text{N}(0^-)$ particles are analyzed by the SHARAQ spectrometer [5], and implanted in the active stopper located at the focal plane of the spectrometer. The active stopper detects delayed γ -rays of 120 keV followed by the isomeric decays of the $^{16}\text{N}(0^-)$ states. It should be noted that a $^{16}\text{N}(0^-)$ particle deposits huge amounts of energy in the active stopper (about four orders of magnitude larger than the delayed γ -ray energy), which produces the dead time for the delayed γ -ray detection. The dead time should be less than ~ 0.5 μs to achieve the detection efficiency higher than 90%.

In order to reduce the dead time, we introduce a CeBr_3 scintillator, which has a short decay constant of $\tau = 19$ ns. Other properties such as a light yield (60,000 photons/MeV) and an attenuation coefficient ($\mu = 4.40$ cm^{-1} for 120-keV γ -ray) are also adequate for the 120-keV γ -ray detection. Based on these excellent properties of the scintillator, we design the active stopper system as shown in Fig. 1. Key features of this system are as follows.

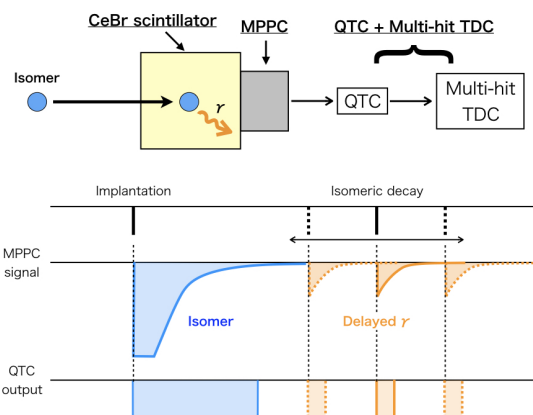


Figure 1. Active stopper system. A timing chart for the operation of this system is also shown. Note that charge information can be obtained from the output width of QTC.

- (1) A photon sensor of this system is exposed to a number of scintillation photons by the isomer ions in the ion stopper. Therefore, the stable operation under the large light yields is required. In order to satisfy this requirement, the Multi Pixel Photon Counter (MPPC) is employed, because, unlike the photomultiplier tube (PMT), it will not suffer from “burn-in” by incident light saturation.
- (2) Timing and charge data are obtained by utilizing a charge-to-time conversion (QTC) technique [6] and a multi-hit time-to-digital converter (TDC) module, such as V1190 by CAEN, that has a long time window (> 50 μs). The combination of these two modules enables the clear identification of a delayed γ -ray event over a long time range of ~ 50 μs following the ion implantation.

In order to check the feasibility of the active stopper, two performance tests were carried out at HIMAC accelerator facility in Chiba. First, we performed an isomer tagging test by using a QTC + multi-hit TDC readout system. Figure 2 shows the experimental setup. A secondary $^{16}\text{N}(0^-)$ beam at 110 MeV/u was produced by the SB2 beam line, and implanted in a plastic scintillator stopper. A typical intensity was 10^3 ppp, and a maximum intensity was 10^5 ppp. A CeBr_3 scintillator coupled with a PMT was used to measure the delayed γ -ray from the $^{16}\text{N}(0^-)$ state. Its charge and timing information was obtained by using a QTC discriminator (GeV γ -1370, Fuji Diamond International Co., Ltd.) and a multi-hit TDC module (V1190, CAEN)

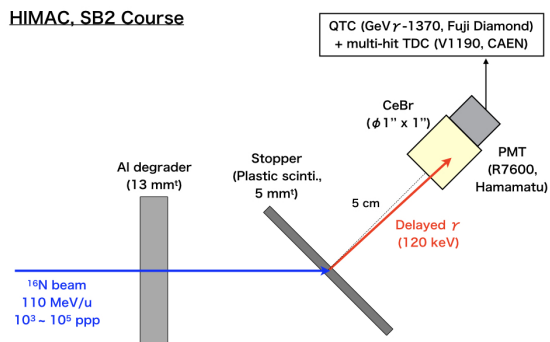


Figure 2. Schematic diagram of the experimental setup for the isomer tagging test with the QTC + multi-hit TDC readout system.

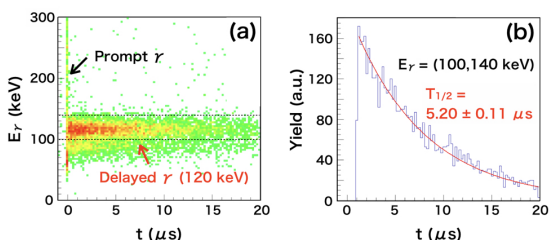


Figure 3. (a) Correlation between the energy and the timing obtained by the QTC + multi-hit TDC system. (b) Timing spectrum for 120-keV γ -ray events.

Figure 3(a) shows correlation between the energy and the timing obtained by the QTC + multi-hit TDC system at an intensity of 10^3 ppp. Here, the start timing is determined by the plastic scintillator stopper. Delayed γ -rays of $E_\gamma = 120$ keV from $^{16}\text{N}(0^-)$ are clearly observed. Figure 3(b) shows a timing spectrum for 120-keV γ -ray events. From this spectrum, the lifetime of $T_{1/2} = 5.20 \pm 0.11 \mu\text{s}$ was obtained. The value is consistent with the known lifetime of $5.25 \mu\text{s}$ within the uncertainties, which validates that the QTC + multi-hit TDC system works properly for isomer tagging over a wide long time window of $20 \mu\text{s}$. Analysis of the data with a high-intensity beam is ongoing.

Next, we studied timing responses of MPPCs at high photon exposure by using a primary ^{16}O beam at 230 MeV/u. The beam was degraded to ~ 120 MeV/u, and implanted in a CeBr_3 scintillator. A typical intensity was 10^3 ppp, and a maximum intensity was 10^6 ppp. A number of photons emitted from the scintillator were detected by various MPPCs. Four Hamamatsu MPPCs were tested: S13360-6050CS, S13360-6025CS, S13360-3050CS, and S13360-3025CS, which have a different sensitive area and pixel size as summarized in Table 1. The MPPC signals were recorded by using a flash ADC (SIS3301, SIS GmbH).

Figures 4(a) and (b) show the S13360-3050CS response to a ^{16}O beam with an intensity of 10^3 ppp. For comparison, the response to a ^{137}Cs γ -source is also shown in Fig. 4(c). As can be seen in Fig. 4(a), the MPPC shows a quick response even under the saturating condition. Owing to the good timing response, the amplitude decreases to the same

Model	sensitive area (mm^2)	pixel size (μm^2)
S13360-6050CS	6×6	50×50
S13360-6025CS	6×6	25×25
S13360-3050CS	3×3	50×50
S13360-3025CS	3×3	25×25

Table 1. Specifications of MPPCs.

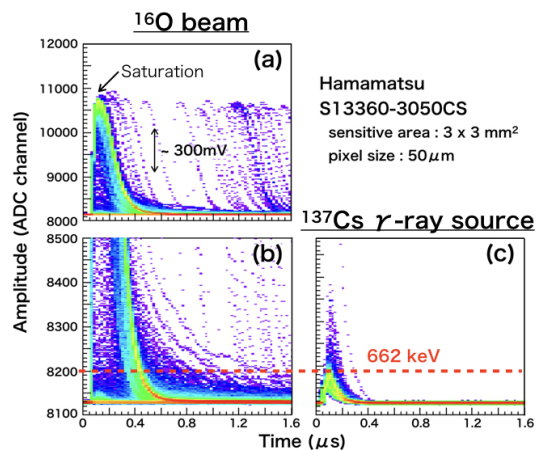


Figure 4. Responses of a MPPC, Hamamatsu S13360-3050CS, to a ^{16}O beam [(a) and (b)], and a ^{137}Cs γ -source [(c)]. (b) is same as in (a) but the vertical axis is zoomed in.

level as that of a ^{137}Cs photopeak after $\sim 0.5 \mu\text{s}$, indicating a high feasibility of the active stopper for microsecond isomers. The other MPPCs also showed similar responses. Further analyses including the beam-intensity dependence are in progress.

From the performance tests described above, a high feasibility of the active stopper is demonstrated. The obtained results will be used to design the details of the active stopper.

References

- [1] P. M. Walker and G. D. Dracoulis, *Nature* **399**, (1999) 35.
- [2] G. D. Dracoulis, P. M. Walker, and F. G. Kondev, *Rep. Prog. Phys.* **79**, (2016) 076301.
- [3] M. Takaki *et al.*, *CNS Ann. Rep.* **94**, (2014) 9.
- [4] M. Dozono *et al.*, *RIKEN Accel. Prog. Rep.* **45**, (2012) 10.
- [5] T. Uesaka, S. Shimoura, H. Sakai, *Prog. Theor. Exp. Phys.* **2012** (2012) 03C007.
- [6] H. Nishio *et al.*, *Nucl. Instrum. Methods Phys. Res. A* **610** (2009) 710.

PANDORA, a large volume low-energy neutron detector with real-time neutron-gamma discrimination

L. Stuhl, K. Yako, M. Sasano^a, J. Yasuda^b, H. Baba^a, S. Ota, and T. Uesaka^a

Center for Nuclear Study, Graduate School of Science, University of Tokyo

^aRIKEN (The Institute of Physical and Chemical Research)

^bDepartment of Physics, Kyushu University

Recent nuclear physics studies are increasingly focused on the region far from the valley of stability, leading to an increase in the intensity of available exotic isotopes. This advancement makes it possible to investigate phenomena with low cross sections, such as inelastic scattering and charge-exchange reactions. Because the cross sections of the charge-exchange reactions are very low, it is crucial to efficiently tag these reaction channels and minimize contaminant events from other reaction channels with larger cross-sections (e.g., elastic scattering, knockout reactions).

The (p, n) charge-exchange reactions at intermediate energies (200–300 MeV/nucleon) are a powerful tool to study the spin-isospin excitations of nuclei. The technique of inverse kinematics [1] enables the (p, n) reactions on exotic nuclei with a high luminosity to be studied. In this technique, neutron detectors are used to measure the time-of-flight (ToF) of low-energy recoil neutrons from a few hundred keV to a few MeV produced from the (p, n) reaction. This methodology has been successfully applied to study the Gamow–Teller strength distribution from ^{56}Ni [2] and ^{132}Sn [3] isotopes. The first generation of neutron detectors designed for these measurements, such as LENDA [4], WINDS [5] and ELENS [6] provide good setups, but they cannot distinguish between neutrons and gamma rays.

Our work focused on the development of PANDORA (Particle Analyzer Neutron Detector Of Real-time Acquisition) detector. PANDORA is based on a plastic scintillator, which is sensitive to the differences between neutrons and gamma rays. This system helps to reduce the trigger rate in online data processing by one order of magnitude, and improve the separation of neutrons and the gamma ray background in offline analysis. This can be realized using a new parameter from the pulse shape discrimination (PSD) method and a ToF method. PANDORA consists of a plastic scintillator bar with dimensions of $2.5 \times 5 \times 30 \text{ cm}^3$ coupled to a photomultiplier tube (PMT) on each end. The detector is designed to measure neutron energies using the ToF technique in the kinetic-energy region from around 100 keV to a few MeV. Figure 1 depicts one bar.

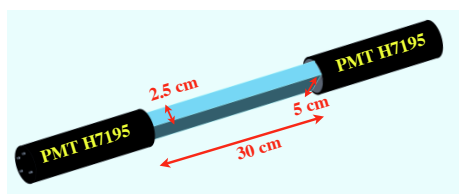


Figure 1. Sketch of one PANDORA detector bar.

The fast plastic scintillator bars are EJ-299-34 produced by Eljen Technology [7]. This is the largest existing sample of EJ-299-34. The manufacturer quotes a light yield of 8600 photons/MeV (at 1 MeV_{ee}) and an emission spectrum dominated by wavelengths around 420–425 nm. The PANDORA scintillator bar is wrapped with two layers of reflective aluminized Mylar foil, and black insulating tape to ensure proper light propagation through the bar as well as light-tightness. The PMTs of PANDORA are 51-mm-diameter-type Hamamatsu H7195 tubes coupled to plastic using EJ-500 colorless epoxy optical cement [8].

PANDORA employs a digital data acquisition system. The detector signals from the anode output of both PMTs are read-out with a 14-bit 500 MSample/s flash ADC waveform digitizer CAEN V1730, which operates with a 2-V full-scale range. The sampling clock of the module (one sample corresponds to a 2-ns time step) is adequate to digitize the signals, where information critical for particle identification is situated in the long tail. A CAEN A3818A optical link is installed for fast communications between the digitizer and the PC of the digital data acquisition system. CAEN’s Digital Pulse Processing for the Pulse Shape Discrimination (DPP-PSD) firmware [9] is installed on the field programmable gate arrays of the digitizer. The system uses a charge comparison method [10] to identify particles. Neutron-gamma discrimination is possible in real-time by digital signal processing based on integrated charge measurements over two different time regions of the input pulses. The PSD parameter is defined as follows:

$$\text{PSD} = \frac{Q_{\text{Long}} - Q_{\text{Short}}}{Q_{\text{Long}}}, \quad (1)$$

where Q_{Long} is the charge integrated in the long gate. Typically, it contains all charges in the signal. Q_{Short} is the charge integrated in the short gate. Defining PSD_{mean} value as the arithmetic mean of PSD values of two single-end readouts, PANDORA exhibits PSD capability comparable to those presented in literature [11]. The scatterplot shown in Fig. 2 provides the most efficient way to assess the online PSD against the offline separation by ToF. It is also clear that only a small fraction (about 9% in case of the PSD_{mean} = 0.15 separation threshold) of the gamma rays are located in the PSD range of neutrons. The figure confirms that in the ToF range of neutrons (ToF > 20 ns), a non-negligible amount of gammas creates a background. The combination of the commonly used ToF with the new online parameter (PSD) will help discriminate fully the detected neutrons not only from prompt gamma rays, but also from the random gamma background originating from the environment.

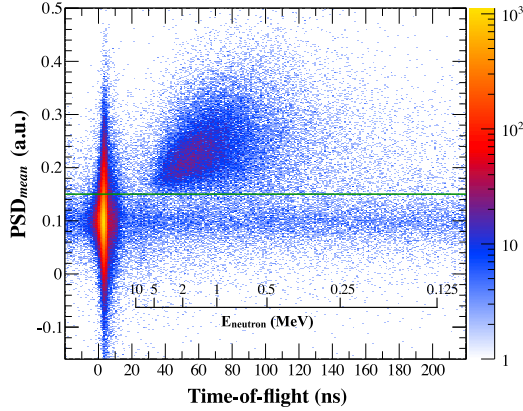


Figure 2. PSD_{mean} vs. ToF spectrum shows a good separation of neutron-like and gamma-like events. The sharp peak below 4 ns corresponds to events identified as gamma rays, while the distribution in the higher ToF region and $PSD_{mean} > 0.15$ represents neutron-like events. The inner scale corresponds to the kinetic energy of the detected neutrons obtained using the ToF method. A large random gamma background can also be observed.

The first on-beam test experiment was performed using the prototype of PANDORA at the Radioactive Isotope Beam Factory (RIBF) in RIKEN using the SHARAQ spectrometer [12] during the SHARAQ10 experiment in parasitic mode.

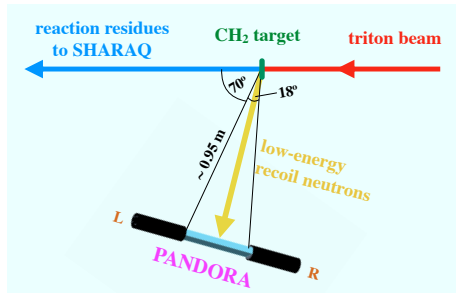


Figure 3. Experimental setup of the first test of PANDORA using a secondary triton beam at RIBF RIKEN.

In the ${}^1\text{H}(t, n){}^3\text{He}$ inverse kinematical reaction at a 310 MeV/nucleon triton energy, we detected neutrons from the (p, n) reaction on a 0.5-mm thick CH_2 target with a density of 0.93 g/cm^3 . Based on the kinematic calculations related to the reaction, the detector bar was placed to cover the laboratory angle region of 70° – 88° to detect neutrons with a kinetic energy of 0.1–9 MeV. The distance between the target and PANDORA was around 0.95 m. Upstream from the target, the F3 thin plastic scintillator of the BigRIPS separator [13] was used as the start detector, while the reaction residues were detected downstream in the focal plane plastic scintillator detectors of the SHARAQ spectrometer. The typical beam intensity was 10^6 particle/sec. Figure 3 shows the related experimental setup.

We used a triple coincidence condition between the start detector, PANDORA, and the focal plane detectors, the trigger rate was less than 25–30 Hz, while the PANDORA self-

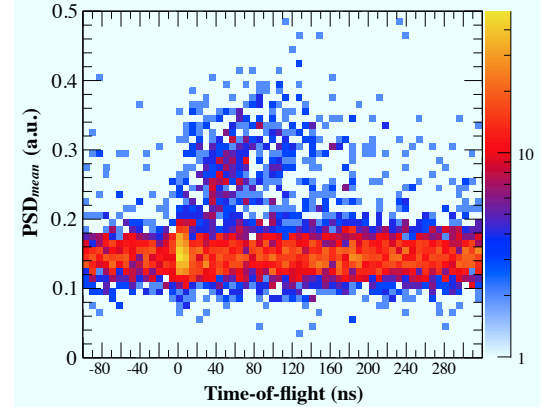


Figure 4. PSD_{mean} vs. ToF spectrum from the first test experiment of PANDORA shows the importance of separating neutrons and random gamma background.

trigger rate was 8–9 kHz. The measurement spanning a couple of hours confirms a good separation of neutrons and gamma rays using the PSD method. Figure 4 shows the PSD_{mean} against the ToF. The spectrum is dominated by a large random gamma background in the ToF range of neutrons ($0.1 < PSD_{mean} < 0.2$). Using the ToF method alone 25% of detected gammas can be removed, while the combination of ToF with PSD improves the separation, resulting in exclusion of more than 90% of gammas. Online separation would have reduced the event rate to 1/5. Therefore PANDORA will be very effective in future high-luminosity experiments.

Further details of PANDORA and its online neutron event separation efficiency are reported in Ref 14.

References

- [1] M. Sasano et al., Phys. Rev. Lett. 107 (2011) 202501.
- [2] M. Sasano et al., Phys. Rev. C 86 (2012) 034324.
- [3] PhD thesis of J. Yasuda, Kyushu University (2017).
- [4] G. Perdikakis et al., Nucl. Inst. Meth. A 686 (2012) 117.
- [5] K. Yako, et al, RIKEN Accel. Prog. Rep. (2012) 45.
- [6] L. Stuhl, et al, Nucl. Inst. Meth. A 736 (2014) 1.
- [7] www.eljentechnology.com/products/plastic-scintillators/ej-299-33a-ej-299-34
- [8] www.eljentechnology.com/products/accessories/ej-500
- [9] www.caen.it/csite/CaenProd.jsp?parent=39&idmod=770
- [10] Y. Kaschuck et al., Nucl. Inst. Meth. A 551 (2005) 420.
- [11] P. Blanc et al., Nucl. Inst. Meth. A 750 (2014) 1.
- [12] T. Uesaka et al., Nucl. Inst. Meth. B 266 (2008) 4218.
- [13] N. Fukuda et al., Nucl. Inst. Meth. B 317 (2013) 323.
- [14] L. Stuhl et al., Nucl. Instr. Meth. A 866 (2017) 164.

Theoretical Nuclear Physics

Shell-model study on double Gamow-Teller transition of ^{48}Ca

N. Shimizu, J. Menéndez, and K. Yako

Center for Nuclear Study, Graduate School of Science, the University of Tokyo

Double Gamow Teller transition has attracted a lot of interest not only as a novel two-phonon excitation mode, but also as a key transition of possible neutrinoless double beta ($0\nu\beta\beta$) decay. In the theoretical study of the nuclear matrix element (NME) of the $0\nu\beta\beta$ decay with the closure approximation, the NME is composed of the Gamow-Teller type, Fermi type, and tensor type contributions. The Gamow-Teller type contribution is largest among them, and is expected to have strong correlation to the NME of the double Gamow Teller transition [1, 2].

On the experimental side, the double isobaric analogue resonance was measured by utilizing pion double charge exchange reaction [3]. In contrast, the double Gamow-Teller resonance (DGTR) was originally discussed by Auerbach *et al.* theoretically in 1989 [4], but it remains difficult to be confirmed experimentally still nowadays.

Recently, an experimental search for the DGTR utilizing the heavy-ion double-charge exchange (HIDCX) reaction of $^{48}\text{Ca}(^{12}\text{C}, ^{12}\text{Be}(0_2^+))^{48}\text{Ti}$ was performed at Research Center for Nuclear Physics, Osaka University and its data analysis is ongoing [5]. This HIDCX reaction is a novel spectroscopic tool based on the ‘‘inverted structure’’ of ^{12}Be in a shell-model sense; the 0_2^+ state of ^{12}Be is dominated by $0\hbar\omega$ configuration, while the ground state has $2\hbar\omega$ excited configuration [6]. Another experiment using the same reaction is planned at RI Beam Factory, RIKEN Nishina Center for further investigation [7]. ^{48}Ca is one of the double-beta-decay nuclides and these DGTR experiments are expected to provide some information to extract the $0\nu\beta\beta$ -decay NME.

In the present report, we present the DGTR of ^{48}Ca predicted by shell model calculations. The model space is taken as the pf shell and the GXPFB interaction is used [8]. The initial state of the DGTR is assumed to be the $J_i^\pi = 0^+$ ground state of the ^{48}Ca throughout this work. The shell-model calculations were performed using the ‘‘KSHELL’’ code [9].

The DGT transition probability is defined as

$$B(\text{DGT}\pm; \lambda) = \frac{1}{2J_i + 1} |\langle f | \mathcal{O}_\pm^{(\lambda)} | i \rangle|^2, \quad (1)$$

where the $|i\rangle$ and $|f\rangle$ are the ^{48}Ca initial-state and the ^{48}Ti final-state wave functions. The DGT operator is

$$\mathcal{O}_\pm^{(\lambda)} = [Y_\pm \times Y_\pm]^{(\lambda)}, \quad (2)$$

where $Y_\pm = \sum_j \sigma(j) \tau_\pm(j)$ is a Gamow-Teller operator with the particle index j . σ is the Pauli matrix and τ_- transforms a neutron into a proton. The rank of the operator, λ , is taken as 0 or 2 since $\lambda = 1$ is prohibited by the symmetry property of a product of two identical one-body operators [10]. In the present work, $J_f = \lambda = 0$ or 2 because of $J_i = 0$. The

derivation of the sum rule for the DGT transition had been given in Refs. [10, 11], and it was recently revisited in [12].

Since the DGT- transition changes two neutrons into two protons the $J_i^\pi = 0_1^+$ ground state of ^{48}Ca is transformed into $J_f^\pi = 0_f^+$ or $J_f^\pi = 2_f^+$ states of ^{48}Ti . The distribution of the DGT transition is numerically obtained by the Lanczos strength function [13, 14].

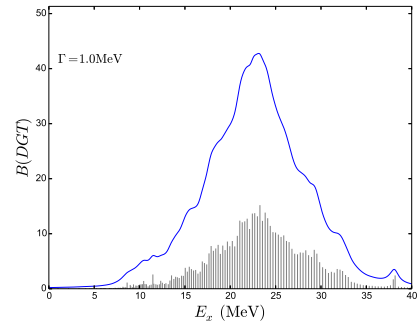


Figure 1. Distribution of the double Gamow Teller transition, $B(\text{DGT}-; \lambda = 2; 0_1^+, ^{48}\text{Ca} \rightarrow 2^+, ^{48}\text{Ti})$, against the excitation energy. The black bars denote the transition probabilities of the states obtained by the 300 Lanczos iterations. The blue curve is obtained by smearing the black bars with $\Gamma = 1$ MeV Lorentzian distribution.

We briefly explain the Lanczos strength function in shell model calculations. We prepare the following wave function as an initial state of the Lanczos method:

$$|\psi_0\rangle = \mathcal{O}^\lambda |i\rangle, \quad (3)$$

where $|i\rangle$ is an initial state of the transition, namely the ground state of ^{48}Ca in this case. We performed a fixed number of the Lanczos iterations, e.g. 300 iterations, and thus obtain 300 states. These states are not the exact eigenstates of the Hamiltonian, but the transition probabilities between these states and $|i\rangle$ are good approximation to the exact values.

Figure 1 shows the $B(\text{DGT}-; \lambda = 2)$ to demonstrate how the Lanczos strength function works. The black bars in the figure show the strengths from the ^{48}Ca ground state to the 300 states obtained by the Lanczos iterations. The distribution is smeared out by Lorentzian with the width $\Gamma = 1$ MeV to simulate the experimental resolution. When we increase the number of iterations, the black bars still evolve but the smeared distribution curve, namely the blue solid curve in Fig. 1, has converged already and does not change.

Figures 2 (a) and (b) show the DGT distribution to the final state with angular momentum J_f and isospin T_f . The isospin dependence is obtained by the Lanczos strength function with the isospin-projected initial state. Owing to

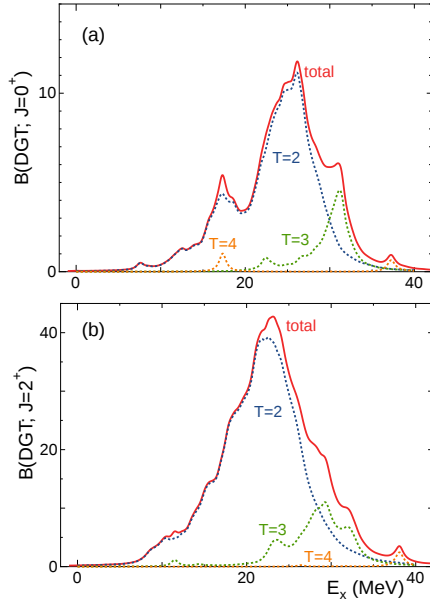


Figure 2. Isospin dependence of the DGT transition of ^{48}Ca against the excitation energy. The final state is (a) $J_f = 0$ and (b) $J_f = 2$. The blue dotted, green dotted, orange dotted, and red solid lines denote the $T_f = 2$, $T_f = 3$, $T_f = 4$, and total strengths where T_f is the isospin of the ^{48}Ti final states.

Eq. (2), J_f is restricted to be 0 or 2. The isospin T_f is taken as $T_f = 2, 3, 4$ since ^{48}Ti consists of two valence protons and six valence neutrons in the pf shell.

The $J_f = 2$ distribution is roughly four times larger than the $J_f = 0$ distribution, which is consistent to the sum-rule values in Ref. [12]. The isospin dependence is also shown, and the $T_f = 2$ component is the major contribution. The $T_f = 3$ contribution makes a small peak around $E_x = 30$ MeV.

In summary, we present the DGT transition distributions of ^{48}Ca predicted by shell-model calculation. The investigation of the relation between the DGT transition matrix element and the $0\nu\beta\beta$ -decay NME is in progress. Further understanding of the practical HIDCX experiment, especially the reaction mechanism regarding the contribution of intermediate process remains as a future problem.

N.S. acknowledges Drs. Yutaka Utsuno and Motonobu Takaki for fruitful discussions. This work has been supported by the Post-K priority issue 9 from MEXT, JICFuS, CNS-RIKEN joint project for large-scale nuclear structure calculations, and JSPS KAKENHI grant (25870168).

References

- [1] T. R. Rodriguez, G. Martínez-Pinedo, Phys. Lett. B **719**, 174 (2013).
- [2] F. Cappuzello, M. Cavallaro, C. Agodi, M. Bondi, D. Carbone, A. Cunsolo and A. Foti, Eur. Phys. J. A **51**, 145 (2015).
- [3] S. J. Greene *et al.*, Phys. Rev. C **25**, 927 (1982).
- [4] N. Auerbach, L. Zamick and D. C. Zheng, Ann. Phys. **192**, 77 (1989).

- [5] M. Takaki *et al.*, CNS Ann. Rep. **94**, 9 (2014).
- [6] R. Meharchand *et al.*, Phys. Rev. Lett. **108**, 122501 (2012).
- [7] T. Uesaka *et al.*, RIKEN RIBF NP-PAC, NP1512-RIBF141 (2015).
- [8] M. Honma, T. Otsuka, and T. Mizusaki, RIKEN Accel. Prog. Rep. **41**, 32 (2008).
- [9] N. Shimizu, arXiv:1310.5431 [nucl-th].
- [10] K. Muto, Phys. Lett. B **277**, 13 (1992).
- [11] P. Vogel, M. Ericson, and J. D. Vergados, Phys. Lett. B **212**, 259 (1988).
- [12] H. Sagawa and T. Uesaka, Phys. Rev. C **94**, 064325 (2016).
- [13] R. R. Whitehead, A. Watt and D. Kelvin, Phys. Lett. **89B**, 313 (1980).
- [14] E. Caurier, G. Martínez-Pinedo, F. Nowacki, A. Poves and A. P. Zuker, Rev. Mod. Phys. **77**, 427 (2005).

Monte Carlo shell model calculations for structure of ^{66}Ni

Y. Tsunoda^a, T. Otsuka^{b,a,c,d}, N. Shimizu^a, M. Honma^e, and Y. Utsuno^f

^aCenter for Nuclear Study, the University of Tokyo

^bDepartment of Physics, the University of Tokyo

^cNational Superconducting Cyclotron Laboratory, Michigan State University, USA

^dInstituut voor Kern- en Stralingsfysica, KU Leuven, Belgium

^eCenter for Mathematical Sciences, University of Aizu

^fAdvanced Science Research Center, Japan Atomic Energy Agency

Nuclear shape is one of the most important properties for the study of the nuclear collectivity. We discuss shape coexistence and other properties of ^{66}Ni nucleus ($Z = 28$, $N = 38$) in this report. Some of our results of the calculations of ^{66}Ni have been published in collaboration with experimentalists [1]. We have investigated shapes and properties of Ni isotopes by using the Monte Carlo shell model (MCSM) calculations [2,3], where our calculations successfully describe the properties extracted by the experiments. Some of our calculations for Ni isotopes were published in Refs. [4–9].

The model space used in our calculations is the full pf shell, the $0g_{9/2}$ and $1d_{5/2}$ orbits for both protons and neutrons. We use the modified A3DA effective interaction as is used in Ref. [4]. We performed MCSM calculations so that the calculation in the large model space is available. In the MCSM, the wave function $|\Psi\rangle$ is represented as the superposition of the projected Slater determinants (MCSM basis vectors) as

$$|\Psi\rangle = \sum_{n,K} f_{n,K} P_{MK}^{J\pi} |\phi_n\rangle,$$

where $P_{MK}^{J\pi}$ is the angular-momentum and parity projector and $|\phi_n\rangle$ is a Slater determinant. We can analyze the nuclear intrinsic shape by using the MCSM basis vector before projection, $|\phi_n\rangle$. This method has been used in the study of Ni isotopes [4, 6, 7]. In this method, we use the figure (referred to as T-plot) of the potential energy surface (PES) with circles indicating the shape of the MCSM basis vector. An example of T-plot is shown in Fig. 1. The PES is calculated by constrained Hartree-Fock method using the shell-model effective interaction. We calculate the quadrupole moments, Q_0 and Q_2 , of the MCSM basis vector before projection and locate a circle at the corresponding place in the PES. The area of the circle is proportional to the overlap probability between the MCSM basis vector $P_{MK}^{J\pi} |\phi_n\rangle$ and the wave function $|\Psi\rangle$. Thus, the distribution pattern of the circles indicates the nuclear intrinsic shape for the eigenstate. Although the $J = 0$ wave function is isotropic, we can analyze intrinsic shape of the 0^+ state because we use the MCSM basis vector before the angular-momentum projection.

We calculated low-lying levels of ^{66}Ni nucleus. Figure 2 shows calculated levels of ^{66}Ni . The positive-parity levels are shown separately by their shape. The shape of each calculated level was determined by using T-plot. Figure 1 shows a T-plot of the four 0^+ states. The 0_1^+ and 0_3^+ states are spherical, the 0_2^+ state is oblate, and 0_4^+ is pro-

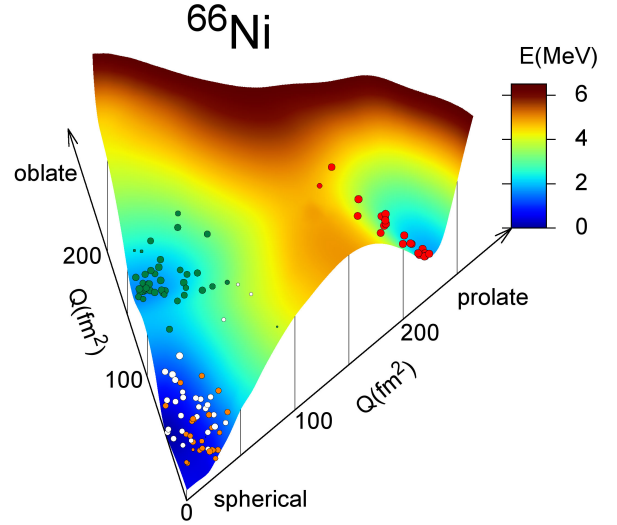


Figure 1. T-plot of the four 0^+ states of ^{66}Ni . The circle corresponds to the MCSM basis vector. The area of the circle is proportional to the largest overlap probability between the MCSM basis vector and the four 0^+ states. The color of the circle represents the state with the largest overlap. The white, green, orange, and red circles correspond to the 0_1^+ , 0_2^+ , 0_3^+ , and 0_4^+ states, respectively. Adapted from Fig. 1 of Ref. [1].

late. The calculated $B(E2; 0^+ \rightarrow 2_1^+)$ with effective charges $e_p = 1.5e$ and $e_n = 0.5e$ are 26, 4.1, 0.01, and 0.006 Weisskopf units (W.u.) for the 0_1^+ , 0_2^+ , 0_3^+ , and 0_4^+ states, respectively. The experimentally evaluated $B(E2; 0_1^+ \rightarrow 2_1^+)$ is 38.0 ± 6.5 W.u. [10]. The lifetimes of the 0_2^+ , 0_3^+ , and 0_4^+ states were measured and $B(E2; 0^+ \rightarrow 2_1^+)$ were obtained experimentally [1]. The experimental $B(E2; 0^+ \rightarrow 2_1^+)$ are 4.3 ± 0.5 , 0.09 ± 0.01 , and 0.21 ± 0.07 W.u. for the 0_2^+ , 0_3^+ , and 0_4^+ states, respectively. Because the calculated 2_1^+ state is spherical and 0_4^+ is largely prolate, $B(E2; 0_4^+ \rightarrow 2_1^+)$ is expected to be small. While $B(E2)$ between the spherical 0_1^+ and 2_1^+ states is not small, $B(E2)$ between the spherical 0_3^+ and 2_1^+ states is small. The main configuration of the calculated 2_1^+ state is $\nu f_{5/2}^{-1} p_{1/2}^{-1}$ with respect to the ^{68}Ni core. While the main configurations of both calculated 0_1^+ and 0_3^+ states are $\nu f_{5/2}^{-2}$ and $\nu p_{1/2}^{-2}$, the relative sign of the two configurations are different for the two states. These two configurations contribute to $B(E2)$ coherently (incoher-

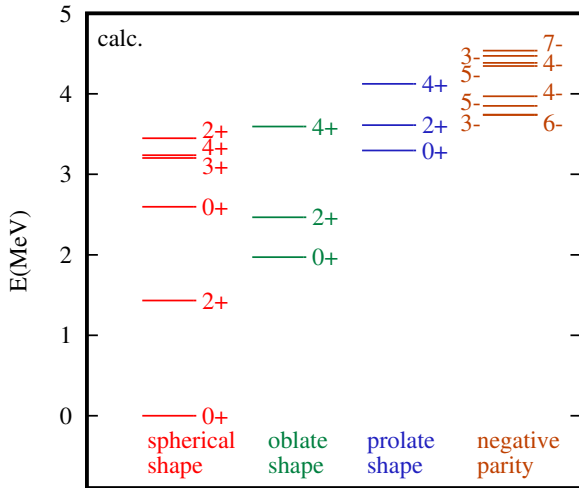


Figure 2. Low-lying levels of ^{66}Ni nucleus calculated by the MCSM. Positive-parity states are shown separately with their shape (spherical, oblate or prolate).

ently) for the 0_1^+ (0_3^+) state.

This work has been supported in part by MEXT as “Priority Issue on post-K computer” (Elucidation of the Fundamental Laws and Evolution of the Universe), JICFuS, and the RIKEN-CNS joint research project on large-scale nuclear-structure calculations. The MCSM calculations were performed on the K computer at the RIKEN AICS (Project ID: hp160211).

References

- [1] S. Leoni *et al.*, Phys. Rev. Lett. **118**, 162502 (2017).
- [2] T. Otsuka, M. Honma, T. Mizusaki, N. Shimizu, and Y. Utsuno, Prog. Part. Nucl. Phys. **47**, 319 (2001).
- [3] N. Shimizu, T. Abe, Y. Tsunoda, Y. Utsuno, T. Yoshida, T. Mizusaki, M. Honma, and T. Otsuka, Prog. Theor. Exp. Phys. **2012**, 01A205 (2012).
- [4] Y. Tsunoda, T. Otsuka, N. Shimizu, M. Honma, and Y. Utsuno, Phys. Rev. C **89**, 031301(R) (2014).
- [5] S. Suchyta *et al.*, Phys. Rev. C **89**, 021301(R) (2014).
- [6] F. Flavigny *et al.*, Phys. Rev. C **91**, 034310 (2015).
- [7] C. J. Chiara *et al.*, Phys. Rev. C **91**, 044309 (2015).
- [8] T. Otsuka, and Y. Tsunoda, J. Phys. G: Nucl. Part. Phys. **43**, 024009 (2016).
- [9] A. I. Morales *et al.*, Phys. Lett. B **765**, 328 (2017).
- [10] B. Pritychenko, M. Birch, B. Singh, and M. Horoi, At. Data Nucl. Data Tables **107**, 1 (2016).

Quantum phase transition in the shape of Zr isotopes

T. Togashi^a, Y. Tsunoda^a, T. Otsuka^{a,b}, and N. Shimizu^a

^aCenter for Nuclear Study, University of Tokyo

^bDepartment of Physics, University of Tokyo

The shape of the atomic nucleus has been one of the primary subjects of nuclear structure. A related interesting problem is the transition from spherical to deformed shapes as a function of the neutron (proton) number N (Z), referred to as shape transition. The shape transition is visible in the systematics of the excitation energies of 2_1^+ state of even-even nuclei: it turns out to be high (low) for spherical (deformed) shapes [1]. The shape transition appears to be rather gradual in most cases, for instance, from ^{148}Sm to ^{154}Sm . On the other hand, the even-even Zr ($Z = 40$) isotopes exhibit an abrupt change in the shape transition from $N = 50$ to $N = 70$. The observed 2_1^+ levels move up and down within the 1–2 MeV region for $N = 50–58$, whereas its energy becomes quite low, around 0.2 MeV for $N \geq 60$ [2]. Namely, a sharp drop of the 2_1^+ level by a factor of ~ 6 occurs at $N = 60$. This abrupt change seems to occur in the structure of the ground state as a function of N , which can be viewed as an example of quantum phase transition (QPT) [3].

The structure of Zr isotopes has been studied by many theoretical approach. Interacting boson model (IBM) calculations [4–6] show a good description of the 2_1^+ levels, although the rapid change of structure is absent. The VAMP-IR calculations [7, 8] provide a result of the ground state with mixing of various shapes at $N = 58$. Density functional theories [9–12], finite range droplet model [13], and macro-micro calculation [14] indicate gradual shape changes.

Shell-model calculations have high capability of calculating those energies precisely in principle. However, since the nuclear deformation is a consequence of the collective motion of many nucleons, the application of the conventional shell-model calculation encounters some limits in the size of the calculation. Shell-model calculations have been performed up to $N = 58$ [15, 16]. The Monte Carlo shell model (MCSM) succeeds in covering the even-even Zr isotopes for $N = 50–70$ and discussing their characteristic shape transition theoretically [17].

The model space of the present work is composed of 8 proton single-particle orbits ($0f_{5/2}$, $1p_{3/2,1/2}$, and the sdg shell), and 8 neutron orbits (the sdg shell, $0h_{11/2}$, $1f_{7/2}$, and $2p_{3/2}$). The largest M -scheme dimension of the present objects reaches 3.7×10^{23} , much beyond the current limit of conventional shell model calculations. The effective Hamiltonian is constructed from existing trustable ones. The JUN45 interaction [18] is used for the f_5pg_9 orbits, namely, $0g_{9/2}$ and below. The SNBG3 interaction [19] is used for the $T = 1$ interaction for the $0g_{7/2}$, $1d_{5/2,3/2}$, $2s_{1/2}$, and $0h_{11/2}$ orbits. The rest of the effective interaction is constructed by V_{MU} [20]. The $T = 0$ part of the effective interaction is kept unchanged, while the $T = 1$ two-body matrix elements are fine-tuned by using the standard method [21].

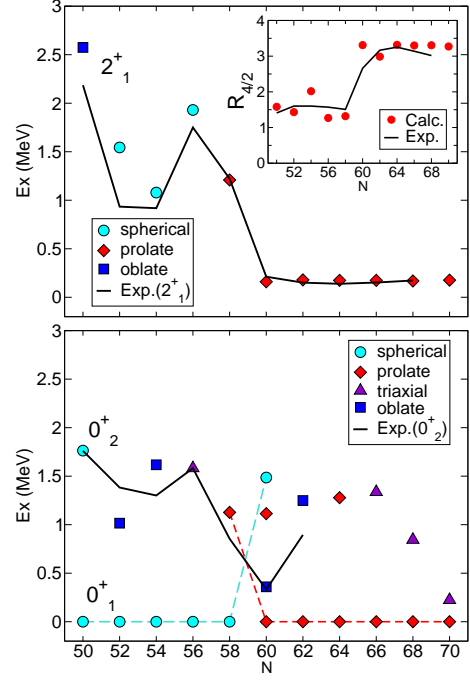


Figure 1. The 2_1^+ and 0_1^+ levels of the Zr isotopes as a function of N . The symbols indicate the present results with the shape classification. Solid lines denotes the experimental data [2]. The inset of the upper shows the ratio between 4_1^+ and 2_1^+ .

Figure 1 shows the excitation energies of 2_1^+ and 0_1^+ states of Zr isotopes and indicates that the present MCSM results reproduce quite well the observed trends. The shape of each calculated state is assigned by a T-plot [22]. The calculated 2_1^+ state is spherical for $N = 52–56$, while it becomes prolate deformed for $N \geq 58$. Its excitation energy drops down at $N = 60$ by a factor of ~ 6 , and stays almost constant, in agreement with experimental data. The ratio between the 4_1^+ and 2_1^+ levels, denoted as $R_{4/2}$, is depicted in the inset of the upper of Fig. 1 in comparison to experiment. The sudden increase at $N = 60$ is seen in both experiment and calculation, approaching the rotational limit, $10/3$, indicative of a rather rigid deformation. The $R_{4/2} < 2$ for $N \leq 58$ suggests a seniority-type structure which results from the $Z = 40$ semi-magicity.

The lower of Fig. 1 demonstrates that the 0_1^+ state is spherical up to $N = 58$, but the spherical 0_1^+ state is pushed up to the 0_4^+ state, unobserved experimentally, at $N = 60$, where the prolate deformed 0_1^+ state comes down to the ground state from the 0_2^+ state at $N = 58$. The abrupt change at $N = 60$ is also discussed for the behavior of $B(E2; 2_1^+ \rightarrow 0_1^+)$ in [17]. We can, thus, identify the change between $N = 58$ and 60 as a QPT, where in general an

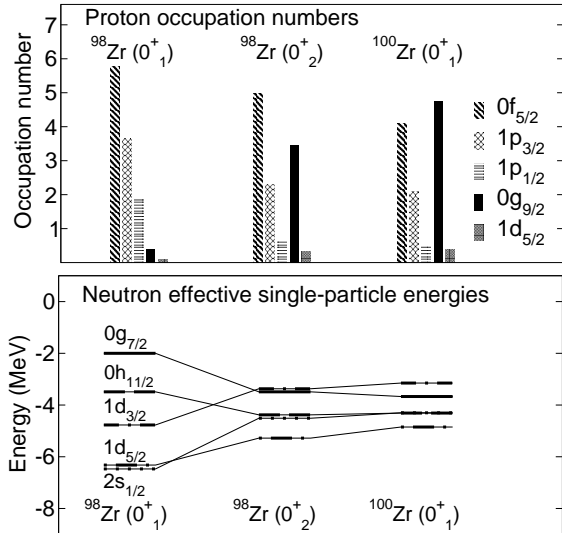


Figure 2. The occupation numbers of the protons and the effective single-particle energies of neutrons for $0^+_{1,2}$ states of $^{98,100}\text{Zr}$.

abrupt change should occur in the quantum structure of the ground state for a certain parameter. The parameter here is the neutron number N . The sharp crossing between spherical and deformed states causes the present QPT. The discontinuities of various quantities, one of which can be interpreted as the order parameter, at the crossing point imply the first-order phase transition.

We now discuss the origin of such abrupt changes. The upper of Fig. 2 displays the occupation numbers of proton orbits for the $0^+_{1,2}$ states of ^{98}Zr and the $0^+_{1,1}$ state of ^{100}Zr . From the spherical $0^+_{1,1}$ to the prolate $0^+_{2,2}$ states of ^{98}Zr , the occupation number of the proton $0g_{9/2}$ orbit increases from 0.4 to 3.5, while those of the pf -shell orbits decrease. The proton $0g_{9/2}$ orbit is more occupied in the prolate $0^+_{1,1}$ state of ^{100}Zr . The lower of Fig. 2 shows the ESPE of neutron orbits. One notices that the ESPEs from $2s_{1/2}$ to $0g_{7/2}$ are distributed over a range of 4 MeV for the $0^+_{1,1}$ state of ^{98}Zr , but are within 2 MeV for the prolate states such as $0^+_{2,2}$ of ^{98}Zr and $0^+_{1,1}$ of ^{100}Zr .

The above two phenomena shown in Fig. 2 are correlated and predicted in the type II shell evolution scenario [22,23], where particular particle-hole excitations can vary the shell structure significantly. To be more concrete, protons in the $0g_{9/2}$ orbit lower the ESPEs of neutron $0g_{7/2}$ and $0h_{11/2}$ orbits more than other orbits. For the $0g_{9/2}$ - $0g_{7/2}$ coupling, the tensor and central forces work coherently, and substantial lowering (~ 2 MeV) occurs. In the $0g_{9/2}$ - $0h_{11/2}$ case, the tensor and central forces work destructively but the net effect is still a lowering, though weaker than the other case. Regarding the central force, the attraction between the $0g_{9/2}$ and $0h_{11/2}$ orbits is stronger than the average due to similarities in radial wave functions, as also mentioned earlier by previous works [24]. The present deformation is primarily a result of the quadrupole component of the effective interaction, and is enhanced by coherent contributions of various configurations (Jahn-Teller effect [25]). These coherent contributions enhance proton excitations to reinforce themselves via proton-neutron interactions. Consequently,

the state with this deformation-optimized shell structure has lower energy than the state with normal shell structure.

References

- [1] A. Bohr and B. R. Mottelson, *Nuclear Structure*, Vol. II (W. A. Benjamin, Reading, MA, 1975).
- [2] NuDat 2.7 β , <http://www.nndc.bnl.gov/nudat2/>.
- [3] S. Sachdev, *Quantum Phase Transitions* (Cambridge University Press, Cambridge, England, 2011).
- [4] J. E. Garca-Ramos, K. Heyde, R. Fossion, V. Hellemans and S. De Baerdemacker, *Eur. Rev. J. A* **26**, 221 (2005).
- [5] M. Boyukata, P. Van Isacker and I Uluer, *J. Phys. G* **37**, 105102 (2010).
- [6] K. Nomura, R. Rodrıguez-Guzman and L. M. Robledo, *Phys. Rev. C* **94**, 044314 (2016).
- [7] A. Petrovici, K. W. Schmid and A. Faessler, *J. Phys. Conf. Ser.* **312**, 092051 (2011).
- [8] A. Petrovici, *Phys. Rev. C* **85**, 034337 (2012).
- [9] R. Rodrıguez-Guzman, P. Sarriguren, L. M. Robledo and S. Perez-Martin, *Phys. Lett. B* **691**, 202 (2010).
- [10] J. Skalski, P.-H. Heenen and P. Bonche, *Nucl. Phys. A* **559**, 221 (1993).
- [11] J. Xiang, Z. P. Li, Z. X. Li, J. M. Yao and J. Meng, *Nucl. Phys. A* **873**, 1 (2012).
- [12] H. Mei, J. Xiang, J. M. Yao, Z. P. Li and J. Meng, *Phys. Rev. C* **85**, 034321 (2012).
- [13] P. Moller, J. R. Nix, W. D. Myers and W. J. Swiatecki, *At. Data Nucl. Data Tables* **59**, 185 (1995).
- [14] J. Skalski, S. Mizutori and W. Nazarewicz, *Nucl. Phys. A* **617**, 282 (1997).
- [15] P. Federman and S. Pittel, *Phys. Rev. C* **20**, 820 (1979).
- [16] K. Sieja, F. Nowacki, K. Langanke and G. Martınez-Pinedo, *Phys. Rev. C* **79**, 064310 (2009).
- [17] T. Togashi, Y. Tsunoda, T. Otsuka and N. Shimizu, *Phys. Rev. Lett.* **117**, 172502 (2016).
- [18] M. Honma, T. Otsuka, T. Mizusaki and M. Hjorth-Jensen, *Phys. Rev. C* **80**, 064323 (2009).
- [19] M. Honma *et al.*, *RIKEN Accel. Prog. Rep.* **45**, 35 (2012).
- [20] T. Otsuka *et al.*, *Phys. Rev. Lett.* **104**, 012501 (2010).
- [21] M. Honma, B. A. Brown, T. Mizusaki and T. Otsuka, *Nucl. Phys. A* **704**, 134 (2002).
- [22] Y. Tsunoda, T. Otsuka, N. Shimizu, M. Honma and Y. Utsuno, *Phys. Rev. C* **89**, 031301(R) (2014).
- [23] T. Otsuka and Y. Tsunoda, *J. Phys. G: Nucl. Part. Phys.* **43**, 024009 (2016).
- [24] A. de Shalit and M. Goldhaber, *Phys. Rev.* **92**, 1211 (1953).
- [25] H. A. Jahn and E. Teller, *Proc. R. Soc. A* **161**, 220 (1937).

Structure of Be and C nuclei in Monte Carlo shell model

T. Yoshida^a, N. Shimizu^a, T. Abe^b and T. Otsuka^{a, b, c, d}

^a Center for Nuclear Study, Graduate School of Science, the University of Tokyo

^b Department of Physics, the University of Tokyo

^c National Superconducting Cyclotron Laboratory, Michigan State University, USA

^d Instituut voor Kern- en Stralingsfysica, KU Leuven, Belgium

In light nuclei such as Be and C isotopes, the α cluster [1, 2] configuration can be one of the important degrees of freedom of motion. The recent *ab initio* calculations [3,4] also describe the α cluster configuration. We have expected that the Monte Carlo shell model (MCSM) also describes such kinds of motions [5]. The effect can be studied through the intrinsic density, occupation number and other observables. We have discussed the existence of α cluster structure in MCSM with the density distribution in the previous report for Be isotopes. The results show that the energies and $B(E2)$ s are in the reasonable region compared with experimental values for the model space with $N_{\text{shell}} = 6$ and $\hbar\omega = 15$ MeV. The breaking of magicity observed in experiments is discussed with occupation number. These analyses are on going combined with the intrinsic density distribution.

We extend these studies to 3α nuclei. It is an intriguing subject to see how the shell model space is related to the 3α cluster motion. As a first step, we calculate the energy levels and its convergence for ^{12}C . The formulation is the same as the previous Be studies. As for the nucleon-nucleon interaction, we apply JISP16 [6]. Here, the Coulomb interaction is added to the Hamiltonian. The center of mass motion is approximately factored out by using the Lawson's method [7]. The numerical calculations are performed on the K computer (RIKEN AICS) and FX10 (the University of Tokyo).

The extrapolation method (using energy variance [8]) is applied for the total energy. The extrapolated results are shown in Fig. 1. The extrapolation method with respect to the energy variance is performed. The reordering method [9] is also applied for the sake of efficiency and stability of fits by using quadratic curves. We notice that results are for the model space with $N_b = 150$ and $\hbar\omega = 15$ MeV. Since the estimated energy depends on the choice of the points for the fit, we use the points which have smaller energy variance sequentially starting from the leftmost point. For instance, we choose 104 and 121 points for the 0_1^+ and 0_2^+ states, respectively from the leftmost point. With these choices, the energy values are stable with respect to the fraction of the selection. In Fig. 2, the energy levels for 0^+ and 2^+ states are shown with the extrapolation methods. The size of the model space is $N_{\text{shell}} = 2, \dots, 6$.

We find that the 2_1^+ energies are around the experimental value. The 0_2^+ energy decreases as the size of the model space increases. In the present N_{shell} values, the 0_2^+ energy is around 11 MeV which is still larger than the experimental one (7.7 MeV). It is possible as the size of the model space increases, the energy gets close to the experimental value.

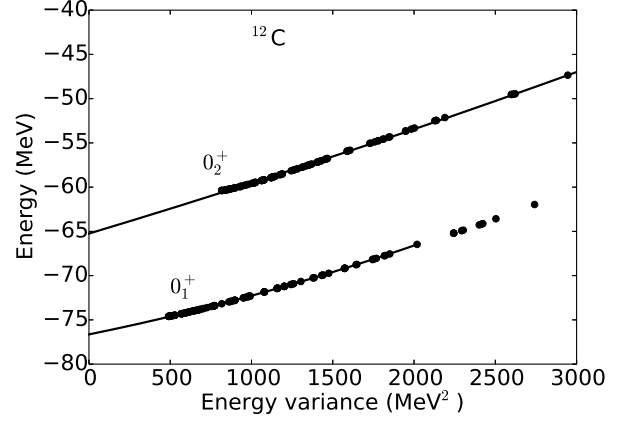


Figure 1. The energy as a function the energy variance. The dots show the calculated energy with the finite model space. The number of basis states are 150 for the point which has the smallest energy both for $0_{1,2}^+$ states.

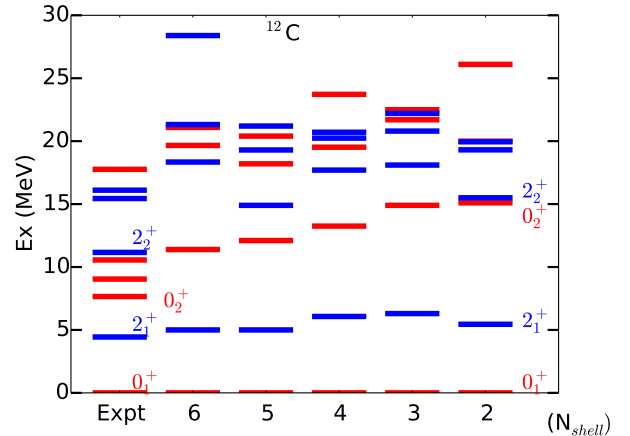


Figure 2. The 0^+ and 2^+ energy (^{12}C) spectrum for each model size. The experimental and present calculation within $N_{\text{shell}} = 6$ are compared. The effect of extrapolation with respect to the energy variance are included.

For further studies, to see the convergence with respect to the model size will be important. The third and fourth states are also shown, which are the candidates of the so-called linear chain states. However the eigen energies (around 20 MeV) are too high. The large deviations compared with the experimental results are not clear at present. More detailed study using the intrinsic density will be the next coming subject.

References

- [1] M. Ito, N. Itagaki, H. Sakurai and K. Ikeda, *Phys. Rev. Lett.* **100**, 182502 (2008).
- [2] N. Itagaki and S. Okabe, *Phys. Rev. C* **61**, 044306 (2000).
- [3] R. B. Wiringa, S. C. Pieper, J. Carlson and V. R. Pandharipande, *Phys. Rev. C* **62**, 014001 (2000).
- [4] P. Maris, J.P. Vary, A.M. Shirokov, *Phys. Rev. C* **79**, 014308 (2009); P. Maris, A.M. Shirokov, and J.P. Vary, *ibid.* **81**, 021301(R) (2010).
- [5] N. Shimizu, T. Abe, Y. Tsunoda, Y. Utsuno, T. Yoshida, T. Mizusaki, M. Honma and T. Otsuka, *Prog. Theor. Exp. Phys.* **2012**, 01A205 (2012).
- [6] A.M. Shirokov, J.P. Vary, A.I. Mazur, S.A. Zaytsev, and T.A. Weber, *Phys. Lett. B* **621**, 96 (2005).
- [7] D. Gloeckner and R. Lawson, *Phys. Lett. B* **53**, 313 (1974).
- [8] N. Shimizu, Y. Utsuno, T. Mizusaki, T. Otsuka, T. Abe, and M. Honma, *Phys. Rev. C* **82**, 061305(R) (2010).
- [9] Shimizu N, Utsuno Y, Mizusaki T, Honma M, Tsunoda Y and Otsuka T 2012, *Phys. Rev. C* **85**, 054301

Search for super and normal deformed states in nuclei around $A = 40$ using large-scale shell-model calculations

Takatoshi Ichikawa^a, Noritaka Shimizu^a, Yutaka Utsuno^{a,b}, and Takaharu Otsuka^{c,d,e}

^aCenter for Nuclear Study, the University of Tokyo, Hongo, Tokyo 113-0033, Japan

^bAdvanced Science Research Center, Japan Atomic Energy Agency, Tokai, Ibaraki 319-1195, Japan

^cDepartment of Physics, the University of Tokyo, Hongo Tokyo 113-0033, Japan

^dNational Superconducting Cyclotron Laboratory, Michigan State University, East Lansing, Michigan 48824, USA

^eInstituut voor Kern- en Stralingsfysica, Katholieke Universiteit Leuven, B-3001 Leuven, Belgium

The investigations of strongly deformed states provide a good opportunity to understand the fundamental properties of quantum many-body systems. Recently, strongly deformed states have been identified by observing γ -ray cascades typical of rotational bands in nuclei around the mass number $A = 40$ such as ^{40}Ca [1]. These states are often called the super deformed (SD) and the normal deformed (ND) states. Mainly two kinds of strongly deformed states have been identified in ^{40}Ca and ^{36}Ar [1, 2]. One is a prolately deformed state with the deformation parameter $\beta \sim 0.2$ called the four-particle-four-hole (4p-4h) state. Another is one with $\beta \sim 0.6$ called the 6p-6h state. Hereafter, we call these deformed states described by the np - mh excitations the $n\hbar\omega$ -dominant state within the sd - pf model space. These new data have triggered interest in whether such strongly deformed state exists in other nuclei around $A = 40$.

The aim of this study is to describe such deformed states using large-scale shell-model calculations. However, at the present time, the descriptions of the $8\hbar\omega$ -dominant states using the shell model are still a challenging task, even if recent computational power was considerably developed. In this study, we, therefore, focus on the $4\hbar\omega$ -dominant state. Instead, we systematically investigate possibilities for the existence of the $4\hbar\omega$ -dominant states in nuclei around $A = 40$.

Many experimental candidates for the $4\hbar\omega$ -dominant state have been suggested in nuclei around $A = 40$. Typical examples are the rotational bands at the bandhead 0^+ energies of 3.352 and 4.329 MeV in ^{40}Ca and ^{36}Ar , respectively [1, 2]. Robust rotational bands up to $J^\pi = 16^+$ build on these bandheads were observed in both ^{40}Ca and ^{36}Ar . In ^{40}Ca , the extent of deformation for the $4\hbar\omega$ -dominant state was also measured by the Doppler shift method. The value thus obtained was $\beta \sim 0.27$ [1]. Recently, the importance of triaxiality for the $4\hbar\omega$ -dominant state in ^{42}Ca has been discussed [3]. Investigations have been also performed in the neutron-rich side such as ^{38}Ar and ^{40}Ar [4, 5]. In addition, in ^{44}Ti , the $4\hbar\omega$ -dominant state has been suggested [6].

Many theoretical calculations have been attempted to reproduce these $4\hbar\omega$ -dominant deformed states. Taniguchi *et al.* have performed the anti-symmetried molecular dynamics (AMD) calculations with the generator coordinate method (GCM) for ^{40}Ca [7]. They pointed out that the $4\hbar\omega$ -dominant state is closely related to the ^{36}Ar - α cluster structure, although they largely overestimated its bandhead

0^+ energy from the experimental data in their calculations. They also showed the importance of triaxiality in ^{40}Ar [8]. Inakura *et al.* performed the cranked Hartree-Fock (HF) calculations without assuming axial symmetry, but they did not calculate energy levels [9]. Bender *et al.* performed the HF-BCS + GCM calculations [10]. Although they showed energy levels for the ND and SD bands, they assumed axial symmetry. Courier *et al.* performed the shell-model calculations and reproduced very well the energy levels and the transition strengths in ^{36}Ar and ^{40}Ca [11, 12]. However, in their calculations, they are necessary for fine-tuning the effective interaction at each system. Their calculations do not have a predictive capability for the existence of the $4\hbar\omega$ -dominant states in various systems.

In this study, we systematically investigate possibilities for the existence of the $4\hbar\omega$ -dominant states in various nuclei around $A = 40$. However, there are not the effective interactions that can describe such deformed states in a wide range of mass systems. It is thus important to construct the effective interaction having a sufficient predictive capability for those states. Then, it is desired to develop a good prescription for modifying the effective interactions already existing in the market.

A key point for describing such deformed states by the shell model is to correctly take into account 4p-4h correlations in calculations around $A = 40$. The 4p-4h correlations would play a dominant role in the emergence of the $4\hbar\omega$ -dominant states. To achieve this, we adopt a prescription proposed by Utsuno and Chiba [13], which correctly takes into account the 4p-4h correlations in the 0_2^+ state of ^{16}O . We apply this method to calculations around $A = 40$. In this prescription, we fine-tune the two-body matrix-elements (TBMEs) so as to reproduce the one-neutron separation energies for ^{41}Ca and ^{40}Ca , corresponding a shell gap for $N = 20$, and the Q values of the alpha decay for ^{44}Ti and ^{40}Ca , corresponding the 4p-4h correlations in the $f_{7/2}$ and $d_{3/2}$ orbitals.

In this study, we adopt the SDPF-M interaction as the basic interaction. The original SDPF-M interaction [14] is one of the most successful interactions to describe nuclear spectroscopic properties around the sd - and pf -shell nuclei. The experimental one-neutron separation energies of ^{41}Ca and ^{40}Ca are 8.36 and 15.6 MeV, respectively [15]. The experimental Q_α values of ^{44}Ti and ^{40}Ca are -5.13 and -7.04 MeV, respectively [15]. To reproduce these four experimental values, we use four parameters to modify the

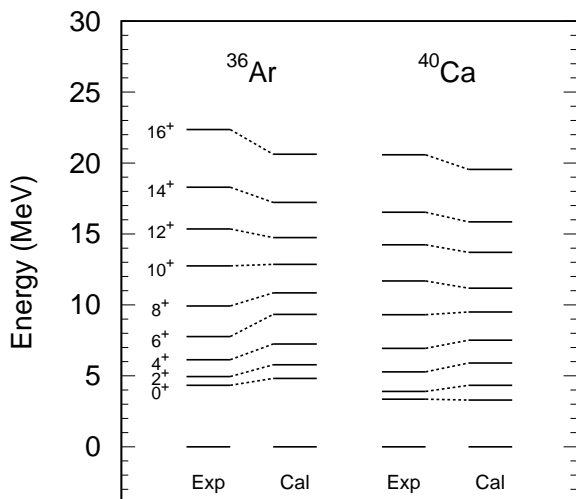


Figure 1. Calculated energy spectra of the $4\hbar\omega$ -dominant states (Cal) for ^{36}Ar , ^{38}Ar , ^{40}Ar , ^{40}Ca , ^{42}Ca , ^{44}Ti , and ^{46}Ti . In comparison, the experimental data (Exp) are also plotted. The experimental data suggested as the $4\hbar\omega$ -dominant states are taken from Refs. [1–6]

SDPF-M interaction: α and β are the scaling factors of the sd - and pf -shell TBMEs, respectively, and δ_{sd} and δ_{pf} are the shifted values of the bare single-particle energies belonging to the sd and pf shells, respectively. We perform shell-model calculations with the truncation allowing up to the $6\hbar\omega$ excitations and determine α , β , δ_{sd} , and δ_{pf} using the Newton-Raphson method. The obtained values are $\alpha = 0.956$, $\beta = 1.59$, $\delta_{sd} = -0.434$ MeV, and $\delta_{pf} = -0.0393$ MeV. From now on, this modified SDPF-M interaction is called the SDPF-M' interaction.

Using the modified effective interaction, we systematically calculate the $4\hbar\omega$ -dominant states in nuclei around $A = 40$. To systematically investigate those, we carry out all calculations with the truncation allowing up to the $6\hbar\omega$ excitation. Within this truncation, the maximum M scheme dimension is about 5.0×10^9 for ^{46}Ti . All calculations are carried out with the KSHELL code [16].

We here show the energy spectra of the obtained $4\hbar\omega$ -dominant states for ^{36}Ar and ^{40}Ca . In these nuclei, the experimental data suggested as the $4\hbar\omega$ -dominant states are available [1, 2]. In our calculations, the $4\hbar\omega$ -dominant states are identified by the fraction of the wave function for each $n\hbar\omega$ configuration. The band members are assigned by checking strong $E2$ transitions between the obtained states. Figure 1 shows the energy spectra of the $4\hbar\omega$ -dominant states thus obtained. We see that the bandhead 0^+ energies of the obtained $4\hbar\omega$ -dominant states are in good agreement with the experimental data. Interestingly, the bandhead 0^+ energies decrease with increasing proton and neutron numbers. Using this effective interaction, we will investigate other physical quantities such as the $E2$ transition. Such investigations are now in progress.

References

- [1] E. Ideguchi *et al.*, Phys. Rev. Lett. **87**, 222501 (2001).
- [2] C.E. Svensson *et al.*, Phys. Rev. Lett. **85**, 2693 (2000).
- [3] K. Hadyńska-Klęk *et al.*, Phys. Rev. Lett. **117**, 062501 (2016).
- [4] D. Rudolph *et al.*, Phys. Rev. C **65**, 034305 (2002).
- [5] E. Ideguchi *et al.*, Phys. Lett. **686**, 18 (2010).
- [6] C.D. O'Leary, M.A. Bentley, B.A. Brown, D.E. Appelbe, R.A. Bark, D.M. Cullen, S. Ertürk, A. Maj, and A.C. Merchant, Phys. Rev. C **61**, 064314 (2000).
- [7] Y. Taniguchi, M. Kimura, Y. Kanada-En'yo, and H. Horiuchi, Phys. Rev. C **76**, 044317 (2007).
- [8] Y. Taniguchi, Y. Kanada-En'yo, M. Kimura, K. Ikeda, H. Horiuchi, and E. Ideguchi, Phys. Rev. C **82**, 011302(R) (2010).
- [9] T. Inakura, S. Mizutori, M. Yamagami, and K. Matsuyanagi, Nucl. Phys. **A710**, 261 (2002).
- [10] M. Bender, H. Flocard, and P.-H. Heenen, Phys. Rev. C **68** 044321 (2003).
- [11] E. Caurier, F. Nowacki, and A. Poves, Phys. Rev. Lett. **95**, 042502 (2005).
- [12] E. Caurier, J. Menéndez, F. Nowacki, and A. Poves, Phys. Rev. C **75**, 054317 (2007).
- [13] Y. Utsuno and S. Chiba, Phys. Rev. C **83**, 021301 (2011).
- [14] Y. Utsuno, T. Otsuka, T. Mizusaki, and M. Honma, Phys. Rev. C **60**, 054315 (1999).
- [15] The experimental data are taken from National Nuclear Data Center (NNDC), "<http://www.nndc.bnl.gov>".
- [16] N. Shimizu, arXiv:1310.5431.

Recent progress in the calculation of exotic nuclei based on nuclear force

N. Tsunoda, T. Otsuka^{a,b,c,d} and N. Shimizu

Center for Nuclear Study, Graduate School of Science, University of Tokyo, 7-3-1, Hongo, Bunkyo-ku, Tokyo, Japan

^a*Department of Physics, University of Tokyo, 7-3-1, Hongo, Bunkyo-ku, Tokyo, Japan*

^b*RIKEN Nishina Center, 2-1 Hirosawa, Wako, Saitama 351-0198, Japan*

^c*National Superconducting Cyclotron Laboratory, Michigan State University, East Lansing, Michigan 48824, USA*

^d*Instituut voor Kernenergie Stralingsfysica, Katholieke Universiteit Leuven, B-3001 Leuven, Belgium*

One of the major goals on nuclear physics is to describe the properties of the nuclei starting from nucleon-nucleon degrees of freedom. Extensive studies are being developed on ab-initio calculations mostly on light mass nuclei, closed shell nuclei and their neighbors. Developments on computational resources help to accelerate those studies. On the other hand, experimental techniques and accelerators are also developing rapidly and make exotic nuclei the frontiers of nuclear physics.

Our attempt here is to describe such exotic nuclei starting from nuclear force as possible as we can. Then, we study the microscopic derivation of effective interaction for the shell model and combined it to large-scale shell-model calculations to access neutron-rich nuclei. In the recent several years, we have studied in this way the physics in so-called “island of inversion”. Since we describe excitation across the $N = 20$ shell gap, it is apparent that we need to include $(sd + pf)$ -shell as the model space, at least. One of the standard approach of deriving effective interactions is called Kuo-Kurenciglowa (KK) method, which is based on many-body perturbation theory. However, this method restricts ourselves to a single major shell, because of the inevitable divergences built in the theory itself [1]. Then we developed extended KK (EKK) method, avoiding these divergences by re-summing the perturbative series in a sophisticated way [2]. Utilizing EKK method, we have succeeded in describing the breaking and restoration of $N = 20$ shell gaps in Ne, Mg and Si isotopes and reproducing experimental observations of 2^+ and 4^+ energies. Comparing to previous works on the “island of inversion”, our method has an advantage in prediction powers, especially on the area where only few experimental data are obtained, because we start from nuclear force without the empirical correction [3]. We have done some experimental collaboration as well [4, 5].

As a next step of this line of study, we focused on the physics of $N = 28, 32, 34$ and 40 magic numbers. It is known that $N = 28, 32$ and 34 magic numbers are well observed in Ca isotopes and the evolution of those shell structure along proton numbers (i.e. Ti, Cr, Fe and Ni isotopes) are of great interest. To describe evolution of those shell structures, it is necessary to incorporate the model space with higher shells, in this case, $(pf + sdg)$ shell at least. The number of two body matrix elements (TBMEs) is so huge in this model space that we needed to develop our computational techniques for the high-performance parallel computing.

In this report, we discuss on the computational progress of the EKK method and its preliminary application to $(pf + sdg)$ -shell nuclei.

First, let us briefly explain EKK method. Using EKK method, we renormalize nuclear force to a restricted model space (P-space), specified by the projection operator P and $Q = 1 - P$. Effective interaction for the shell model is expressed by the following equation,

$$H_{\text{eff}} = H_{\text{BH}}(\xi) + \sum_{k=1}^{\infty} \frac{1}{k!} \frac{d^k \hat{Q}(\xi)}{d\xi^k} \{H_{\text{eff}} - \xi\}^k, \quad (1)$$

where H_{eff} is effective interaction, H_{BH} is so-called Bloch-Holowitz Hamiltonian, \hat{Q} is \hat{Q} -box. The operator \hat{Q} -box is defined as

$$\hat{Q}(\xi) = PVP + PVQ \frac{1}{\xi - QH_0Q} QVP, \quad (2)$$

where H_0 is unperturbed Hamiltonian and V is its perturbation. Note that in Eq. (1) ξ is an arbitrary parameter which determines the origin of Taylor-series like equation and therefore the final results is not affected by the choice of ξ .

The most expensive part is evaluation of the \hat{Q} -box in Eq. (2). The \hat{Q} -box is evaluated by diagrammatic perturbative expansion, for most cases, up to third order in the interaction V . Figure. 1 shows the second order diagrams of

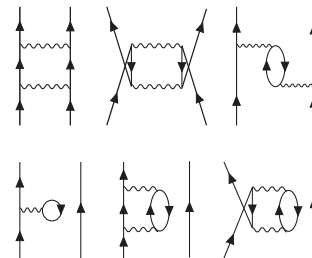


Figure 1. Diagrams included in \hat{Q} -box of the second order.

\hat{Q} -box. In third order, the number of diagrams is about 70. For each TBME, we need to calculate all the diagrams one by one. Then we extend the computational code for MPI parallel computation. All the TBMEs and diagrams are distributed to different nodes, and each of them is calculated with openMP parallelization.

Figure. 2 shows the efficiency of the parallel computing. The test calculation is done with model space of $(sd + pf)$ -shell and in Fig. 2(a) only proton-proton channels are calculated and in Fig. 2(b) all the channels are calculated. In this

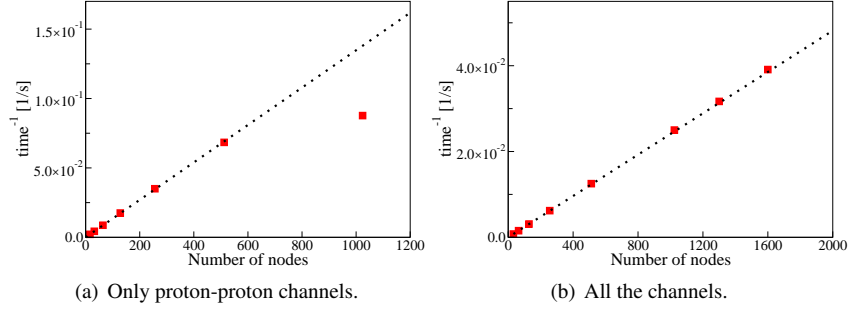


Figure 2. Efficiency of parallel computation via EKK code.

model space, number of TBMEs are 376 for proton-proton channels and in total 2116. We can see that the sufficient parallel efficiency is obtained with the number of nodes which is equals to or slightly greater than the number of TBMEs.

Finally, we would like to discuss about the recent application of this EKK method with large-scale computations. We have calculated the effective interactions in $(pf + sdg)$ -shell, whose number of TBMEs is 6380 in total. Since number of hole states is also larger than $(sd + pf)$ -shell case, the calculation requires much larger computational resources than the previous case. Therefore, we start from a preliminary calculation.

We start from χN^3LO interaction and short-range repulsion is removed by using its V_{lowk} interaction with cutoff $\Lambda = 2.0 \text{ fm}^{-1}$. Based on this V_{lowk} interaction we derived the effective interaction for the shell model interaction via EKK method. Then, Fujita-Miyazawa three-body force is added as effective twobody interaction by integrating out the degrees of freedom of third particle as hole state of ^{40}Ca core. Here we restrict ourselves to 13 major shells as $(P+Q)$ space in this case and the single particle energies are also modified. We will adopt larger Q -space in the near future which is possible via parallelized EKK code discussed before and large-scale computational resources. Since the shell model calculation also needs huge computational resources, we present the calculations with truncated model space.

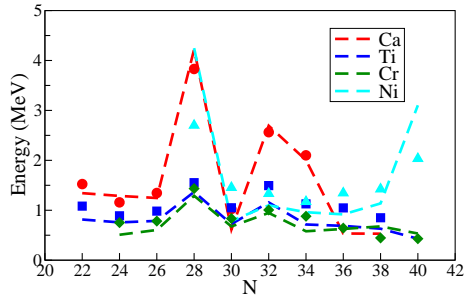


Figure 3. Excitation energies of first 2^+ states of even-even Ca, Ti, Cr and Ni isotopes. The model space of shell model calculation is $(pf + sdg)$ -shell and at most 4p4h excitation beyond $N = 40$ shell gap is taken into account, with some truncation.

Figure 3 shows energies of first 2^+ states on even-even Ca, Ti, Cr and Ni isotopes. The model space of shell model calculation is $(pf + sdg)$ -shell and at most 4p4h excitation beyond $N = 40$ shell gap is taken into account, with some truncation. Maximum dimension of M -scheme basis is about 10^{10} . The calculation reproduces experimental E_{2^+} values overall, where E_{2^+} values of neutron-rich Ti isotopes are too small and these are too large in ^{56}Ni and ^{68}Ni for example. As we discussed before, there are several points to be improved in the derivation of the effective interaction, but we consider that this preliminary result promises us a good description of these nuclei starting from realistic nuclear force in the future.

In summary, we implemented a new computational code of EKK method for MPI+openMPI parallel computation. The test calculation shows satisfactory strong scaling. Then we presented the preliminary results for $(pf + sdg)$ -shell nuclei, which shows good agreement to experimental data overall with some small discrepancies. We expect that this study for $(pf + sdg)$ -shell nuclei will be promising.

The Lanczos shell-model calculation is performed with the code “ KSHELL ” [6]. This work was supported in part by Grants-in-Aid for Scientific Research (23244049,15K05090). It was supported in part by HPCI Strategic Program (hp140210, hp150224, hp160221), in part by MEXT and JICFuS as a priority issue (Elucidation of the fundamental laws and evolution of the universe) to be tackled by using Post ‘K’ Computer, and also by CNS-RIKEN joint project for large-scale nuclear structure calculations.

References

- [1] T. Kuo, E. Osnes, Lecture Notes in Physics, **364**, 1 170 (1990).
- [2] N. Tsunoda, K. Takayanagi, M. Hjorth-Jensen, T. Otsuka, Phys. Rev. C **89**, 024313 (2014).
- [3] N. Tsunoda, T. Otsuka, N. Shimizu, M. Hjorth-Jensen, K. Takayanagi, and T. Suzuki, Phys. Rev. C **95**, 021304 (2017).
- [4] H. Nishibata et al., submitted to Phys. Rev. C. (2018)
- [5] B. Fernandez-Domnguez et al., Phys. Lett. B **779**, 124 (2018).
- [6] N. Shimizu, arXiv:1310.5431v1 [nucl-th] (2013)

Other Activities

The 15th CNS International Summer School CNSSS16

N. Imai, T. Gunji, E. Hiyama^a, H. Liang^a, S. Michimasa, Y. Mizoi^b, S. Ota, T. Otsuka, H. Sakai^a, H. Sakurai^{a,c}, N. Shimizu, S. Shimoura, H. Ueno^a, T. Uesaka^a, Y. Utsuno^d, K. Yako, H. Yamaguchi, and T. Yoshida

Center for Nuclear Study, Graduate School of Science, University of Tokyo

^a*RIKEN Nishina Center*

^b*Faculty of Engineering, Osaka Electro-Communication University*

^c*Department of Physics, Univ. of Tokyo*

^d*Advanced Science Research Center, Japan Atomic Energy Agency*

The 15th CNS International Summer School (CNSSS16) was hosted by Center for Nuclear Study (CNS) from 24th to 30th in August, 2016. The school was supported by RIKEN Nishina Center and Asian Nuclear Physics Association (ANPhA). The venue was the Nishina hall in the Wako campus of RIKEN.

The summer school was the fifteenth one in the series which aimed at providing graduate students and postdocs with basic knowledge and perspectives of nuclear physics. It consisted of lectures by leading scientists in the fields of both experimental and theoretical nuclear physics. Each lecture started with an introductory talk from the fundamental point of view and ended with up-to-date topics in the relevant field.

The list of the lecturers and the title of lectures are following:

- Prof. Martin Freer (Birmingham, UK) “Clustering in Nuclei”
- Prof. Ulli Koester (Institute of Laue Langevin, France) “Production and applications of radioactive isotopes”
- Prof. Y.Z. Qian (Minnesota Univ. USA) “Overview of stellar evolution and nucleosynthesis”
- Prof. Masayuki Yamagami (Aizu, Japan) “Shape and independent particle motion in nuclei: the basic ideas from microscopic collective models”
- Dr. Kenta Itahashi (RIKEN, Japan) “Mesic atoms and mesic nuclei –Introducing to meson-nuclear bound system–”
- Dr. Daisuke Suzuki (RIKEN, Japan) “Missing mass spectroscopy with radioactive isotope beam”
- Dr. Kotaro Kyutoku (iTHES, RIKEN, Japan) “Gravitational-wave astronomy and prospects of its application to nuclear physics”
- Prof. Yasuhiro Sakemi (CNS, Japan) “CP violation in elementary particles and composite systems”

Eight lecturers and ninety-one participants joined the school from seven countries. Three lectures and seventeen participants came from foreign institutes. The time of each class was 50 minutes. There was 10 minutes break between



Figure 1. A group photos of the participants of CNSSS16 with the lecturers.

the class to encourage the participants to communicate the lecturers. They talked each other in free discussion times such as breaks, lunch times, welcome and poster session in a relaxed atmosphere. Figure 1 presents a group photo of all the participants with the lecturers.

There were four “Young Scientist Session”, where twenty-three oral presentations and fourteen poster presentations were given by graduate students and postdocs.

Because the web server which stores all information about the summer school was broken, some information is planned to move to a new web site soon.

The organizers appreciate Nishina Center for providing the venue as well as the accommodations. We are grateful to supports from ANPhA. We thank administration staffs of the CNS for their helpful supports. We also thank graduate students and postdocs in the CNS for their dedicated efforts. Finally we acknowledge all the lectures and participants for their contributions to the CNSSS16.

References

- [1] H. Shinomiya and T. Matsuo, Phys. Rev. C 84, 044317 (2011).
- [2] K. Wimmer et al, Phys. Rev. Lett., 105, 252501(2011).
- [3] H. Chatbi, M. Vergnat and G. Marchal, Applied physics letters 64, 1210 (1994)
- [4] <http://www.srim.org/>.

- [5] W. M. Arnold Bik and F.H.P.M. Habraken, Reports on Progress in Physics 56, 859 (1993).

Laboratory Exercise for Undergraduate Students

S. Ota, M. Niikura^a, N. Kitamura, T. Saito^a, K. Yako, H. Sakurai^{a,b} and S. Shimoura

Center for Nuclear Study, Graduate School of Science, University of Tokyo

^a*Department of Physics, University of Tokyo*

^b*RIKEN Nishina Center*

Nuclear scattering experiments were performed as a laboratory exercise for undergraduate students of the University of Tokyo. This program was aiming at providing undergraduate students with an opportunity to learn how to study subatomic physics by using an ion beam from an accelerator. In 2015, 31 students attended this program.

The four beam times were scheduled in the second semester for third-year students, and 8 students participated in each beam time. The experiments were performed at the RIBF using a 26-MeV alpha beam accelerated by the AVF cyclotron. The alpha beam extracted from the AVF cyclotron was transported to the E7B beam line in the E7 experimental hall. The scattering chamber has two separate target ports which enable us to perform two independent experiments without opening the chamber during the beam time. In each beam time, the students were divided into two groups and took one of the following two subjects:

- (1) Measurement of elastic scattering of incident alpha particle with ^{197}Au , to learn how to determine nuclear size.
- (2) Measurement of gamma rays emitted from the cascade decay of highly excited ^{154}Gd and ^{184}Os , to learn the nuclear deformation.

Before the experiment, the students took a course on the basic handling of the semiconductor detectors and electronic circuits at the Hongo campus, and attended a radiation safety lecture at RIKEN. They also joined a tour to the RI beam factory at RIKEN.

In the $\alpha+^{197}\text{Au}$ measurement, α particles scattered with the Au target with a thickness of $1\ \mu\text{m}$ were detected using a silicon PIN-diode located 15-cm away from the target. A collimator with a diameter of 6 mm was attached on the silicon detector. The energy spectrum of the scattered α particles was recorded by a multi-channel analyzer (MCA) system. The beam was stopped by a Faraday cup located downstream of the scattering chamber. The cross section for the alpha elastic scattering was measured in the angular range of $\theta_{\text{lab}} = 20-150^\circ$.

The measured cross section was compared with the calculated cross section of the Rutherford scattering. The cross section was also analyzed by the potential model calculation, and the radius of the ^{197}Au nucleus was discussed. Some students obtained the radius of $\sim 10\ \text{fm}$ by using a classical model where the trajectory of the α particle in the nuclear potential is obtained using the Runge-Kutta method. Others tried to understand the scattering process by calculating the angular distribution using the distorted wave Born approximation method with a Coulomb wave function and

a realistic nuclear potential.

In the measurement of gamma rays, excited states in ^{154}Gd and ^{184}Os nuclei were populated by the $^{152}\text{Sm}(\alpha,2n)$ and $^{182}\text{W}(\alpha,2n)$ reactions, respectively. The gamma rays emitted from the cascade decay of the rotational bands were measured by a high-purity germanium detector located 30-cm away from the target. The energy of the gamma ray were recorded by the MCA system. The gain and the efficiency of the detector system had been calibrated using standard gamma-ray sources of ^{22}Na , ^{60}Co , ^{133}Ba , and ^{137}Cs . The gamma rays from the 10^+ and 8^+ states in ^{154}Gd and ^{184}Os , respectively, were successfully identified. Based on the energies of the gamma rays, the moment of inertia and the deformation parameters of the excited states were discussed by using a classical rigid rotor model and a irrotational fluid model. The students found that the reality lies between the two extreme models. The initial population among the levels in the rotational band was also discussed by taking the effect of the internal conversion into account.

It was the first time for most of the students to use large experimental equipments. They learned basic things about the experimental nuclear physics and how to extract physics from the data. We believe this program was very impressive for the students. The authors would like to thank Dr. Y. Uwamino, the CNS accelerator group, and the RIBF cyclotron crew for their helpful effort in the present program.

Appendices

**Symposium, Workshop, Seminar, PAC and
External Review**

CNS Reports

Publication List

Talks and Presentations

Personnel

Symposium, Workshop, Seminar, Colloquium, and PAC

A. Symposium and Workshop

- (1) The second SEA workshop on Low Energy Nuclear Physics (SEA2016)
Jun. 26 – 28, 2016, Center for Nuclear Study, the University of Tokyo, RIKEN
- (2) Mini workshop in the framework of JSPS-FWO collaboration
Nov. 29, 2016, the University of Tokyo, Hongo, Japan
- (3) 仁科記念講演会「ニホニウム発見」
Dec. 5, 2016, the University of Tokyo, Hongo, Japan

B. CNS Seminar

- (1) Takashi Inoue (Nihon U.): “Nuclear force from QCD on lattice and its application”, Feb. 8, 2017, the University of Tokyo, Hongo, Japan

C. Program Advisory Committee for Nuclear-Physics Experiments at RI Beam Factory

- (1) The 17th NP-PAC meeting
Date: December 1-3, 2016
Place: RIBF Conference Hall on the 2nd floor of the RIBF Building

CNS Reports

#95 “CNS Annual Report 2015”

Edited by T. Gunji, and Y. Kishi March, 2017

Publication List

A. Original Papers

- (1) S. Hayakawa, S. Kubono, D. Kahl, H. Yamaguchi, D.N. Binh, T. Hashimoto, Y. Wakabayashi, J.J. He, N. Iwasa, S. Kato, T. Komatsubara, Y.K. Kwon, T. Teranishi: “First direct measurement of the $^{11}\text{C}(\alpha, p)^{14}\text{N}$ stellar reaction by an extended thick-target method”, *Physical Review C* **93**, 065802 (2016).
- (2) H. Yamaguchi, D. Kahl, S. Hayakawa, Y. Sakaguchi, K. Abe, T. Nakao, T. Suhara, N. Iwasa, A. Kim, D.H. Kim, S.M. Cha, M.S. Kwag, J.H. Lee, E.J. Lee, K.Y. Chae, Y. Wakabayashi, N. Imai, N. Kitamura, P. Lee, J.Y. Moon, K.B. Lee, C. Akers, H.S. Jung, N.N. Duy, L.H. Khiem, and C.S. Lee: “Experimental investigation of linear-chain structured nucleus in ^{14}C ”, *Physics Letters B* **766**,11 (2017).
- (3) L. Yang, C.J. Lin, H.M. Jia, D.X. Wang, L.J. Sun, N.R. Ma, F. Yang, Z.D. Wu, X.X. Xu, H.Q. Zhang, Z.H. Liu, and P.F. Bao: “Optical model potentials for $^6\text{He}+^{64}\text{Zn}$ from $^{63}\text{Cu}(^7\text{Li}, ^6\text{He})^{64}\text{Zn}$ reactions”, *Physical Review C* **95**, 034616 (2017).
- (4) R. G. Pizzone, G. D’Agata, M. La Cognata, I. Indelicato, C. Spitaleri, S. Blagus, S. Cherubini, P. Figuera, L. Grassi, G. L. Guardo, M. Gulino, S. Hayakawa, R. Kshetri, L. Lamia, M. Lattuada, T. Mijatovic, M. Milin, D.H. Miljanic D., L. Prepolec, G. G. Rapisarda, S. Romano, M. L. Sergi, N. Skukan, N. Soic, V. Tokic, A. Tumino, and M. Uroic: “First Measurement of the $^{19}\text{F}(\alpha, p)^{22}\text{Ne}$ Reaction at Energies of Astrophysical Relevance”. *Astrophysical Journal*, **836**, 57 (2017).
- (5) O. Beliuskina, A.O. Strelakovsky, A.A. Aleksandrov, I.A. Aleksandrova, H.M. Devaraja, C. Heinz, S. Heinz, S. Hofmann, S. Ilich, N. Imai, D.V. Kamanin, M. Kis, G.N. Knyazheva, C. Kozuharov, E.A. Kuznetsova, J. Maurer, G.V. Mishinsky, M. Pomorski, Yu.V. Pyatkov, O.V. Strelakovsky, M. Trager and V.E. Zhuchk: “Pulse-height defect in single-crystal CVD diamond detectors”, *Eur. Phys. J. A* **53**, 32 (2017).
- (6) M. Klintefjord, K. Hadynska-Klek, A. Gorgen, C. Bauer, F.L. Bello Garrote, S. Bonig, B. Bounthong, A. Damyanova, J.P. Delaroche, V. Fedosseev, D.A. Fink, F. Giacoppo, M. Girod, P. Hoff, N. Imai, W. Korten, A.C. Larsen, J. Libert, R. Lutter, B.A. Marsh, P.L. Molkanov, H. Naidja, P. Napiorkowski, F. Nowacki, J. Pakarinen, E. Rapisarda, P. Reiter, T. Renstrom, S. Rothe, M.D. Seliverstov, B. Siebeck, S. Siem, J. Srebrny, T. Stora, P. Thole, T.G. Tornyi, G.M. Tveten, P. Van Duppen, M.J. Vermeulen, D. Voulot, N. Warr, F. Wenander, H.De Witte, M. Zielinska: “Structure of low-lying states in ^{140}Sm studied by Coulomb excitation”, *Phys. Rev. C* **93**, 054303 (2016).
- (7) J. Lee, H. Liu, P. Doornenbal, M. Kimura, K. Minomo, K. Ogata, Y. Utsuno, N. Aoi, K. Li, M. Matsushita, H. Scheit, D. Steppenbeck, S. Takeuchi, H. Wang, H. Baba, E. Ideguchi, N. Kobayashi, Y. Kondo, S. Michimasa, T. Motobayashi, H. Sakurai, M. Takechi, and Y. Togano: “ Asymmetry dependence of reduction factors from single-nucleon knockout of ^{30}Ne at 230 MeV/nucleon ”, *Progress of Theoretical and Experimental Physics* 2016, 083D01 (2016).
- (8) C. Babcock, H. Heylen, M. L. Bissell, K. Blaum, P. Campbell, B. Cheal, D. Fedorov, R. F. Garcia Ruiz, W. Geithner, W. Gins, T. Day Goodacre, L.K. Grob, M. Kowalska, S. M. Lenzi, B. Maass, S. Malbrunot-Ettenauer, B. Marsh, R. Neugart, G. Neyens, W. Nrtershuser, T. Otsuka, R. Rossel, S. Rothe, R. Snchez, Y. Tsunoda, C. Wraith, L. Xie, and X. F. Yang: “ Quadrupole moments of odd-A $^{53-63}\text{Mn}$: Onset of collectivity towards N=40 ”, *Physics Letters B* **760**, 387 (2016).
- (9) H. Heylen, M. De Rydt, G. Neyens, M. L. Bissell, L. Caceres, R. Chevrier, J. M. Daugas, Y. Ichikawa, Y. Ishibashi, O. Kamalou, T. J. Mertzimekis, P. Morel, J. Papuga, A. Poves, M. M. Rajabali, C. Stdel, J. C. Thomas, H. Ueno, Y. Utsuno, N. Yoshida, and A. Yoshimi: “ High-precision quadrupole moment reveals significant intruder component in $^{33}_{13}\text{Al}_{20}$ ground state ”, *Physical Review C* **94**, 034312 (2016).
- (10) T. Togashi, Y. Tsunoda, T. Otsuka, and N. Shimizu: “ Quantum Phase Transition in the Shape of Zr isotopes ”, *Physical Review Letters* **117**, 172502 (2016).
- (11) C. Kremer, S. Aslanidou, S. Bassauer, M. Hilcker, A. Krugmann, P. von Neumann-Cosel, T. Otsuka, N. Pietralla, V. Yu. Ponomarev, N. Shimizu, M. Singer, G. Steinhilber, T. Togashi, Y. Tsunoda, V. Werner, and M. Zweidinger: “ First Measurement of Collectivity of Coexisting Shapes Based on Type II Shell Evolution: The Case of ^{96}Zr ”, *Physical Review Letters* **117**, 172503 (2016).

- (12) H. Heylen, C. Babcock, R. Beerwerth, J. Billowes, M. L. Bissell, K. Blaum, J. Bonnard, P. Campbell, B. Cheal, T. Day Goodacre, D. Fedorov, S. Fritzsche, R. F. Garcia Ruiz, W. Geithner, Ch. Geppert, W. Gins, L. K. Grob, M. Kowalska, K. Kreim, S. M. Lenzi, I. D. Moore, B. Maass, S. Malbrunot-Ettenauer, B. Marsh, R. Neugart, G. Neyens, W. Nrtershuser, T. Otsuka, J. Papuga, R. Rossel, S. Rothe, R. Snchez, Y. Tsunoda, C. Wraith, L. Xie, X. F. Yang, and D. T. Yordanov: “ Changes in nuclear structure along the Mn isotopic chain studied via charge radii ”, *Physical Review C* **94**, 054321 (2016).
- (13) A. I. Morales, G. Benzoni, H. Watanabe, Y. Tsunoda, T. Otsuka, S. Nishimura, F. Browne, R. Daido, P. Doornenbal, Y. Fang, G. Lorusso, Z. Patel, S. Rice, L. Sinclair, P.-A. Sderstrm, T. Sumikama, J. Wu, Z. Y. Xu, A. Yagi, R. Yokoyama, H. Baba, R. Avigo, F. L. Bello Garrote, N. Blasi, A. Bracco, F. Camera, S. Ceruti, F. C. L. Crespi, G. de Angelis, M.-C. Delattre, Zs. Dombradi, A. Gottardo, T. Isobe, I. Kojouharov, N. Kurz, I. Kuti, K. Matsui, B. Melon, D. Mengoni, T. Miyazaki, V. Modamio-Hoybjor, S. Momiyama, D.R. Napoli, M. Niikura, R. Orlandi, H. Sakurai, E. Sahin, D. Sohler, H. Schaffner, R. Taniuchi, J. Taprogge, Zs. Vajta, J. J. Valiente-Dobon, O. Wieland, and M. Yalcinkaya: “ Type II shell evolution in $A=70$ isobars from the $N \geq 40$ island of inversion ”, *Physics Letters B* **765**, 328 (2017).
- (14) N. Paul, A. Corsi, A. Obertelli, P. Doornenbal, G. Authelet, H. Baba, B. Bally, M. Bender, D. Calvet, F. Chteau, S. Chen, J.-P. Delaroche, A. Delbart, J.-M. Gheller, A. Giganon, A. Gillibert, M. Girod, P.-H. Heenen, V. Lapoux, J. Libert, T. Motobayashi, M. Niikura, T. Otsuka, T. R. Rodrguez, J.-Y. Rouss, H. Sakurai, C. Santamaria, N. Shimizu, D. Steppenbeck, R. Taniuchi, T. Togashi, Y. Tsunoda, T. Uesaka, T. Ando, T. Arici, A. Blazhev, F. Browne, A. M. Bruce, R. Caroll, L. X. Chung, M.L. Corts, M. Dewald, B. Ding, F. Flavigny, S. Franchoo, M. Grska, A. Gottardo, A. Jungclaus, J. Lee, M. Lettmann, B. D. Linh, J. Liu, Z. Liu, C. Lizarazo, S. Momiyama, K. Moschner, S. Nagamine, N. Nakatsuka, C. Nita, C. R. Nobs, L. Olivier, Z. Patel, Z. Podolyk, M. Rudigier, T. Saito, C. Shand, P.-A. Sderstrm, I. Stefan, R. Orlandi, V. Vaquero, V. Werner, K. Wimmer, and Z. Xu: “ Are There Signatures of Harmonic Oscillator Shells Far from Stability? First Spectroscopy of ^{110}Zr ”, *Physical Review Letters* **118**, 032501 (2017).
- (15) N. Tsunoda, T. Otsuka, N. Shimizu, M. Hjorth-Jensen, K. Takayanagi, and T. Suzuki: “ Exotic neutron-rich medium-mass nuclei with realistic nuclear forces ”, *Physical Review C* **95**, 021304(R) (2017).
- (16) V. Tripathi, R. S. Lubna, B. Abromeit, H. L. Crawford, S. N. Liddick, Y. Utsuno, P. C. Bender, B. P. Crider, R. Dungan, P. Fallon, K. Kravvaris, N. Larson, A. O. Macchiavelli, T. Otsuka, C. J. Prokop, A. L. Richard, N. Shimizu, S. L. Tabor, A. Volya, and S. Yoshida: “ β decay of $^{38,40}\text{Si}$ ($T_z=+5,+6$) to low-lying core excited states in odd-odd $^{38,40}\text{P}$ isotopes ”, *Physical Review C* **95**, 024308 (2017).
- (17) H.N. Liu, J. Lee, P. Doornenbal, H. Scheit, S. Takeuchi, N. Aoi, K.A. Li, M. Matsushita, D. Steppenbeck, H. Wang, H. Baba, E. Ideguchi, N. Kobayashi, Y. Kondo, G. Lee, S. Michimasa, T. Motobayashi, A. Poves, H. Sakurai, M. Takechi, Y. Togano, J.A. Tostevin, and Y. Utsuno: “ Intruder configurations in the ground state of ^{30}Ne ”, *Physics Letters B* **767**, 58 (2017).
- (18) He Wang, Hideaki Otsu, Hiroyoshi Sakurai, DeukSoon Ahn, Masayuki Aikawa, Takashi Ando, Shouhei Araki, Sidong Chen, Nobuyuki Chiga, Pieter Doornenbal, Naoki Fukuda, Tadaaki Isobe, Shunsuke Kawakami, Shoichiro Kawase, Tadahiro Kin, Yosuke Kondo, Shunpei Koyama, Shigeru Kubono, Yukie Maeda, Ayano Makinaga, Masafumi Matsushita, Teiichiro Matsuzaki, Shin'ichi Michimasa, Satoru Momiyama, Shunsuke Nagamine, Takashi Nakamura, Keita Nakano, Megumi Niikura, Tomoyuki Ozaki, Atsumi Saito, Takeshi Saito, Yoshiaki Shiga, Mizuki Shikata, Yohei Shimizu, Susumu Shimoura, Toshiyuki Sumikama, Par-Anders Soderstrom, Hiroshi Suzuki, Hiroyuki Takeda, Satoshi Takeuchi, Ryo Taniuchi, Yasuhiro Togano, Junichi Tsubota, Meiko Uesaka, Yasushi Watanabe, Yukinobu Watanabe, Kathrin Wimmer, Tatsuya Yamamoto, Koichi Yoshida: “Spallation reaction study for the long-lived fission product ^{107}Pd ”, *Prog. Theor. Exp. Phys.* 2017, 021D01 (2017).
- (19) P. Doornenbal, H. Scheit, S. Takeuchi, N. Aoi, K. Li, M. Matsushita, D. Steppenbeck, H. Wang, H. Baba, E. Ideguchi, N. Kobayashi, Y. Kondo, J. Lee, S. Michimasa, T. Motobayashi, A. Poves, H. Sakurai, M. Takechi, Y. Togano, K. Yoneda: “Mapping the deformation in the island of inversion: Inelastic scattering of ^{30}Ne and ^{36}Mg at intermediate energies”, *Phys. Rev. C* **93**, 044306 (2016).
- (20) D.Q. Fang, Y.G. Ma, X.Y. Sun, P. Zhou, Y. Togano, N. Aoi, H. Baba, X.Z. Cai, X.G. Cao, J.G. Chen, Y. Fu, W. Guo, Y. Hara, T. Honda, Z.G. Hu, K. Ieki, Y. Ishibashi, Y. Ito, N. Iwasa, S. Kanno, T. Kawabata, H. Kimura, Y. Kondo, K. Kurita, M. Kurokawa, T. Moriguchi, H. Murakami, H. Ooishi, K. Okada, S. Ota, A. Ozawa, H. Sakurai, S. Shimoura, R. Shioda, E. Takeshita, S. Takeuchi, W.D. Tian, H.W. Wang, J.S. Wang, M. Wang, K. Yamada, Y. Yamada, Y. Yasuda, K. Yoneda, G.Q. Zhang, T. Motobayashi: “Proton-proton correlations in distinguishing the two-proton emission mechanism of ^{23}Al and ^{22}Mg ”, *Phys. Rev. C* **94**, 044621 (2016).

- (21) H. Wang, N. Aoi, S. Takeuchi, M. Matsushita, T. Motobayashi, D. Steppenbeck, K. Yoneda, H. Baba, Zs. Dombradi, K. Kobayashi, Y. Kondo, J. Lee, H. Liu, R. Minakata, D. Nishimura, H. Otsu, H. Sakurai, D. Sohler, Y. Sun, Z. Tian, R. Tanaka, Zs. Vajta, Z. Yang, T. Yamamoto, Y. Ye, R. Yokoyama: “First spectroscopic information from even-even nuclei in the region “southeast” of ^{132}Sn : Neutron-excitation dominance of the 2+1 state in ^{132}Cd ”, Phys. Rev. C **94**, 051301 (2016).
- (22) E. Ideguchi, G.S. Simpson, R. Yokoyama, Mn. Tanaka, S. Nishimura, P. Doornenbal, G. Lorusso, P. Aoderstrom, T. Sumikama, J. Wu, Z. Y. Xu, N. Aoi, H. Baba, F. L. Bello Garrote, G. Benzoni, F. Browne, R. Daido, Y. Fang, N. Fukuda, A. Gottardo, G. Gey, S. Go, N. Inabe, T. Isobe, D. Kameda, K. Kobayashi, M. Kobayashi, I. Kojouharov, T. Komatsubara, T. Kubo, N. Kurz, I. Kuti, Z. Li, M. Matsushita, S. Michimasa, C.B. Moon, H. Nishibata, I. Nishizuka, A. Odahara, Z. Patel, S. Rice, E. Sahin, H. Sakurai, H. Schaffner, L. Sinclair, H. Suzuki, H. Takeda, J. Taprogge, Zs. Vajta, H. Watanabe, A. Yagi: “ μ s isomers of $^{158,160}\text{Nd}$ ”, Phys. Rev. C **94**, 064322 (2016).
- (23) M. Dozono, T. Uesaka, S. Michimasa, M. Takaki, M. Kobayashi, M. Matsushita, S. Ota, H. Tokieda, S. Shimoura: ” Separated flow operation of the SHARAQ spectrometer for in-flight proton-decay experiments”, Nucl. Instr. Meth. Phys. Res. A **830**, 233–242 (2016).
- (24) R. Yokoyama, S. Go, D. Kameda, T. Kubo, N. Inabe, N. Fukuda, H. Takeda, H. Suzuki, K. Yoshida, K. Kusaka, K. Tanaka, Y. Yanagisawa, M. Ohtake, H. Sato, Y. Shimizu, H. Baba, M. Kurokawa, D. Nishimura, T. Ohnishi, N. Iwasa, A. Chiba, T. Yamada, E. Ideguchi, T. Fujii, H. Nishibata, K. Ieki, D. Murai, S. Momota, Y. Sato, J.W. Hwang, S. Kim, O.B. Tarasov, D.J. Morrissey, B.M. Sherrill, G. Simpson, C.R. Praharaj: “New K isomers in the neutron-rich N=100 isotones ^{162}Sm , ^{163}Eu , and ^{164}Gd ”, Phys. Rev. C **95**, 034313 (2017).
- (25) J. Wu, S. Nishimura, G. Lorusso, P. Moller, E. Ideguchi, P.H. Regan, G.S. Simpson, P. A. Soderstrom, P.M. Walker, H. Watanabe, Z.Y. Xu, H. Baba, F. Browne, R. Daido, P. Doornenbal, Y.F. Fang, G. Gey, T. Isobe, P.S. Lee, J.J. Liu, Z. Li, Z. Korkulu, Z. Patel, V. Phong, S. Rice, H. Sakurai, L. Sinclair, T. Sumikama, M. Tanaka, A. Yagi, Y.L. Ye, R. Yokoyama, G.X. Zhang, T. Alharbi, N. Aoi, F.L. Bello Garrote, G. Benzoni, A.M. Bruce, R.J. Carroll, K.Y. Chae, Z. Dombradi, A. Estrade, A. Gottardo, C.J. Griffin, H. Kanaoka, I. Kojouharov, F.G. Kondev, S. Kubono, N. Kurz, I. Kuti, S. Lalkovski, G.J. Lane, E.J. Lee, T. Lokotko, G. Lotay, C. B. Moon, H. Nishibata, I. Nishizuka, C.R. Nita, A. Odahara, Zs. Podolyak, O.J. Roberts, H. Schaffner, C. Shand, J. Taprogge, S. Terashima, Z. Vajta, S. Yoshida: “94 β -Decay Half-Lives of Neutron-Rich ^{55}Cs to ^{67}Ho : Experimental Feedback and Evaluation of the r-Process Rare-Earth Peak Formation”, Phys. Rev. Lett. **118**, 0722701 (2017).
- (26) A.I. Morales, G. Benzoni, H. Watanabe, Y. Tsunoda, T. Otsuka, S. Nishimura, F. Browne, R. Daido, P. Doornenbal, Y. Fang, G. Lorusso, Z. Patel, S. Rice, L. Sinclair, P.A. Soderstrom, T. Sumikama, J. Wu, Z.Y. Xu, A. Yagi, R. Yokoyama, H. Baba, R. Avigo, F.L. Bello Garrote, N. Blasi, A. Bracco, F. Camera, S. Ceruti, F.C.L. Crespi, G. de Angelis, M.C. Delattre, Zs. Dombradi, A. Gottardo, T. Isobe, I. Kojouharov, N. Kurz, I. Kuti, K. Matsui, B. Melon, D. Mengoni, T. Miyazaki, V. Modamio-Hoybjor, S. Momiyama, D.R. Napoli, M. Niikura, R.Orlandi, H.Sakurai, E.Sahin, D.Sohler, H.Schaffner, R.Taniuchi, J.Taprogge, Zs. Vajta, J.J. Valiente-Dobon, O. Wieland, M. Yalcinkaya: “Type II shell evolution in A=70 isobars from the $N \geq 40$ island of inversion”, Phys. Lett. **B 765**, 328 (2017).
- (27) A. Adare *et al.* [PHENIX Collaboration], “Angular decay coefficients of J/ψ mesons at forward rapidity from $p + p$ collisions at $\sqrt{s} = 510$ GeV, ” Phys. Rev. **D 95**, 092003 (2017).
- (28) J. Adam *et al.* [ALICE Collaboration], “W and Z boson production in p-Pb collisions at $\sqrt{s_{NN}} = 5.02$ TeV,” JHEP **1702**, 077 (2017).
- (29) J. Adam *et al.* [ALICE Collaboration], “Determination of the event collision time with the ALICE detector at the LHC,” Eur. Phys. J. Plus **132**, no. 2, 99 (2017).
- (30) A. Adare *et al.* [PHENIX Collaboration], “Measurement of the relative yields of $\psi(2S)$ to $\psi(1S)$ mesons produced at forward and backward rapidity in pp, p+Al, p+Au, and $^3\text{He}+\text{Au}$ collisions at $\sqrt{s_{NN}} = 200$ GeV,” Phys. Rev. C **95**, no. 3, 034904 (2017).
- (31) A. Adare *et al.* [PHENIX Collaboration], “Nonperturbative-transverse-momentum effects and evolution in dihadron and direct photon-hadron angular correlations in pp collisions at $\sqrt{s} = 510$ GeV,” Phys. Rev. **D 95**, no. 7, 072002 (2017).
- (32) J. Adam *et al.* [ALICE Collaboration], “Jet-like correlations with neutral pion triggers in pp and central Pb Pb collisions at 2.76 TeV,” Phys. Lett. **B 763**, 238 (2016).

- (33) J. Adam *et al.* [ALICE Collaboration], “ J/ψ suppression at forward rapidity in Pb-Pb collisions at $\sqrt{s_{NN}} = 5.02$ TeV”, Phys. Lett. **B 766**, 212 (2017).
- (34) J. Adam *et al.* [ALICE Collaboration], “Enhanced production of multi-strange hadrons in high-multiplicity proton-proton collisions,” Nature Phys. **13**, 535 (2017).
- (35) J. Adam *et al.* [ALICE Collaboration], “Higher harmonic flow coefficients of identified hadrons in Pb-Pb collisions at $\sqrt{s_{NN}} = 2.76$ TeV,” JHEP **1609**, 164 (2016).
- (36) A. Adare *et al.* [PHENIX Collaboration], “Measurements of double-helicity asymmetries in inclusive J/ψ production in longitudinally polarized p+p collisions at $\sqrt{s} = 510$ GeV,” Phys. Rev. **D 94**, no. 11, 112008 (2016).
- (37) J. Adam *et al.* [ALICE Collaboration], “Elliptic flow of electrons from heavy-flavour hadron decays at mid-rapidity in Pb-Pb collisions at $\sqrt{s_{NN}} = 2.76$ TeV,” JHEP **1609**, 028 (2016).
- (38) J. Adam *et al.* [ALICE Collaboration], “D-meson production in p-Pb collisions at $\sqrt{s_{NN}} = 5.02$ TeV and in pp collisions at $\sqrt{s} = 7$ TeV,” Phys. Rev. **C 94**, no. 5, 054908 (2016).
- (39) J. Adam *et al.* [ALICE Collaboration], “Measurement of azimuthal correlations of D mesons and charged particles in pp collisions at $\sqrt{s} = 7$ TeV and p-Pb collisions at $\sqrt{s_{NN}} = 5.02$ TeV,” Eur. Phys. J. **C 77**, no. 4, 245 (2017).
- (40) J. Adam *et al.* [ALICE Collaboration], “Pseudorapidity dependence of the anisotropic flow of charged particles in Pb-Pb collisions at $\sqrt{s_{NN}} = 2.76$ TeV,” Phys. Lett. **B 762**, 376 (2016).
- (41) J. Adam *et al.* [ALICE Collaboration], “Correlated event-by-event fluctuations of flow harmonics in Pb-Pb collisions at $\sqrt{s_{NN}} = 2.76$ TeV,” Phys. Rev. Lett. **117**, 182301 (2016).
- (42) J. Adam *et al.* [ALICE Collaboration], “Measurement of transverse energy at midrapidity in Pb-Pb collisions at $\sqrt{s_{NN}} = 2.76$ TeV,” Phys. Rev. **C 94**, no. 3, 034903 (2016).
- (43) J. Adam *et al.* [ALICE Collaboration], “Centrality dependence of charged jet production in p-Pb collisions at $\sqrt{s_{NN}} = 5.02$ TeV,” Eur. Phys. J. **C 76**, no. 5, 271 (2016).
- (44) J. Adam *et al.* [ALICE Collaboration], “Centrality dependence of $\psi(2S)$ suppression in p-Pb collisions at $\sqrt{s_{NN}} = 5.02$ TeV,” JHEP **1606**, 050 (2016).
- (45) J. Adam *et al.* [ALICE Collaboration], “Measurement of D-meson production versus multiplicity in p-Pb collisions at $\sqrt{s_{NN}} = 5.02$ TeV,” JHEP **1608**, 078 (2016).
- (46) J. Adam *et al.* [ALICE Collaboration], “Particle identification in ALICE: a Bayesian approach,” Eur. Phys. J. Plus **131**, no. 5, 168 (2016).
- (47) J. Adam *et al.* [ALICE Collaboration], “Anisotropic flow of charged particles in Pb-Pb collisions at $\sqrt{s_{NN}} = 5.02$ TeV,” Phys. Rev. Lett. **116**, no. 13, 132302 (2016).
- (48) J. Adam *et al.* [ALICE Collaboration], “Production of $K_0^*(892)$ and $\phi(1020)$ in p-Pb collisions at $\sqrt{s_{NN}} = 5.02$ TeV,” Eur. Phys. J. **C 76**, no. 5, 245 (2016).
- (49) J. Adam *et al.* [ALICE Collaboration], “Multiplicity dependence of charged pion, kaon, and (anti)proton production at large transverse momentum in p-Pb collisions at $\sqrt{s_{NN}} = 5.02$ TeV,” Phys. Lett. **B 760**, 720 (2016).
- (50) J. Adam *et al.* [ALICE Collaboration], “Multipion Bose-Einstein correlations in pp, p-Pb, and Pb-Pb collisions at energies available at the CERN Large Hadron Collider,” Phys. Rev. **C 93**, no. 5, 054908 (2016).
- (51) J. Adam *et al.* [ALICE Collaboration], “Multi-strange baryon production in p-Pb collisions at $\sqrt{s_{NN}} = 5.02$ TeV,” Phys. Lett. **B 758**, 389 (2016).
- (52) J. Adam *et al.* [ALICE Collaboration], “Centrality dependence of the charged-particle multiplicity density at midrapidity in Pb-Pb collisions at $\sqrt{s_{NN}} = 5.02$ TeV,” Phys. Rev. Lett. **116**, no. 22, 222302 (2016).
- (53) J. Adam *et al.* [ALICE Collaboration], “Measurement of an excess in the yield of J/ψ at very low p_T in Pb-Pb collisions at $\sqrt{s_{NN}} = 2.76$ TeV,” Phys. Rev. Lett. **116**, no. 22, 222301 (2016).
- (54) J. Adam *et al.* [ALICE Collaboration], “Pseudorapidity and transverse-momentum distributions of charged particles in proton-proton collisions at $\sqrt{s} = 13$ TeV,” Phys. Lett. **B 753**, 319 (2016).

- (55) J. Adam *et al.* [ALICE Collaboration], “Inclusive quarkonium production at forward rapidity in pp collisions at $\sqrt{s}=8$ TeV,” *Eur. Phys. J. C* **76**, no. 4, 184 (2016).
- (56) A. Adare *et al.* [PHENIX Collaboration], “Measurements of directed, elliptic, and triangular flow in Cu+Au collisions at $\sqrt{s_{NN}}=200$ GeV,” *Phys. Rev. C* **94**, no. 5, 054910 (2016).
- (57) A. Adare *et al.* [PHENIX Collaboration], “Azimuthally anisotropic emission of low-momentum direct photons in Au+Au collisions at $\sqrt{s_{NN}}=200$ GeV,” *Phys. Rev. C* **94**, no. 6, 064901 (2016).
- (58) J. Adam *et al.* [ALICE Collaboration], “Measurement of electrons from heavy-flavour hadron decays in p-Pb collisions at $\sqrt{s_{NN}} = 5.02$ TeV,” *Phys. Lett. B* **754**, 81 (2016).
- (59) J. Adam *et al.* [ALICE Collaboration], “Azimuthal anisotropy of charged jet production in $\sqrt{s_{NN}} = 2.76$ TeV Pb-Pb collisions,” *Phys. Lett. B* **753**, 511 (2016).
- (60) J. Adam *et al.* [ALICE Collaboration], “Direct photon production in Pb-Pb collisions at $\sqrt{s_{NN}} = 2.76$ TeV,” *Phys. Lett. B* **754**, 235 (2016).
- (61) J. Adam *et al.* [ALICE Collaboration], “Centrality evolution of the charged-particle pseudorapidity density over a broad pseudorapidity range in Pb-Pb collisions at $\sqrt{s_{NN}}=2.76$ TeV,” *Phys. Lett. B* **754**, 373 (2016).
- (62) J. Adam *et al.* [ALICE Collaboration], “Measurement of Ds+ production and nuclear modification factor in Pb-Pb collisions at $\sqrt{s_{NN}} = 2.76$ TeV,” *JHEP* **1603**, 082 (2016).
- (63) J. Adam *et al.* [ALICE Collaboration], “Multiplicity and transverse momentum evolution of charge-dependent correlations in pp, p-Pb, and Pb-Pb collisions at the LHC,” *Eur. Phys. J. C* **76**, no. 2, 86 (2016).
- (64) J. Adam *et al.* [ALICE Collaboration], “Transverse momentum dependence of D-meson production in Pb-Pb collisions at $\sqrt{s_{NN}}=2.76$ TeV,” *JHEP* **1603**, 081 (2016).
- (65) A. Adare *et al.* [PHENIX Collaboration], “Scaling properties of fractional momentum loss of high-pT hadrons in nucleus-nucleus collisions at $\sqrt{s_{NN}}$ from 62.4 GeV to 2.76 TeV,” *Phys. Rev. C* **93**, no. 2, 024911 (2016).
- (66) A. Adare *et al.* [PHENIX Collaboration], “Transverse energy production and charged-particle multiplicity at midrapidity in various systems from $\sqrt{s_{NN}}=7.7$ to 200 GeV,” *Phys. Rev. C* **93**, no. 2, 024901 (2016).
- (67) A. Adare *et al.* [PHENIX Collaboration], “ ϕ meson production in the forward/backward rapidity region in Cu+Au collisions at $\sqrt{s_{NN}}=200$ GeV,” *Phys. Rev. C* **93**, no. 2, 024904 (2016).
- (68) A. Adare *et al.* [PHENIX Collaboration], “Forward J/ψ production in U+U collisions at $\sqrt{s_{NN}}=193$ GeV,” *Phys. Rev. C* **93**, no. 3, 034903 (2016).
- (69) A. Adare *et al.* [PHENIX Collaboration], “Dielectron production in Au+Au collisions at $\sqrt{s_{NN}}=200$ GeV,” *Phys. Rev. C* **93**, no. 1, 014904 (2016).
- (70) A. Adare *et al.* [PHENIX Collaboration], “Single electron yields from semileptonic charm and bottom hadron decays in Au+Au collisions at $\sqrt{s_{NN}}=200$ GeV,” *Phys. Rev. C* **93**, no. 3, 034904 (2016).
- (71) A. Adare *et al.* [PHENIX Collaboration], “Centrality-dependent modification of jet-production rates in deuteron-gold collisions at $\sqrt{s_{NN}} =200$ GeV,” *Phys. Rev. Lett.* **116**, no. 12, 122301 (2016).
- (72) J. Adam *et al.* [ALICE Collaboration], “Study of cosmic ray events with high muon multiplicity using the ALICE detector at the CERN Large Hadron Collider,” *JCAP* **1601**, no. 01, 032 (2016).
- (73) J. Adam *et al.* [ALICE Collaboration], “Centrality dependence of pion freeze-out radii in Pb-Pb collisions at $\sqrt{s_{NN}}=2.76$ TeV,” *Phys. Rev. C* **93**, no. 2, 024905 (2016).
- (74) J. Adam *et al.* [ALICE Collaboration], “Event shape engineering for inclusive spectra and elliptic flow in Pb-Pb collisions at $\sqrt{s_{NN}}=2.76$ TeV,” *Phys. Rev. C* **93**, no. 3, 034916 (2016).
- (75) J. Adam *et al.* [ALICE Collaboration], “Elliptic flow of muons from heavy-flavour hadron decays at forward rapidity in Pb-Pb collisions at $\sqrt{s_{NN}}=2.76$ TeV,” *Phys. Lett. B* **753**, 41 (2016).
- (76) J. Adam *et al.* [ALICE Collaboration], “Production of light nuclei and anti-nuclei in pp and Pb-Pb collisions at energies available at the CERN Large Hadron Collider,” *Phys. Rev. C* **93**, no. 2, 024917 (2016).

- (77) J. Adam *et al.* [ALICE Collaboration], “Differential studies of inclusive J/ψ and $\psi(2S)$ production at forward rapidity in Pb-Pb collisions at $\sqrt{s_{NN}}=2.76$ TeV,” JHEP **1605**, 179 (2016).
- (78) J. Adam *et al.* [ALICE Collaboration], “Forward-central two-particle correlations in p-Pb collisions at $\sqrt{s_{NN}} = 5.02$ TeV,” Phys. Lett. **B 753**, 126 (2016).
- (79) A. Adare *et al.* [PHENIX Collaboration], “Measurement of higher cumulants of net-charge multiplicity distributions in Au+Au collisions at $\sqrt{s_{NN}}=7.7-200$ GeV,” Phys. Rev. **C 93**, no. 1, 011901 (2016).
- (80) J. Adam *et al.* [ALICE Collaboration], “Centrality dependence of the nuclear modification factor of charged pions, kaons, and protons in Pb-Pb collisions at $\sqrt{s_{NN}}=2.76$ TeV,” Phys. Rev. **C 93**, no. 3, 034913 (2016).
- (81) A. Adare *et al.* [PHENIX Collaboration], “Measurement of parity-violating spin asymmetries in W^\pm production at midrapidity in longitudinally polarized p+p collisions,” Phys. Rev. **D 93**, no. 5, 051103 (2016).
- (82) A. Adare *et al.* [PHENIX Collaboration], “Measurement of the higher-order anisotropic flow coefficients for identified hadrons in Au+Au collisions at $\sqrt{s_{NN}} = 200$ GeV,” Phys. Rev. **C 93**, no. 5, 051902 (2016).
- (83) B. Abelev *et al.* [ALICE Collaboration], “Measurement of electrons from beauty hadron decays in pp collisions at $\sqrt{s}=7$ TeV,” Phys. Lett. **B 721**, 13 (2013) Erratum: [Phys. Lett. **B 763**, 507 (2016)].
- (84) J. Yasuda *et al.*: “Inverse kinematics (p,n) reactions studies using the WINDS slow neutron detector and the SAMURAI spectrometer”, Nucl. Instr. and Meth. In Phys. Res. **B 376**, 393 (2016).
- (85) A. Krasznahorkay *et al.*: “Observation of anomalous internal pair creation in ^8Be : A possible indication of a light, neutral boson”, Phys. Rev. Lett. **042501** (2016).
- (86) J.C. Zamora *et al.*: “First measurement of isoscalar giant resonances in a stored-beam experiment”, Phys. Lett. **B 763**, 16 (2016).
- (87) P. Russotto *et al.*: “Results of the ASY-EOS experiment at GSI: The symmetry energy at supra-saturation density”, Phys. Rev. **C 94**, 034608 (2016).

B. Proceedings

- (1) D. Kahl, A. A. Chen, S. Kubono, H. Yamaguchi, D. N. Binh, J. Chen, S. Cherubini, N.N. Duy, T. Hashimoto, S. Hayakawa, N. Iwasa, H.S. Jung, S. Kato, Y.K. Kwon, S. Nishimura, S. Ota, K. Setoodehnia, T. Teranishi, H. Tokieda, T. Yamada, C.C. Yun and L.Y. Zhang: “Experimental investigation of the $^{30}\text{S}(\alpha, p)$ thermonuclear reaction in x-ray bursts”, EPJ Web of Conferences 109, 04005 (2016).
- (2) Y.B. Wang, S.J. Jin, L. Jing, Z.Y. Han, X.X. Bai, B. Guo, Y.J. Li, Z.H. Li, G. Lian, J. Su, L.J. Sun, S.Q. Yan, S. Zeng, W.P. Liu, H. Yamaguchi, S. Kubono, J. Hu, D. Kahl, J.J. He, J.S. Wang, X.D. Tang, S.W. Xu, P. Ma, N.T. Zhang, Z. Bai, M.R. Huang, B.L. Jia, S.L. Jin, J.B. Ma, S.B. Ma, W.H. Ma, Y.Y. Yang, L.Y. Zhang, H.S. Jung, J.Y. Moon, C.S. Lee, T. Teranishi, H.W. Wang, H. Ishiyama, N. Iwasa, T. Komatsubara and B.A. Brown: “Two measurements of the $^{22}\text{Na}+p$ resonant scattering via thick-target inverse-kinematics method”, EPJ Web of Conferences 109, 04010 (2016).
- (3) S. Kubono, H. Yamaguchi, S. Hayakawa, S.Q. Hou and J.J. He, “Explosive Nuclear Burning in the pp-Chain Region and the Breakout Processes”, EPJ Web of Conferences 109 01001 (2016).
- (4) S. Hayakawa, C. Spitaleri, N. Burtebayev, A. Aimaganbetov, P. Figuera, M. Fisichella, G.L. Guardo, S. Igamov, I. Indelicato, G. Kiss, S. Kliczewski, M. La Cognata, L. Lamia, M. Lattuada, E. Piasecki, G. G. Rapisarda, S. Romano, S. B. Sakuta, R. Siudak, A. Trzcinska, A. Tumino and A. Urkinbayev: “Indirect Study of the $^{16}\text{O} + ^{16}\text{O}$ Fusion Reaction Toward Stellar Energies by the Trojan Horse Method”, Nucleus Nucleus 2015 (NN2015), Catania, Italy, EPJ Web of Conferences 109, 09013 (2016).
- (5) H. Yamaguchi, D. Kahl, S. Hayakawa, Y. Sakaguchi, Y. Wakabayashi, T. Hashimoto, S. Cherubini, M. Gulino, C. Spitaleri, G.G. Rapisarda, M. La Cognata, L. Lamia, S. Romano, S. Kubono, N. Iwasa, T. Teranishi, T. Kawabata, Y.K. Kwon, D.N. Binh, L.H. Khiem, N.N. Duy, S. Kato, T. Komatsubara, A.Coc, N. de Sereville, F.Hammache, G. Kiss and S. Bishop: “Studying astrophysical reactions with low-energy RI beams at CRIB”, EPJ Web of Conferences 117, 09005 (2016).

- (6) G. D'Agata, C. Spitaleri, R.G. Pizzone, S. Blagus, P. Figuera, L. Grassi, G.L. Guardo, M. Gulino, S. Hayakawa, I. Indelicato, R. Kshetri, M. La Cognata, L. Lamia, M. Lattuada, T. Mijatovi, M. Milin, D. Miljanic, L. Prepolec, M.L. Sergi, N. Skukan, N. Soic, V. Tokic, A. Tumino and M. Uroic: "First evidences for $^{19}\text{F}(\alpha, p)^{22}\text{Ne}$ at astrophysical energies", 8th European Summer School on Experimental Nuclear Astrophysics, S. Tecla, Italy, J. of Phys.: Conf. Series, 703, 012016 (2016).
- (7) M. Mazzocco, A. Boiano, C. Boiano, M. La Commara, C. Manea, C. Parascandolo, D. Pierroutsakou, C. Signorini, E. Strano, D. Torresi, H. Yamaguchi, D. Kahl, L. Acosta, P. Di Meo, J.P. Fernandez-Garcia, T. Glodariu, J. Grebosz, A. Guglielmetti, N. Imai, Y. Hirayama, H. Ishiyama, N. Iwasa, S.C. Jeong, H.M. Jia, N. Keeley, Y.H. Kim, S. Kimura, S. Kubono, J.A. Lay, C.J. Lin, G. Marquinez-Duran, I. Martel, H. Miyatake, M. Mukai, T. Nakao, M. Nicoletto, A. Pakou, K. Rusek, Y. Sakaguchi, A.M. Sanchez-Benitez, T. Sava, O. Sgouros, C. Stefanini, F. Soramel, V. Soukeras, E. Stiliaris, L. Stroe, T. Teranishi, N. Toniolo, Y. Wakabayashi, Y.X. Watanabe, L. Yang and Y.Y. Yang, " ^7Be - and ^8B -reaction dynamics at Coulomb barrier energies", EPJ Web of Conferences 117, 060006 (2016).
- (8) H. Yamaguchi, D. Kahl, S. Hayakawa, L. Yang, Y. Sakaguchi, K. Abe, H. Shimizu, and CRIB Collaboration, "Overview of the activities at the low-energy beam separator CRIB", Il Nuovo Cimento 39C, 358 (2016).
- (9) D. Kahl, H. Yamaguchi, H. Shimizu, K. Abe, O. Beliuskina, S. M. Cha, K.Y. Chae, Z. Ge, S. Hayakawa, M.S. Kwag, D. H. Kim, J. Y. Moon, S.Y. Park, L. Yang: "Explosive destruction of ^{26}Al ", Il Nuovo Cimento 39C, 362 (2016).
- (10) S. Hayakawa: "Trials for the cosmological ^7Li problem with ^7Be beams at CRIB and collaborating studies", Il Nuovo Cimento 39C 370 (2016).
- (11) S.M. Cha, K.Y. Chae, K. Abe, S.H. Bae, S.H. Choi, D.N. Binh, N.N. Duy, K.I. Hahn, S. Hayakawa, B. Hong, H.S. Jung, D. Kahl, L.H. Khiem, A. Kim, D.H. Kim, E.J. Kim, G.W. Kim, M.J. Kim, K.J. Kwag, M.S. Kwag, Y.K. Kwon, C.S. Lee, E.J. Lee, S.I. Lim, B. Moon, J.Y. Moon, T. Nakao, S.Y. Park, H. Shimizu, H. Yamaguchi, L. Yang, and G. Zhuang, "Study of alpha cluster structure in ^{22}Mg ", Il Nuovo Cimento 39C, 371 (2016).
- (12) S. Hayakawa, C. Spitaleri, N. Burtebayev, A. Aimaganbetov, S.V. Artemov, P. Figuera, M. Fisichella, G.L. Guardo, S. Igamov, I. Indelicato, G.G. Kiss, S. Kubono, M. La Cognata, L. Lamia, M. Lattuada, M. Nassurlla, E. Piasecki, G.G. Rapisarda, S. Romano, S.B. Sakuta, A. Trzcinska, A. Tumino, A. Urkinbayev, and T. Zholdybayev, "Trojan Horse Method for the Oxygen-Burning Process Reactions", JPS Conf. Proc. 14, 020406 (2017).
- (13) H. Yamaguchi, D. Kahl, S. Hayakawa, Y. Sakaguchi, K. Abe, H. Shimizu, Y. Wakabayashi, T. Hashimoto, S. Cherubini, M. Gulino, C. Spitaleri, G. G. Rapisarda, M. La Cognata, L. Lamia, S. Romano, S. Kubono, N. Iwasa, T. Teranishi, T. Kawabata, Y. K. Kwon, D. N. Binh, L. H. Khiem, N. N. Duy, S. Kato, T. Komatsubara, A. Coc, N. de Sereville, F. Hammache, G. Kiss, and S. Bishop, "Experimental Studies of Light-Ion Nuclear Reactions Using Low-Energy RI Beams", JPS Conf. Proc. 14, 010503 (2017).
- (14) D. Kahl, A. A. Chen, S. Kubono, H. Yamaguchi, D. N. Binh, J. Chen, S. Cherubini, N. N. Duy, T. Hashimoto, S. Hayakawa, N. Iwasa, H. S. Jung, S. Kato, Y. K. Kwon, S. Nishimura, S. Ota, K. Setoodehnia, T. Teranishi, H. Tokieda, T. Yamada, C. C. Yun, and L. Y. Zhang, " $^{30}\text{S}(\alpha, p)$ Thermonuclear Reaction Rate from Experimental Level Structure of ^{34}Ar ", JPS Conf. Proc. 14, 020510 (2017).
- (15) K. Abe, S. Hayakawa, H. Yamaguchi, and L. Lamia, "Feasibility Study for the $^7\text{Be}+n$ Reaction Measurements by Trojan Horse Method at CRIB", JPS Conf. Proc. 14, 020507 (2017).
- (16) Marisa Gulino, Silvio Cherubini, Claudio Spitaleri, Giuseppe Gabriele Rapisarda, Marco La Cognata, Livio Lamia, Rosario Gianluca Pizzone, Stefano Romano, Shigeru Kubono, Hidetoshi Yamaguchi, Seya Hayakawa, Yasuo Wakabayashi, Naohito Iwasa, Seigo Kato, Tetsuro Komatsubara, Takashi Teranishi, Alain Coc, Nicolas de Sereville, Fairouz Hammache, Gabor Kiss, Shawn Bishop, and Dam Nguyen Binh: "The $^{18}\text{F}(n, \alpha)$ Reaction: First Study of n-Induced Reaction on a Radioactive Nucleus Using the Trojan Horse Method", JPS Conf. Proc. 14, 021104 (2017).
- (17) N. Shimizu, Y. Utsuno, Y. Futamura, T. Sakurai, T. Mizusaki, T. Otsuka, " Stochastic estimation of level density in nuclear shell-model calculations ", EPJ Web of Conferences 122, 02003 (2016).
- (18) T. Sumikama, D.S. Ahn, N. Fukuda, N. Inabe, T. Kubo, Y. Shimizu, H. Suzuki, H. Takeda, N. Aoi, D. Beaumel, K. Hasegawa, E. Ideguchi, N. Imai, T. Kobayashi, M. Matsushita, S. Michimasa, H. Otsu, S. Shimoura, T. Teranishi:

“First test experiment to produce the slowed-down RI beam with the momentum-compression mode at RIBF”, Proceedings of 17th International Conference on Electromagnetic Isotope Separators and Related Topics (EMIS2015), Nucl. Instr. Meth. Phys. Res. B 376, 180–184 (2016)

- (19) J. Yasuda, M. Sasano, R.G.T. Zegers, H. Baba, W. Chao, M. Dozono, N. Fukuda, N. Inabe, T. Isobe, G. Jhang, D. Kameda, T. Kubo, M. Kurata-Nishimura, E. Milman, T. Motobayashi, H. Otsu, V. Panin, W. Powell, H. Sakai, M. Sako, H. Sato, Y. Shimizu, L. Stuhl, H. Suzuki, S. Tangwanchaoen, H. Takeda, T. Uesaka, K. Yoneda, J. Zenihiro, T. Kobayashi, T. Sumikama, T. Tako, T. Nakamura, Y. Kondo, Y. Togano, M. Shikata, J. Tsubota, K. Yako, S. Shimoura, S. Ota, S. Kawase, Y. Kubota, M. Takaki, S. Michimasa, K. Kisamori, C.S. Lee, H. Tokieda, M. Kobayashi, S. Koyama, N. Kobayashi, T. Wakasa, S. Sakaguchi, A. Krasznahorkay, T. Murakami, N. Nakatsuka, M. Kaneko, Y. Matsuda, D. Mucher, S. Reichert, D. Bazin, J.W. Lee: “Inverse kinematics (p,n) reactions studies using the WINDS slow neutron detector and the SAMURAI spectrometer”, Proceedings of 17th International Conference on Electromagnetic Isotope Separators and Related Topics (EMIS2015), Nucl. Instr. Meth. Phys. Res. B 376, 393–396 (2016)
- (20) H. Sako et al. [J-PARC Heavy-Ion Collaboration], “Studies of high density baryon matter with high intensity heavy-ion beams at J-PARC,” Nucl. Phys. A 956, 850 (2016).
- (21) T. Gunji [ALICE Collaboration], “Overview of recent ALICE results,” Nucl. Phys. A 956, 11 (2016)
- (22) C. Zhao, T. Gunji et al., “First performance results of the ALICE TPC Readout Control Unit 2,” JINST 11, no. 01, C01024 (2016).
- (23) K. Itahashi et al., “Precision spectroscopy of pionic atoms and chiral symmetry in nuclei”, MESON 2016 14th International Workshop on meson production, properties and interaction, EPJ Web Conf. 130 (2016) 01017
- (24) M.L. Cortes et al., “Inelastic scattering of ^{72}Ni , ^{74}Ni off a proton target”, XXI INTERNATIONAL SCHOOL ON NUCLEAR PHYSICS, NEUTRON PHYSICS AND APPLICATIONS & INTERNATIONAL SYMPOSIUM ON EXOTIC NUCLEI (ISEN-2015), J. of Phys. Conf. 724, (2016) 012008
- (25) L. Stuhl et al.: “A newly developed wrapping method for scintillator detectors”, J. of Phys. Conf. Ser. 665, 012050 (2016).
- (26) T. Krll et al.: “Nuclear reactions in the storage ring ESR with EXL”, J. of Phys. Conf. Ser. 724, 012026 (2016).
- (27) M. Sasano et al.: “Study of Gamow-Teller transitions from ^{132}Sn via the (p,n) reaction at 220 MeV/u in inverse kinematics”, Eur. Phys. J. Conf. 107, 06003 (2016).
- (28) R. Reifarth et al.: “Nuclear astrophysics with radioactive ions at FAIR”, J. of Phys. Conf. Ser. 665, 012044 (2016).

C. Theses

- (1) S. Hayashi: “ J/ψ Production in p-Pb collisions at $\sqrt{s_{NN}} = 5.02$ TeV “ PhD Thesis, the University of Tokyo, March 2017.
- (2) M. Kobayashi: “Direct mass measurements of neutron-rich Ca isotopes”, PhD Thesis, the University of Tokyo, March 2017.
- (3) S. Masuoka: “Measurement of $^4\text{He}(^8\text{He}, ^8\text{Be})$ reaction for verifying tetra-neutron resonance”, Master Thesis, the University of Tokyo. March 2017.
- (4) Y. Yamaguchi: “Development of event-building system for data acquisition modules based on waveform digitizers for segmented Ge detectors”, Master Thesis, the University of Tokyo. March 2017.
- (5) K. Kawata: “Development of isomer beam towards study of isomerinduced reactions”, Master Thesis, the University of Tokyo. March 2017.
- (6) T. Kitamura: “Nuclear structure of ^{35}Si via proton resonant elastic scattering”, Master Thesis, the University of Tokyo. March 2017.

- (7) K. Abe: “Indirect measurement of the ${}^7\text{Be}+n$ Big-bang nucleosynthesis reactions by the Trojan horse method and radio-isotope beam”, Master Thesis, the University of Tokyo. March 2017.

D. Other Publications

- (1) 下浦 享: “テトラ中性子の探査”, ISOTOPE NEWS, 749, 7–9 (2017)
- (2) 下浦 享: “RI ビームを用いたテトラ中性子研究”, 原子核研究, 61, 70–77 (2017)

Talks and Presentations

A. Conferences

- (1) H. Yamaguchi (oral): “Study on alpha-cluster levels in non-4n nuclei using low-energy RI beams”, 11th International Conference on Clustering Aspects of Nuclear Structure and Dynamics, May 23-27, 2016, Conference Center of the Università di Napoli Federico II, Napoli, Italy.
- (2) H. Shimizu (oral): “Searching for the origin of galactic Al-26 with an experiment using isomeric Al-26 beam ”, NIC-XIV School, June 13–16, 2016, Niigata University, Niigata, Japan.
- (3) H. Yamaguchi (oral, invited): “Experimental studies of light-ion nuclear reactions using low-energy RI beams”, the 14th International Symposium on Nuclei in the Cosmos (NIC-XIV), June 19–24, 2016, Toki Messe, Niigata, Japan.
- (4) H. Yamaguchi (oral): “Overview of CRIB projects”, the Second Sicily-East Asia Workshop on Low Energy Nuclear Physics (SEA2016), June 26–28, 2016, CNS, the University of Tokyo, Wako, Saitama, Japan.
- (5) S. Hayakawa (oral): “Trials for the cosmological ${}^7\text{Li}$ problem with ${}^7\text{Be}$ beams at CRIB and collaborating studies”, the Second Sicily-East Asia Workshop on Low-energy Nuclear Physics (SEA2016), June 26-28, 2016, CNS, the University of Tokyo, Wako, Saitama, Japan.
- (6) H. Yamaguchi (oral): “Recent activities at the low-energy RI beam separator CRIB”, RIBF users meeting 2016, Sep. 8-9, 2016, RIKEN, Wako, Saitama, Japan.
- (7) H. Yamaguchi (oral): “Overview of recent experiments at CRIB”, SKKU mini workshop, Oct. 11, 2016, Sungkyunkwan University, Suwon, Korea.
- (8) S. Hayakawa (oral): “Upcoming CRIB experiment: ${}^7\text{Be} + n$ reaction measurements by the Trojan horse method”, SKKU mini Workshop, Oct. 11, 2016, Suwon, Korea.
- (9) H. Yamaguchi (oral): “Introduction of the low-energy RI beam facility CRIB and recent research activities at CRIB”, Nuclear Physics Seminar, Oct. 25, 2016, Beihang University, Beijing, China.
- (10) N. Imai, “OEDO and proton resonance elastic scattering” (invited) HIAS2016 2016/9/18-20, Canberra, Australia
- (11) N. Imai, “Physics program with low-energy RI beams” (invited) 2016/11/16-18 Daejeong, Korea, RNC-RISP RIB physics workshop
- (12) N. Shimizu, “ Shape phase transition and shell evolution in large-scale shell-model calculations ”, 8th Workshop on Quantum Phase Transitions in Nuclei and Many-Body Systems, Jun. 6-9, 2016, Prague, Czech Republic.
- (13) Y. Utsuno (invited), N. Shimizu, T. Otsuka, “ Shell-model applications to gamma-ray strength function and level density ”, NUSPIN 2016 Workshop of the Nuclear Spectroscopy Instrumentation Network and AGATA Physics Workshop, Jun. 27-Jul. 1, 2016, Venice, Italy.
- (14) N. Tsunoda, “ Island of Inversion by microscopically derived shell-model Hamiltonian ”, Direct Reactions with Exotic Beams (DREB) 2016, Jul. 11-15, 2016, Halifax, Canada.
- (15) Y. Tsunoda, “ Monte Carlo shell model calculations for structure of nuclei around $Z=28$ ”, The 15th CNS International Summer School, Aug. 24-30, 2016, Wako, Japan.
- (16) N. Shimizu, “ Large-scale shell-model studies for exotic nuclei and nuclear level densities ”, International Conference Nuclear Theory in the Supercomputing Era - 2016, Sep. 19-23, 2016, Khabarovsk, Russia.
- (17) N. Shimizu, “ Clustering structure in no-core Monte Carlo shell model ”, Workshop on Nuclear Cluster Physics (WNCP2016), Nov. 14-17, 2016, Yokohama, Japan.
- (18) J. Menendez, “ Towards double-beta decay matrix elements with theoretical uncertainties ”, First Tsukuba-CCS-RIKEN joint workshop on microscopic theories of nuclear structure and dynamics, Dec. 12-16, 2016, Tsukuba, Japan.

- (19) N. Shimizu, “ Nuclear shell-model calculations in HPC ”, First Tsukuba-CCS-RIKEN joint workshop on microscopic theories of nuclear structure and dynamics, Dec. 12-16, 2016, Tsukuba, Japan.
- (20) Y. Utsuno, S. Yoshida, N. Shimizu, T. Otsuka, T. Togashi, T. Suzuki, M. Honma, “ Shell-model study of Gamow-Teller and first-forbidden β decay in the N=28 region ”, 6th Workshop on Nuclear Fission and Spectroscopy of Neutron-Rich Nuclei, Mar. 20-24, 2017, Chamrousse, France.
- (21) S. Shimoura (invited): “Tetraneutron states populated via $^4\text{He}(^8\text{He}, ^8\text{Be})$ reaction”, The 11th International Conference on Clustering Aspects of Nuclear Structure and Dynamics (Cluster16), May. 23–27, 2016, Naples, Italy.
- (22) S. Shimoura (Oral): “Tetra-neutron states populated by $^4\text{He}(^8\text{He}, ^8\text{Be})$ reaction”, The 9th International Conference on Direct Reactions with Exotic Beams (DREB2016), July 11–15, 2016, Halifax, Canada.
- (23) S. Shimoura (invited): “Interplay between reaction and structure in nuclear physics”, International Symposium on Modern Technique and its Outlook in Heavy ion Science (MOTO16), June 26–27, 2016, Rikkyo University, Tokyo, Japan.
- (24) M. Dozono (Oral): “Separated flow operation of the SHARQA spectrometer for in-flight proton-decay experiments”, International Symposium on Modern Technique and its Outlook in Heavy ion Science (MOTO16), June 26–27, 2016, Rikkyo University, Tokyo, Japan.
- (25) S. Michimasa (Invited): “New Beamline with Optimized Energy-degrading Optics of RI beams”, The Second Sicily-East Asia Workshop on Low Energy Nuclear Physics (SEA2), June 26–28, 2016, Nishina Hall, RIKEN, Wako, Saitama, Japan.
- (26) S. Shimoura: “Experimental studies of the tetra-neutron system by using RI-beam”, RIBF Discussion on the tetra-neutron system, August 3, 2016, Tohoku University, Sendai, Japan
- (27) S. Shimoura (invited): “Experimental studies of the tetra-neutron system by using RI-beam”, The 23rd European Conference on Few-Body Problems in Physics, Aug. 8–12, 2016, Aarhus, Denmark.
- (28) S. Michimasa (Invited): “Recent Achievement of OEDO/SHARQA system”, RIBF Users Meeting 2016, September 8–9, 2016, RIBF Conference Hall, RIKEN, Wako, Saitama, Japan.
- (29) S. Shimoura (invited): “Charge Exchange Reaction of RI Beam to Populate Exotic States”, International Nuclear Physics Conference (INPC2016), Sep. 11–16, 2016, Adelaide, Australia.
- (30) S. Michimasa (Oral): “Sharaq Spectrometer: High-resolution Spectroscopy Using Exotic Beams And Reactions”, International Nuclear Physics Conference (INPC2016), Sep. 11–16, 2016, Adelaide, Australia.
- (31) S. Michimasa (Oral): “OEDO Beamline: New Energy-degrading Ion Optics of RI Beams”, International Nuclear Physics Conference (INPC2016), Sep. 11–16, 2016, Adelaide, Australia.
- (32) R. Yokoyama (Oral): “Role Of Hexadecupole Deformation In The Shape Evolution Of Neutron-rich Nd Isotopes”, International Nuclear Physics Conference (INPC2016), Sep. 11–16, 2016, Adelaide, Australia.
- (33) M. Kobayashi (Oral): “Time-of-flight Mass Measurements Of Neutron-rich Calcium Isotopes Beyond N=34 ”, International Nuclear Physics Conference (INPC2016), Sep. 11–16, 2016, Adelaide, Australia.
- (34) M. Takaki (Oral): “Search for Double Gamow-Teller Resonance via Heavy-ion Double Charge Exchange Reaction”, International Nuclear Physics Conference (INPC2016), Sep. 11–16, 2016, Adelaide, Australia.
- (35) S. Shimoura (invited): “Tetra-neutron system populated by exothermic double-charge exchange reaction $^4\text{He}(^8\text{He}, ^8\text{Be})$ at 190 MeV/u”, The 22nd International Spin Symposium, Sep. 25–30, 2016, Champaign, IL, USA.
- (36) S. Shimoura (invited): “Tetra-neutron system studied by $^4\text{He}(^8\text{He}, ^8\text{Be})$ ”, ECT* Workshop on Physics beyond the limits of stability: exploring the continuum, Oct. 17–21, 2016, Trento, Italy
- (37) S. Michimasa (Invited): “New energy-degraded beam project at RIBF – OEDO project –”, KPS 2016 Fall Meeting, October 19–21, 2016, Kimdaejung Convention Center, Gwangju, Korea.
- (38) S. Shimoura (invited): “Tetra-neutron system studied by $^4\text{He}(^8\text{He}, ^8\text{Be})$ ”, Workshop on Nuclear Cluster Physics (WNCP2016), Oct. 17–21, 2016, Kanto-Gakuin University, Yokohama, Japan

- (39) S. Shimoura (invited): “Tetra-neutron system studied by using RI beam”, International Symposium on Neutron Star Matter (NSMAT2016), Recent Progress in Observations, Experiments and Theories, Oct. 21–24, 2016, Tohoku University, Sendai, Japan
- (40) S. Shimoura (invited): “Tetra-neutron system populated by reaction of exotic beam”, ESNT Workshop on Dynamics of highly unstable exotic light nuclei and few-body systems, January 30–February 3, 2017, Saclay, France
- (41) T. Gunji (Oral) for the ALICE Collaboration: “ Low mass dielectron measurements in pp, p-Pb, and Pb-Pb collisions with ALICE at the LHC ”, The 8th International Conference on Hard and Electromagnetic Probes of High-energy Nuclear Collisions (Hard Probes 2016), 9/23-27, 2016, Wuhan, China
- (42) T. Gunji (Oral) for the ALICE Collaboration: “ Physics with heavy-ions and Dark Photon Searches at the LHC-ALICE experiment ”, Aspen workshop on Particle Physics in 2017 : From the LHC to Dark Matter and Beyond, 3/20-25, 2017, Aspen, Colorado, USA, 3/20-3/25
- (43) Y. Watanabe (Oral) ; “ Experimental overview on hadronic resonance production in high-energy nuclear collisions ”, The 16th International Conference on Strangeness in Quark Matter (Strangeness in Quark Matter 2016), 6/26-7/1, 2016, Berkeley, USA
- (44) Y. Watanabe (Oral) for the ALICE Collaboration, “ ALICE Overview ”, 33rd Winter Workshop on Nuclear Dynamics, 1/8-14, 2017, Salt Lake City, USA
- (45) S. Ota (invited), “CNS Active Target (CAT) for high-intensity beam experiment and the first experiment at RIBF”, Workshop on Software for Time Projection Chamber for Nuclear Physics Experiments, Aug. 8-10, 2016, MSU, US
- (46) H. Tokieda (invited), “Event Search Algorithm for CAT”, Workshop on Software for Time Projection Chamber for Nuclear Physics Experiments, Aug. 8-10, 2016, MSU, US
- (47) C. Iwamoto (invited), “Simulation for high-intensity heavy-ion beam injection in CAT”, Workshop on Software for Time Projection Chamber for Nuclear Physics Experiments, Aug. 8-10, 2016, MSU, US
- (48) L. Stuhl et al. (oral): “A new low-energy plastic scintillation neutron detector for real time pulse shape discrimination”: The 26th International Nuclear Physics Conference (INPC2016), Sep 11–16, 2016, Adelaide, Australia.
- (49) 富樫智章、角田佑介、大塚孝治、清水則孝、“ Zr 同位体における形の量子相転移のモンテカルロ殻模型による研究 ”、研究会「クラスター・平均場の両側面から見る原子核構造の多様性とそのダイナミクス」、Jan. 19-20, 2017、大阪市立大学、大阪
- (50) 角田直文、“ Medium-mass nuclei from nuclear force ”、基研研究会「核力に基づく核構造、核反応物理の展開」、Mar. 27-29, 2017、京都大学基礎物理学研究所、京都
- (51) 下浦 享 (invited): “イオンビームを用いた原子核研究と放射線計測技術の現状と課題”, 放射線科学とその応用第186委員会 第19回研究会, 2016年5月19日, 東京大学山上会館, 東京
- (52) 下浦 享 (invited): “RI ビームを用いた原子核物理学研究と放射線測定技術”, 第62回放射線計測研究会, 2016年10月15日, 三菱総合研究所, 東京
- (53) S. Shimoura (invited): “Tetra-neutron system populated by exothermic double-charge exchange reaction”, 基研研究会「核力に基づく核構造、核反応物理の展開」, 2017年3月27–29日, 京都大学, 京都.
- (54) 小高康熙 (oral): 「4次元エミッタンスデータによる AVF 入射軌道解析」, 第13回 AVF 合同打合せ, 2016年10月27-28日, 東北大学 CYRIC
- (55) 大城幸光 (oral): 「CNS イオン源の現状」, 第13回 AVF 合同打合せ, 2016年10月27-28日, 東北大学 CYRIC
- (56) 大田晋輔 (invited), “CNS Active Target”、新学術領域『中性子星核物質』第二回検出器ワークショップ
- (57) S. Hayakawa, C. Spitaleri, N. Burtebayev, A. Aimaganbetov, S.V. Artemov, P. Figuera, M. Fisichella, G.L. Guardo, S. Igamov, I. Indelicato, G.G. Kiss, S. Kubono, M. La Cognata, L. Lamia, M. Lattuada, M. Nassurlla, E. Piasecki, G.G. Rapisarda, S. Romano, S.B. Sakuta, A. Trzcinska, A. Tumino, A. Urkinbayev, and T. Zholdybayev (poster): “Trojan Horse Method for the Oxygen-Burning Process Reactions”, The 14th International Symposium on Nuclei in the Cosmos (NIC2016), Jun. 19-24, Niigata, Japan

- (58) K. Abe, S. Hayakawa, H. Yamaguchi, and L. Lamia (poster) : “Feasibility Study for the ${}^7\text{Be}+n$ Reaction Measurements by Trojan Horse Method at CRIB”, The 14th International Symposium on Nuclei in the Cosmos (NIC2016), Jun. 19-24, Niigata, Japan
- (59) T. Togashi, “ E1 strength function in Monte Carlo shell model ”, The 15th CNS International Summer School, Aug. 24-30, 2016, Wako, Japan.
- (60) T. Yoshida, “ Structure of Be and C isotopes with large-scale shell model calculations ”, The 15th CNS International Summer School, Aug. 24-30, 2016, Wako, Japan
- (61) H. Murakami for the ALICE Collaboration, “Measurements of neutral mesons in pp collisions at $\sqrt{s} = 5.02$ TeV via conversion method with ALICE”, Quark Matter 2017, Feb. 5-11, 2017, Chicago, USA

B. JPS Meetings

- (1) 早川勢也 (oral) : “ トロイの木馬法による ${}^7\text{Be}+n$ ビッグバン元素合成反応の測定 (Measurement of the ${}^7\text{Be}+n$ Big-Bang nucleosynthesis reactions by the Trojan horse method) ”, 日本物理学会 第 72 回年次大会, 3 月 17 日 ~ 20 日, 大阪大学
- (2) 清水英樹 (oral) : “ CRIB における ${}^{26}\text{Al}$ 異性核反応の宇宙線観測への寄与の研究 (Study on e contribution of isomeric aluminum-26 reaction to cosmic gamma-ray observation with CRIB) ”, 日本物理学会 第 72 回年次大会, 3 月 17 日 ~ 20 日, 大阪大学
- (3) N. Kitamura et al., “ Shell structure of ${}^{35}\text{Si}$ studied by proton resonance scattering ”, JPS 2016 fall meeting
- (4) O. Beliuskina et al., “ Pulse height defect in CVD Diamond Detectors ”, JPS 2016 fall meeting
- (5) N. Imai, “ Single particle structure studies with the transfer reaction and the resonance elastic reaction ” (invited) JPS meeting 2017, symposium for New aspects of direct reactions in probing exotic nuclei
- (6) 角田佑介、大塚孝治、清水則孝、本間道雄、宇都野穰、“ 大規模殻模型計算による $Z=28$ 近傍の核構造の研究 ”、日本物理学会 2016 年秋季大会、Sep. 21-24, 2016、宮崎大学木花キャンパス、宮崎
- (7) 富樫智章、角田佑介、大塚孝治、清水則孝、“ Zr 同位体における形の量子相転移のモンテカルロ殻模型による研究 ”、日本物理学会 2016 年秋季大会、Sep. 21-24, 2016、宮崎大学木花キャンパス、宮崎
- (8) 吉田亨、清水則孝、阿部喬、大塚孝治、“ Be, C 同位体の intrinsic 状態のモンテカルロ殻模型による研究 ”、日本物理学会 2016 年秋季大会、Sep. 21-24, 2016、宮崎大学木花キャンパス、宮崎
- (9) 市川隆敏、清水則孝、宇都野穰、大塚孝治、“ 大規模殻模型計算による質量数 $A=40$ 領域における $4p-4h$ 変形状態の系統的探索 ”、日本物理学会第 72 回年次大会、Mar. 17-20, 2017、大阪大学豊中キャンパス、大阪
- (10) 宇都野穰、藤田佳孝、“ 二核子配位のカモフテラー遷移と陽子中性子対相関 ”、日本物理学会第 72 回年次大会、Mar. 17-20, 2017、大阪大学豊中キャンパス、大阪
- (11) 清水則孝、富樫智章、大塚孝治、宇都野穰、吉田聡太、“ ベイズ統計による殻模型計算解析 ”、日本物理学会第 72 回年次大会、Mar. 17-20, 2017、大阪大学豊中キャンパス、大阪
- (12) 角田直文、大塚孝治、鈴木俊夫、高柳和雄、清水則孝、Morten Hjorth-Jensen、“ 核力に依拠した有効相互作用による殻模型計算でみる「逆転の島」の新しい様相 ”、日本物理学会第 72 回年次大会、Mar. 17-20, 2017、大阪大学豊中キャンパス、大阪
- (13) 角田佑介 (受賞講演)、“ Ni 同位体における新奇な変形共存現象と核子配位に依存した殻進化の研究 ”、日本物理学会第 72 回年次大会、Mar. 17-20, 2017、大阪大学豊中キャンパス、大阪
- (14) 富樫智章、角田佑介、大塚孝治、清水則孝、“ Zr 同位体とその近傍核における形の量子相転移のモンテカルロ殻模型による研究 ”、日本物理学会第 72 回年次大会、Mar. 17-20, 2017、大阪大学豊中キャンパス、大阪
- (15) S. Masuoka 他: “複数中性子識別のための反跳陽子飛跡検出器の開発 II”, JPS Fall meeting, September 21–24, 2016, Miyazaki University, Miyazaki, Japan

- (16) Y. Yamaguchi, 他: “DSP を用いた多重ガンマ線検出用 Ge 検出器アレイの為のデータ収集系の開発 2”, JPS Fall meeting, September 21–24, 2016, Miyazaki University, Miyazaki, Japan
- (17) M. Kobayashi 他: “飛行時間法を用いた中性子数 34 近傍 Ca 同位体の質量測定”, JPS Fall meeting, September 21–24, 2016, Miyazaki University, Miyazaki, Japan
- (18) R. Yokoyama, 他: “中性子過剰 Nd 同位体の变形進化における十六重極変形の効果”, JPS Fall meeting, September 21–24, 2016, Miyazaki University, Miyazaki, Japan
- (19) S. Shimoura (invited): “New energy degraded beam line at RIBF – OEDO”, 「超重元素の新展開」シンポジウム, JPS Spring meeting, March 17–20, 2017, Osaka University, Osaka, Japan
- (20) S. Hayashi for the ALICE Collaboration, “Dielectron production from Heavy Quarks in p-Pb collisions at $\sqrt{s_{NN}} = 5.02$ TeV with the ALICE detector “, JPS 2016 Autumn Meeting, Sep. 21-24, University of Miyazaki, Miyazaki, Japan
- (21) K. Terasaki for the ALICE Collaboration, “ Search for exotic dibaryons and study of baryon-baryon correlations at LHC-ALICE ”, JPS 2016 Autumn Meeting, Sep. 21-24, University of Miyazaki, Miyazaki, Japan
- (22) Y. Sekiguchi for the ALICE Collaboration, “ ”Study of two particle correlations in p-Pb collisions at $\sqrt{s_{NN}} = 5.02$ TeV with ALICE ”, JPS 2016 Autumn Meeting, Sep. 21-24, University of Miyazaki, Miyazaki, Japan
- (23) 大田晋輔, “重水素アクティブ標的を用いた錫領域不安定核の巨大共鳴の測定” 日本物理学会第 72 回年次大会、2017 年 3 月 17 日-2017 年 3 月 20 日、大阪大学
- (24) 小高康照: 「ペーパーポット型エミッタンス測定器を用いた理研 AVF サイクロトロン入射系の解析」, 第 13 回日本加速器学会年会, 2016 年 8 月 8-10 日, 幕張メッセ国際会議場

C. Lectures

- (1) 道正新一郎: 親子講演会 「卒業生が語る “私の夢 原子核と宇宙”」, Jan. 21, 2017. 鴻巣市立大芦小学校, 埼玉県鴻巣市.

D. Seminars

- (1) T. Gunji, “Frontiers of Quark-Gluon Plasma Physics with high-energy heavy-ion collisions”, KMI Colloquium, Nagoya, 12/21, 2016
- (2) S. Shimoura: “RI ビームによる核反応と核応答”, 第 4 回中性子核物質ウィンタースクール, February 24–26, 国立天文台
- (3) S. Shimoura: “Tetra-neutron system studied by double-charge exchange reaction ${}^4\text{He}({}^8\text{He}, {}^8\text{Be})$ ” April 25, 2016, Tokyo Institute of Technology, Tokyo, Japan

Personnel

Director

SHIMOURA, Susumu

*Professor, Graduate School of Science
Center for Nuclear Study*

Scientific Staff

SAKEMI, Yasuhiro

Professor

YAKO, Kentaro

Associate Professor

IMAI, Nobuaki

Associate Professor

SHIMIZU, Noritaka

Project Associate Professor

YAMAGUCHI, Hidetoshi

Lecturer

WIMMER, Kathrin

Lecturer

MICHIMASA, Shin'ichiro

Assistant Professor

GUNJI, Taku

Assistant Professor

OTA, Shinsuke

Assistant Professor

Guest Professors

UTSUNO, Yutaka

JAEA

MIZOI, Yutaka

Osaka Electro-Communication University

Technical Staff

KOTAKA, Yasuteru

Technical Assistants

YOSHIMURA, Kazuyuki

OHSHIRO, Yukimitsu

KATAYANAGI, Mamoru

Post Doctoral Associates

MATSUSHITA, Masafumi

HAYAKAWA, Seiya

IWAMOTO, Chihiro

TOGASHI, Tomoaki

ICHIKAWA, Takatoshi

DOZONO, Masanori

WATANABE, Yosuke

SCHROCK Philipp

STUHL Laszlo

TSUNODA, Naofumi

TSUNODA, Yusuke

YOKOYAMA, Rin

Graduate Students

TOKIEDA, Hiroshi

SEKIGUCHI, Yuko

YAMAGUCHI, Yuki

NAKAJIMA, Ryo

KAWATA, Keita

ABE, Kejiro

SHIMIZU, Hideki

KOBAYASHI, Motoki

KOBAYASHI, Motoki

MASUOKA, Soichiro

HAYASHI, ShinIchi

TERASAKI, Kohei

KITAMURA, Noritaka

Administration Staff

OKI, Mikio

YAMAMOTO, Ikuko

ENDO, Takako

KISHI, Yukino

SOMA, Yuko

Committees

Steering Committee

FUKUDA, Hiroo	<i>Department of Biological Science, Graduate School of Science, UT</i>
YAMANOUCHI, Kaoru	<i>Department of Chemistry, Graduate School of Science, UT</i>
HASEGAWA, Shuji	<i>Department of Physics, Graduate School of Science, UT</i>
SHIMOURA, Susumu	<i>Center for Nuclear Study, Graduate School of Science, UT</i>
SAKEMI, Yasuhiro	<i>Center for Nuclear Study, Graduate School of Science, UT</i>
YAKO, Kentaro	<i>Center for Nuclear Study, Graduate School of Science, UT</i>
SAKURAI, Hiroyoshi	<i>Department of Physics, Graduate School of Science, UT</i>
NAGAMIYA, Shoji	<i>RIKEN</i>
MORI, Toshinori	<i>International Center for Elementary Particle Physics, UT</i>
TAKAHASHI, Hiroyuki	<i>Department of Nuclear Engineering and Management, Graduate School of Engineering, UT</i>

